

INTEGRATED PACKAGING SOLUTIONS AND HOTPLATES FOR A MINIATURE ATOMIC CLOCK AND OTHER MICROSYSTEMS

THÈSE N° 6020 (2013)

PRÉSENTÉE LE 6 DÉCEMBRE 2013

À LA FACULTÉ DES SCIENCES ET TECHNIQUES DE L'INGÉNIEUR
LABORATOIRE DE PRODUCTION MICROTECHNIQUE 2
PROGRAMME DOCTORAL EN SYSTÈMES DE PRODUCTION ET ROBOTIQUE

ÉCOLE POLYTECHNIQUE FÉDÉRALE DE LAUSANNE

POUR L'OBTENTION DU GRADE DE DOCTEUR ÈS SCIENCES

PAR

Fabrizio VECCHIO

acceptée sur proposition du jury:

Prof. P.A. Farine, président du jury
Prof. P. Ryser, Dr T. Maeder, directeurs de thèse
Dr C. Affolderbach, rapporteur
Dr D. Jurkow, rapporteur
Prof. H. Shea, rapporteur



ÉCOLE POLYTECHNIQUE
FÉDÉRALE DE LAUSANNE

Suisse
2013

*Ad Alessandro:
che questo manoscritto ti ispiri a compiere grandi opere nella tua vita*

La vita è troppo breve per sprecarla a realizzare i sogni degli altri.

Oscar Wilde
1854-1900

Abstract

This thesis aimed at developing innovative packaging solutions for a miniature atomic clock and other microsystems in the cm-scale, i.e. somewhat larger than what is practical for full "chip-scale" device-package integration using clean-room technologies for fabrication of microelectromechanical systems (MEMS). Besides well-defined and robust mechanical attachment, such packaging solutions must provide reliable electrical interconnection with the other system components, and, if needed, additional functions such as local temperature control, insulation from electrical magnetic or temperature perturbations, chemical separation (hermeticity).

In order to accomplish this objective, different packaging technologies and modules were developed, fabricated and characterized in the frame of this thesis, with particular emphasis on the packaging of a miniature double-resonance (DR) rubidium atomic clock, which is an ideal demonstration platform given the associated large variety of requirements.

First, the possibility of encapsulating the reactive Rb metal in ceramic / glass substrates using soldering was explored, with the aim to achieve simple and reliable fabrication of miniature atomic clock elements such as the reference cell and the Rb lamp. After a thorough literature review investigation of the metallurgical interactions between rubidium and materials used in packaging such as solder (Sn, Pb, Bi..) and thick-film metallizations metals (Ag, Pd, Au, Pt...), an innovative design for a Rb reference cell (dimensions $10 \times 12 \text{ mm}^2$) is presented. The cell is based on a multifunctional low-temperature cofired ceramic (LTCC) spacer, closed by two glass windows allowing light transmission and acting as lids. Bonding is achieved by low-temperature soldering, avoiding exposing Rb to high temperatures.

The use of LTCC as the main substrate material for Rb vapor cells in principle allows further integration of necessary functions for the Rb lamp and reference cell, such as temperature regulation, excitation / microwave resonator electrodes, impedance-matching passive components (lamp), and coil for static magnetic field generation (reference). In this work, to test the hermeticity of the bonding, a pressure sensor was integrated into the cell by replacing one of the glass windows by a membrane comprising an integrated piezoresistive Wheatstone bridge. In this frame, a new lamination technique for LTCC is proposed. The technique consists in applying a hot-melt adhesive on top of the LTCC green tape, and allows good bonding of the tapes even at low lamination pressure. This technique is particularly attractive for the lamination of LTCC microfluidic devices or membrane pressure sensors, because the low pressure applied during lamination does not affect the shape of the channels in a microfluidic device, or the membrane of the sensor. The resulting cells are shown to be hermetic, and a Rb response could be measured by the project partners. However, heating resulted in loss of this response, indicating Rb depletion by undesired reactions between Rb and the sealing metals or contaminants. This result is somewhat in line with studies made in

parallel with the present work on low-temperature indium thermocompression bonding. Therefore, although the results are promising, further optimisation of metallizations, solders and package design is required.

An important generic function that may be integrated into LTCC is temperature control. In this frame, a multifunctional LTCC hotplate was designed, fabricated and studied. This device allows controlling the temperature of any object in the cm-scale, such as the abovementioned Rb vapor cells (reference or lamp) and other temperature-sensitive elements used in miniature atomic clocks such as lasers and impedance-matching passive components. Full thermal analysis, mathematical calculations, finite-element simulations and laboratory experiments were performed. The excellent structurability and modest thermal conductivity of LTCC make it much better suited than standard alumina for integrated hotplates, resulting in conduction losses in the LTCC structure being small compared to surface losses by conduction and convection. It is therefore concluded that insulation and/or vacuum packaging techniques are necessary to achieve optimized low-power operation.

Although we have seen that LTCC is an excellent integrated packaging platform, there are some limitations for carrying relatively massive components such as the DR atomic clock resonator cavity structure, which in general is a solid metal part. Therefore, an alternative hotplate technology platform, was developed, based on the combination of standard fiberglass-reinforced organic-matrix printed-circuit board (PCB), combined with thick-film alumina heaters. The PCB acts as high-strength, low-cost and readily available mechanical carrier, electrical interconnect and thermal insulator, and the thick-film heaters provide local temperature regulation, with the high thermal conductivity of alumina ensuring good local temperature uniformity. Therefore, such a hybrid PCB- Al_2O_3 platform constitutes an attractive alternative to LTCC hotplates for benign operating conditions.

In conclusion, this work introduced several innovative packaging solutions and techniques, which were successfully applied to various dedicated modules carrying the elements of miniature atomic clocks. Beyond this application, these developments allow us to envision efficient packaging of a wide variety of new miniature devices. Also, new areas for further investigations are suggested, such as long-term metallurgical interactions of alkali metals with solders, hermeticity, optimization of temperature distribution and thermal insulation techniques, as well as reliability at high-temperatures and under severe thermal cycling.

Keywords: Miniature atomic clock, electronic packaging of microsystems, LTCC technology, low-pressure lamination.

Abstract (Italiano)

Lo scopo di questa tesi era di sviluppare soluzioni innovative per il packaging di un orologio atomico in miniatura ed altri microsistemi di dimensioni nell'ordine di qualche cm, quindi leggermente più grandi di un microsistema "chip scale", completamente assemblato in camera pulita. Oltre a ben definite e robuste connessioni meccaniche, tali soluzioni di packaging devono garantire un'affidabile interconnessione elettrica tra tutti i componenti del microsistema e, se necessarie, altre funzioni come il controllo della temperatura locale, isolamento e schermatura da perturbazioni elettriche o magnetiche, ermeticità.

Al fine di raggiungere questo obiettivo, nel corso di questa tesi differenti tecnologie di packaging sono state studiate e differenti moduli sono stati concepiti, fabbricati e caratterizzati, con particolare enfasi sul packaging di un orologio atomico double-resonance (DR) a rubidio, che è una piattaforma dimostrativa ideale per questa applicazione, data la complessità del sistema e la grande varietà di requisiti associati.

Lo studio è iniziato con l'esplorare la possibilità di incapsulare il rubidio, metallo alcalino molto reattivo, tra un substrato di vetro e uno di ceramica saldati tra di loro, con lo scopo di proporre una procedura semplice ed affidabile per la produzione di importanti componenti dell'orologio atomico, come la cellula di riferimento e la lampada Rb. Dopo un riesame approfondito delle interazioni metallurgiche che accadono tra il Rb e i materiali utilizzati per la saldatura (Sn, Pb, Bi...) e le tipiche metallizzazioni utilizzate nella tecnologia thick film (Ag, Pd, Au, Pt...), la tesi presenta un design innovativo per la cellula di riferimento (dimensioni di $10 \times 12 \text{ mm}^2$). La cellula è costituita da un modulo in LTCC (Low-Temperature Co-Fired Ceramics), saldato con due finestre in vetro che permettono il passaggio del fascio di luce proveniente dalla lampada Rb o dal modulo laser.

L'utilizzo di un modulo LTCC nella cellula permette l'integrazione di importanti funzioni supplementari, come il controllo di temperatura, l'aggiunta di elettrodi di eccitazione e di risonatori per la lampada Rb, l'aggiunta di componenti passivi come filtri LC e bobine. Per testare l'ermeticità della saldatura, un sensore di pressione è stato integrato nel modulo LTCC, rimpiazzando una delle finestre in vetro con una membrana di resistenze piezoresistive collegate in configurazione ponte di Wheatstone. Nello sviluppo di questo sensore abbiamo concepito una nuova tecnica per la laminazione LTCC. La tecnica introdotta prevede l'applicazione di una colla a caldo sulla superficie di ogni strato di LTCC durante la fabbricazione. Grazie alla presenza della colla a caldo, è possibile ottenere una buona interpenetrazione dei differenti strati LTCC e una conseguente buona solidificazione del modulo, anche applicando bassa pressione durante la laminazione. Questa tecnica si presta in maniera ottimale alla fabbricazione di dispositivi microfluidici o sensori di pressione a membrana in LTCC, in quanto la bassa pressione applicata durante la laminazione non influisce sulla forma dei canali in un dispositivo microfluidico, o sulla

membrana del sensore. Le cellule in Rb fabbricate sono ermetiche, la presenza di Rb è stata comprovata dai nostri partner di ricerca. Tuttavia, il riscaldamento della cellula provoca la repentina perdita del segnale di Rb nella cellula, indicando probabile eccessiva reattività del metallo alcalino. Questo risultato è in linea con gli studi effettuati in parallelo con il presente lavoro sulla termocompressione dell'indio a bassa temperatura. Anche se i risultati sono molto promettenti, un'ulteriore ottimizzazione delle metallizzazioni, saldature e del design del modulo di packaging deve essere effettuato.

Un'importante funzione generica che può essere integrata in un modulo LTCC è il controllo della temperatura. Per questo motivo, una placca riscaldante multifunzione in LTCC è stata progettata, realizzata e studiata. Il dispositivo fabbricato consente di controllare la temperatura di qualsiasi oggetto di dimensioni comprese nel range di qualche cm, come le summenzionate cellule di riferimento Rb e altri elementi termosensibili usati nell'orologio atomico, come i laser e i componenti passivi. Un'analisi termica completa, con calcoli matematici, simulazioni agli elementi finiti ed esperienze in laboratorio, è stata effettuata sul modulo prodotto. L'eccellente strutturabilità e la modesta conducibilità termica dell'LTCC rendono questo materiale molto più adatto dell'allumina standard per la fabbricazione di moduli di riscaldamento, anche se tali placche riscaldanti in LTCC presentano comunque importanti perdite termiche, sia per conduzione che per convezione. Si conclude pertanto che un'efficiente isolamento termico e/o tecniche di packaging a bassa pressione sono necessarie per ottenere buone performance.

Nonostante l'LTCC sia una soluzione eccellente per il packaging integrato di microsistemi, vi sono limitazioni quando vi è la presenza di componenti le cui dimensioni superano i cm e relativamente pesanti, come la cavità risonante nell'orologio atomico DR. Pertanto, una soluzione alternativa per placche riscaldanti è stata sviluppata. Questa soluzione prevede la combinazione di PCB standard organico rinforzato di fibre di vetro con mini-riscaldatori in allumina basati sulla tecnologia thick-film. Il PCB è un supporto a basso costo e facilmente reperibile, e ad alta resistenza meccanica; i mini-riscaldatori forniscono controllo di temperatura locale e, grazie alla buona conducibilità termica dell'allumina, assicurano buona uniformità della temperatura. Pertanto questi sistemi PCB-Al₂O₃ costituiscono un'ottima alternativa alla placca riscaldante LTCC in condizioni operative benigne.

Questa tesi ha introdotto diverse soluzioni per il packaging di un orologio atomico in miniatura. Al di là di questa applicazione, i moduli presentati consentono di immaginare un packaging efficiente per una vasta gamma di microsistemi. Inoltre, nuove aree per ulteriori indagini si sono aperte, come studi a lungo termine sull'interazione metallurgica tra metalli alcalini con saldature, ottimizzazione del controllo di temperatura, tecniche per l'isolamento termico, affidabilità dei sistemi ad alte temperature e a diversi severi cicli termici.

Parole chiave: Orologio atomico miniatura, packaging elettronico di microsistemi, tecnologia LTCC, laminazione a bassa pressione

Acknowledgments

Writing the acknowledgments is something special....you feel like at the end of a long journey, an important step of your life is over. Many things come into my mind: I have crossed many persons during these years and want to thank them for their participation, their help or simply for their friendship....

I want to start with the two principal persons in charge of my success of today: my thesis director, Prof. Peter Ryser, and my co-director, Dr. Thomas Maeder. Prof. Ryser gave me the possibility to start the PhD in LPM, a very well equipped lab with many stimulating ideas. He was always available and ready to dispense advices, and not only from a scientific point of view. He is a true example to follow for everyday life, his values of honesty, work and respect became my values as well. Dr. Thomas Maeder, my thesis co-director, believed in me also in the worst moments, even when nobody trusted in me anymore, neither myself. I will never forget the words “Fabrizio....rigueur, rigueur, RIGUEUR!!!”. During these four years he was not only a simple co-director: he was for me a professor, a mentor, an example, a coach, a motivator, a friend. My success is almost all the success of these two persons: they took, in 2009, a young engineer, polite and well prepared, and they transform him into a professional, a doctor with high technical skills, sure of himself and attached to important values such as family and respect. I will be eternally indebted with them.

My colleague Conor Slater deserves also a special mention. His large knowledge of the electronic world was for me a source of inspiration and a motivation to improve and learn more and more. His kindness and his availability are rare to find, and with his precious help I solved many problems that I was not able to solve by myself, so a part of this PhD is also for him! Thank you, “Engineer Slater”, and all the best!

Moreover, I gratefully thank:

- Prof. Farine Pierre André, Prof. Herbert Shea, Dr. Christoph Affolderbach, Prof. Dominik Jurków for kindly accepting to be the members of the thesis jury for the private defense and for having read my thesis;
- Dr. Yannick Fournier, who received me at LPM in July 2009 and taught me many things, including LTCC circuit design and fabrication;
- My colleague Gael Farine: it was great to share the office with you, Gael, great moments. I also thank you for the scientific discussions and opinion exchanges we had;
- My colleague Bo Jiang: we worked in close collaboration for the low-pressure lamination technique....it was a hard work, thanks for the collaboration and the support;

Acknowledgments

- Madame Karine Genoud, probably the best secretary in the world. She is able to organize all our stuff in the lab, and she always proposes nice things such as Christmas dinners or activities to perform together. These things enrich the lab of team attitude and friendship, thank you!
- Dr. Vinu Venkatraman : the first year was hard for both, but finally we both arrived at the end. Congratulations for your PhD, Dr. Vinu, and thanks for the close collaboration and also for the nice funny moments together. Almost all, thanks for having encouraged me at the beginning of the PhD, when everything looked dark to me!!
- Mr. Matthias Garcin: thank you for being always available to perform the work we asked you in the best way. Even if you pretend to be bad, we all know that you are a very nice person!!!
- The Swiss National Science Foundation for funding our research project and all the members of the MACQS project for their participation, discussion, meetings and aperos!
- Finally, all the members of LPM (and in particular again Bo, Conor and Gael) for the joyful moments spent together eating, drinking, running, making sports, dancing and so on..

I reserve these last lines for my family. First, thanks to my brother Massimo and to my sister Silvia, for their continuous support through my years of study, for their precious advices, for being always ready to help me and also for the nice and happy moments spent together. Special thanks to Massimo for the help he gave me in many topics such as informatics, in which I am not exactly the best, and also for fixing my computer when it doesn't work!!!!

Thanks to my parents, Antonio Vecchio e Luisa De Astis. The unconditional love that you feel for me is something special. Even in the darkest moments, when everything goes wrong for me, I have these two persons that will always love me and do everything to help me. If today I am this kind of person, it is mainly because of your education, for the values and the love that you were able to transmit to me. So, really, there is no word to express my infinite gratitude to you: I can also say that I am proud to be your son.

Finally, I want to mention my better half, Anabela. Thanks for your support and your encouragements during the bad moments. Thanks for your smile, for your eternal good mood, for being so special, and for the true love you feel for me. Thanks for being you, simply, my eternal love, my special, very, very important person... And, almost all, thanks for giving me the most precious thing of my life: Alessandro. I love you both.

Ringraziamenti

Scrivere i ringraziamenti è qualcosa di speciale.... ci si sente alla fine di un lungo viaggio, una tappa importante della mia vita è finita. Molte cose mi tornano alla mente: ho incorciato diverse persone in questi anni e voglio ringraziare tutti per la loro partecipazione, il loro aiuto o semplicemente per la loro amicizia....

Voglio iniziare con i due principali responsabili del mio successo di oggi: il mio direttore di tesi, il Prof. Peter Ryser, e il mio co-direttore, il Dottor Thomas Maeder. Il professor Ryser mi ha dato la possibilità di iniziare il dottorato di ricerca all'LPM, un laboratorio molto ben attrezzato e con tante idee stimolanti. Era sempre disponibile e pronto a dispensare consigli, e non solo da un punto di vista scientifico. Il professore è un vero esempio da seguire per la vita quotidiana, i suoi valori di onestà, di lavoro e rispetto sono diventati anche i miei valori. Il Dr. Thomas Maeder, il mio co-direttore di tesi, ha creduto in me anche nei momenti peggiori, anche quando nessuno aveva più fiducia in me, nemmeno io stesso. Non dimenticherò mai le sue parole " Fabrizio rigore, rigore, rigore ! ". Durante questi quattro anni Thomas non è stato un semplice co- direttore: è stato per me un professore, un mentore, un esempio, un allenatore, un motivatore, un amico. Il mio successo è dovuto a queste due persone, ed è dunque anche il loro successo: hanno preso, nel 2009, un giovane ingegnere, educato e ben preparato, e lo hanno trasformato in un professionista, un dottore con elevate competenze tecniche, sicuro di sé e attaccato a valori importanti come la famiglia e il rispetto. Sarò eternamente indebitato con loro .

Anche il mio collega Conor Slater merita una menzione speciale. La sua grande conoscenza del mondo elettronico è stata per me una fonte di ispirazione e una motivazione per migliorare e imparare sempre di più. La sua gentilezza e la sua disponibilità sono rari da trovare, e con il suo prezioso aiuto ho risolto molti problemi che non ero in grado di risolvere da solo, per cui una parte di questo dottorato è anche sua! Grazie, "Engineer Slater", e buona continuazione!

Inoltre, ringrazio di cuore:

- Prof. Farine Pierre André , Prof. Herbert Shea , Dr. Christoph Affolderbach , Prof. Dominik Jurkow per aver gentilmente accettato di essere i membri della giuria tesi per la difesa privata e per aver letto la mia tesi;
- Dr. Yannick Fournier, che mi ha accolto all'LPM nel luglio 2009 e mi ha insegnato molte cose , compresa la fabbricazione di circuiti LTCC;
- Il mio collega Gaël Farine: è stato bello condividere l'ufficio con te, Gaël, gran bei momenti. Ti ringrazio anche per i dibattiti scientifici e gli scambi di opinione che abbiamo avuto;

Ringraziamenti

- Il mio collega Bo Jiang: abbiamo lavorato in stretta collaborazione per la tecnica di laminazione a bassa pressione.... è stato un duro lavoro, grazie per la collaborazione e il sostegno;
- Karine Genoud, probabilmente la migliore segretaria del mondo. Lei è in grado di organizzare tutte le nostre cose in laboratorio , e propone sempre belle iniziative come cene di Natale o di attività da svolgere insieme . Queste cose arricchiscono il laboratorio di spirito di squadra e di amicizia , grazie!
- Dr. Vinu Venkatraman: il primo anno è stato difficile per entrambi, ma alla fine siamo entrambi arrivati alla fine . Congratulazioni per il tuo dottorato, Dr. Vinu, e grazie per la collaborazione e anche per i momenti divertenti piacevoli insieme. Soprattutto , grazie per avermi incoraggiato ad inizio del dottorato, quando tutto sembrava buio per me !
- Matthias Garcin: grazie per essere sempre a disposizione e per eseguire il lavoro che ti chiediamo nel migliore dei modi. Anche se fai finta di essere cattivo, sappiamo tutti che sei una brava persona !
- Lo “Swiss National Science Foundation” per aver finanziato il nostro progetto di ricerca e tutti i membri del progetto MACQS per la loro partecipazione, discussione, incontri e aperitivi!
- Infine, tutti i membri dell’LPM (e in particolare di nuovo Bo , Conor e Gael) per i momenti gioiosi trascorsi insieme a mangiare, bere, correre, fare sport, fare festa....

Mi riservo queste ultime righe per la mia famiglia . Grazie a mio fratello Massimo ed a mia sorella Silvia, per il loro continuo supporto durante i miei anni di studio, per i loro preziosi consigli, per essere sempre pronti ad aiutarmi nel momento del bisogno e per i momenti piacevoli e felici trascorsi insieme. Un ringraziamento speciale a Massimo per l'aiuto che mi ha dato in molte materie come l'informatica, in cui io non sono proprio il massimo, e anche per aggiustare il mio computer ogni volta che non funziona ! !

Grazie ai miei genitori, Antonio Vecchio e Luisa De Astis . L'amore incondizionato che provano per me è qualcosa di speciale. Anche nei momenti più bui, quando tutto va male per me, avrò sempre i miei genitori che mi amano e pronti a fare tutto per aiutarmi. Se oggi sono la persona che sono, è soprattutto grazie della vostra educazione, ai valori e all'amore che siete stati in grado di trasmettermi. Davvero, non ci sono parole per esprimere la mia infinita gratitudine per voi: posso solo dire che sono orgoglioso di essere vostro figlio .

Infine, “dulcis in fundo”, riservo le ultime righe per la mia dolce metà, Anabela. Grazie per il tuo sostegno e i tuoi continui incoraggiamenti nei momenti difficili. Grazie per il tuo sorriso, per il tuo eterno buon umore, per essere così speciale, e per l'amore che provi per me . Grazie per essere te, semplicemente. Sei il mio eterno amore, la mia persona molto, molto speciale,... e, soprattutto, grazie per avermi dato la cosa più preziosa della mia vita: Alessandro. Vi amo entrambi.

Table of Contents

Abstract.....	i
Abstract (Italiano).....	iii
Acknowledgments	v
Ringraziamenti.....	vii
Table of Contents	ix
List of abbreviations and symbols	xiii
Abbreviations	xiii
Symbols	xiv
1 Introduction.....	1
1.1 Challenges in Microsystem Packaging	1
1.2 Overview of Miniature Hotplates.....	2
1.3 The MACQS Project	7
1.3.1 The objective of our laboratory in the project	7
1.4 Thesis Structure.....	8
2 State of the Art	11
2.1 History of Time Measurement	11
2.2 Atomic Clocks: Compromise between precision and dimensions	13
2.3 Double Resonance Atomic Clock: Principle of Functioning and Block Diagram.....	14
2.4 State of the art of Chip Scale Atomic Clocks.....	17
2.5 LTCC Technology: What it is.....	21
2.6 LTCC Circuit Manufacturing.....	22
2.6.1 Materials involved	23
2.6.2 Slitting, blanking, pre-conditioning the green tape	25
2.6.3 Via punching - laser cutting.....	25
2.6.4 Via filling – screen printing.....	26
2.6.5 Stacking and lamination	27
2.6.6 Firing	28

Table of Contents

2.6.7	Post-firing and post-processing	30
2.6.8	Final inspection and test	30
2.7	Rubidium: Properties, behaviour & Dispensing methods.....	31
2.7.1	Summary of reaction of Rb with other elements	34
2.7.2	Review of Rb/Cs dispensing method.....	37
3	Reference cell of Atomic Clock: Design, Fabrication and Test	39
3.1	The Reference Cell: the Original Concept Idea	39
3.2	Metallurgical Interactions in the Reference Cell System.....	41
3.2.1	Interactions between Rb and metallization metals	41
3.2.2	Reactions between Rb and solder metals	43
3.2.3	Conclusions of the metallurgical literature analysis.....	49
3.3	Innovative and Practical Solution proposed for Rb Handling.....	49
3.3.1	Study of gas dissolution into the dodecane	50
3.4	Refined Design of the Cell and Test Modules Developed	54
3.4.1	Principle of functioning of the integrated pressure sensor	55
3.5	Fabrication of the Cell.....	56
3.5.1	Design of LTCC spacer	56
3.5.2	Fabrication of LTCC spacer	59
3.5.3	Fabrication of glass windows	60
3.5.4	Rb dispensing and sealing	60
3.6	Wetting Tests.....	60
3.6.1	Procedure and melting profile	61
3.6.2	Wetting tests on LTCC substrate.....	62
3.6.3	Summary of wetting tests on LTCC	67
3.6.4	Wetting tests on glass substrate	67
3.6.5	Conclusions of the wetting tests	69
3.7	Test Bench for Testing the Hermeticity of the Sealing.....	69
3.8	Results of the Hermeticity Test.....	70
3.8.1	Reaction to pressure changes.....	71
3.8.2	Reaction to temperature changes	75

3.8.3	Long-term measurements	77
3.8.4	Discussion of the results of the hermeticity tests	80
3.9	Test Performed on Cells with Rb	80
3.10	Conclusions	83
3.11	Possible Improvements to this Technique.....	84
4	New lamination technique for LTCC.....	85
4.1	Introduction	85
4.2	State of the Art of Lamination Techniques for LTCC	87
4.2.1	Application of adhesive tape	87
4.2.2	Application of solvents or glues	88
4.2.3	Application of a sacrificial layer or of an insert material	89
4.2.4	Conclusion: need to introduce a new technique	90
4.3	Basic Idea of the Developed Technique.....	90
4.4	Composition of the Adhesive Layer.....	92
4.5	Fabrication Parameters	93
4.6	Results	95
4.6.1	Densification.....	95
4.6.2	Membrane flatness.....	96
4.6.3	Effect of the adhesive layer on the piezoresistive paste	98
4.7	Conclusions and outlook	99
5	Thermal studies on LTCC.....	101
5.1	Introduction	101
5.2	Design and Fabrication of the LTCC Heater	102
5.2.1	Concept and design of the device	102
5.2.2	Fabrication and description of the device.....	102
5.3	Thermal Analysis of the Designed Device.....	105
5.3.1	Physical and thermal analysis.....	105
5.4	Thermal Simulations Performed	110
5.4.1	Simulation of the effects of free convection.....	116
5.5	Experimental Results.....	117

Table of Contents

5.5.1	Thermal conductivity measurement system	119
5.5.2	Best heating performance – experimental configuration.....	120
5.5.3	Comparison between the best heating performance and the ideal one.....	122
5.6	Discussion of the Results	123
5.7	Conclusions	124
6	Packaging Solutions Provided for Microsystems.....	125
6.1	Introduction	125
6.2	The Frequency-stabilized Laser	125
6.3	Integrated Mini-lamp Module	128
6.3.1	Alternative Solution for the Packaging of the Rb mini-lamp	131
6.4	Miniature Double-Resonance Atomic Clock	135
6.4.1	Refined packaging system for microwave cavity.....	136
6.4.2	The assembled miniature atomic clock demonstrator	140
6.4.3	Performance and comparison with the device currently on the market	141
7	Conclusions.....	145
7.1	Summary	145
7.2	Hermetic package for Rb vapor cell.....	146
7.3	Low-pressure, low-temperature lamination of LTCC.....	146
7.4	LTCC hotplate.....	147
7.5	Applications and PCB-ceramic hybrid hotplate for large payloads.....	148
	References.....	151
	Curriculum Vitae.....	167

List of abbreviations and symbols

Abbreviations

ATBC	Acetyl Tributyl Citrate
CPT	Coherent Population Trapping
CTE	Coefficient of Thermal Expansion
DBD	Dielectric Barrier Discharge
DR	Double Resonance
EC	Ethylcellulose
HTCC	High Temperature Co-Fired Ceramics
HTCR	Hot Temperature Coefficient of Resistance
LGR	Loop Gap Resonator
LTCC	Low Temperature Co-Fired Ceramics
MCM	Multi-Chip Module
MEMS	MicroElectroMechanical System
MLC	Multi-Layer Ceramic
PCB	Printed Circuit Board
PEG-400	Polyethylene glycol (molecular weight ~ g/mol)
PVB	Polyvinylbutyral
RMA	Rosin Mildly Activated
SMD	Surface Mounted Device
TEG-EH	Triethylene glycol bis (2-Ethylhexanoate)
VCSEL	Vertical Cavity Surface Emitting Laser

List of Abbreviations and Symbols

Symbols

h	Convection film coefficient
H	Henry's coefficient
k	Thermal conductivity
L	Length
Nu	Nusselt number
p	Pressure
P	Power
Pr	Prandtl number
Q	Heating power
Ra	Rayleigh number
S	Cross section
T	Temperature
ρ	Electrical resistivity
σ	Standard deviation, electrical conductivity (depending on the case)
$\sigma^2(\tau)$	Allan variance
$\sigma(\tau)$	Allan deviation
σ_r	Flexural strength (rupture stress)

1 Introduction

This thesis aimed at developing integrated packaging solutions and miniature heating plates in the cm-scale. In this introduction, after a brief glance of the issues involved with microsystem packaging, an overview of miniature hotplates is given. Low-Temperature Co-fired Ceramic (LTCC) is widely used for this application, as it combines good efficiency and relative low manufacturing cost. However, according to the user's needs, such hotplates may be not the best solution, especially when a heavy device should be temperature-stabilized. After introducing LTCC heating plate, the concept of an innovative hotplate developed in the frame of this thesis is presented, and finally the technological and scientific objectives of this thesis are given.

1.1 Challenges in Microsystem Packaging

Micromachined sensors and microsystems have made significant progress during the past two decades and many devices have been successfully presented or commercialized for a large number of applications, such as pressure sensors and transducer for automotive and industrial processing applications [1]–[4], accelerometers and inertial sensors for consumer applications [5]–[9], microsystems for industrial process control [10], [11]. Other devices are acquiring a large volume of commercial market, such as Microelectromechanical systems (MEMS) for optical communications systems (optical MEMS) [12]–[15], MEMS for wireless communication systems (RF MEMS) [16], [17], and biomedical microsystems [18]–[20]. All these applications need a reliable, stable and low-power packaging solution, which often causes an improvement of the performance of the microsystem [21]. Several are the technological challenges related with the packaging of a microsystem. These can be categorized under four general topics:

- Mechanical attachment
- Electrical connection
- Temperature control
- Encapsulation and protection

Figure 1. 1 shows an example of an efficient packaging solution for a microsystem.

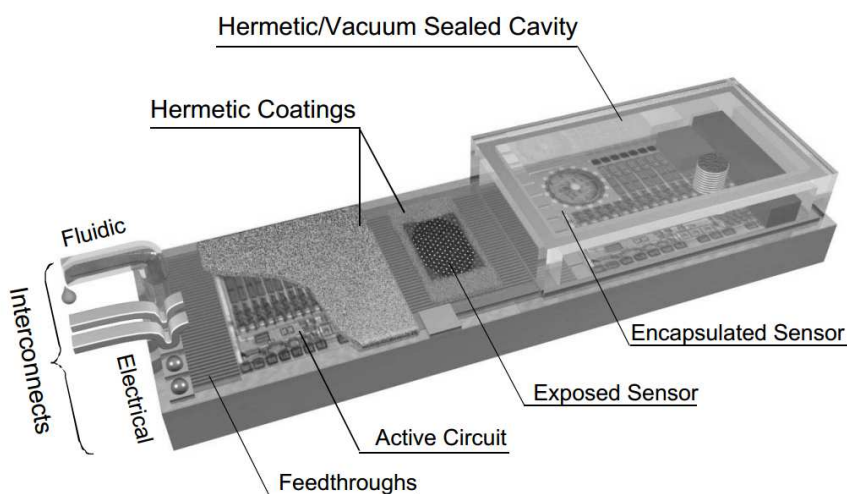


Figure 1. 1: Packaging and interconnection for a microsystem. Image taken from [22].

In particular, the elements of a microsystem need to be attached mechanically to the main body with a robust connection, and reliable electrical connections must be provided. Moreover, some components need to work at a well-defined temperature. Some parts of the microsystem may need to be encapsulated or hermetically sealed; in some instances a vacuum medium which is stable over many years is required (such as in the reference cell of an atomic clock). Often, the packaging should be resistant to harsh environments (such as for a MEMS for space technology); in other cases, it needs to be compatible with the media it operates in (as for example in biomedical microsystems). In this thesis, there is a review of the current technologies used for the packaging of a microsystem, with particular emphasis on mesoscale (cm-scale) systems. After the global literature review, we focused our attention on different mesoscale systems: the packaging requirements of such microsystems were stated, and finally we provided an efficient packaging solution which ensured mechanical attachment, electrical connection, thermal control and protection of the sensible parts of the microsystem.

1.2 Overview of Miniature Hotplates

Miniature hotplates are widely used in microelectronics and in particular in microsystems or systems-on-a-chip, whenever there is the need for local temperature regulation (see for example [23]–[32]). A miniature hotplate mainly consists of a small substrate with an electric heating resistor integrated on it. Usually, it is also equipped with a temperature sensing resistor, which provides a precise measurement of the actual temperature and therefore allows precise temperature control. MEMS microheaters, with lateral dimensions ranging from ca. 20 μm to 500 μm , typically use a platinum heating and sensing resistor in

form of serpentine. The use of one single resistor which acts as heater and temperature sensor at the same time allows a significant reduction of the dimensions of the hotplate. Because of its very small size, which limits the surface losses by convection and radiation, the power consumption of a MEMS microheater is very reduced, it can achieve temperatures of 500°C with less than 1 W input power [24], [29]. Such heaters are designed to control the temperature of devices in the mm scale; when an object of larger dimensions must be temperature-stabilized, a MEMS microheater becomes too expensive to fabricate. Moreover, MEMS heaters are too fragile to carry a heavy device. Whenever there is the need to control the temperature of a device in the cm scale, other kinds of hotplates, still miniature, but not in the MEMS scale, are used, and this particular area of research was the main topic of this thesis. The work presented here focuses on different solutions for miniature hotplates in the cm scale. Such hotplates consume more power in comparison to MEMS, and, due to their larger dimensions, natural convection in air becomes an important factor; therefore thermally insulating the hotplate becomes a stringent requirement to get a satisfactory heating performance in terms of power consumption. In this specific area (miniature hotplates in the cm scale), one possible solution, widely used and illustrated in the literature with various examples, is to use LTCC (Low Temperature Co-fired Ceramic) technology (for more details about LTCC technology, see chapter 2). LTCC technology, as highlighted by Dr. Fournier in his thesis [33, p. 18] came to fill a technological gap, between MEMS and macrosystems. Before the development of LTCC technology, in the early 1980's, there was a dimensional gap between MEMS (20 to 500 μm) and macrosystems (from 2 cm on), covered only to a limited extent by classical thick-film technology on ceramic / glass substrates, and that gap is now well covered by LTCC, which allows easy fabrication of devices in the range 1 mm to several cm. LTCC is a particular material, mainly constituted by a mixture of ceramics and glass. In particular, LTCC is a dielectric substrate (dielectric constant between 6 and 7) with relatively good thermal conductor ($k \approx 3 \text{ W} \cdot \text{m}^{-1} \cdot \text{K}^{-1}$). The modest dielectric constant of LTCC and low loss at high frequencies, allow the widespread of this technology to microwave and HF circuits. Moreover, LTCC technology, thanks to its excellent 3D structurability, gives the possibility to fabricate complicated devices, with different shapes, holes and cavities. With LTCC we can fabricate multi-layer modules; therefore we can integrate in one small device the heating resistor on one layer and the temperature sensing resistor on the other layer. Keeping these two elements separated allows a better and more precise temperature regulation. Thanks to the mentioned characteristics, together with reduced fabrication cost, LTCC is now widely used for fabrication of miniature hotplates.

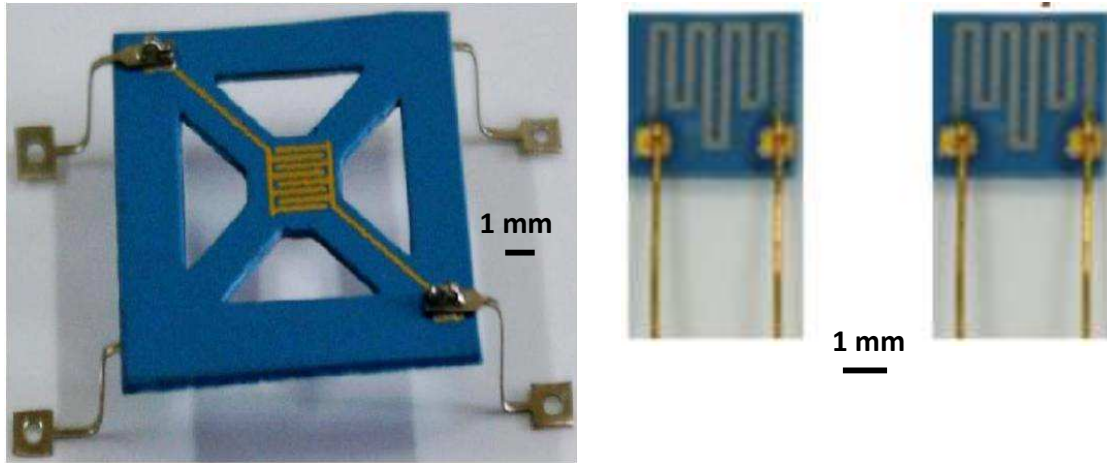


Figure 1. 2: Examples of LTCC hotplate. Images taken from [34], [35]

LTCC hotplates are designed for controlling the temperature of small devices. One of the limits of these heating modules is in fact the low flexural strength of LTCC materials (for example, for DuPont 951 green tape, $\sigma_r \approx 320$ MPa, [36]). This means that, in case this hotplate constantly carries a relatively heavy device, or it is constantly submitted to a mechanical stress, the lifetime of the LTCC hotplate becomes critical [37]–[39]. Another physical issue related with the fabrication and use of LTCC hotplates is the shrinkage mismatch between the tape and the screen-printed pastes. This aspect has been studied in details by Dr. Birol in his thesis [40], and discussed in some of his publications [41], [42]. The alternative presented in this thesis is the conception of single or multiple hotplates using a PCB as a mechanical support, and thick film alumina (Al_2O_3) heaters, bonded on the PCB support (see Figure 1. 3 for an example). This system offers numerous advantages with respect to the LTCC hotplate. In particular:

1. FR-4, the material used to fabricate PCB, is cheap and very robust (flexural strength = 550 MPa, [43]), so the system can withstand higher mechanical stress with respect to an LTCC hotplate.
2. FR-4, with its low thermal conductivity (Maueny estimated, in 2005, $k = 0.25 \text{ W} \cdot \text{m}^{-1} \cdot \text{K}^{-1}$, [44], while other research yields very similar values, see for example [45], [46] , is not only a support for the system, but it gives the possibility to create different thermally independent zones (see for example Figure 1. 3, a hotplate with three independent thermal zones). The creation of different thermal zones is further promoted by the presence of holes to better insulate the different zones.
3. Al_2O_3 has higher thermal conductivity than LTCC ($k \approx 30 \text{ W} \cdot \text{m}^{-1} \cdot \text{K}^{-1}$, [47]), which ensures a better temperature homogeneity within the heated part;

4. Thick film circuit is easier and cheaper to fabricate with respect to an LTCC module.

Table 1. 1 compares the properties of LTCC and FR4:

	LTCC (DuPont 951)	Standard FR-4
CTE (ppm/K)	5.8	14 to 17
Thermal conductivity ($\text{W} \cdot \text{m}^{-1} \cdot \text{K}^{-1}$)	3	0.25
Young's Modulus (GPa)	120	24
Density (g/cm^3)	3.1	1.9
Flexural strength (MPa)	320	550
Relative permittivity	7.8	4.8
Dissipation factor (at 3 GHz)	0.006	0.012

Table 1. 1: Comparison of the properties of LTCC DuPont 951 and standard FR4. LTCC data are taken from [36]. FR4 data are taken from [43], [44], [48].

So, from the above consideration, we can understand that this system combines the advantages of a PCB substrate (robust, cheap, thermally rather insulating, easy to machine) with those of a ceramic element (good thermal conductor, easy fabrication, stable, well-defined characteristics). An example of a multiple hotplate based on PCB and hybrid heater, developed in the frame of this work, is illustrated in Figure 1. 3.

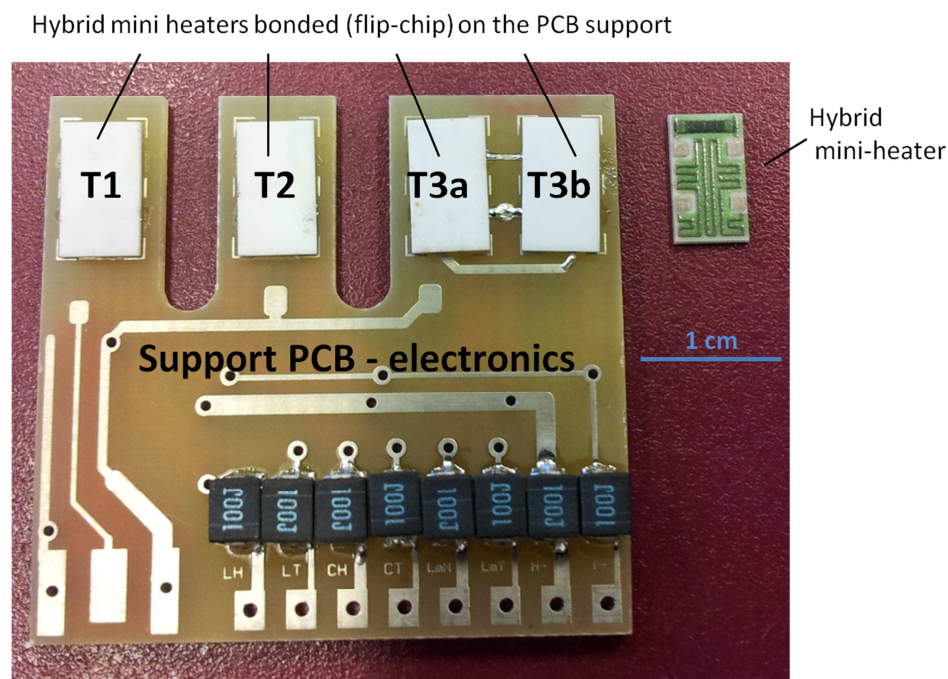


Figure 1. 3: The yellow is the PCB support which can optionally carry some electronics. The identical thick film mini-heaters are flip-chip soldered on top of the PCB support. In this case, three different, ideally independent temperature zones are created (T1, T2, T3), so we have a triple hotplate. The larger T3 is stabilized by two heaters connected in series.

This system has some drawbacks. In particular, the major issue is the difference in thermal expansion of the two materials involved: the Coefficient of Thermal Expansion (CTE) of FR-4 is between 14 to 17 ppm/K (as shown in Table 1. 1), while the Al_2O_3 has a CTE of ca. 6 ppm/K, [47]. This means that at high temperature, the different dilatation of the two materials may cause excessive stresses that may lead to the rupture of the system [49]–[51]. Moreover, the FR-4 cannot withstand continuously temperatures higher than ca. 200°C. In order to overcome the first problem, the ceramic heaters should be designed to be small enough, in order to limit the differential thermal dilatation; in case a large zone must be heated, more heaters can be connected side by side on the same zone, such as the zone T3 in the Figure 1. 3. Another important issue that should be taken into account is that many important physical properties of FR-4, such as thermal dilatation, thermal and electrical conductivity, permittivity, may change because of some factors such as ageing, humidity penetration and presence of solvent in the environment. Therefore, these systems are not always perfectly reproducible, and, when designing this kind of hotplate, one should take into account this, and ideally estimate and validate the physical properties of the hotplate through thermal simulations. However, using the due fabrication precaution, these systems become an

alternative to the LTCC for many applications where the temperatures to achieve are below ca. 180°C, and they are particularly attractive when the device to be temperature-stabilized is relatively heavy, because in this case an LTCC hotplate may not withstand the weight of the device. In the frame of this thesis, we were in general asked to provide accurate temperature control for devices in the cm scale. For each case, after a specific analysis, we chose the best suited technology, given the requirements and specifications.

1.3 The MACQS Project

Most of the work of this thesis was carried out in the frame of the Miniature Atomic Clocks and Quantum Sensors (MACQS) research project¹. The overall objective of this project was to develop reliable, ideally batch-fabricable processes to fabricate the key components of a Double Resonance (DR) Rubidium Compact Atomic Clock (for more details about the structure of the DR Rubidium Atomic Clock, see following chapter). The ambitious objective at the beginning of the project was to integrate the different components fabricated in a first clock demonstrator. The DR Atomic Clock uses a relatively large (in the cm scale) resonance cavity to apply a magnetic field which is resonant with the frequency of the light emitted by the alkali atoms at their hyperfine transition. The presence of this large cavity in the atomic clock, make this system larger in volume with respect to the other atomic clock using the Coherent Population Trapping (CPT) technique, in which the cavity is not present. The advantage is that DR allows a typically five times better short-term stability with respect to CPT [52]. The project involved different laboratories, each one with a different area of expertise, and each one with a different task, toward this common objective.

1.3.1 The objective of our laboratory in the project

The technological objectives of our lab, LPM, in the frame of the MACQS project, were mainly two:

- 1. Develop an efficient solution for the packaging of the atomic clock, providing proper interconnection of the various parts and local temperature control of some elements of the system;**
- 2. Develop a new and innovative design for the reference cell, using low-temperature sealing techniques.**

In order to accomplish the first objective, various miniature hotplates based on LTCC technology or on the alternative composed by the PCB + thick-film mini-heaters presented in Figure 1. 3, were designed and tested. According to the particular needs, we adopted the

¹ Swiss National Science Foundation "Sinergia" grant CRSI20-122693/1

technology that better fitted the application. In a DR atomic clock, the temperatures to achieve do not exceed 130°C, and the device to temperature-stabilize are in the cm-scale, so we are exactly in the case where the use of these devices is particularly attractive.

In order to accomplish the second objective, eutectic low-temperature solder pastes were investigated as a sealing solution instead of the traditional anodic bonding, which involves high temperatures and needs long time to be performed, therefore causing an important evaporation of the alkali metal during the sealing process.

A Ph.D. thesis is not only technology, but it is mostly science. So, beside the pure technological challenges, this thesis had also some crucial scientific aspects that had to be studied. The scientific objectives of this thesis were:

- **Study the metallurgic interactions between Rb and commonly-used solder materials and other metals such as Ag, Pd, Au:** this metallurgic investigation is needed to estimate the capability of the fabricated reference cell to keep the hermeticity without degradation by interdiffusion of Rb into the metals which may potentially constitute the sealing ring,
- **Advanced thermal investigation and modeling of the LTCC heating module and its materials:** LTCC dielectric itself, conductors, resistors: this thermal investigation is needed to ensure the most precise temperature control (ideally the cell should be temperature-stabilized with a precision of less than 0.01 K) and estimate the influence of conduction and convection losses to the heating power required.

1.4 Thesis Structure

This thesis report is constructed in the following way:

- **Chapter II** introduces the state of the art of time-measurement devices, giving particular emphasis to the atomic clock, which is to date the most modern and precise device conceived to give a time reference. The chapter continues with LTCC technology, describing the novelties and advantages that it brings, and the procedures to fabricate LTCC circuits and 3D structures. Finally, there is a description of elemental rubidium (together with the other metallic alkali elements); its chemical and physical properties are introduced in order to understand the issues that we may encounter when trying to hermetically encapsulate it. Moreover, together with a concept idea for the design and fabrication of the reference cell, there is a literature analysis of the metallurgical interactions between rubidium and the materials that may potentially be used for the sealing;
- **Chapter III** presents our innovative design for the cell, including an LTCC spacer to add special functions to the cell. Low-temperature eutectic solder alloys were used to

hermetically seal the Rubidium. In order to prove the hermeticity of different solder alloys and other bonding techniques, various tests were carried out using an electronic test bench. The results of these tests were also described in Chapter 3.

- **Chapter IV** presents an innovative LTCC lamination technique that we developed during our research to fabricate membrane pressure sensors. This technique, an improvement to the standard thermocompression technique, allows the application of low pressure during lamination, and may therefore be used to produce LTCC pressure sensors avoiding the typical membrane deflection due to excessive pressure applied during the lamination. The fabricated pressure sensors were used to monitor the pressure inside the reference cell of the atomic clock. The proposed technique is an innovative, efficient and practical solution for laminating delicate LTCC structures, avoiding the deformation of cavities or holes.
- **Chapter V** describes the LTCC multifunctional heating plate fabricated in the frame of this research. In order to estimate the power consumption of the device, an extensive thermal investigation was carried out, and also finite-element modeling was performed; the influence of conduction and convection on the heating is studied. The objective was to estimate the amount of heating power used by our LTCC module to heat the atomic clock components, in order to evaluate the suitability of the designed device for low-power operation of the miniature atomic clock.
- **Chapter VI** introduces the different packaging solutions provided for the atomic clock components. The packaging solutions include the use of LTCC technology, or standard thick film modules, or PCB. In most cases, the packaging solution provided allowed to reduce size and/or power consumption of an already existing microsystem. In other cases (like for the Rb Double Resonance demonstrator), the packaging solution allowed achieving proper and efficient connection of the key blocks of the microsystem, together with local temperature control.
- **Chapter VII** makes a summary of all the results achieved with an outlook on the possible future improvements of the techniques and devices described in this thesis.

2 State of the Art

This chapter will introduce the fundamental concepts needed for understanding the work of this thesis. The first introduced topic is the atomic clock: what it is, how it works, and the actual state of the art. Next, LTCC technology is introduced and discussed: what it is, the procedure to follow in order to produce LTCC circuits and 3D structures, and, the advantages it offers with respect to other technologies. Finally, we describe the Rb atom, since it will be used in the reference cell: its physical properties and its chemical behavior will be illustrated.

2.1 History of Time Measurement

The concept of time exists since the beginning of life in the world, and human being is actually governed by this concept. Philosophers say that time is part of the fundamental structure of the universe, a dimension independent of events, in which events occur in sequence. For sure, time is the concept to measure the duration of an event. Since thousands of years, Man invents and fabricates devices able to measure and keep track of time (Figure 2. 1, [53], [54]): the ancient Egyptians divided the day into two periods of 12 hours each, and used large obelisks (Figure 2. 1a) to track the movement of the Sun (so-called shadow clocks). The Ancient Greeks invented the water clocks (they called it *clepsydra*, (Figure 2. 1b) literallyly water thief), also employed by the Ancient Persians, to measure time. Another ancient device employed to measure time is the candle clock, used in China and Japan (Figure 2. 1c).

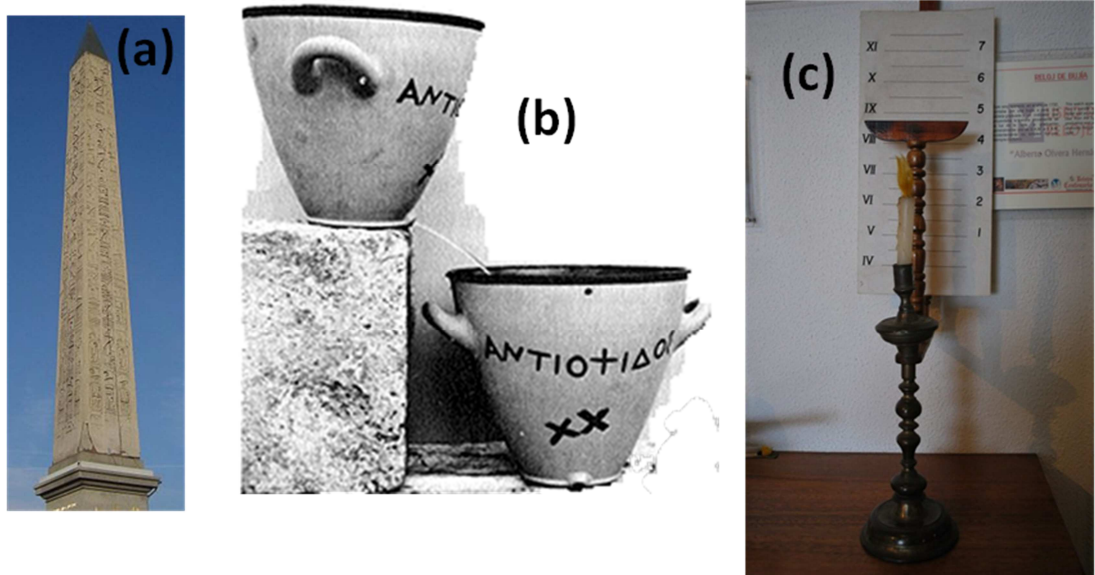


Figure 2. 1: (a) a shadow clock, in which the obelisk is used to follow the movement of the sun and have indication of the time elapsed [54]. (b), an outflow water clock, in which time is measured by the regulated air flow of the water into the vessel [53]. (c), a candle clock, in which a burning candle is used to measure the time [54].

Through the centuries, Man invented ever more sophisticated devices to measure time ever more precisely: the first clock in the history which was able to transfer the rotational energy into intermittent motions was introduced by Ancient Greeks in 3rd century BC [55]. Arabic engineers in the 11th century improved the idea of water clocks, adding gears and weights which had the function to drive the clock [56], [57]. The invention of watches was encouraged by the innovation brought by the verge escapement mechanism [58], which was used to drive the first mechanical watches. This mechanism consisted of a crown escaped wheel, a *verge*, which had two flags called pallets, and a balance in the shape of a wheel.

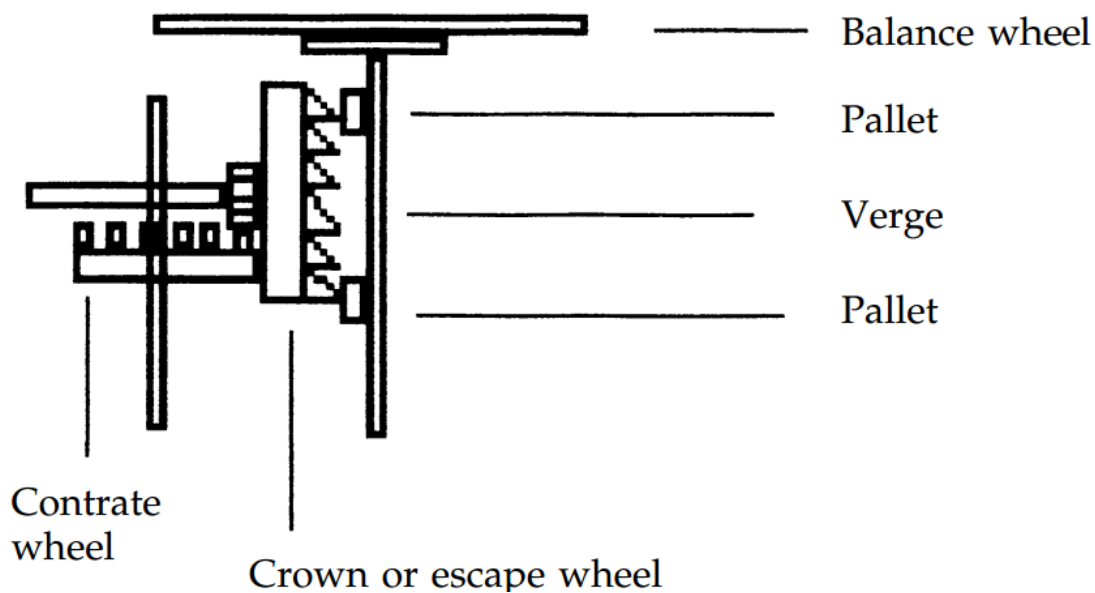


Figure 2. 2: The verge escapement mechanism was the bas of the first clocks. Image taken from [58]

Watches based on this idea were invented in Europe in 14th century, and became the standard devices to measure time. The first watches based on the verge escapement mechanism were not carried in the pocket, but were hung from a chain draped around the neck [59]. They were followed by spring-powered clock and pocket watches in the 16th century. The introduction of pendulum clock in 17th century considerably improved the accuracy and precision of time measurement devices. In modern age, during the 20th century, the electronic quartz oscillators [60], [61] were invented: they use the mechanical resonance of a vibrating crystal of piezoelectric [62] material to create an electrical signal with a precise frequency; the frequency is then used to measure time. However, a crystal oscillator's resonance frequency depends on a number of external factors, such as humidity, vibration, radiation, that can cause the clock to either speed up or slow down. Finally, in modern age, atomic clocks [63], [64] were invented and achieved a new fundamental breakthrough in time measurement. Atomic clocks are devices which measure time in a very accurate way; their frequency stability is given in

terms of Allan variance and Allan deviation [65]. The Allan variance, usually denoted as $\sigma^2(\tau)$ is defined as one half of the time average of the squares of the differences between successive readings of the frequency deviation sampled over the sampling period, commonly denoted as τ :

$$\sigma^2(\tau) = \frac{1}{2} (y_{n+1} - y_n)^2 \quad \text{Eq. 2. 1}$$

In Eq. 2. 1, τ is the observation time and y_n is the n -th fractional frequency average over the observation time. The Allan variance depends on the time period used between samples: therefore it is a function of the sample period, likewise the distribution being measured, and is displayed as a graph rather than a single number. A low Allan variance is a characteristic of a clock with good stability over the measured period. However, since it is presented as a number and not as a graph Allan deviation $\sigma(\tau)$ is universally preferred to give indication of the stability of atomic clocks. The Allan deviation is simply defined as the square root of the Allan variance:

$$\sigma(\tau) = \sqrt{\sigma^2(\tau)} \quad \text{Eq. 2. 2}$$

The Allan deviation of the Cs NIST fountain atomic clock, which is the most accurate atomic clock in the world, is reduced down to $< 4 \cdot 10^{-16}$ over an observation time of 1s [66]: this means that this device does not gain or lose a second in 20 million years! Man has accomplished the mission started thousands of years ago: to fabricate a device able to measure the time in the most accurate way.

2.2 Atomic Clocks: Compromise between precision and dimensions

Different models of atomic clocks were reported in the literature, which exploits different techniques to measure time and frequency. In general, atomic clocks use the frequency of the electromagnetic radiation that electrons emit when they change energy level to measure the time. All atomic clocks provide highly accurate and stable frequency reference, but their frequency stability (Allan deviation) is directly related with their dimensions. The already cited Cs fountain frequency standard (Figure 2. 3a), with an Allan deviation of $< 4 \cdot 10^{-16}$, is the most accurate frequency reference in the world, but has a volume of several m^3 and consumes hundreds of watts of power. It is important to specify that for portable applications, such as GPS and navigation systems, the size and the power consumption of the clock are critical aspects. Reducing these two factors by providing an efficient packaging solution is a hot topic of research and it is also the principal area of interest of this thesis. In the last decades, the so-called Chip Scale Atomic Clocks (CSAC) [67], were introduced. These devices provide precise time and frequency standards for portable applications, such as navigation and digital communication systems and data synchronization [67]–[70]. Even if they are called “Chip Scale Atomic Clock”, only the single constituent parts of these systems really have the size of a chip, but the overall physics package (including connections,

shielding and electronics) of these devices is far larger than this: the smallest atomic clock reported in the literature so far occupies a volume of 12 mm^3 , consumes 195 mW of power, and has a short term frequency stability of 4×10^{-11} [71], but this is for the physics package only, without the electronics integrated. The smallest atomic clock available in the market was developed by Symmetricom, and has a stability of 10^{-10} , a volume of 16 cm^3 and a power consumption of 110 mW (Figure 2. 3b), and this is with all the electronics integrated.

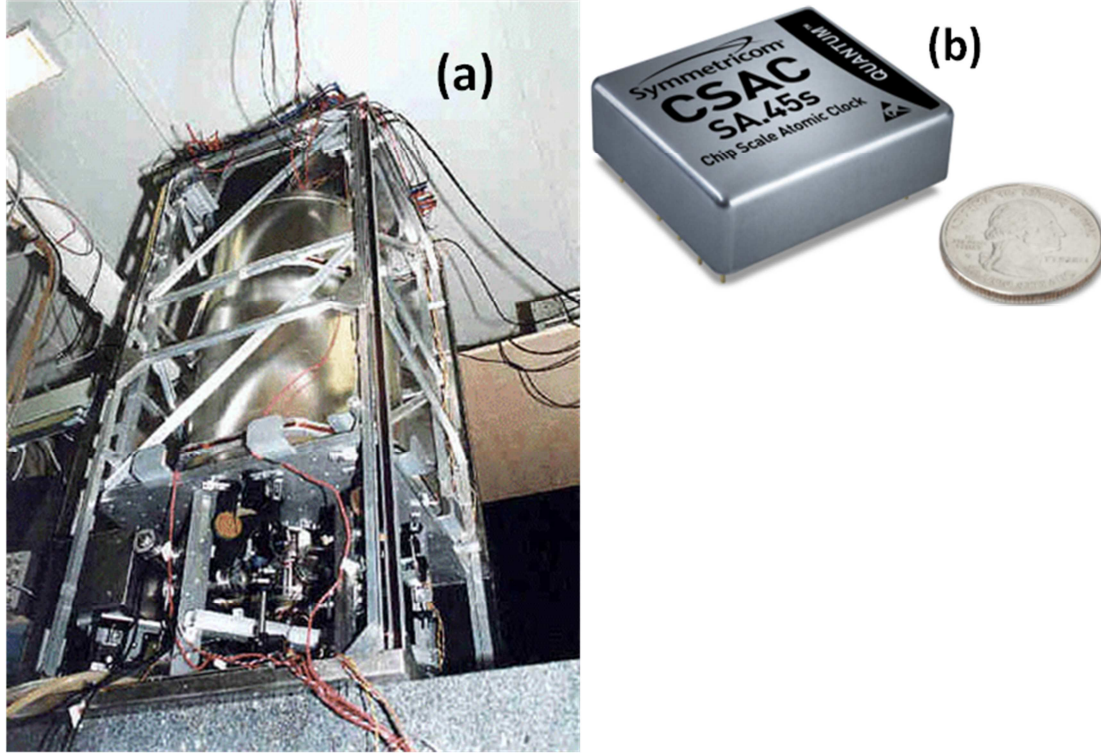


Figure 2. 3: (a), the Cs fountain atomic clock. Image taken from [72] (b), the CSAC commercialized by Symmetricom. Image taken from [73].

2.3 Double Resonance Atomic Clock: Principle of Functioning and Block Diagram

Atomic clocks use the electron's transition frequencies (the microwave signal that electrons in atoms emit when they change energy levels), as a frequency standard for its timekeeping element. This frequency is used to electronically stabilize a crystal oscillator's RF frequency; therefore, the stability of atomic structure is transferred to the clock's tick rate. Alkali metals (and in particular Rb and Cs) are commonly used as references in atomic clocks for a simple, practical reason: because of their single valence electron, their microwave frequencies are easily accessible. The MACQS project aimed to develop a Double Resonance (DR) Rubidium Compact Atomic Clock [67], [74]. This clock uses the transition between two hyperfine states of ^{87}Rb as frequency reference. The ground state of Rb is split into two hyperfine levels by the

magnetic-dipole interaction between the single valence electron and the nucleus. These two hyperfine levels are labeled by the total angular-momentum quantum number F ($F = 1, F = 2$). Each hyperfine level is then further split into several Zeeman sublevels, labeled by the quantum number m_f . The so-called 0-0 transition, between the $F = 2, m_f = 0$ and $F = 1, m_f = 0$ states, with a frequency of $\nu_0 = 6.8347$ GHz, is the transition used in a Rb Double Resonance (DR) atomic clock to stabilize the oscillations of a crystal oscillator. This 0-0 transition is preferred because its frequency is not affected by stray magnetic fields. Figure 2. 4 illustrates this physical phenomenon.

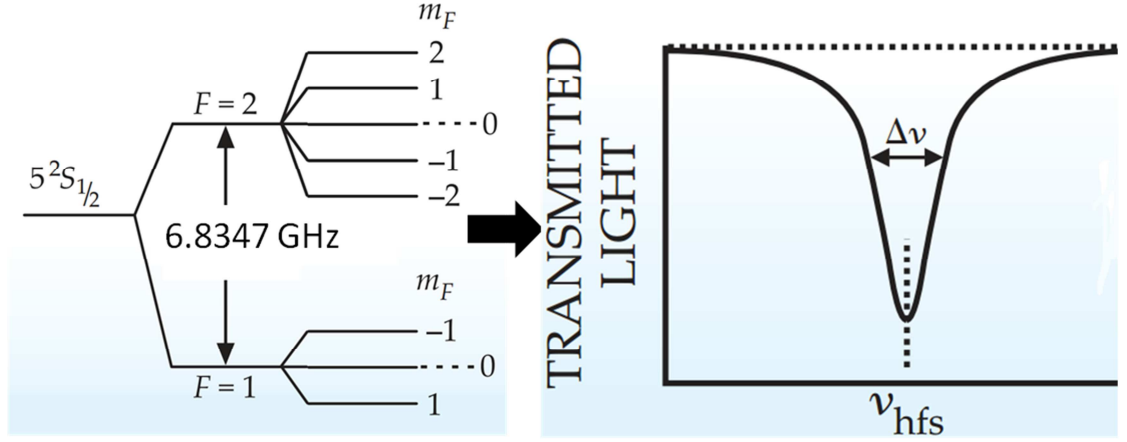


Figure 2. 4: The ground state of ^{87}Rb is split into two hyperfine levels, labeled by their total quantum number F . The hyperfine levels are further split into several Zeeman sublevels, labeled by the quantum number m_f . The transition between the two $m_f = 0$ sublevels produces a radiation of 6.8347 GHz, used to stabilize a crystal oscillator's frequency.

The double resonance atomic clock consists of several simple modules. First, a light source produces light resonant with the ^{87}Rb absorption line. The next part is the reference cell, which contains the alkali atoms in their metallic vapor state together with a buffer gas. The light is directed to the reference cell, and the alkali metal atoms are ground-state polarized. The clock transition is detected by applying a microwave field to the atoms; this is done via a microwave cavity (another fundamental element of the DR atomic clock), which is placed around the reference cell. The light power transmitted through the cell has a narrow dip, caused by the resonance itself, as shown in Figure 2. 4. The frequency of a voltage-controlled quartz oscillator is then locked to this narrow dip using phase-sensitive detection. Between the light source and the reference cell, an ^{85}Rb filter is placed, to filter out the ^{85}Rb absorption lines from the light which is then sent to the reference cell. This filter is particularly useful because, due to a coincidence in nature, the absorption lines of ^{87}Rb $F=2$ state are nearly degenerate with those of ^{85}Rb $F=3$ state. Thus, the ^{85}Rb filter can eliminate the $F=2$ spectral component from the ^{87}Rb light beam, so when the filtered light beam reaches the ^{87}Rb atoms contained in the reference cell, it preferentially excites atoms out of the $F=1$ state. The easy and efficient filtering of the light beam is one of the principal advantages that the use of Rb offers with respect to the use of Cs in the reference cell of

an atomic clock. Cs has only one stable isotope, so for clocks based on this metal no filtering is possible. As a result, Rb clocks are more compact and cheaper than Cs cells, while Cs-clocks have a better stability. Figure 2. 5 illustrates the structure of a DR Rb atomic clock.

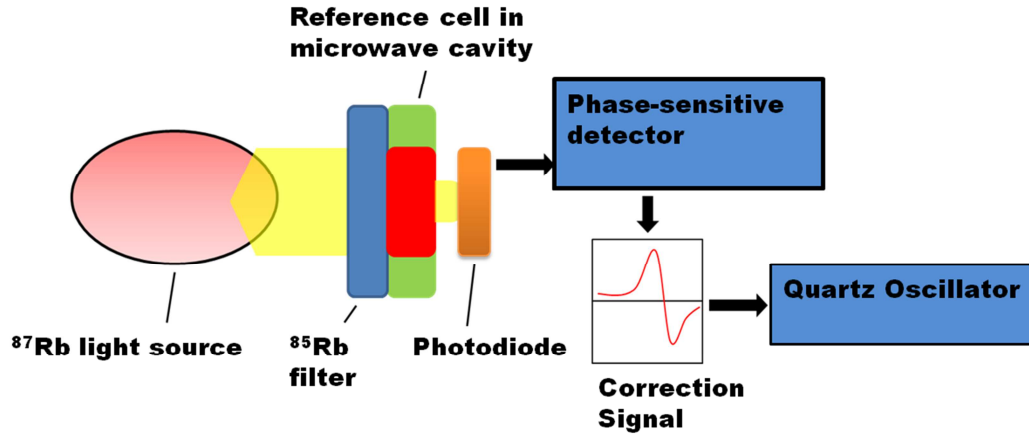


Figure 2. 5: The structure of a DR Rb atomic clock.

The atomic clock is a complex structure, and several are the engineering challenges involved in the fabrication of such device. The fabrication becomes still more challenging in the case of a Chip Scale Atomic Clock, because we add the complexity of being small in all the parts we develop and to fabricate a low-power consuming device.

Our laboratory, LPM (Laboratoire de Production Microtechnique), with a vast expertise in thick-film and LTCC technology, electronic packaging and microfabrication, was involved in the already described MACQS (Miniature Atomic Clock and Quantum Sensors) research project. This research project started with the goal to propose new techniques to batch-fabricate the key components of a Double Resonance (DR) Rubidium Compact Atomic Clock, and, ideally, put together the fabricated components to constitute a working atomic clock demonstrator. In this context, the research effort of LPM (and therefore my personal effort also) was focused on the following two objectives:

1. The development of the reference cell using solder sealing, a quick, low-temperature bonding technique which should minimize evaporation of the alkali metal during the sealing process;
2. The realization of the electronic packaging, interconnection and temperature control of the various parts of the atomic clock.

Several are the issues related with the fabrication of the reference cell. First, this system must be filled with non oxidized rubidium. Rubidium is a very reactive metal, especially with oxygen and water. This makes the handling of this metal very challenging and the fabrication becomes critical; moreover, the encapsulation of the alkali metal must be completely hermetic, avoiding any air penetration into the

packaging, otherwise the rubidium will react with the oxygen and lose its properties. Inside the cell, together with Rb, a buffer gas is commonly added. Since the alkali atoms lose their spin polarization when colliding with the cell walls, the function of the buffer gas is to reduce the mean free path.

Regarding the second objective, the packaging of the components of the atomic clock, the major issues were related with the temperature control: in fact, some parts must be stabilized at a very precise and well-defined temperature (for example, the reference cell works at 70°C), and high precision is wished, ideally 0.01°C. The difficulty is compounded by the fact that the different parts of the atomic clock have different working temperatures and, being a miniature system, the components are very close to each other. Therefore, efficient thermal insulation must be provided, so that the temperature of one part does not affect the temperature of the other parts of the system.

2.4 State of the art of Chip Scale Atomic Clocks

Considerable effort has been devoted in recent times to the fabrication of low-power, chip-scale packaged atomic clocks. The effort to miniaturize and to reduce the power consumption of atomic clocks is due to the fact that a low-dimension, low-power device may be used in important applications such as wireless base stations and telecom networks and in portable equipment for navigation and positioning.

In 2004, Knappe et al. [75] presented the first miniature atomic clock. This clock was based on the Coherent Population Trapping (CPT) technology: this means that the presence of the large resonance cavity is not needed in the atomic clock, and this allows significant reduction of the dimensions. The disadvantage is that the stability of such clocks is usually five times less than the DR-based atomic clocks. The physics package of the miniature atomic clock presented in 2004 by Knappe et al. was based on microelectromechanical system (MEMS) fabrication techniques; in particular, the reference cell (filled with Cs) was fabricated using anodic bonding [76] of borosilicate glass and Si. The heater used consisted of a planar structure made from a film of indium-tin oxide (ITO) deposited by photolithography on a thin glass substrate. The total volume of the clock was only 9.5 mm³, its fractional frequency instability was 2.5×10^{-10} at 1 s of integration and the total power dissipated was 75 mW, mainly dominated by the power required to heat the cell and the VCSELs. It is important to specify that this system was not yet a fully functional compact frequency reference. It lacked a local oscillator and the miniaturized control electronics to stabilize the cell and laser temperatures and lock the laser wavelength. The physics package of this clock is showed in Figure 2.6.

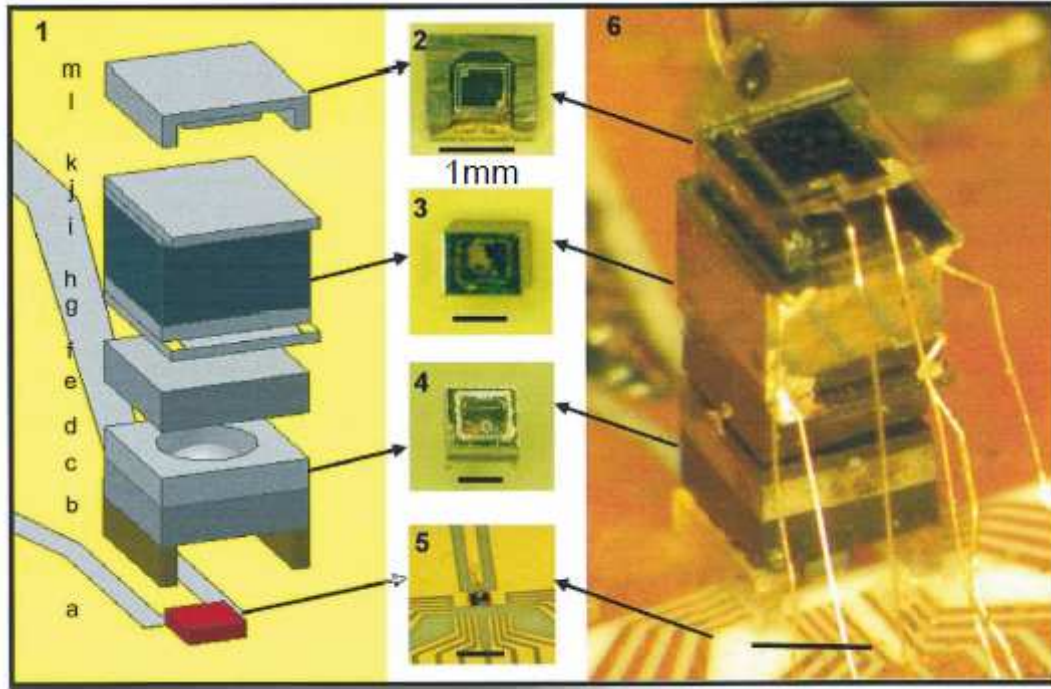


Figure 2. 6: Physics package of the miniature atomic clock presented by Knappe in 2004: (1), Schematic assembly, (2), Photodiode assembly, (3), cell assembly, (4) Optics assembly, (5) laser assembly, (6), the full atomic clock physics package presented. The black lines all indicate 1 mm. Image taken from [75].

In 2007, the Symmetricom team presented the last version of their Chip Scale Atomic Clock (CSAC) [77] using again CPT as the interrogation scheme. The total dissipated power of this clock was 125 mW, the frequency stability was 1.6×10^{-10} at 1 s of integration and the total volume of the physics package was 15 cm^3 . The reference cell of this clock was fabricated using a similar technique than the previous described system: a silicon body 2 mm square and 2 mm thick was anodically-bonded with a transparent Pyrex window. The fabricated cell and the VCSEL laser were placed onto a polyimide ($k = 0.2 \text{ W} \cdot \text{m}^{-1} \cdot \text{K}^{-1}$) support structure which provided minimal thermal conductivity, limiting conduction loss. On top of the polyimide support, a Pt heater and temperature sensor was patterned (upper suspension). On the lower suspension of the polyimide heater system, bond-pads for flip-chip attachment of the VCSEL were patterned. An illustration of such heater is shown in Figure 2. 7; this figure also shows an illustration of the physics packaging as well as a photo of the final product.

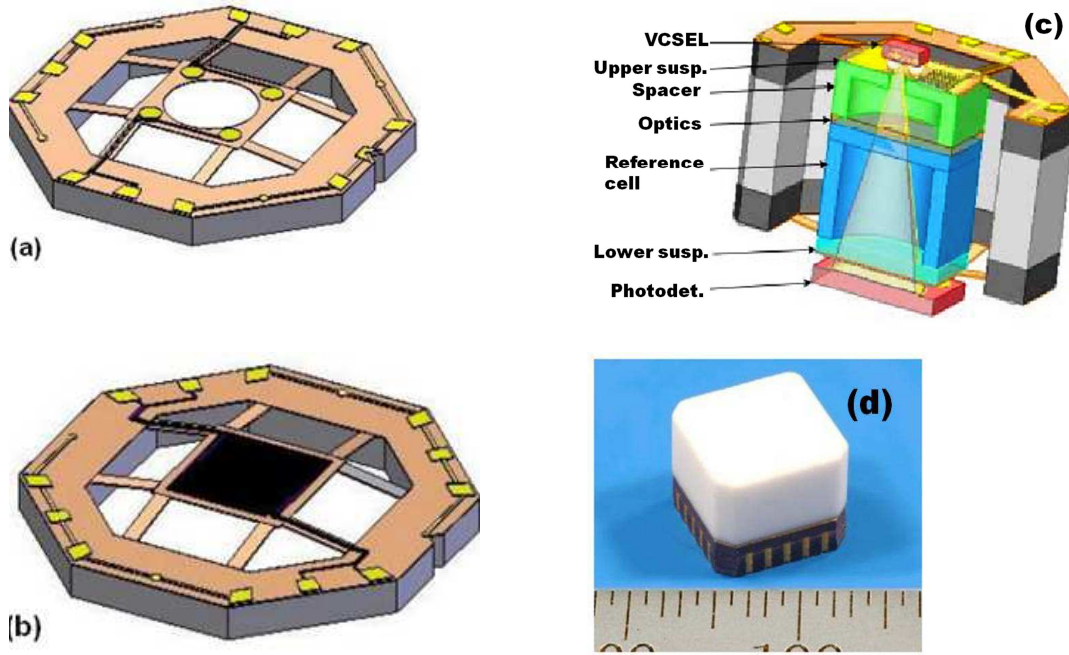


Figure 2. 7:(a) polyimide heater, lower suspension, with the bond pads for the flip-chip attachment of the VCSEL. (b), polyimide heater, upper suspension, including the Pt resistive heater and temperature sensor: (c) illustration of the physics package of the clock. (d) photo of the final product. Images taken from [78].

A further improvement of the miniature atomic clock was presented by De Natale et al. in 2008 [79]. They were able to fabricate a system with a total volume of 1 cm^3 with the electronics integrated, a power consumption of 30 mW and an Allan deviation better than 1×10^{-11} . They configured the system in a way so that the VCSEL and the reference cell could share a common heater: this allowed an important reduction of the size and of the power consumption of the system. In this system, the heaters were again MEMS-based, consisting of a Pt resistor patterned on top of an insulating material, so they use the same concept illustrated in Figure 2. 7. The reference cell of this system was made out of single Si crystal, etched to form the cavity which contains metallic Cs and anodically-bonded with a glass window. Figure 2. 8 shows a photo of the physics package of the miniature atomic clock developed by this group.

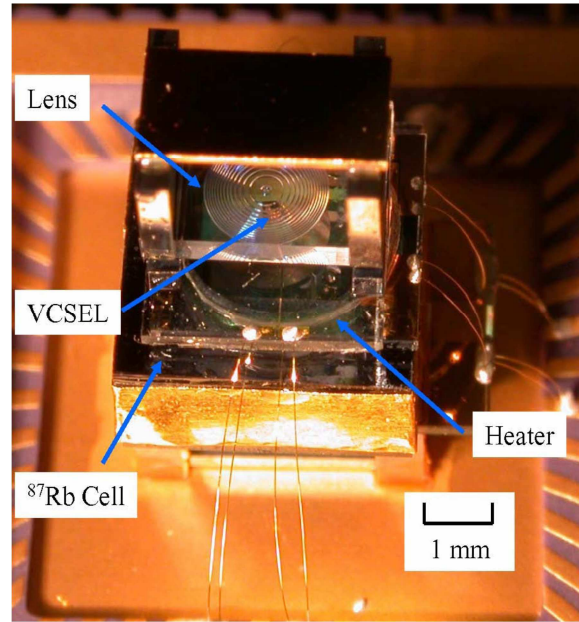


Figure 2. 8: Physics package assembly of the CSAC developed by De Natale et al. Image taken from [79].

Finally, the MACQS (Miniature Atomic Clock and Quantum Sensors) project started on July 2009, with the objective to fabricate a Double Resonance (DR) rubidium atomic clock. This project aimed to use alternative approaches (i.e. using Rb instead of Cs in the reference cell, and using DR instead of CPT as interrogation scheme) for atomic clock fabrication, without need to be smaller or better with respect to the already cited systems. In a DR atomic clock the presence of a large microwave cavity (dimensions ranging several cm) is needed, so the miniaturization level of the final system will not be comparable with the already cited clocks, based on MEMS technologies, and which use CPT as interrogation scheme. Nevertheless, the objective of the MACQS project was to introduce new fabrication techniques and innovative designs to batch-fabricate the parts of a DR atomic clock. The batch-fabrication allows to reliably and modularly producing the different components, therefore drastically decreasing the production cost of the system. In this well-defined size (mesoscale, like the size of a DR atomic clock), ceramic technologies such as Low-Temperature Co-fired Ceramic [80]–[83] (see the following for more details about this technology) offer several advantages, such as ease of 3D structuration, capability for manufacturing suspended heaters for local temperature control and possibility to easily integrate active elements such as sensors. The MACQS project aimed to use LTCC technology for the packaging of the atomic clock, in particular to design LTCC heaters for temperature stabilization of the cell and of the VCSEL. This was something that was not attempted before the beginning of this project, even if another European project, the MAC-TFC (MEMS Atomic Clocks for Timing and Frequency Control & Communication) [84], [85] started almost in parallel with the MACQS project, and one of its objectives was to use LTCC technology for the packaging of an atomic clock.

2.5 LTCC Technology: What it is

It is time now to introduce the next concept, fundamental to understand the work accomplished in this thesis: LTCC technology [81], [86]. LTCC (Low Temperature Co-fired Ceramic) technology was developed by DuPont in the early 1980's to fabricate electronic circuits essentially for military systems [87], [88]. This technology was proposed as an evolution of the HTCC (High Temperature Co-fired Ceramics), in which the ceramic substrate was fired at a temperature higher than 1000°C, while for LTCC substrates, thanks to the presence of glass in the ceramic, the firing peak temperature is usually below 900°C (see the following for more details). Essentially, commercial LTCC composites are mainly constituted by a mixture of glass and ceramics, which can be used for developing electronic circuits and packaging systems and offers outstanding performance especially for high-frequency applications. Because of the very low achievable dielectric dissipation factors, LTCC rapidly became the standard platform for high-frequency applications such as Bluetooth (2.45 GHz), wireless LANs (2.45 and 5 GHz) and broadband access connection systems (5.8-40 GHz) [82], [89]–[91]. The commercialization of the technology in the late 1980s, encouraged by manufacturers such as DuPont, Heraeus and Ferro, broadened the application areas to avionics and automotive industries [92]. An important feature of LTCC technology is that conductor wires and passives may be integrated in the substrate by screen printing, bringing different advantages over SMD (Surface Mountable Device) components, such as:

- Active/passive trimming of the resistors;
- Gain of space;
- Increased packaging efficiency and interconnect density
- Cost reduction.

Another very important advantage offered by the use of LTCC is that this technology features excellent 3D structuration possibilities and excellent interconnection reliability for high density packaging, therefore allowing size reduction of the device [33, pp. 14–16]. In fact, with LTCC it is possible to easily create multi-layer modules (MLC, Multilayer Ceramic) instead of the standard single-layer board (MCM, Multi-Chip Module) [93], [94]. In a standard thick film circuit which uses Al_2O_3 as substrate, the components are flip-chip soldered, or attached and wire-bonded on one layer, which is previously printed with electronic connection wires and resistors. It is also possible to create a Multi-Chip Module on a standard thick film circuit, by printing a layer of dielectric paste on top of a first layer of tracks, and then on the dielectric paste we can print new tracks and passives. In this case, the tracks can communicate from one layer to the other through electrical vias which cross the dielectric layer. Although possible, this process becomes rather impractical for very complex circuits, and does not allow good 3D structuration. On the other hand, by stacking many layers of LTCC, it is possible to integrate most of the active and passive electronic components on different layers, forming a complex and high-density multifunctional system in which the resistors or capacitors may be embedded or buried in-between the ceramic substrate

[95], [96]. The components that, because of their complexity, cannot be integrated (operational amplifiers, IC chips), may be flip chip soldered or wire-bonded on top of the LTCC module, as in the case of an alumina substrate. Figure 2. 9 shows a standard thick film circuit, compared with a multi-layer module.

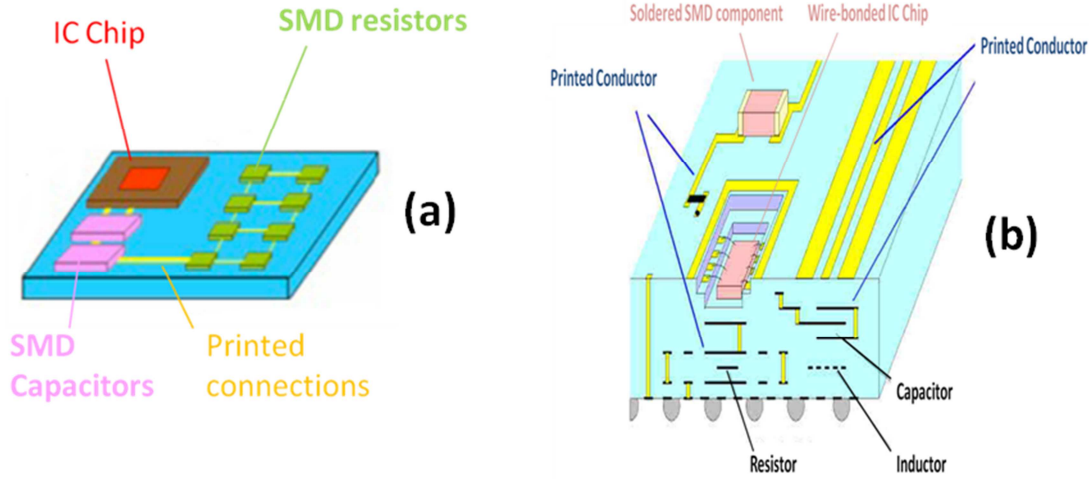


Figure 2. 9: (a) A simple microelectronic thick film package in which the components are confined into one single layer. (b), an advanced microelectronic package in which components are integrated into multiple layers, and the IC chip is finally wire-bonded on the surface. Images taken from [33].

The outstanding properties of LTCC materials made this technology very attractive also for microelectronics packages. In such packages there is the need of low dielectric constant for a good signal transmission, low dissipation factor, capability to withstand high temperatures and high pressures, smooth surface, physical and chemical stability, low-cost when produced in series, and finally Coefficient of Thermal Expansion (CTE) close to that of Si as most of IC attached on the substrate are Si-based (CTE of Si is 2.6 ppm/K [97], while LTCC from DuPont DP951 has a CTE of 5.8 ppm/K). LTCC technology covers most of these requirements and therefore it is widely used now for microelectronics packaging and microsystems [83], [98]. Moreover, in recent years, LTCC was employed in a wide variety of applications beyond electronics, such as fabrication of microtechnology devices and ceramic sensors [30], [31], [32], [33], [35], [105], [106], fabrication of biomedical devices [103], microfluidic systems [107]–[109].

2.6 LTCC Circuit Manufacturing

The manufacturing of an LTCC circuit requires numerous steps; however, all of them are simple and repeatable. The quality of the final product only depends on the fabrication: it is necessary to pay careful attention to the quality of the fabrication process and make everything with the maximum precision, but the required cleanliness standards are much less stringent than for silicon devices. In the following, we will make a description of the manufacturing steps of LTCC, starting from the material that

constitute the substrate and ending with the final inspection of a solid, resistant, multifunctional highly integrated module.

2.6.1 Materials involved

As its name suggests, LTCC (Low Temperature Cofired Ceramics) is a ceramic material which is cofired together with screen-printed thick film pastes at low temperature (here, “low” means ca. 875°C). During the firing, when the temperature is above ca. 700°C, sintering [110] of the substrate happens, leading to the formation of a monolithic and dense device at ca. 850°C, and inducing a shrinkage from 0 to 18% in the X-Y planar directions (the value of shrinkage in X and Y directions are usually not the same) and from 15% to 44% in the Z direction (thickness) [111], [112]. The total shrinkage depends on the particular LTCC composition used, and sometimes it varies also from one production batch to the other, even if they contain the same green tape (“green tape” is the term used to define the unfired LTCC tape). The impossibility to precisely predict the shrinkage remains a limitation of this technology, because it causes dimensional uncertainty and lack of repeatability in the fabrication. However, new trends show that Heraeus manufacturer was able to fabricate an LTCC green tape with almost no X-Y shrinkage [113] (total X-Y shrinkage is less than 1%), while there are techniques to constrain the shrinkage of the tape during the sintering. The most attractive technique in this sense was described by Rabe in 2005 [114]: he combined during lamination the green tape with an already sintered rigid substrate (sacrificial layer). During firing, the sintered substrate significantly limits the green tape lateral shrinkage (total shrinkage was less than 0.5%). The objective of his research is to get a repeatable fabrication process, so all the effort is focused to get zero X-Y shrinkage during firing. The LTCC substrate (which is the substrate where all the active components are placed onto) consists of three main components, mixed in different ratio:

- Ceramic material;
- Glass;
- Organic binder.

The actual LTCC tape is formed, using the above mentioned materials, following the tape casting [115] process. The addition of glass into the ceramic is important to lower the sintering temperature [116]. The organic vehicle, in which the glass and the ceramics are dispersed, is comprised of a polymeric binder which is initially dissolved in a volatile solvent during the fabrication of the tape, and other optional constituents such as plasticizer, release agents and stabilizing agents [86, pp. 105–110]. The binder provides strength and toughness to the unfired tape, surrounding the glass and ceramic particles, but it is also partly responsible for the final shrinkage of the tape after firing: the less is the amount of binder, the less will be the dimensional change of the tape. The volatile solvent, whose function is to dissolve the binder, is then driven off right after the tape casting. The commercial LTCC is therefore provided without this solvent.

Finally, the plasticizer determines the plasticity, workability of the LTCC green tape (before firing). “Cofire” means that the ceramic substrate is fired together with the metals or other layers deposited on it. Since the firing peak temperature is below 900°C, there is the possibility to integrate in an LTCC circuit metals with high electric conductivity, such as Ag and Au, because their melting point is still safely above the firing peak temperature of the LTCC. These metals are used for the electrical connections on the substrate, because in this case a good electrical conductivity of the constituent material is wished in order to decrease the losses. Alloys of Ag-Pd, Ag-Pt, usually with an important content of Pd or Pt, are also integrated in an LTCC circuit, mainly to provide migration- and solder-resistant surface conductors. These alloys are used for the heating meanders, where a relatively high electrical resistivity of the constituent material is wished: in this case, a higher resistance with respect to the connection wires is in fact necessary to ensure local heating. Moreover, pure Pt is also integrated in an LTCC circuit: because of its well defined TCR (Temperature Coefficient of Resistance), it is used as constituent material for a temperature sensing resistor. All these metals and alloys, as shown in Table 2. 1, have a relative low melting point, bounded by Ag. Therefore, “Low” in LTCC usually means a firing temperature of the tape compatible with Ag, i.e. < 900°C, with a reasonable margin below its melting point; this is possible thanks to the presence of glass into the ceramic, which ensure high sintered density of the substrate with relative low temperature. This is the principal advantage of LTCC with respect to the similar and earlier developed technology, HTCC (High Temperature Co-firing Ceramic) [117]–[119]. HTCC, based on an aluminum oxide substrate (Al_2O_3) uses, in alternative to noble metals, high-melting elements such as Molybdenum (Mo) and Tungsten (W), with manganese (Mn) as a reactive bonding element. However, these metals have lower electrical conductivity with respect to the noble metals, which results in higher high-frequency conductor losses, and the firing process takes place in a wet hydrogen environment incompatible with many functional materials. Alternatively, specialized HTCC modules with Pt conductors may be fired in air, but the associated high costs confine them to niche applications.

LTCC	Substrate		Conductors used		
	Material	Firing temperature (°C)	Material	Melting point (°C)	Electrical resistivity at 20°C (nΩ·m)
	Glass / ceramic mixture	900 to 1000	Cu	1083	16.78
			Au	1063	22.14
			Ag	960	15.87
			Ag-Pd	960 to 1555	15.87 to 30
			Ag-Pt	960 to 1186	15.87 to 30
HTCC	Alumina ceramics	1600 to 1800	Mo	2610	53.4
			W	3410	52.8
			Mo-Mn	1246 to 1500	53.4 to 100

Table 2. 1: Summary of the materials used in LTCC and HTCC technology.

2.6.2 Slitting, blanking, pre-conditioning the green tape

The ceramic LTCC green tape is provided in large quantities. Therefore, the desired amount of tape to be used is cut away from the roll using a blade (Figure 2. 10). Afterwards, the tapes are pre-conditioned in the oven at relatively high temperatures, usually around 120°C, for 15 to 30 minutes. The thermal preconditioning treatment drives off any residual solvents and releases any stress that may be attributed to the tape casting operation [120].

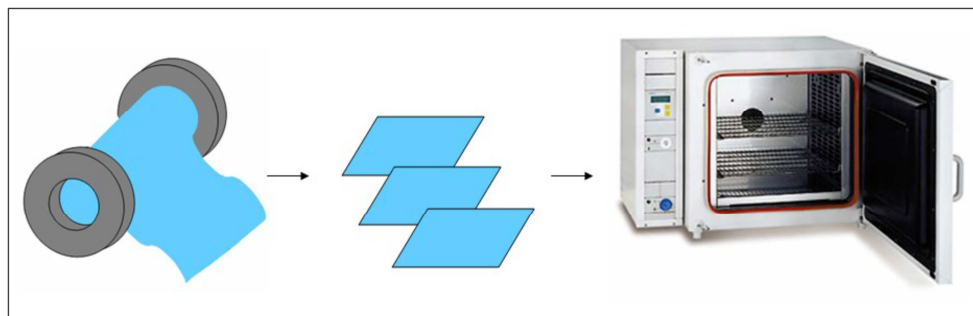


Figure 2. 10: Slitting from the starting roll, blanking and pre-conditioning of the tapes.

2.6.3 Via punching - laser cutting

Vias can be punched on the single tapes using a specific punching machine, or, alternatively, cut out by a laser. The same laser can be used to create channels, holes

and cavities on the tape. Figure 2. 11 shows a cross section of the LTCC tape before and after the process of via punching.



Figure 2. 11: Via punching.

2.6.4 Via filling – screen printing

The vias of each layer are filled with a specific conductive paste, consisting of pure Ag or Ag-Pd, Ag-Pt, or, in case high reliability is needed, Au. There are specific via filler machines which are able to quickly realize this operation. The other main components of the circuit (connections and resistances) consist of specific thick film pastes which are developed to be physically and chemically compatible with the LTCC tape [121]; they are deposited on the tapes by screen-printing [122]. The screen-printing principle is illustrated in Figure 2. 12. A screen is a porous fine woven mesh supported by an aluminum frame [123]. The density of the mesh, in number of lines per inch, is an important factor: the smaller the mesh number, the larger is the size of the hole, therefore allowing greater volume of ink deposition. The image of the layout to be printed onto the substrate is deposited over the screen. The LTCC tape to be printed is placed at a small distance to the screen, onto an aluminum porous table connected to a vacuum pump. The vacuum pump, through the pores of the aluminum table, applies a negative differential pressure to the tape, avoiding any movements of the LTCC during the printing process. Finally, a squeegee passes onto the mesh, applying pressure, forcing the paste to be deposited on top of the LTCC substrate by passing through the holes of the mesh.

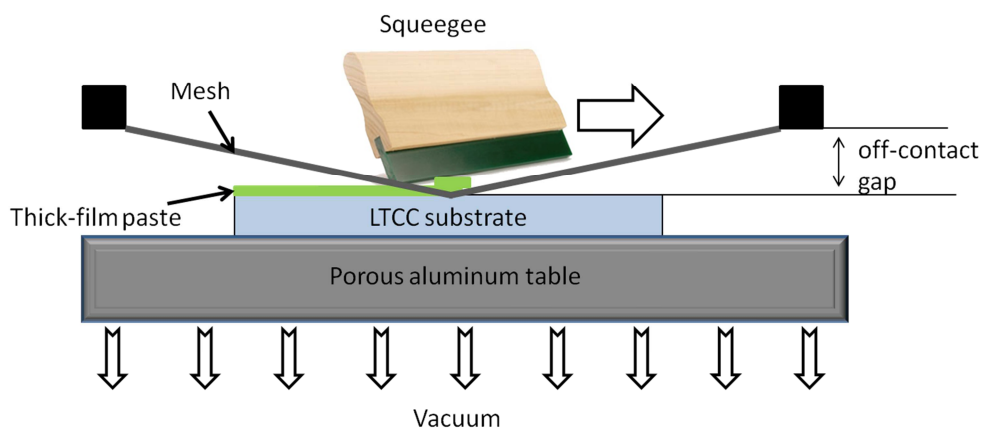


Figure 2. 12: Screen-printing process.

The screen-printed paste is first leveled at ambient temperature and then dried at a precise temperature, indicated by the manufacturer (typically between 80 and 120°C). The drying process solidifies the paste by driving off the solvents that were added to the

paste for improving its rheology and printability. Finally, an accurate inspection of the quality of the printing is advisable.

When comparing the fabrication of an LTCC circuit with that of a classical thick film element, this step is quite similar: in both LTCC and thick film fabrication, the screen printing process is similar: the only difference is the substrate where the paste is deposited. In some case, the composition or the rheology of the paste used is different, depending on the substrate where it must be deposited: for example, DuPont manufactures special pastes whose printability is excellent on LTCC.

2.6.5 Stacking and lamination

The LTCC sheets, once printed, are aligned and stacked one onto the other. The stacked LTCC sheets are then laminated [86, pp. 154–165]. The purpose of the lamination process is to transform several LTCC green sheets into a single substrate (Figure 2. 13).

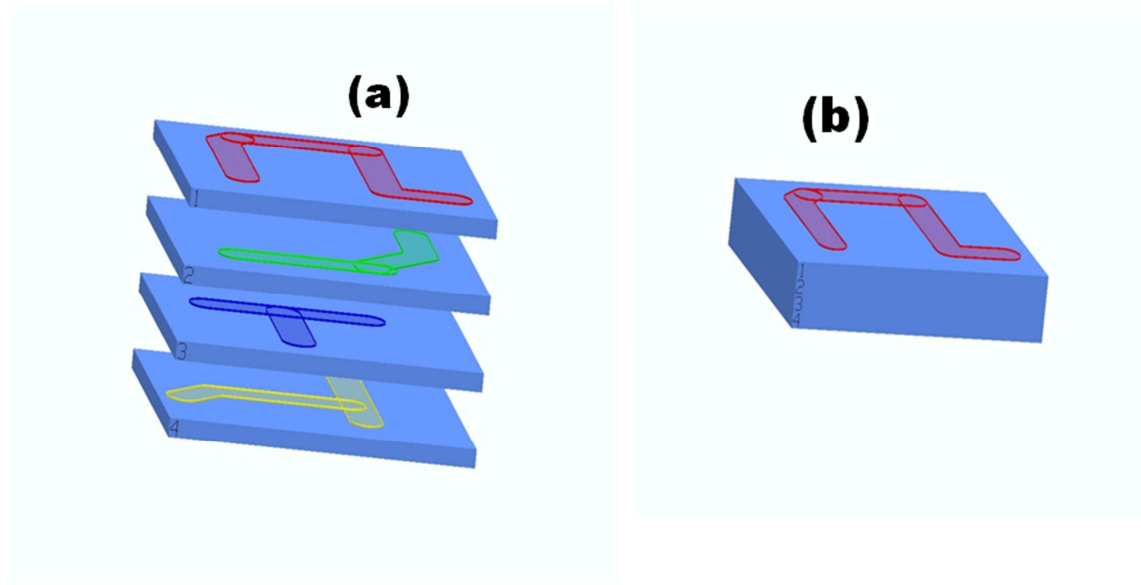


Figure 2. 13: Lamination process: (a) the single tapes, screen-printed, before lamination. (b), after the lamination, the single tapes become a unique substrate.

The traditional technique for lamination is thermocompression, which consists in applying high pressure and elevated temperatures to the green tapes for a certain amount of time. In the uniaxial lamination, performed in our lab using an uniaxial press, the tapes are pressed between two heated metal plates. Typical values are 70°C, 200 bar (20 MPa), for 10 minutes [124]. This is a delicate operation: the high pressure applied could cause problems with cavities and windows, as well as higher shrinkage tolerances. Another way is to use an isostatic press: in this case, the stacked tapes are vacuum packaged in a foil and pressed in hot water. Typical values are 70°C, 350 bar, 10 minutes [6]. The isostatic press must be avoided in case the structure has internal cavities, since it will surely deform them.

The principle of thermocompression is the following: due to the elevated temperature, the organic binder contained into the single green tapes becomes plastic, and the various tapes are joined by interpenetration of the plastic binder into the particles of the two tapes. Moreover, the applied pressure forces the ceramic particles and glass from all the tapes together. Therefore, high pressure is necessary to ensure the excellent bonding of the various tapes. Figure 2. 14 shows the tapes before and after lamination.

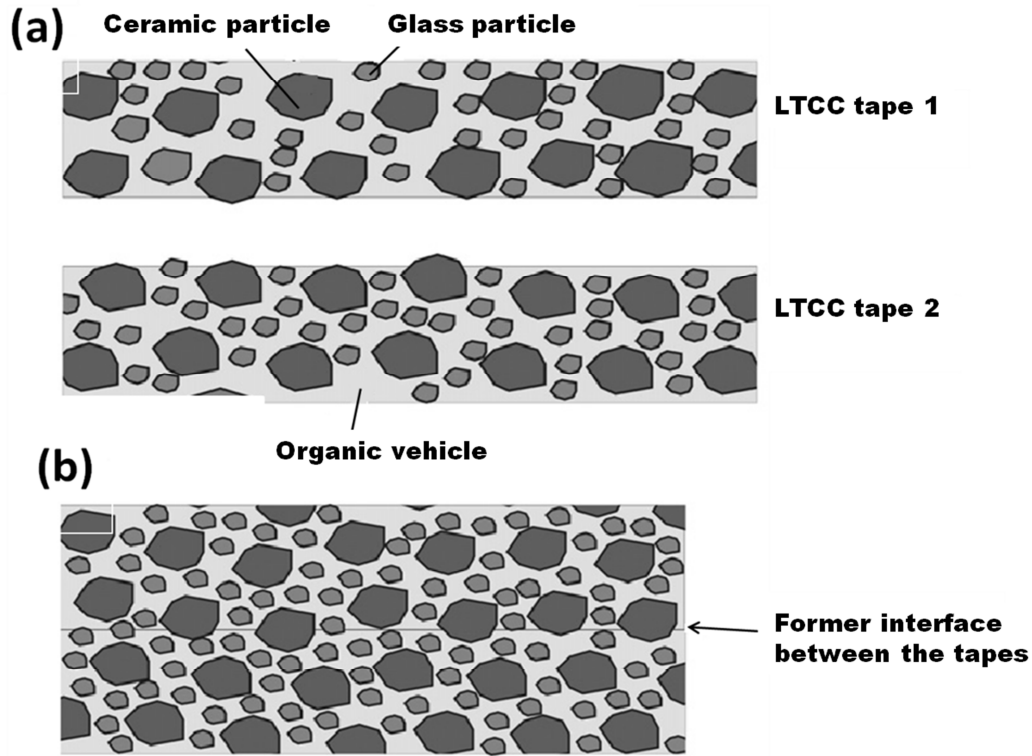


Figure 2. 14: (a) The tapes before lamination; (b), the tapes after lamination. Image taken from [125].

A hot topic of research is the conception of new lamination techniques, alternative to the thermocompression technique, which allow good bonding between the tapes at low pressure, by adding some solvents or adhesive tapes on top of the tapes; see Chapter IV for more details about this.

2.6.6 Firing

Once laminated, the LTCC module is usually fired in air and sintering of the material occurs. Often, the thick film pastes which were screen-printed on top of the LTCC green tapes are fired together with the substrate, at temperatures below 900°C (co-fired). Alternatively, the thick film pastes can be printed on sintered LTCC sheets and then fired separately (post-fired). The firing process is usually performed in two steps: first, the organic vehicle is slowly driven off, and then the module is further heated up to the firing (sintering) temperature. The organic burnout ends at a temperature of ca. 450 – 500 °C; it is a process which may have some drawbacks such as delamination, bubble formation in correspondence with the passives, increased porosity of the LTCC

tape. So, the heating rate at this stage must be slow; moreover sufficient time should be given to ensure that the binder is completely driven off at the selected dwell temperature. Once the entire organic vehicle has been driven off, the peak temperature can be achieved with a high heating rate, and it is kept for some time, typically 20 to 30 minutes, to ensure the complete solidification of the LTCC tape. At this stage, the glass melts, it wets and penetrates the void space between the ceramic particles and joins the tapes together, enabling to achieve a strong final structure (viscous sintering, [126]). Since the sufficient viscous flow of the glass is the key mechanism to get a good solidification of the system, in order to improve the sintered density of the LTCC composite, it is necessary to control the softening point of the glass, as well as its volume and powder particle size to increase its fluidity[127], [128]. The effect of the firing profile on the sintering of the LTCC were investigated by Makarovic et al. [129]. In particular, the sintering temperature must be carefully respected (it is usually specified by the manufacturer), otherwise the formation of internal pores in observed is the composite. The pores are sometimes caused by insufficient sintering, and sometimes by excessive sintering causing the occurrence of gas within the material. When the glass melts, the decomposition of batch materials such as hydroxides, carbonates and sulfates may release large volumes of corresponding gases (H_2O , CO_2 and SO_3), with some CO and CO_2 also possibly generated by oxidation of residual carbon. Most of these gases are evacuated but a small quantity of gas forms bubbles and remains in the glass or dissolves inside the glass melt, creating the pores observed in Figure 2. 15. To prevent the creation of pores, it is important to use raw materials containing little dissolved gas, and reducing the time during the firing process at temperature ranges where the gas is liberated. This is the reason why after the first step of organic burnout, the heating rate should be faster.

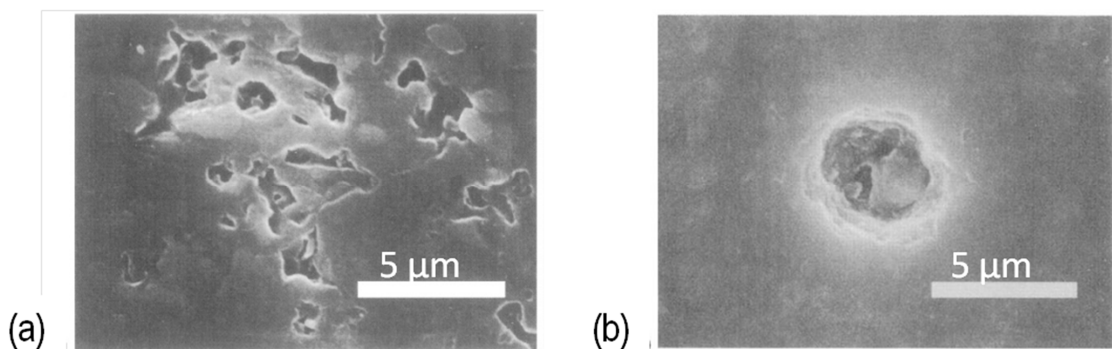


Figure 2. 15: Microstructure of glass/ceramics sintered at different temperature: (a), 800°C, we observe the pores due to insufficient sintering, which are angular. 1100°C, we observe the pores due to excessive sintering, which are spherical. Images taken from [86, p. 35].

During the sintering process, premature crystallization of the glass should be avoided, as it hinders further densification of the material. When glass crystallization happens, some parasitic crystalline phases such as quartz and cristobalite (forms of SiO_2) are precipitated and they alter the properties of the resulting LTCC: due to the presence of

such crystalline phases, the control of important properties of LTCC such as CTE becomes impossible. Therefore, densification should occur before extensive crystallization, which may set a lower limit on the heating rate. Ideally, controlled crystallization, i.e. of the right crystalline phase and after densification, is initiated by reaction with the ceramic, which diffuses in the glass during the latter stage of sintering. A typical such desired crystalline phase is anorthite in the glass, which results in a mechanically strong and thermally stable glass-ceramic material with controlled CTE [130]. Finally, the cooling of the module is performed. The firing profile, which is crucial for the quality of the final product, is given by the manufacturer[36], [131]. A typical firing profile is illustrated in Figure 2. 16.

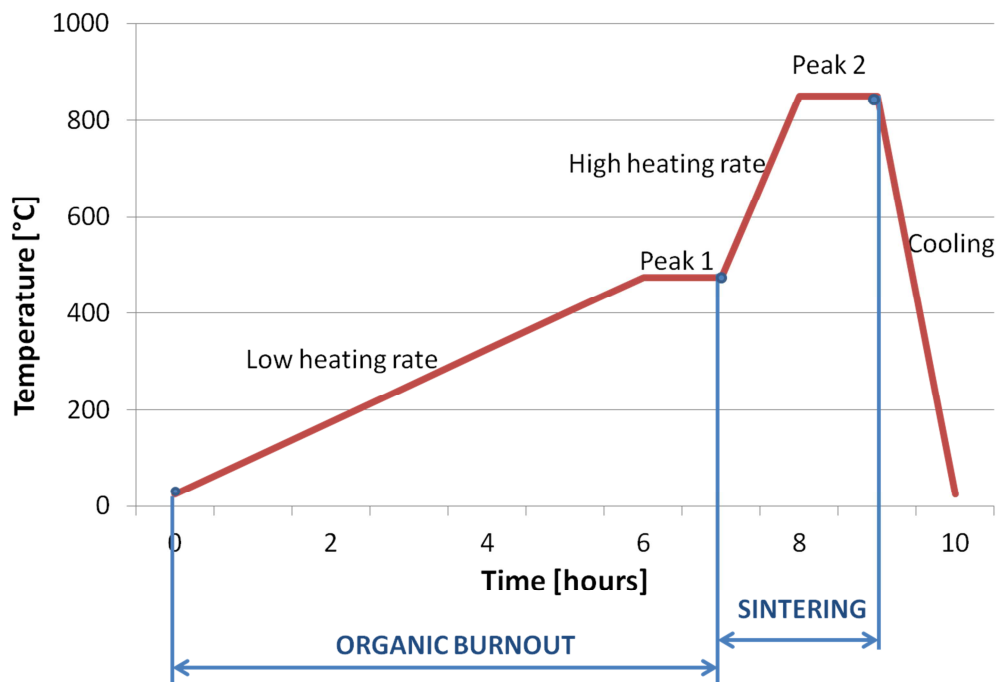


Figure 2. 16: An example of firing profile of LTCC.

2.6.7 Post-firing and post-processing

After firing, the LTCC module can be printed again with the passives (the resistors, for example), or other pastes, which need to be fired separately (post-fired). Other manipulations can be performed, such as wire-bonding of IC chips, or soldering of SMD components etc.

2.6.8 Final inspection and test

After firing, the module is inspected; the electrical connections are tested. The module is also cut to the final size. The overall procedure to produce LTCC circuits, as already explained, is mechanical and repetitive, but it demands to pay careful attention to all the steps, which the LTCC tapes are clean without dust, the alignment during screen-

printing and also stacking is precise, the temperatures and pressure values are well-defined, in order to ensure the good quality of the final product. The overall procedure is illustrated again in Figure 2. 17:

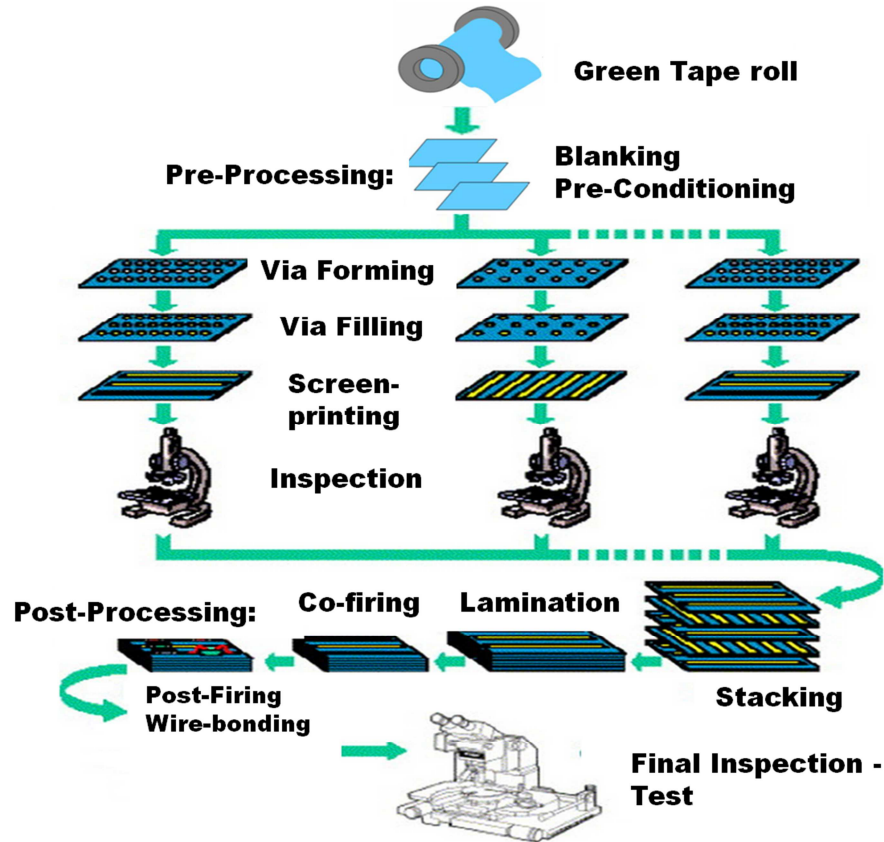


Figure 2. 17: LTCC manufacturing from a roll to a multifunctional module. Image taken from [80].

2.7 Rubidium: Properties, behaviour & Dispensing methods

It is time now to introduce and describe the metallic rubidium and its place among alkali metals. This description is important because one of our objectives in the MACQS project was to develop the reference cell of the atomic clock: this cell contains Rubidium, so it is important to know the characteristics of the element that we are going to manipulate, also for ensuring long life to the final product.

Rubidium is a chemical element whose symbol is Rb. Its atomic number is 37 and it is part of the alkali metal group of the period table, as we can see in Figure 2. 18.

The image shows a standard periodic table of elements. The first column, Group 1A, is highlighted with a red box and labeled 'Alkali Metals' in red text. The elements in this group are Hydrogen (H), Lithium (Li), Sodium (Na), Potassium (K), Rubidium (Rb), Cesium (Cs), and Francium (Fr). The atomic number 37 is shown for Rubidium (Rb). The table also shows other groups and elements, with some elements in the bottom row (period 7) labeled with 'U' followed by a number (e.g., Uub, Uuh, Uuo).

Figure 2. 18: In the periodic table, Rb is present with the atomic number 37, on the column of the alkali metals, together with Li, Na, K, Cs, Fr.

As all alkali metals, Rb has only one electron in its valence orbit. This, and the consequent strong magnetic-dipole interaction of the valence electron with the nucleus, causes the splitting of the ground state of Rb into two hyperfine levels [132]. The hyperfine structure of their energy levels is common for alkali metals, because of their similar electronic configuration, and it is the reason why they are widely used for the reference base in atomic clocks. In particular Rb and Cs are widely used in this application: the use of Rb allows the fabrication of a cheaper and more compact device, still providing good short-term stability. Rb clocks are more compact with respect to Cs atomic clock because of the easy and efficient filtering of the $F=2$ spectral component from the ^{87}Rb light beam already explained in paragraph 2.3. On the other side, because isotopic filtering of the light is impossible with Cs, these clocks are larger in volume, more power consuming and more expensive with respect to the Rb clocks, but they have better long-term stability [60]. Rb is silver in color in its free unoxidized state, has low density for metals (See Table 2.2), has a low melting point (See Table 2.2), it is soft and easily worked in the solid state [133], See Table 2. 2 for the physical properties of Rb.

Melting point	312.46 K (39.31°C)
Boiling point	961 K (688°C)
Density	$1.532 \text{ g}\cdot\text{cm}^{-3}$
Critical point	2093 K, 16 MPa
Vapor pressure at 25°C	$5.22 \cdot 10^{-5} \text{ Pa}$ ($3.92 \cdot 10^{-7} \text{ torr}$)

Table 2. 2: Physical properties of Rb. Data taken from [132], [134], [135].

For the vapor pressure, it is valid the model presented in [135], whose equation may be re-written as:

$$\log_{10} \left(\frac{p_v}{p_{atm}} \right) = A - \frac{T_{ref}}{T} \quad \text{Eq. 2. 3}$$

,where p_v is the vapor pressure in atmospheres, p_{atm} is the atmospheric pressure, T is the temperature in K and A and T_{ref} are summarized in Table 2.3; the curve of the vapor pressure of rubidium is illustrated in Fig. 2.19

	A	$T_{ref} [K]$
Solid State	4.857	4215
Liquid State	4.312	4040

Table 2. 3: Values of constants A and of T_{ref} to be used in Eq. 2.3 (vapor pressure of Rb).

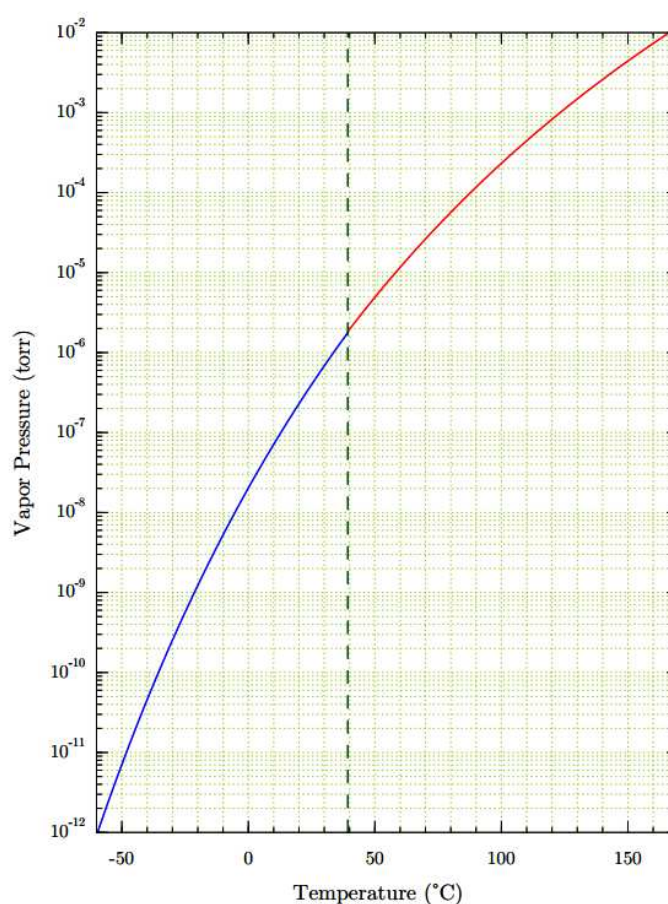


Figure 2. 19: Vapor pressure of rubidium following the model described by Eq. 2. 3. The vertical dot line indicates the melting point. Graphic taken from [135].

The chemical properties of rubidium are consequence of its electronic configuration with only one electron in the valence orbit. So, it is a strong reducing agent, its electronegativity is very low, it is a good conductor of electricity and heat and its

Chapter II: State of the Art

Young's modulus is low (considering that it is a metal). See Table 2. 4 for chemical and other properties of Rubidium.

Oxidation state	1 (strongly basic oxide)
Electronegativity	0.82 (Pauling scale)
Atomic radius	248 pm
Crystal structure	Body-centered cubic
Electrical resistivity at 300 K	$13.32 \cdot 10^{-8} \Omega \cdot \text{m}$
Thermal conductivity	$58.2 \text{ W} \cdot \text{m}^{-1} \cdot \text{K}^{-1}$
Young's modulus at 300 K	2.4 GPa

Table 2. 4: Physical and other properties of Rb. Data taken from [132], [135], [136].

2.7.1 Summary of reaction of Rb with other elements

Regarding his behavior in nature, Rb has extremely violent reactions with numerous compounds; therefore improper handling can cause dangerous accidents, and its manipulation for the fabrication of atomic clocks reference cell is a critical issue. In particular:

- 1) Rubidium burns and usually explodes violently when in contact with water [133]. The explosion is caused by the secondary reaction of liberated hydrogen with the oxygen of the air. The following are the chemical reactions that happen when Rb is in contact with water:



The heat liberated by reaction (*) is most likely sufficient to cause reaction (**) to occur; the liberated hydrogen will be ignited by the heat, causing an explosion. When such an explosion occurs, the unreacted metal is usually scattered over a wide area, where it can cause further trouble

- 2) In air, and even more so in oxygen, metallic rubidium has tendency to rapidly tarnish. The tarnishing process is relatively colorful, finally leading to the formation of an orange-yellow compound, the Rb dioxide, commonly called Rb superoxide, with the following chemical reaction [133], [137]:



Of course, when evolved in Rb superoxide, the alkali metal loses all its original properties. The resulting compound is still a powerful corrosive agent and attacks biological tissue (eyes, skin), clothing, and many materials of construction.

- 3) Rubidium does not spontaneously react with nitrogen [133], because too much energy is required to break the triple bond in N_2 and for the formation of the

azide N^{3-} ions. The only alkali metal which spontaneously reacts with N_2 is the lightest of alkali, lithium (forming the azide LiN_3). Sodium azide (NaN_3) and potassium azide (KN_3), while existing, are extremely unstable and tend to decompose back into their constituent elements [138], [139]. Rb azide (RbN_3) can be constituted in laboratory and this compound, which is metastable in air, is used to dispense Rubidium inside the reference-cell (see the following).

- 4) Halogens (fluorine, chlorine and bromine) tend to form ionic bonding with the very electropositive Rb atom, forming halide salts, with formula RbX , where X is the halogen [140], as usual for alkali metals.
- 5) Rb reacts with carbon, in particular with graphite, forming the carbide RbC_8 . In this compound, the Rb is only partially ionized (50-70%); upon exposure of RbC_8 to O_2 , it undergoes extensive decomposition involving the expulsion of the alkali metal. Another possibility is when Rb is completely ionized in contact with graphite, forming the carbide RbC_{24} . The metal-graphite bonding in this case is stronger, and this compound is not extensively decomposed by interaction with O_2 [141].
- 6) Rb reacts with alcohols in basically the same manner as the other alkali react with water, but the reaction proceeds more slowly [133], forming alkoxide salts with evolution of H_2 .
- 7) Expectedly, Rb does not react with noble gases (He, Ne, Ar, Kr, Xe) [133].

The logical consequence of the first two points is that rubidium must be kept away from air and water during cell fabrication, otherwise it will either oxidize forming rubidium superoxide (in contact with dry air), or progressively transform into RbOH (in contact with humid air), or violently explode (in contact with water). Moreover, once sealed, the cell must be hermetic, avoiding all air ingress, which would oxidize the alkali metal. The cell can contain, together with Rb, a buffer gas, which, as a consequence of point 3), can be nitrogen, or, as a consequence of point 6), can be a noble gas (usually argon is used, [142]–[144]). A deeper literature analysis on alkali metals, presenting tests performed at temperatures which are significantly higher with respect to our application, gave us more detailed information about the behavior of these metals in different situations, and their compatibility with complex systems involving for example the presence of ceramics and metals. In particular:

- Alkali metals are not aggressive to Nickel (Ni) and Iron (Fe) and also Ni-alloys and many steels; after exposing these metals for a maximum exposure time of 500 hours at 870°C , with various liquid alkali metals (including cesium), their surface does not present roughness or sign of penetration of the alkali metal [145].
- Refractory materials (Niobium, Molybdenum, Tantalum, Tungsten and Rhenium) and their alloys, after exposition with liquid alkali metals during 300 hours at 1000°C do not show significant changes in their structure and physical

properties. They have low solubility in alkali metals, even if a slight solubility is observed at high temperatures (1000°C) [145].

- Similar studies on the eutectic system "NaK" (eutectic mixture of both alkali metals Na and K) show that some high-temperature braze alloys containing precious metals (Ag, Au, Pt) are severely attacked when exposed to liquid NaK at 140°C for 500 hours. However, some braze alloys are not attacked by liquid NaK; in particular, the braze alloy composed by 60% Ag, 30% Cu, 10% Sn is not attacked, probably because of the presence of the tin in the system, which has low solubility with alkali metals (see Figure 3. 3, phase diagram Rb-Sn). Also the alloy composed by 71.8% Ag, 28% Cu, 0.2% Li is apparently resistant to NaK, since after the exposition it lost some weight, but only in a minimal part [146].
- The same research shows that liquid NaK is compatible with silicones at room temperature, but a degradation of the silicone is observed at 140°C [146].
- The eutectic system NaK is compatible with the majority of common-use polymers and plastic materials (saturated polyolefins, polycarbonate, polypropylene) and epoxy at temperatures below 140°C, and most probably also at higher temperatures [146].
- Tests proved that the ceramic materials BeO, Al₂O₃, Y₂O₃, exposed with liquid Potassium (K), during 500 hours at 870°C, are not attacked by the alkali metal [147];
- The same tests show that high temperature braze alloys based on vanadium (V), niobium (Nb) and zirconium (Zr), have a satisfactory behavior when in contact with potassium, even if, after exposition of the system for 500 hours at 870°C, the braze presented a certain surface roughening and dissolution; the dissolution is more evident when the concentration of oxygen in the chamber increased [147].
- The same research confirmed the compatibility of the alkali metal with some plastic materials and polymers: manipulations were done using polyethylene tubes, and they did not affect the composition of the alkali metal [147].

Therefore, a priori, from the above reported tests, we can affirm that rubidium should be compatible with a system containing ceramics and metals and that the use of some polymers (such as a plastic micropipette) to manipulate liquid rubidium is allowed, at least at low temperatures and for short times. The common high-temperature braze alloys containing precious metals may experiment problems when in contact with Rb. However, results on the alloy containing 10% of tin are encouraging, because this alloy did not show degradation when in contact with eutectic NaK; therefore, using a tin alloy for performing the sealing may be a possibility.

2.7.2 Review of Rb/Cs dispensing method

The literature of atomic clocks presents several techniques to handle and dispense the Rb during the fabrication of the reference cells. These techniques are mainly based on three principles:

- 1) Dispense a droplet of pure alkali metal into the pre-forms by pipetting. The alkali metal is kept in an anaerobic glove box, where the sealing process is also performed [71], [148], [149] .
- 2) Dispense a thin film of alkali azide RbN_3 or CsN_3 into the cell. The RbN_3 compound does not form spontaneously, so it is prepared in the laboratory [150]. The RbN_3 is dispensed into the cell by thermal evaporation. Alternatively, CSEM Switzerland dispensed the RbN_3 compound by dissolving it in water and simply pipetting it into the pre-forms. After being dispensed into the cell, it is decomposed into its constituent materials by cycles of UV light [151] or by thermolysis [152];
- 3) Laser activation of a latent small, pill-like solid alkali source dispenser inside an anodically bonded cell [153] .

The first technique is safe and straightforward, but the whole sealing procedure must be performed in a glove box, which is not very practical.

The second technique introduces safety issues, because the RbN_3 and CsN_3 compounds are highly toxic and explosive. Additionally, they emit gases inside the cell after sealing, which are absorbed by a getter which is introduced into the system. The laser activation technique elegantly solves the reactivity problem, but the problem of gas emission is still present. The presence of a getter for these cells is therefore necessary, but it will trap most of the gases present into the cell, making this method difficult to conciliate with the presence of a buffer gas into the cell.

For these reasons, we decided to develop an innovative method to dispense Rb into the reference cell. The method is described in details in the following chapter. The proposed technique is based on the first described approach (pipetting of a droplet of pure alkali metal into the pre-forms), but, thanks to the presence of a protection solvent, the sealing process does not need to be performed in the glove box.

3 Reference cell of Atomic Clock: Design, Fabrication and Test

In this chapter we will illustrate our original concept idea for the fabrication of the reference cell for an atomic clock. The metallurgical interactions that happen between rubidium and the metals that may potentially be introduced in the design of the reference cell are investigated, in order to understand the potentialities of the proposed design. The chapter then continues in detailing the procedure to dispense Rubidium inside the cell and to fabricate the reference cell for the atomic clock, using an innovative low-temperature sealing technique and a multifunctional LTCC spacer. Finally, the chapter describes the tests performed to find out the best composition for the sealing ring and the tests carried out to prove the hermeticity of the sealed cell.

3.1 The Reference Cell: the Original Concept Idea

In the development of a miniature atomic clock, obtaining an alkali vapor cell that is reliable and stable, yet also easily fabricated is arguably the most challenging part; it is a hot topic of research and many different designs are proposed in the literature [142], [154], [155]. Besides being small, the cell must be filled with an alkali metal (Rb, used in this work, or Cs), sealed, and heated during operation to generate a significant vapor pressure. The technology may be used both for the reference cell and the light source (Rb lamp). However, alkali metals are very reactive with oxygen and water, and therefore they must be protected from air before and during the sealing process, and the resulting cell must be completely hermetic in order to avoid its rapid degradation. The most widely used approach to fabricate a hermetic mini-cell is the use of anodic bonding [76] to close the cells. The problem of this well-known and standard sealing process is that it requires relatively high temperatures ($\sim 450^{\circ}\text{C}$) and long times (a few hours), which often causes evaporation or excessive reactions of the alkali metal. In order to solve this problem, we investigated low-temperature sealing techniques, and in particular the use of eutectic low-temperature solder alloys [156]–[160]. At the time we started the research, no previous attempts of realization of atomic clock reference cell using solder as a bonding technique were reported, so this was a very challenging and innovative topic of research. In parallel with our research, Dr. Straessle studied the possibility to use a different low-temperature bonding technique: she used thermocompression of indium to bond two silicon-glass pre-forms together, with Rb dispensed inside it [161], [162]. The thermocompression of indium is performed at low temperatures (ca. 140°C) and allowed production of hermetic cells. The cells were kept

Chapter III: Reference Cell of Atomic Clock: Design, Fabrication and Test

several months in air, at room temperature, without significant oxidation of alkali metal [163]–[165]. However, she reported in her thesis (result still not published) that the cells became inactive after 20 days if kept at 80°C [166], probably because the high temperature accelerates the Rb-In interaction.

Our original idea at the base of the realization of the cell was to bond two glass substrates (the substrate must be transparent to allow the light coming from the light source to pass through for exciting the alkali metal atoms) using solder paste, with the rubidium collocated in-between them. In order to realize a stable seal, the solder paste was dispensed on top of a metallization ring (made of noble metals, to be defined), so that it will adhere and remain located on top of such metallization, avoiding its spreading all over the substrate. The bonding of both substrates that formed the reference cell (with the Rb in-between) is then realized by melting the solder (see Figure 3. 1 for the original concept idea of fabrication of the cell, and Figure 3. 9 for the detailed and refined design of the cell finally developed).

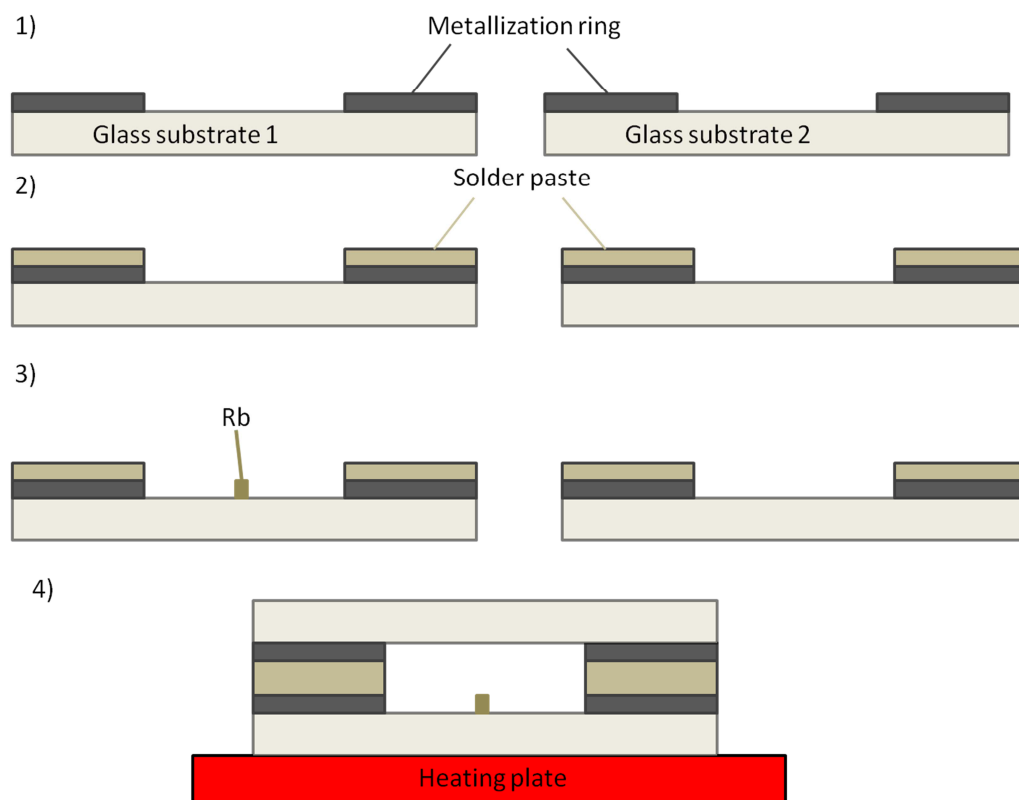


Figure 3. 1: Concept idea of the design and fabrication of the cell

3.2 Metallurgical Interactions in the Reference Cell System

The cell, conceived as above, is a system which involves metals of different nature and behavior: the metallization ring is made of a noble metal (Ag, Ag-Pd, Au), the solder paste (depending on which eutectic alloy will be preferred) is an alloy of Sn, Pd, Bi, Ag, and in-between there is the pure Rb droplet. A literature study was carried out in order to evaluate and establish the interactions between the various metals present into the system.

3.2.1 Interactions between Rb and metallization metals

First of all, the interaction between the rubidium and the metals which may potentially be used in the metallization ring were studied. The objective was to find a metal which is not miscible with Rb, otherwise the diffusion of Rb into the metallization can cause the degradation of the seal. Ideally, the system of the metal with rubidium should form neither eutectics nor intermetallic compounds and the two metals should ideally not be soluble into each other at the working temperature of the reference cell (ca. 70°C). If these three requirements are met, we can be sure that Rb will stay stable in its original state for the whole lifetime of the cell. The first metal that was investigated was gold, and it was found to be a poor choice for the metallization, because of the large solubility of Au into liquid Rb, even at low temperatures. In fact, as we can see in the phase diagram illustrated in Figure 3. 2, we have 5 mol% Au dissolution in Rb at ca. 380 K; therefore, even at moderate temperatures, the gold of the metallization ring would dissolve significantly into liquid Rb. Moreover, looking at the phase diagram of the system Au-Rb, the formation of intermetallic compounds is observed, such as AuRb, Au₂Rb and Au₅Rb [167], [168]. The formation of a low-melting eutectic system formed by 98.6 mol% of Rubidium and 1.4 mol% of gold is observed at an eutectic temperature of 312.48 K. The formation of these compounds is not desirable, because the presence of Rb into the joint will probably cause the failure of the sealing, penetration of oxygen into the packaging and the end of the clock operation. The phase diagram of Au and Rb is illustrated in Figure 3. 2, and Table 3. 1 summarizes their principal interactions.

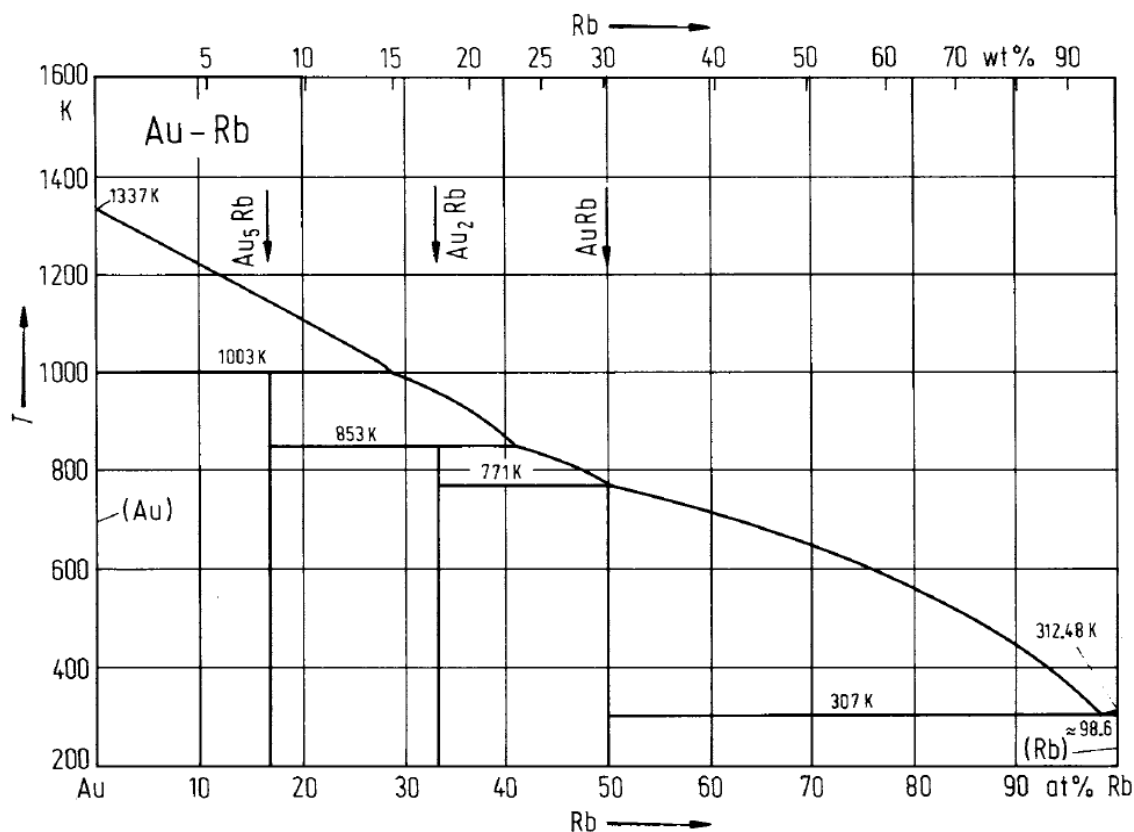


Figure 3. 2: Phase diagram Rb-Au shows solubility of Rb into Au. Image taken from [167].

Temperature of 5% dissolution of Au into Rb	380 K
Intermetallic compounds observed (melting point)	AuRb (771 K) Au ₂ Rb (~850 K) Au ₅ Rb (~1000 K)
Eutectic compounds observed (melting point)	98.6% Rb – 1.4% Au (312.48 K)

Table 3. 1: Summary of interactions between Rb and Au

Another possibility for the metallization is to use silver, so the interactions between Ag and Rb were investigated. This system has been studied in details, among others, by Kienast et al. in 1961 [169]. They studied the interactions between alkali metals and metals of group 11 (Cu, Ag, Au). They found that Ag and Rb do neither form intermetallic nor eutectic compounds. The two metals have very low mutual solubility at 100°C (lower than 0.1%). The same study also confirmed the formation of intermediate phases between Rb and Au. In 1991, Predel and Madelung studied again the Ag-Rb system, without tracing the phase

diagram, but confirming that no intermediate phases are formed and that the mutual solubility of the two metals is lower than 0.1% [170].

Other metals that can be used for the metallization are Palladium (Pd) and Platinum (Pt). Also in this case, the phase diagram is not available, but experiments showed that Rb has a solubility limit below 0.1 mol% into both Pd and Pt up to at least 900 K [168], and no intermetallic compounds are observed between these metals.

Finally, the best choice for the metallization ring is to use an alloy of Ag-Pd, since the formation of intermetallic compounds or eutectics is not expected between Pd and Rb, and expected at high temperatures for Ag. Moreover, the solubility of the metal into liquid Rb is expected to be lower than 0.1% at 70°C.

3.2.2 Reactions between Rb and solder metals

The next step was to study the interactions between rubidium and the metals which may potentially be used for the solder ring. Again, the objective was to find a metal which has very low solubility into rubidium, i.e. a metal which do not diffuse into liquid rubidium at the working temperature of the cell (ca. 70°C), in order to preserve the purity of the alkali metal avoiding to enrich it with impurities. The first metal investigated was tin (Sn). Studies confirm the formation of intermetallic compounds between Rb and Sn which melt at very high temperature [171] (Figure 3. 3 and Table 3. 2, typically from 570°C for RbSn to 890°C, which is the highest temperature of Rb-Sn liquidus, for Rb₂Sn₃), despite of the low melting points of both pure Rb and pure Sn. The formation of the intermetallics in this case is not problematic as long as they do not affect the purity of Rb: in this case, the high melting point of the intermetallic compound formed and their appearance as line phases, i.e. essentially stoichiometric compounds with a very low composition range are the factors that suggest a low rate of interaction of Sn and Rb, by formation of passive compounds on the surface of Sn. We cannot precisely establish a temperature which corresponds to dissolution of 5 mol% of Sn into Rb, because the left-hand side of the diagram is only tentative: a dot line suggests how the curve might look like, and in the case that this line is correct, the corresponding temperature is ca. 600°C, so most likely high enough to ensure that in our application Rb will not contain significant Sn impurities. Moreover, low-melting eutectics with significant Rb-Sn intermixing are absent throughout the whole composition range.

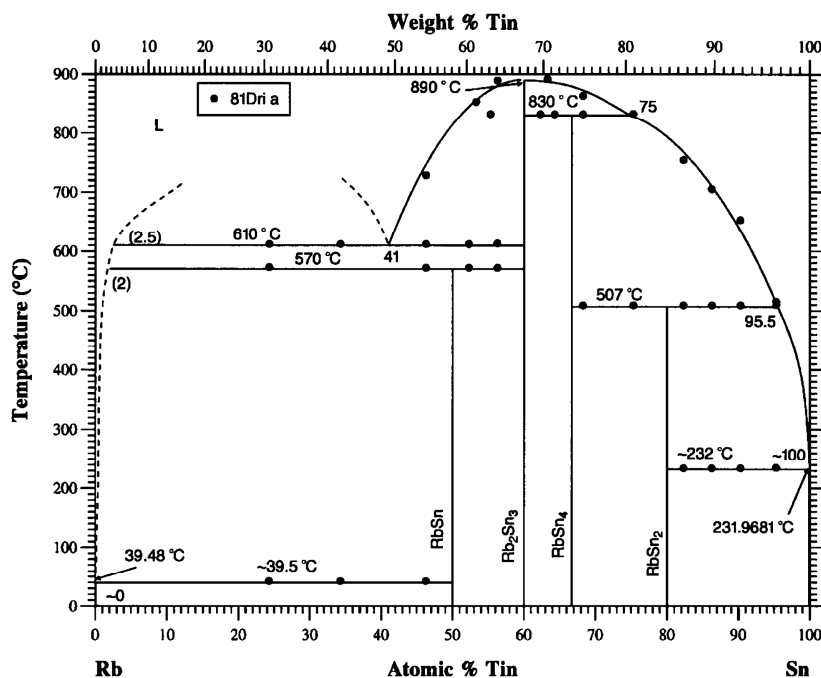


Figure 3. 3: The Rb-Sn phase diagram . Image taken from [171] (RbSn₄ & RbSn₂ mistakenly swapped in the diagram).

Temperature of 5% dissolution of Sn into Rb	Probably ~600°C										
Intermetallic compounds observed	<table border="1"> <thead> <tr> <th>Compound</th><th>Melting point</th></tr> </thead> <tbody> <tr> <td>RbSn₄</td><td>507°C</td></tr> <tr> <td>RbSn₂</td><td>830°C</td></tr> <tr> <td>Rb₂Sn₃</td><td>890°C</td></tr> <tr> <td>RbSn</td><td>570°C</td></tr> </tbody> </table>	Compound	Melting point	RbSn ₄	507°C	RbSn ₂	830°C	Rb ₂ Sn ₃	890°C	RbSn	570°C
Compound	Melting point										
RbSn ₄	507°C										
RbSn ₂	830°C										
Rb ₂ Sn ₃	890°C										
RbSn	570°C										
Eutectic compounds observed (melting point)	No										

Table 3. 2: Principal interaction observed between Rb and Sn.

Another possible material for the solder is Bismuth (Bi). The Rb-Bi system is not described in the metallurgy literature; in alternative, we can consider the K-Bi and Cs-Bi systems, which have been studied in the literature [172] : the corresponding phase diagrams of these systems are shown in Figure 3. 4 and Figure 3. 5, and the principal interactions between the metals are summarized in Table 3. 3 and in Table 3. 4. Looking at the periodic table shown in Figure 2. 18, Rb is situated in-between K and Cs in the column of the alkali metals, therefore we can interpolate its behavior, which should be intermediate between K and Cs. Looking at the phase diagram of K-Bi, the presence of intermetallic compounds with high melting point

(KBi_2 at 565°C and K_3Bi at $\sim 660^\circ\text{C}$) is observed. The temperature for 5% dissolution of Bi into K is ca. 280°C . No low-melting eutectics are observed in the phase diagram.

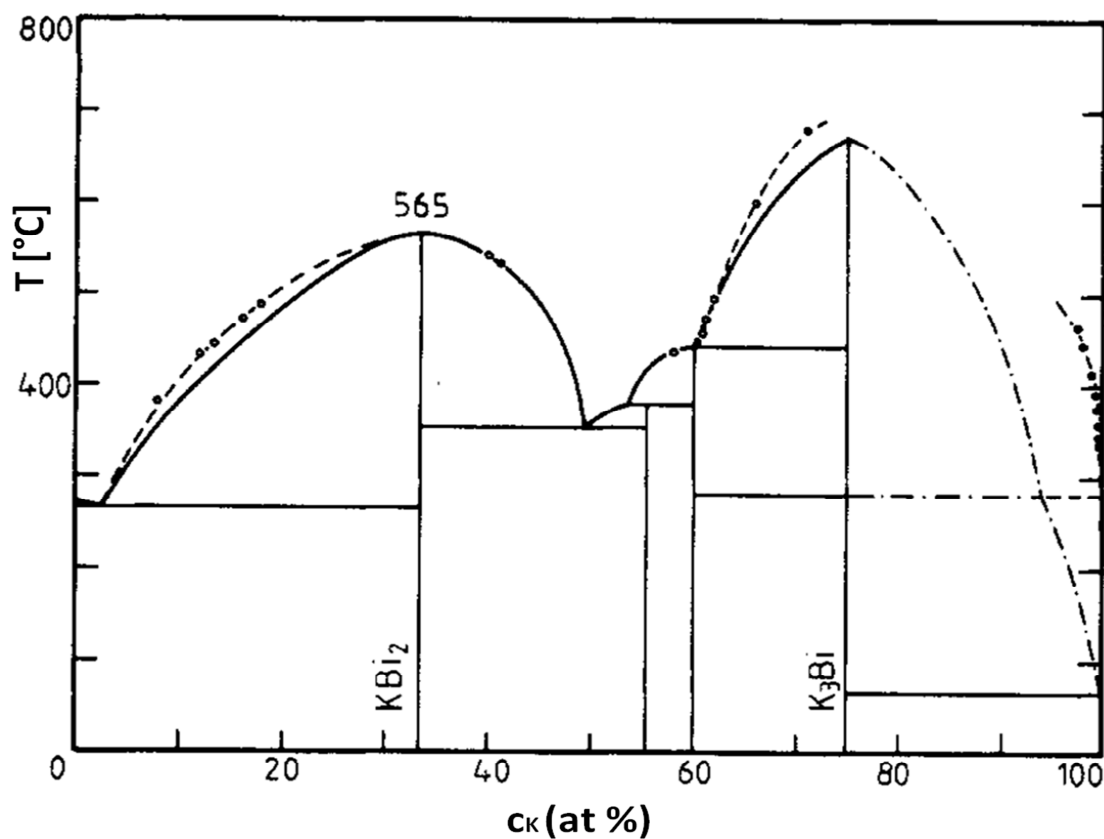


Figure 3. 4: The K-Bi phase diagram. Image taken from [172].

Temperature of 5% penetration of Bi into Rb	$\sim 250^\circ\text{C}$	
Intermetallic compounds observed	<i>Compound</i>	<i>Melting point</i>
	KBi_2	565°C
	$\sim \text{K}_5\text{Bi}_4$	$\sim 430^\circ\text{C}$
	K_3Bi_2	$\sim 380^\circ\text{C}$
	K_3Bi	$\sim 660^\circ\text{C}$
Eutectic compounds observed (melting point)	No	

Table 3. 3: Principal interactions between K and Bi.

Looking at the phase diagram of Cs-Bi, formation of intermetallic compounds with high melting point is also observed (the higher liquidus temperature in this case is 635°C), while no low-melting eutectic is reported. We cannot precisely establish a temperature which corresponds to the dissolution of 5% of Bi into liquid Cs, because the left-hand side of the diagram is only tentative: a dot line suggests how the curve might look like, and in the case that this line is correct, the temperature at which 5% of Bi dissolves into 95% of Cs is ca. 200°C.

Overall, Bi-Rb interactions are expected to be very similar to Bi-K or Bi-Cs, given the fact both latter phase diagrams are almost the same.

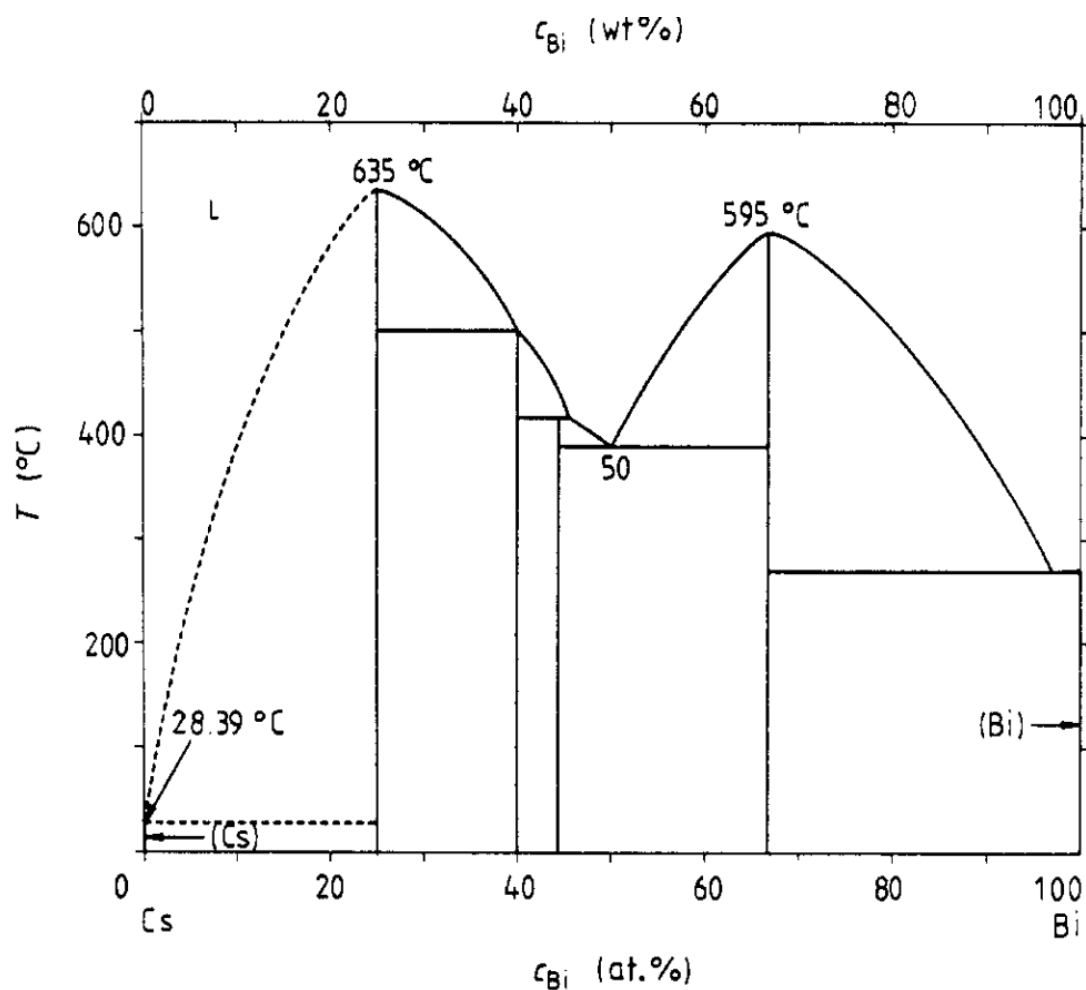


Figure 3. 5: The Cs-Bi phase diagram. Image taken from [172].

Temperature of 5 % dissolution of Bi into Cs	~250°C	
Intermetallic compounds observed	<i>Compound</i>	<i>Melting point</i>
	CsBi ₂	595°C
	~Cs ₅ Bi ₄	~420°C
	Cs ₃ Bi ₂	~500°C
	Cs ₃ Bi	635°C
Eutectic compounds observed (melting point)	No	

Table 3. 4: Summary of the principal interaction observed between Cs and Bi.

In comparison with Sn, Bi is probably less preferable, with somewhat lower-melting intermetallics and (presumably) higher solubility in liquid Rb.

Lead (Pb) is another potential metal that can be used for the solder ring. Looking at the phase diagram of Pb-Rb (Figure 3. 6 & Table 3. 5), the formation of different intermetallic compounds with high melting point is observed [173]: the liquidus curve has a maximum temperature of 874 K (601°C). Dissolution of 5% of Pb into liquid Rb is observed at a temperature of ca. 700 K (427°C), but this is only an estimation (dot line on the right hand side of the diagram only “suggests” the curve). No low-melting eutectic systems which may affect the system are observed.

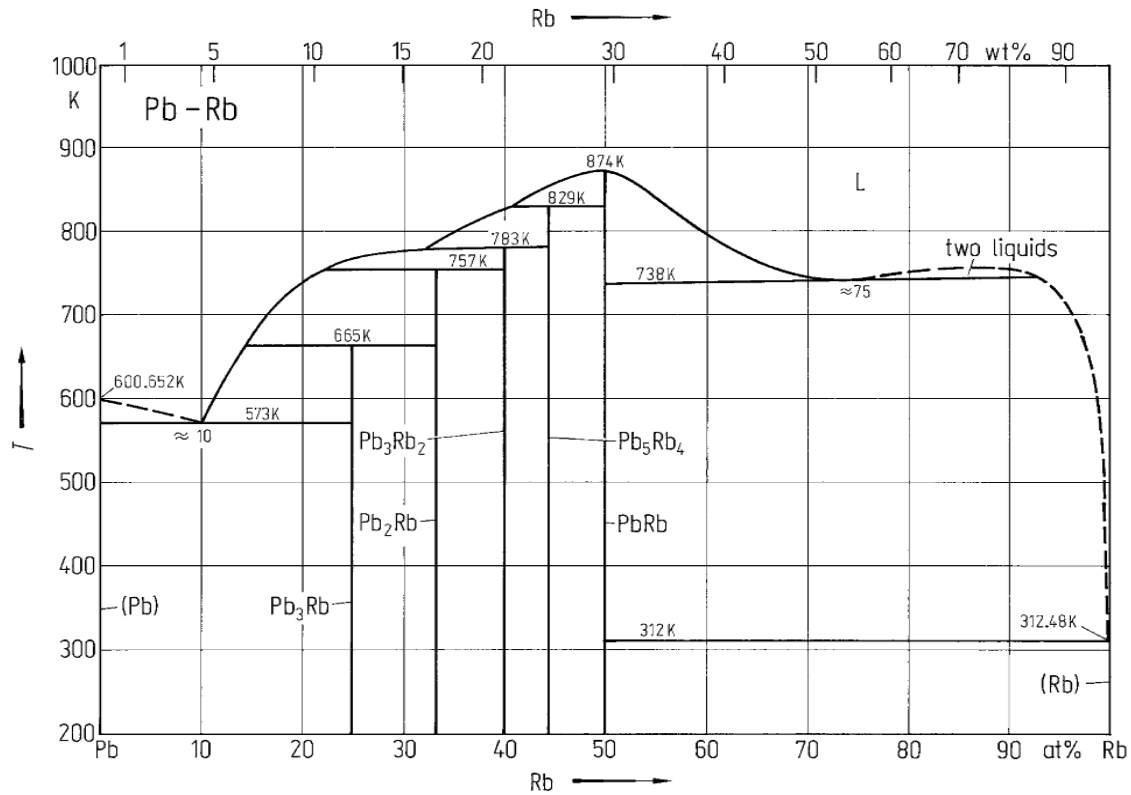


Figure 3. 6: Phase diagram Rb-Pb. Image taken from [173].

Temperature of 5% dissolution of Pb into Rb	Probably ~730 K / ~460°C	
Intermetallic compounds observed	<i>Compound</i>	<i>Melting point</i>
	Pb_3Rb	665 K / 392°C
	Pb_2Rb	757 K / 484°C
	Pb_3Rb_2	783 K / 510°C
	Pb_5Rb_4	829 K / 556°C
	$PbRb$	874 K / 601°C
Eutectic compounds observed (melting point)	No	

Table 3. 5: Summary of the principal interactions between Rb and Pb.

3.2.3 Conclusions of the metallurgical literature analysis

At the end of our theoretical investigation regarding the design and the low-temperature sealing technique proposed for the reference cell of the atomic clock, and in particular after the metallurgical analysis of the metallurgical literature regarding the interactions between Rb and the metals that can potentially be part of the reference cell, we can affirm the following:

- Liquid Rb has low solubility and it does not form intermetallic compounds or eutectic systems with Ag and Pd, therefore these metals can be used for the metallization ring of the reference cell without affecting the purity of the alkali metal and they will not cause the degradation of the sealing. Gold must be avoided, as it significantly dissolves into Rb.
- Despite the low melting point of both Rb and traditional solder metals (Sn, Bi, Pb, Bi), these systems form intermediate compounds with much higher melting points than the pure metals; moreover, solder metals (except possibly Bi) exhibit very limited solubility and very low levels of mixing with the alkali liquids. The intermetallics formed are line phases, with essentially stoichiometric compositions, with a trend to even ionic bonding in so-called Zintl phases due to the large electronegativity difference [174]. This indicates formation of inert, passive layers on the solder surface, with low interdiffusion.

The above conclusions are very encouraging, suggesting the proposed technique of soldering on thick-film metallizations potentially may be used to seal alkali metals such as Rb. Of all solder metals, Sn is preferred, as it seems to yield the highest-melting intermetallics and have the lowest solubility in Rb.

3.3 Innovative and Practical Solution proposed for Rb Handling

In this research, we developed a new, innovative, practical and safe solution to handle, store for long term avoiding oxidation, and dispense the Rb inside the mini-cell. As previously explained, Rb should be kept away from air and water during all manipulations. In order to protect avoid the oxidation of Rb, we store the alkali metal inside a large ‘pool’ of dodecane (C₁₂ alkane, [175]). The dodecane is hydrophobic, so it does not readily take up water and at the same time it protects the Rb from oxygen. First, the Rb is slightly heated up to its melting point, and dispensed into the cell using a glass micropipette, staying under the dodecane. Then, the lid is placed onto the cell, and the resulting assembly (in a small dodecane pool) is rapidly transferred into a vacuum soldering chamber, and first progressively heated up to 80°C at 20 mbar of N₂ to gently evaporate the dodecane while avoiding outright boiling. After this step, the cell is heated up to the soldering temperature in the final desired atmosphere, and thus the solder is melted to realize the sealing. This method prevents Rb

oxidation during the sealing process, and allows easy handling under ambient conditions. For long-term storage, the box containing the dodecane pool is simply closed and placed into a glove box, where the dodecane provides additional protection against residual moisture. Stored in this way, the alkali metal maintains its original properties for ca. 90 days. Figure 3.7 shows the storage and the dispensing technique of rubidium.

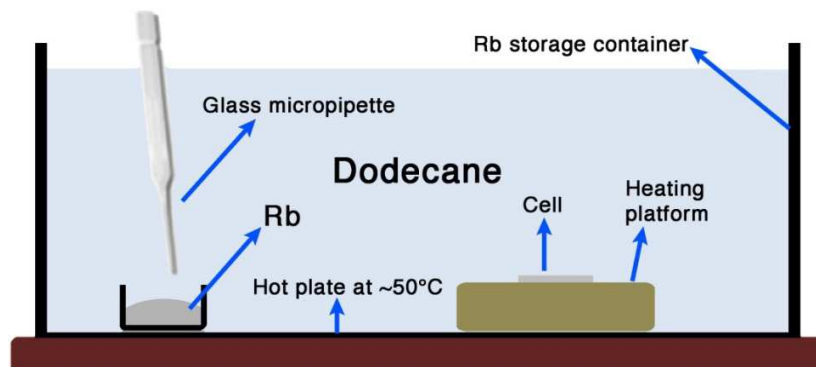


Figure 3. 7: A schematic diagram showing Rb storage and dispensing

3.3.1 Study of gas dissolution into the dodecane

The dodecane has been chosen to protect rubidium because it does not readily take up water or oxygen, so it should efficiently protect rubidium. The dissolution of gases inside the dodecane was investigated, because if a significant amount of gas diffuses into the liquid solvent, when this will be placed in low-pressure atmosphere it will violently boil to evacuate the gas particles diffused. The violent boiling of the dodecane should be avoided, because it will cause undesired movements of the glass lid, leading to a poor bonding. Instead of boiling, a gentle evaporation of the dodecane is wished, which would avoid any movement of the lid; the evaporation of the solvent can happen only when the amount of gas dissolved is poor. Two cases were investigated: in the first case, the dodecane is kept in the glove box (so in N₂ atmosphere), and in the second case the dodecane is kept in air at atmospheric pressure. In both cases, the amount of gas dissolved into the solvent was calculated.

The dodecane is kept into the glove box

In this case, the dodecane is in contact with ~100 kPa (~1 atm) of essentially pure N₂, at 25°C (298 K), as the glove box is kept only very slightly (< 1 kPa) above ambient atmospheric pressure. Henry's law [176] states that at a constant temperature, the amount of a given gas that dissolves in a given type and volume of liquid is directly proportional to the partial pressure of that gas in equilibrium with that liquid. Mathematically, we can write Henry's law, in its simplest form valid for low concentrations, as follows:

$$p_{gas} = H_{gas} \cdot c_{gas} \quad \text{Eq. 3. 1}$$

, where:

- p_{gas} is the partial pressure of the gas (in the gas phase) in equilibrium with the liquid
- c_{gas} is the concentration of the gas in the liquid
- H_{gas} is the gas' Henry constant with respect to the liquid (here dodecane)

The solubility of nitrogen in dodecane has been determined previously, in particular:

- Battino et al. [177], in their extensive 1984 review of N_2 solubility data in liquids from many studies, retain a dissolved molar fraction of 0.123%, at 25°C and 101.3 kPa, which corresponds to $H_{N_2} = 18.8 \text{ kPa}/(\text{mol}/\text{m}^3)$ and roughly matches the general trend for N_2 solubility in n-alkanes they report.
- From the high-pressure data of Gao et al. [178], taken at somewhat elevated temperatures (71, 104 and 138°C), we extract by fitting down to low pressures and 25°C a rough estimate of $H_{N_2} \sim 18.6 \text{ kPa}/(\text{mol} \cdot \text{m}^3)$.
- From recent studies by Hesse, Battino et al. [179], we get $H_{N_2} = 17.7 \text{ kPa}/(\text{mol} \cdot \text{m}^3)$ at 25°C.

The value retained in this research is the latter, which were performed with high accuracy with well-controlled substances. The saturation concentration of nitrogen in dodecane corresponding to glove box ('gb') storage is given by:

$$c_{N_2,gb} = \frac{p_{N_2}}{H_{N_2}} = \frac{100}{17.7} = 5.6 \text{ mol}/\text{m}^3 \quad \text{Eq. 3. 2}$$

We can now estimate the volume of nitrogen (expressed as the volume in the gaseous state) stored at saturation per volume of liquid dodecane, starting from the equation of ideal gases and substituting into it the relationships and the values calculated in Eq. 3. 1 and Eq. 3. 2 :

$$p_{gas} \cdot V_{gas} = n_{gas} \cdot R \cdot T$$

$$H_{gas} \cdot c_{gas} \cdot V_{gas} = c_{gas} \cdot V_{liquid} \cdot R \cdot T$$

$$\frac{V_{gas}}{V_{liquid}} = \frac{R \cdot T}{H_{gas}} = L_{gas} \quad \text{Eq. 3. 3}$$

, where

- R is the ideal gas constant, 8.31 J/mol/K
- T is the temperature, here ~298 K
- $L_{gas} = V_{gas}/V_{liquid}$ is the volume ratio between the "stored" gas and the liquid, also known as the Ostwald coefficient [180], and is roughly pressure-independent at low pressures

For nitrogen in dodecane, we get:

$$L_{N_2} = \frac{8.31 \cdot 298}{17'734} = 13.9\% \quad \text{Eq. 3. 4}$$

The dodecane is kept in air (saturated by air)

We make the following assumptions:

- Temperature: 298 K (25°C)
- Pressure: 100 kPa (~1 atm)
- Relative humidity (RH) of air: 50%
- Composition of dry air: 78% N₂, 21% O₂, 1% Ar
- Independent (ideal) behavior of the gases with respect to dissolution in dodecane, in line with the conclusions of Battino et al. [177]
- Low-pressure limit, i.e. linear dissolution behavior according to Henry's law
- Negligibly low volume change of liquid dodecane from gas dissolution

Knowing that:

$$RH = \frac{p_{vap}}{p_{sat}} \quad \text{Eq. 3. 5}$$

, where p_{vap} is the pressure of the vapor present into the humid air considered, and p_{sat} is the saturation pressure of air at the temperature considered (so at 298 K). The saturation pressure of air at 298 K is 3.16 kPa [181], so we can calculate the pressure of vapor into the humid air:

$$p_{vap} = p_{sat} \cdot RH = 3.16 \cdot 0.5 = 1.58 \text{ kPa} \quad \text{Eq. 3. 6}$$

From Eq. 3. 6 we know that into ~100 kPa of humid air with relative humidity of 50%, we have 1.58 kPa of H₂O and 98.42 kPa of dry air. Knowing that the composition of dry air is 78% of N₂, 21% of O₂ and 1% of Ar. Table 3. 6 summarizes the pressure of the different gases in contact with the saturated dodecane, as well as the corresponding Henry and Ostwald constants.

Gas	Pressure p_{gas} [kPa]	Henry constant in dodecane H_{gas} [Pa/(mol/m ³)]	Ostwald coefficient in dodecane L_{gas}
N ₂	76.77	17'734 [179]	14%
O ₂	20.67	10'092 [179]	25%
Ar	0.98	8'884 [179]	28%
Water vapor (H ₂ O)	1.58	1'180 [182]	210%

Table 3. 6: The pressures of individual gases dissolved in dodecane and their Henry and Ostwald constants.

For O₂ and Ar in dodecane, we retain the same high-quality source as for N₂ [179], noting relatively good agreement with previous work for O₂ [183]. For H₂O, we use data for liquid-liquid solubility, fitted by Tsonopoulos [182] based on data by Schwartzberg [184], by considering, given the negligible solubility of dodecane in water, that the liquid H₂O phase is thermodynamically equivalent to water in the gas phase at saturation pressure. Making the assumptions of mutual independence of the gases with respect to dissolution in dodecane [177] and linear Henry behavior, we then calculate the molar concentration of the different gases into saturated dodecane, and also express it in terms of dodecane volume (by multiplying the corresponding Ostwald coefficient by the molar fraction in humid air). The results are shown in Table 3. 7.

Gas	Molar concentration c_{gas} [mol/m ³]	Volume of individual gas/volume of saturated dodecane
N ₂	4.33	10.7%
O ₂	2.05	5.1%
Ar	0.11	0.3%
Vapor (H ₂ O)	1.34	3.3%
Total	7.83	19.4%

Table 3. 7: Molar concentration of the different gases into saturated dodecane in humid air, and volume of the gas diffused in percentage of dodecane volume

With respect to the first case, when the nitrogen is kept into the glove box and it is saturated by pure N_2 , there is more gas dissolved in the liquid dodecane overall, and this is the first negative effect to keep the dodecane in air instead of in glove box, in N_2 atmosphere. Rather than boiling, however, the major concern here is potential attack of the Rb by O_2 and H_2O , of which significant concentrations may dissolve into dodecane. For these reasons, the dodecane pool must be kept in the glove box, in an atmosphere of pure nitrogen, and only exposed to air briefly, during handling. Deaeration may be performed upon returning to the glove box, by the usual pumping/purging procedure of the airlock. To further decrease oxygen and water impurities, absorbents such as Na, Na:benzophenone, CaH_2 , etc. may be used.

3.4 Refined Design of the Cell and Test Modules Developed

The concept design presented in Figure 3. 1 was refined, because after some preliminary sealing tests performed with such design, we faced a technical issue: the alkali metal moved onto the sealing ring during the fabrication process, hindering the formation of a stable joint. Figure 3. 8 shows a non-working cell fabricated.

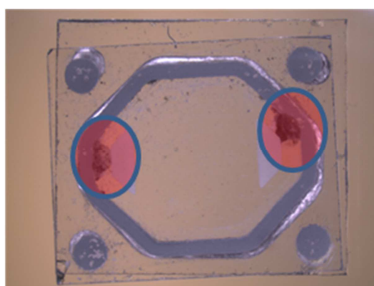


Figure 3. 8: A non-working reference cell produced following the first design presented in Fig. 3.1. The red circles highlight the Rb droplets, which moved onto the sealing ring during the fabrication.

In order to solve this problem, we proposed for the cell an innovative structure composed by Pyrex glass (top and bottom wall) and an LTCC module (in-between spacer). The cross section of the cell is illustrated in Figure 3. 9a. The LTCC spacer is equipped with a Rubidium reservoir for better confinement of the alkali metal (Figure 3. 9c); the liquid droplet is dispensed inside the reservoir, and this will avoid any movement of the alkali metal during the sealing. Moreover, in this work, a test variant of this spacer was produced, where the bottom of the vapor cell cavity was closed with an integrated pressure sensor, consisting of an LTCC membrane carrying a thick-film Wheatstone bridge and thus allowing monitoring of the cell pressure (Figure 3. 9b). The overall dimensions of the developed cells are $10 \times 15 \times 3 \text{ mm}^3$.

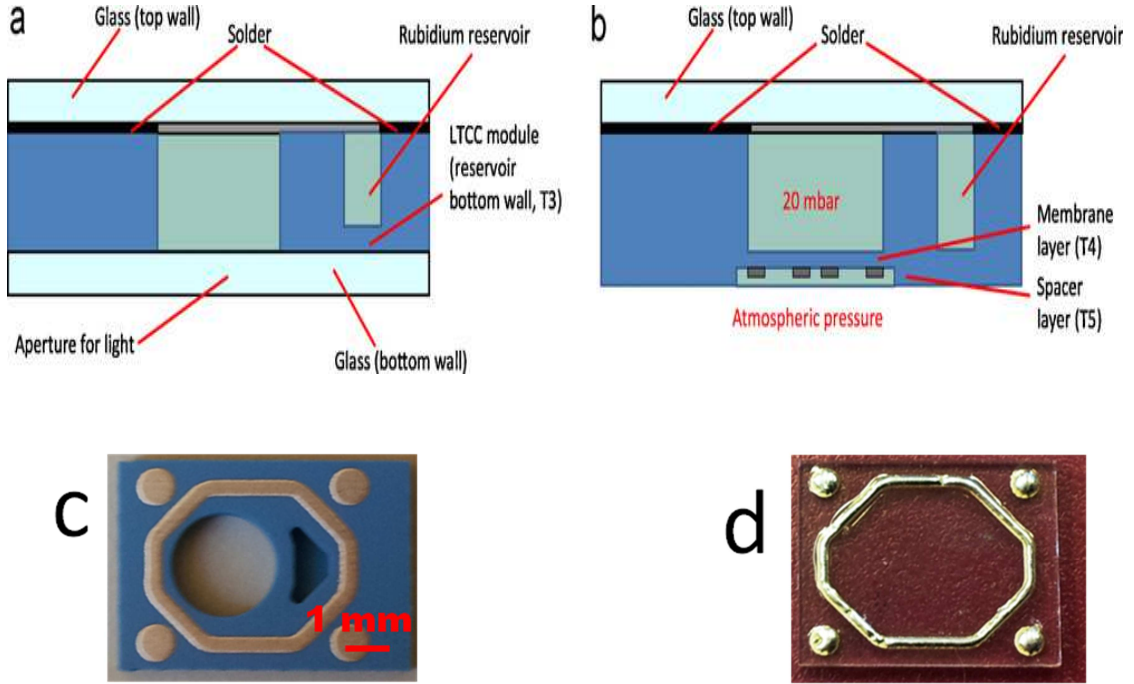


Figure 3. 9: Schematic cross section of the final (a) and test (b) vapor cells. (c), Top view of the LTCC spacer for the final cell, with the Rb reservoir. (d), top view of the glass top and bottom wall.

When producing the test modules illustrated in Fig. 3.10c we faced another technical issue: due to the high pressure applied during the lamination, the membrane of the sensor was deformed, and this caused lack of sensitivity and often a not-working pressure sensor. In order to solve this problem, we investigated and conceived an innovative lamination technique for LTCC, which allows achieving an excellent bonding between the tapes with a low lamination pressure (3.5 MPa instead of 20 MPa applied using the traditional technique). All this will be explained in detail in Chapter 4.

3.4.1 Principle of functioning of the integrated pressure sensor

In the test module, as explained, the bottom wall consists of four piezoresistors connected in a Wheatstone bridge configuration. This series of piezoresistor is responsible for pressure monitoring, and it is called the membrane of the pressure sensor. Membrane pressure sensors are described in details by Dr. Fournier in his thesis [33], and main publications ([3], [185]). For further details about the functioning of membrane pressure sensors, also see the patent [186], and the publications [187]–[190]. We can see in Figure 3. 10b, that after sealing, one side of the membrane is at atmospheric pressure, while the other side is at 20 mbar (adjustable low-pressure inside the cell). This pressure difference across the membrane cause a deflection of the resistors, as shown in Figure 3. 9c:

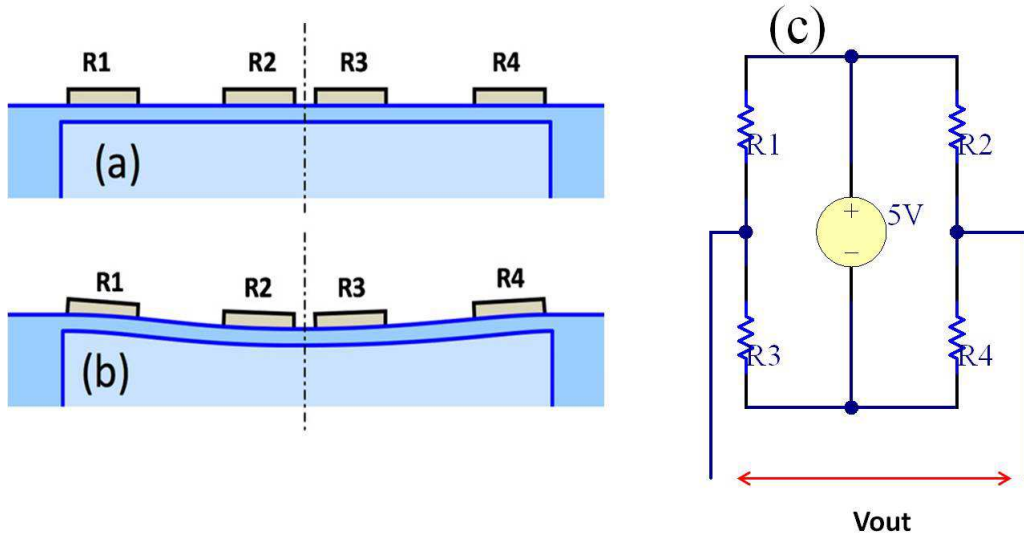


Figure 3.10: Schematic drawing of piezoresistive pressure-sensing membrane integrated in LTCC spacers, (a), before and (b), after sealing. The resistors are connected in a Wheatstone bridge configuration (c) and 5V are imposed across the bridge.

From the unflexed (a) to the flexed (b) configuration, the resistance of R1-R4 changes due to the strain in the resistive films. In particular, R2 and R3 are under compression and R1 and R4 are under tension. The resistors have originally the same value of resistance (nominally); therefore, if one applies 5V across the bridge when the membrane is not flexed, the output voltage V_{out} should be nominally 0 V. When the membrane is flexed, the geometry of the resistors, and therefore their value of resistance, will change, and this will cause a change of the output voltage.

3.5 Fabrication of the Cell

The overall dimensions of the developed cells are $10 \times 15 \times 3 \text{ mm}^3$. The choice of the final dimensions of the cell was due to a practical reason: we can also fabricate smaller cells (with a width which may be decreased up to 1 mm), but this was not needed for this work. In fact, using the Double Resonance approach for an interrogation scheme, a microwave cavity of dimensions ranging several cm is anyway needed in the system. Making a smaller cell is therefore useless because the total size of the system will not decrease. The fabrication process of the cell consists in the following steps: design and fabrication of the LTCC spacer, fabrication of the glass windows and finally dispensing of Rb and sealing.

3.5.1 Design of LTCC spacer

The LTCC spacers fabricated in this work for the envisioned mini-cells are rectangular-shaped of dimension $14 \times 10 \times 2 \text{ mm}^3$, with a vapor cavity of $\varnothing 5 \text{ mm}$.

The different modules of the spacer are built using five different layers, designated T1-T5. Table 3. 8 summarizes the function of the five layers, a photo of the different layers of the LTCC spacer is shown in Figure 3. 11, and Figure 3. 12 shows the 3D structure of the spacer, in which the different layers are stacked one onto the other and then fired to form a compact module. T1 carries the metallization and the corresponding solder ring screen-printed on top of it. The sealing ring consists of a regular octagon (total side-to-side distance of 10 mm) with four lateral dots (diameter 1.7 mm) which have the function to increase the mechanical strength of the bonding. Two holes are present on this layer: a round one, which will be the window for letting the light beam pass through, and a trapezoidal one, for the Rb reservoir. T2 is identical to T1, but consists of only "bare" LTCC, i.e. without metallization or solder: stacked many times, it has the function to increase the thickness of the LTCC module. T3 only has the hole for the window, and serves as the "floor" of the Rb reservoir. In the final version of the cell, T3 is bonded to the glass bottom wall using the same sealing ring present in T1. For test purposes, a sequence of T4 & T5 may be used instead of T3; the bottom of the cell is closed in this case by an LTCC membrane (T4) with a screen-printed pressure-sensing thick-film piezoresistive bridge on the bottom, i.e. outside of the cell. T5 is used as a spacer to protect the resistor and conductor on T4 from contact and consequent sticking with the alumina carrier during firing.

Layer	Present in the final cell (Figure 3. 9a)	Present in the test module (Figure 3. 9b)	Function of the layer
T1	Yes	Yes	Sealing top ring, Rb reservoir and window light
T2	Yes	Yes	Stacked many times to increase the thickness of the Rb reservoir
T3	Yes	No	Sealing bottom ring and "floor" for Rb reservoir in the final cell
T4	No	Yes	Membrane pressure sensor
T5	No	Yes	Prevent the T4 membrane from sticking with alumina during firing

Table 3. 8: Description of the different layers that compose the LTCC spacers for the final cell and for the test module.

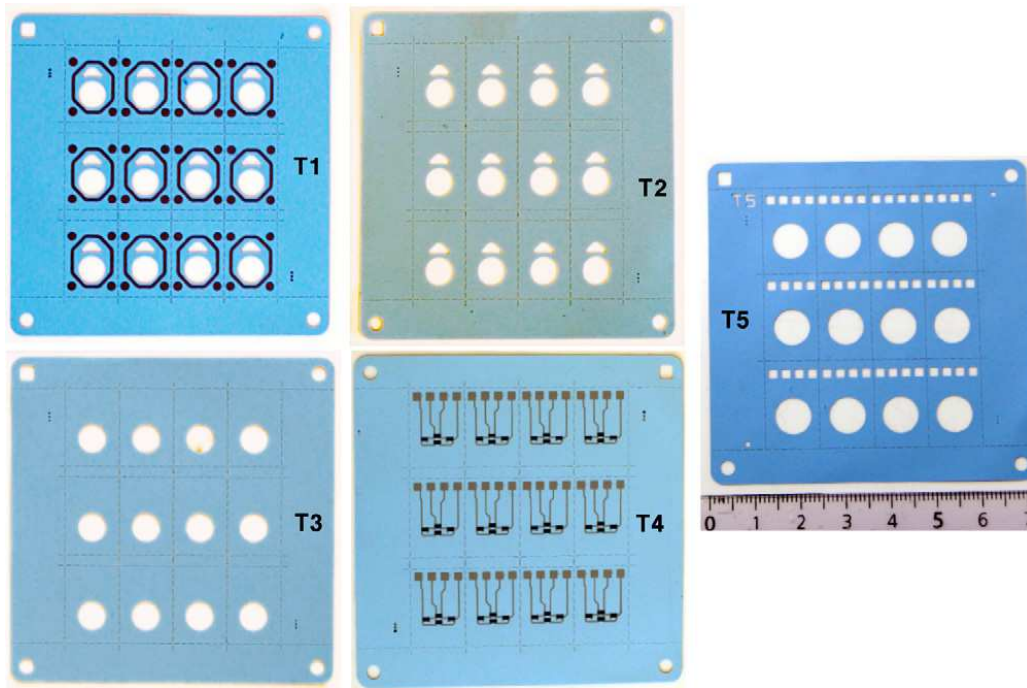


Figure 3.11: Photograph of the five different layers T1 -T5. T4 and T5, the layers which correspond to the membrane of the pressure sensor, are present only in the test module.

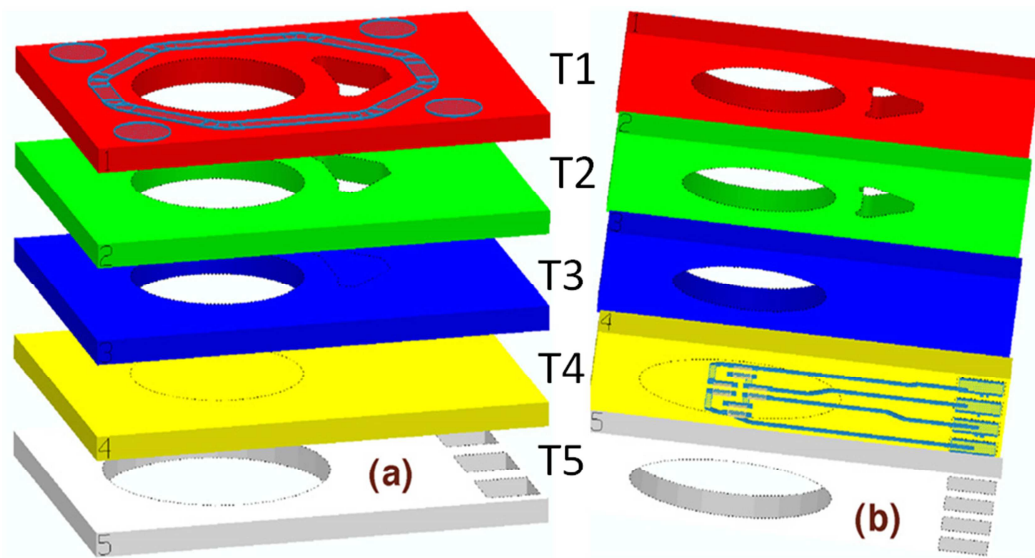


Figure 3.12: 3D view of the five different layers which compose the LTCC spacer (in the test module).

In the test module, one side of the membrane is under partial vacuum after sealing, and the other side is at atmospheric pressure (Figure 3. 9b), therefore, the output voltage of the

Wheatstone bridge monitors the pressure difference across the membrane and, correcting for atmospheric pressure variations, allows measurement of the inside pressure. As the resistors lie on the outer surface and only the bare LTCC is exposed to Rb, no significant degradation of the membrane is expected. Additionally, the LTCC cell frame is very stiff, effectively insulating the membrane from parasitic stresses arising from the soldering of the glass lid.

3.5.2 Fabrication of LTCC spacer

The process for fabricating the LTCC spacer is the standard process described in paragraph 2.5. In particular, the following steps were carried out to fabricate this device:

- Laser cutting of the LTCC tape
- Screen-printing of the metallization layers (for more details about the composition of the metallization layer, see the following), of the resistors for the membrane (for the test modules) and the various connections;
- Precise stacking and lamination of the LTCC module
- Co-firing, with a standard LTCC cycle having a top dwell of 20 min at 875°C
- Screen-printing and reflow of the solder paste on top of the metallization layer (for more details about the solder paste used, see the following)
- Thorough cleaning of the solder flux in an ultrasonic bath with ethanol
- The substrate is then broken apart along the pre-cut dot line to separate each single sample.

A photo of the resulting LTCC test module (with membrane for pressure monitoring) is shown in Figure 3. 13:

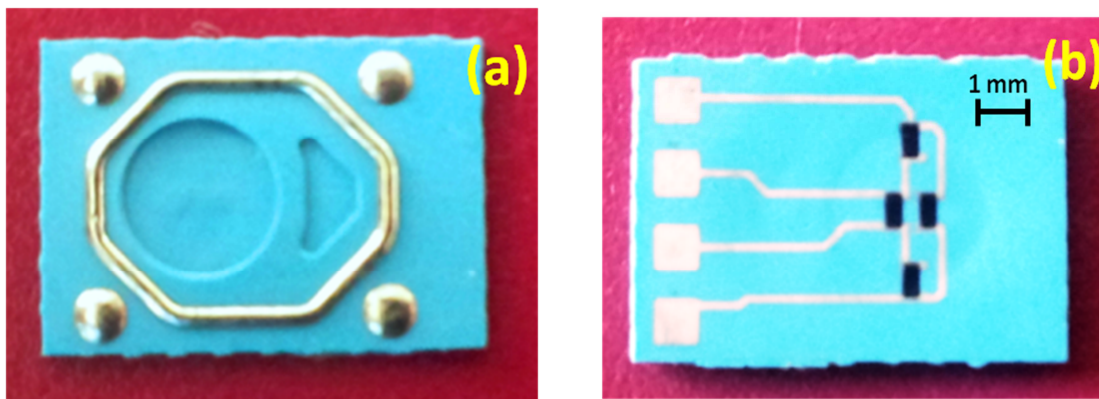


Figure 3. 13: A photo of the LTCC test module produced: (a), top view, with the sealing ring. (b), bottom view, with the piezoresistive Wheatstone bridge.

3.5.3 Fabrication of glass windows

The top and bottom windows of the cell consists of standard glass slides (dimension $75 \times 25 \text{ mm}^2$, 0.5 mm thick) that are metalized and "pre-tinned" with solder in a similar manner to the LTCC module: in particular, the process consists of metallization, solder print & reflow and cleaning steps. The main difference lies in the metallization process (see following section): different pastes were tested, and the metallization is post-fired onto glass. The slides are then sawed to get different samples of $10 \times 10 \text{ mm}^2$. A photo of the fabricated glass slides that acts as bottom and top window of the cell is shown in Figure 3. 14.



Figure 3. 14: The glass slide acting as bottom and top window of the reference cell.

3.5.4 Rb dispensing and sealing

Once all elements (LTCC spacer, bottom and top glass windows) have been fabricated, the bottom glass window is bonded with the LTCC spacer. At this stage, since Rb has not yet been dispensed into the reservoir, the bonding technique may be also performed at high temperature and at atmospheric pressure (for example, anodic bonding). Then, once the bottom wall is bonded with the LTCC spacer, Rb is dispensed into the dedicated reservoir following the procedure described in paragraph 3.3. After rapidly transferring the system into the vacuum chamber, precise alignment of top wall and LTCC spacer is done, and finally, the cell is gradually heated in vacuum to evaporate the dodecane without boiling, melt the solder to realize the sealing.

3.6 Wetting Tests

Before starting the production of the various elements (LTCC spacer and glass windows), different solder / metallization combinations were studied. The objective of this preliminary

study was to find out the combination that exhibited the best wetting, i.e. the combination in which the solder paste wets homogeneously the metallization ring. A good and reliable wetting of the metallization is the prerogative to get a stable and hermetic seal.

3.6.1 Procedure and melting profile

Three different solder pastes were tested on top of different metallization rings (see the following for more details about the composition of the metallization ring). Table 3. 9 shows the composition of the solder pastes used and their melting point.

Solder paste composition	Common name of the solder alloy	Melting point [°C]
58Bi 42Sn [156], [191]	Sn-Bi	139
62.5Sn 36.5Pb 1Ag [192]	Sn-Pb-Ag / Sn62	179
Sn96.5 Ag3.5 [157], [158], [160], [193]–[195]	Sn96	221

Table 3. 9: Composition of the solder pastes tested and their melting point. The compositions are given in percentage of weight.

The solder paste was manually dispensed (in open air atmosphere) using a syringe dispenser on top of the metallization ring. Then, always in open air, the sample was heated up, first to a temperature slightly lower than the melting point of the solder, in order to evaporate the solder flux and also to drive off the impurities which were deposited on the paste during our manipulation. Finally, the sample was heated at temperatures higher than the melting point of the solder paste, and this temperature was kept for ca. 30 seconds, in order to ensure the total melting of the solder paste. After some attempts, the best melting profiles, which yielded to the best wetting, were established for each solder paste. The melting profiles used are summarized in Table 3. 10.

Solder paste	Drying	Melting
Sn-Bi	120°C, 120 seconds	170°C, 10 seconds
Sn-Pb-Ag	160°C, 120 seconds	210°C, 10 seconds
Sn-Ag-Cu	200°C, 120 seconds	250°C, 10 seconds

Table 3. 10: Melting profiles adopted for the different solder pastes.

The composition of the metallization ring of the LTCC spacer is not the same of that of the glass, because with the LTCC it is possible to use standard thick film pastes, which are fired at temperatures around 850°C. On the other side, the glass windows cannot be fired at 850°C (the softening point of glass is ca. 720°C, [196]), so special pastes fired at low temperatures

were tested for the metallization ring of the glass. The wetting was visually judged using an optical microscope. The wetting angle was not measured, because the surface of the metallization ring, where the solder was dispensed, is not flat due to screen-printing limitations (the surface of screen-printed tracks is never flat, but always a bit wavy): therefore the measurement of the wetting angle is not a reliable way to judge the wetting in this case. However, using an optical microscope and carefully observing the result, we were able to judge and state the sample exhibiting good and poor wetting.

3.6.2 Wetting tests on LTCC substrate

In order to evaluate the wetting behavior of the different metallization-solder combinations, a first small production of the sensors was done; we fabricated a total of 72 samples, corresponding to 7 substrates; each substrate contained 12 samples. Two pastes were tested for the metallization ring on LTCC:

- ESL 9562G, which consists of Ag mixed with ca. 4% of Pd and Pt;
- ESL 9635G, which is an Ag-Pd alloy, with Ag:Pd \approx 3:1.

Moreover, one, two, and three layers of metallization were tested, in order to see if the thickness of the ring affects the wetting. Table 3. 11 summarizes the composition of the metallization ring of the samples, and Table 3. 12 summarizes the different combinations of solder/metallization tested to find out the best wetting.

Substrate no.	Samples	Composition of the metallization ring	Firing temperature (45 min total firing time, 10 min at peak)
1	1a – 1l	1 layer of Ag ESL 9562G	850°C
2	2a – 2l	2 layers of Ag ESL 9562G	850°C
3	3a – 3l	3 layers of Ag ESL 9562G	850°C
4	4a – 4l	2 layers of ESL 9562G + 1 layer of Ag-Pd ESL 9635G	850°C
5	5a – 5l	1 layer of Ag-Pd ESL 9635G	850°C
6	6a – 6l	2 layers of Ag-Pd ESL 9635G	850°C
7	7a – 7l	3 layers of Ag-Pd ESL 9635G	850°C

Table 3. 11: Summary of the metallization rings for the wetting test.

Samples	Composition of metallization ring	Solder paste tested
1a – 1d	1 layer of Ag ESL 9562G	Sn-Bi
1e-1h	1 layer of Ag ESL 9562G	Sn-Pb-Ag
1i – 1l	1 layer of Ag ESL 9562G	Sn96
2a – 2d	2 layers of Ag ESL 9562G	Sn-Bi
2e – 2h	2 layers of Ag ESL 9562G	Sn-Pb-Ag
2i – 2l	2 layers of Ag ESL 9562G	Sn96
3a – 3d	3 layers of Ag ESL 9562G	Sn-Bi
3e – 3h	3 layers of Ag ESL 9562G	Sn-Pb-Ag
3i – 3l	3 layers of Ag ESL 9562G	Sn96
4a-4d	2 layers of Ag ESL 9562G + 1 layer of Ag-Pd ESL 9635G	Sn-Bi
4e – 4h	2 layers of Ag ESL 9562G + 1 layer of Ag-Pd ESL 9635G	Sn-Pb-Ag
4i – 4l	2 layers of Ag ESL 9562G + 1 layer of Ag-Pd ESL 9635G	Sn96
5a – 5d	1 layer of Ag-Pd ESL 9635G	Sn-Bi
5e – 5h	1 layer of Ag-Pd ESL 9635G	Sn-Pb-Ag
5i – 5l	1 layer of Ag-Pd ESL 9635G	Sn96
6a – 6d	2 layers of Ag-Pd ESL 9635G	Sn-Bi
6e – 6h	2 layers of Ag-Pd ESL 9635G	Sn-Pb-Ag
6i – 6l	2 layers of Ag-Pd ESL 9635G	Sn96
7a – 7d	3 layers of Ag-Pd ESL 9635G	Sn-Bi
7e – 7h	3 layers of Ag-Pd ESL 9635G	Sn-Pb-Ag
7i – 7l	3 layers of Ag-Pd ESL 9635G	Sn96

Table 3. 12: A summary of the combinations solder/metallization ring tested to find out the best wetting.

3.6.2.1 Sn-Bi wetting on LTCC substrate

In the metallurgy literature, the wetting of the Sn-Bi paste is judged poor, because in most cases it does not homogeneously wet the metallization surface [197]–[199]. In our case, using the traditional technique (simply dispensing the solder paste on top of the metallization ring), the wetting was poor and always left significant residues that were very hard to clean off. In Figure 3. 15, there are photos of three samples showing the poor wetting obtained using the standard procedure:

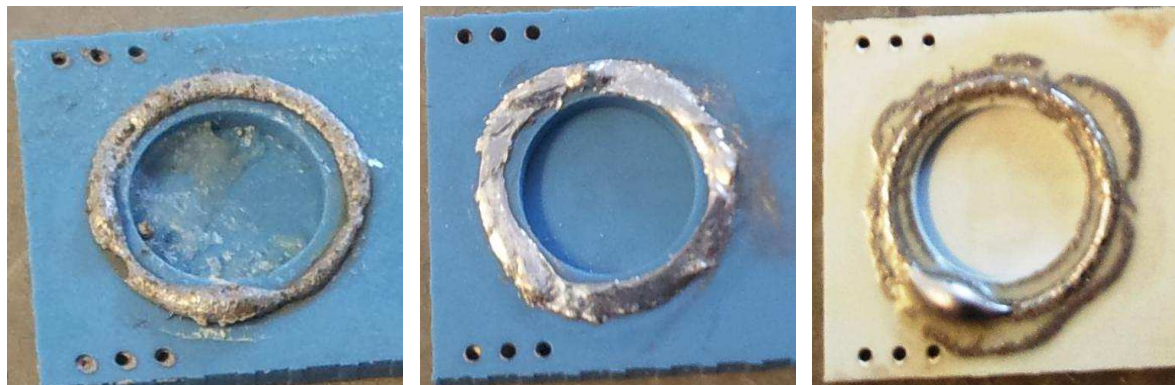


Figure 3. 15: The wetting of Sn-Bi solder was bad on the three different metallization rings

In the three cases, the wetting was poor, and leaves a large amount of impurities that proved impossible to clean, even with the ultrasonic bath. To achieve better wetting, after having dispensed the solder paste on top of the metallization ring, we dispensed, on top of the solder paste, a layer of RMA (Rosin Mildly Activated) flux [200], [201], and then we fired the sample. RMA flux is a composition of rosin with an activating agent (typically an acid that helps dissolving the oxides present on the surface of the solder balls and of the metallization) which increases the wettability of the solder. The residue (the activating agent) is relatively corrosive and should be cleaned out, also to avoid any kind of reaction with the Rb and to avoid pollution of the atmosphere inside the cell. Figure 3. 16 shows this procedure.

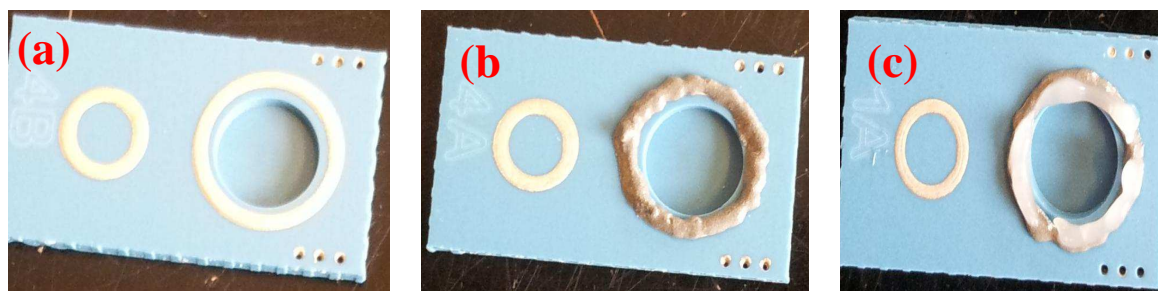


Figure 3. 16: Procedure adopted to get better wetting of Sn-Bi solder: (a), the sample at the beginning of the test, with the metallization ring. (b), the sample with Sn-Bi solder on top of the metallization ring. (C), the sample with RMA flux dispensed on top of the solder paste.

Dispensing this large amount of flux before firing increased the wettability of the Sn-Bi solder paste, and finally good results were obtained for some substrates. The role of the flux, crucial in this case to increase the wettability of the solder, is described in various publications. In particular, J.F. Shipley explained that the principal advantage brought by the

flux is that it chemically reduces surface metal oxides, preparing clean surface [202]. This means that Sn-Bi solder better adheres on top of a metal oxide, because the chemical reaction that leads to a good wetting only happens in the presence of a metal oxide. The best wetting is observed for samples that came from substrate n.7 and n.4. Substrates n.1 and n.2 gave very bad wetting, even with RMA flux dispensed. In the other substrates, there was wetting, but not homogeneous and not perfect. Figure 3. 17 shows photographs of a sample whose wetting was poor (substrate n.2), and of the best sample obtained with Sn-Bi (substrate n.4).

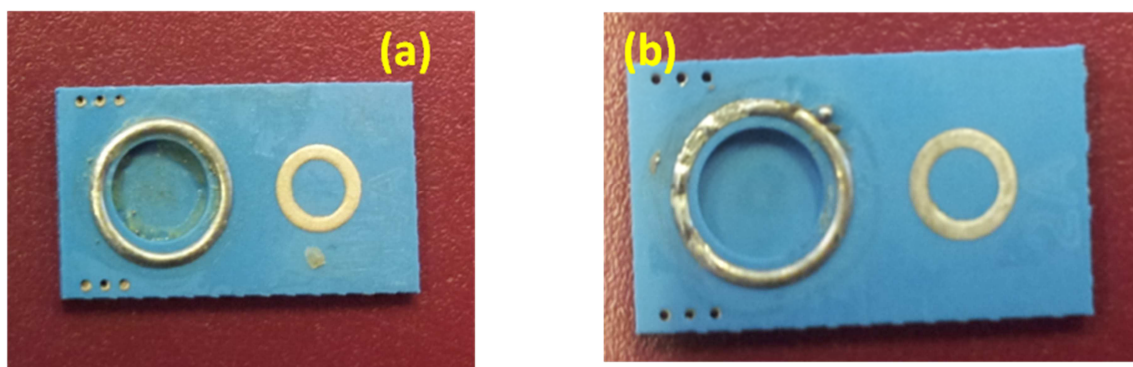


Figure 3. 17: (a), The best wetting obtained with Sn-Bi; (b), an example of poor wetting obtained with Sn-Bi plus RMA flux.

For the sample in Figure 3. 17a, the wetting is judged good, but flux residue remains visible, even after having carefully cleaned it with the ultrasonic bath. This is because of the large amount of flux dispensed. This solder paste, even if it has the advantage of low-melting point which is wished for many applications, does not have good performance; it is very difficult to handle, an extra-application of flux is necessary, which at the end leaves visible residues that are very hard to remove. Moreover, the wetting is poor for many samples, probably due to the low reflowing temperature. Moreover, at high temperatures, there is a rapid dissolution of the metallization into the solder which causes the embrittlement of the joint [203], [204].

3.6.2.2 Sn-Pb-Ag wetting on LTCC substrate

The wetting of Sn-Pb-Ag paste was really good, on all metallization variants. Particularly good wetting is registered on substrates n.3 and n.4. A photo of this result is shown in Figure 3. 18:



Figure 3. 18: An example of the wetting of Sn-Pb-Ag solder paste.

As we can see, the wetting is perfect and there is no trace of the residues of the flux after having cleaned the sample with the ultrasonic bath. This solder paste adhered very well also on the other metallization rings – there is no sample whose wetting was found to be poor. The better wettability of Sn-Pb-Ag solder with respect to the Sn-Bi solder has been found also observed in other work [205], [206], and has been attributed to the absence of bismuth, which causes wetting problems, and to a higher reflowing temperature, which promotes better wetting and flux activity.

3.6.2.3 Sn-Ag wetting on LTCC substrate

Sn96 wetting on metallization was good on substrates n.4,5,6,7 and poor on substrates n.1,2,3. Apparently, this solder paste only wets Ag-Pd ESL 9635G paste well, because all the samples whose last layer of metallization was Ag ESL 9562G exhibited poor wetting. Previous researchers proved that the wettability of this solder paste is adequate on Ag and Ag-Pd, but not good on Cu metallizations; the wetting may be improved by reflowing the sample in nitrogen atmosphere [157], [194], [206]. Figure 3. 19 shows photographs of poor and good wetting obtained with Sn-Ag solder.

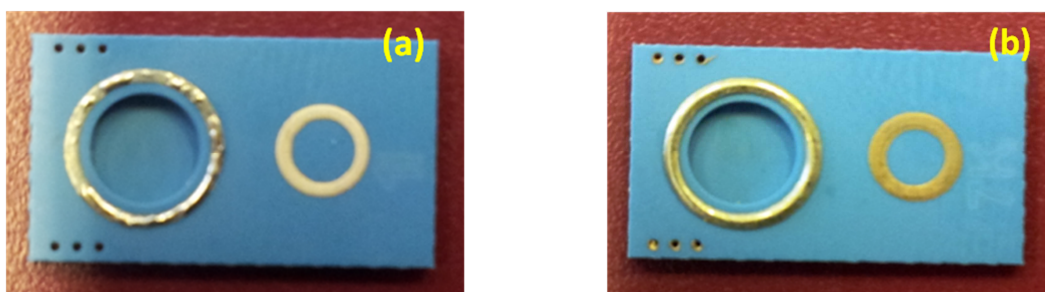


Figure 3. 19: (a), poor wetting obtained with Sn-Ag-Cu solder. (b), good wetting obtained with Sn-Ag-Cu solder.

3.6.3 Summary of wetting tests on LTCC

Finally, we can affirm the following:

- 1) Sn-Bi solder is not reliable, its wettability is really poor on all kind of metallization, and therefore it is not advised. If it is really needed to use this solder alloy because of its low melting point, in order to get a good wetting, it is advised to dispense a layer of RMA flux on top of the solder paste. Using this technique, a sufficient wetting is registered on top of metallization composed by 2 layers of Ag ESL 9562G and one layer of Ag-Pd ESL 9635G, or, in alternative, 3 layers of Ag-Pd ESL 9635G. However, even if the wetting is sufficient, a large amount of residues of the flux is visible, even after thorough cleaning in the ultrasonic bath.
- 2) Sn-Pb-Ag solder clearly yields the best wettability on all the metallization tested. Particularly good wetting is observed on top of metallization composed by three layers of Ag ESL 9562G or, in alternative, 2 layers of Ag ESL 9562G and one layer of Ag-Pd ESL 9635G
- 3) Sn-Ag solder only wets on top of the metallization in Ag-Pd ESL 9635G. For these substrates, the wetting was good.
- 4) Substrate n.4 (whose metallization consisted of 2 layers of Ag ESL 9562G and one layer of Ag-Pd ESL 9635G) seems the best choice, because exhibits good wettability for all the three solder pastes tested.
- 5) The best solder paste for this application is Sn-Pb-Ag, combining excellent wetting on the chosen metallization and lower melting point with respect to Sn-Ag.

3.6.4 Wetting tests on glass substrate

As already explained, the composition of the metallization ring of the LTCC cannot be the same as that of the glass, because the pastes used for LTCC are fired at 850°C, so above the softening point of the glass. For the metallization ring of the glass we tested different pastes, which are fired at low temperatures. In particular, the pastes tested on the glass were:

- 1) ESL 590G, conductor paste from ESL, in which pure silver is mixed with an important quantity of glass frit in order to lower the firing temperature, [207];
- 2) ESL 9912A, mixed bonded silver conductor form ESL, with a wide firing temperature range, [208].

Also in this case, a small production of glass windows was done in order to test the wetting of the chosen solder paste, Sn-Pb-Ag, on top of the different metallization rings. Again, from one glass substrate we got 12 samples. Table 3. 13 summarizes the metallization rings tested for the glass substrates.

Substrate no.	Samples	Composition of the metallization ring	Firing temperature (45 min total time, 10 min at peak)
1	1a – 1l	2 layers of ESL 590G	525°C
2	2a – 2l	3 layers of ESL 590G	525°C
3	3a – 3l	2 layers of ESL 9912A	625°C
4	4a – 4l	2 layers of ESL 9912A	625°C

Table 3. 13: A summary of the metallization rings tested for the glass window.

3.6.4.1 Sn-Pb-Ag wetting on top of ESL 590G metallization

On top of the paste ESL 590G the wetting of Sn-Pb-Ag solder paste was poor, and increasing the thickness of the metallization by screen-printing 2, 3 or more layers of paste did not help getting a sufficient wetting. The bad wetting is probably due to the presence of a significant quantity of glass frit into the metallization: in fact, the solder pastes only adhere on top of metals, and a significant presence of glass frit into the metallization prevents the wetting. Figure 3. 20 shows a photo of a glass window with the solder Sn-Pb-Ag and ESL 590D as metallization, and whose wetting was poor.



Figure 3. 20: An example of bad wetting of the solder Sn-Pb-Ag on top of the ESL 5092D metallization ring.

3.6.4.2 Sn-Pb-Ag wetting on top of ESL 9912A metallization

In this case, the wetting was good. Such metallization paste, in fact, only contains a minimal part of glass (ca.1%) and this increase the wettability. Particularly good wetting was observed when three layers of metallization paste were screen-printed, because the increased thickness of the ring slows down the dissolution mechanism of the solder into the metallization. Figure 3. 21 shows a sample with the solder Sn-Pb-Ag and the paste ESL 9912A as metallization, and whose wetting was good.



Figure 3. 21: An example of good wetting of the solder Sn-Pb-Ag on top of the ESL 9912A metallization ring.

3.6.5 Conclusions of the wetting tests

At the end of the wetting tests, we were able to propose a good metallization/solder combination which ensures a homogeneous wetting of the solder, for the LTCC spacer and for the glass windows. The combinations retained are resumed in Table 3. 14.

Component	Metallization ring composition	Solder ring
LTCC spacer	2 layers of ESL 9562G + 1 layer of Ag-Pd ESL 9635G	Sn-Pb-Ag
Glass window	3 layers of ESL 9912A	Sn-Pb-Ag

Table 3. 14: The composition of the metallization and solder rings for the LTCC spacer and for the glass window.

3.7 Test Bench for Testing the Hermeticity of the Sealing

The test modules equipped with the Wheatstone bridge for pressure monitoring shown in Figure 3. 13, were used to test the hermeticity of the sealing. The test cells were collocated inside a box, and a cycle of controlled pressure was introduced into the box using the instrument DPI 520 ATE Pressure Controller (5 bars abs), connected through GPIB to a PC. The box was also controlled in temperature. A Labview program was written to acquire the data, provide the temperature control and the pressure control for the box, and to register the outputs of the Wheatstone bridges into a text file. The output of the sensors was amplified used an analogue amplifier card with gain 100, mounted on a motherboard used in our lab for

the acquisition and the conditioning of various signals. A LabJack U6 PRO was used to interface the motherboard and the electronics with the PC and the LabView. A photo of the test bench is shown in Figure 3. 22.

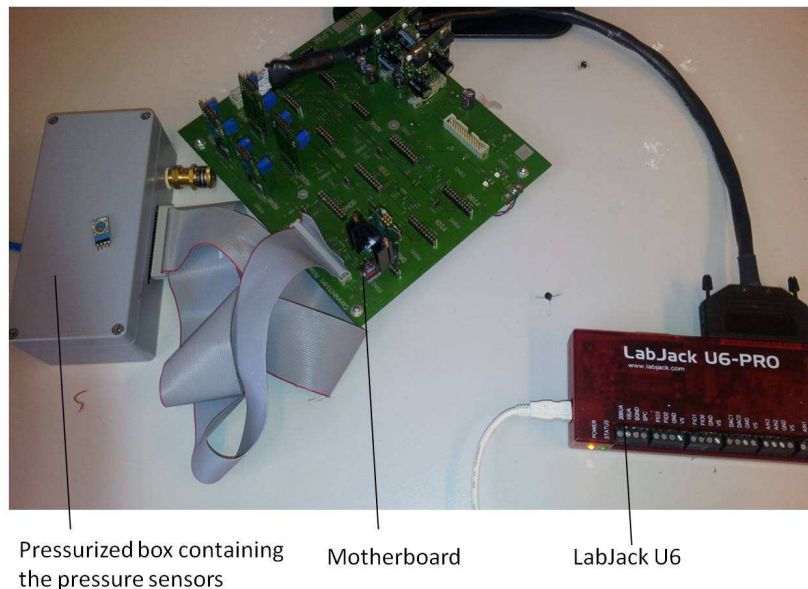


Figure 3. 22: The test bench used to test the sealing. The test cells with pressure sensors are introduced into a box, and the pressure inside the box is regulated using a Labview program. The Labjack U6-PRO is used to interface the external hardware (motherboard with amplification cards) with a PC.

3.8 Results of the Hermeticity Test

Different bonding techniques were tested: first, bonding using ESL 590G paste (silver with a significant presence of glass frit) was tested. The paste was dispensed by screen-printing on top of the LTCC test module and on top of the glass window; the substrates were manually aligned and fired at the nominal firing temperature of the paste (450°C peak, 45 minutes profile). This paste was chosen because it contains a good amount of glass frit, so it perfectly adheres on top of the glass cap. Moreover, it is fired at a temperature still below the glass transition temperature, so it is compatible with glass. Finally, this technique is a reference of high-temperature (450°C is already high temperature for our application), but hermetic sealing technique. The hermeticity of some cells sealed with solder paste was also evaluated. Two different types of solder pastes were tested: Sn-Pb-Ag and Sn-Bi (Sn-Ag melting point is judged too high for this application in which low temperature is desired). The solder paste was manually dispensed on top of a metallization layer, whose composition is detailed in Table 3. 14. Moreover, we also tested some substrates bonded using two organic adhesives: a silicone (Dow Corning Q5-8401, [209]) and an epoxy resin (EPOTEK 354 [210]). Both were

tested in order to have references of air-tight, but non-hermetic seals with different gas permeabilities (silicone > epoxy). Finally, in order to have a reference of an “open” sample we also monitored the output of a non-sealed pressure sensor.

3.8.1 Reaction to pressure changes

After bonding, the sensors were introduced into the box. As a first test, the box was temperature-stabilized at 35°C, in order to eliminate the problems related with TCR (Temperature Coefficient of Resistance) of the resistors by keeping a constant temperature during the measurements. Inside the box, a 20-minutes (total) pressure profile was programmed, starting from 100 kPa and increasing of 10 kPa each minute, up to 200 kPa, and then going back to 110 kPa (Figure 3. 23).

Afterwards, another pressure profile was also tested, with more important pressure changes, to see how the reactivity of the sensor when submitted at a sudden and abrupt pressure change, and also the reliability of the hermeticity. A sudden increase/decrease of pressure of 50 kPa was then introduced into the box (Figure 3. 24).

Each sensor was supplied with 5 V and their output, amplified with a gain of 100 by a differential Input Amplifier Card (IAC), was monitored. For each value of pressure, after having waited enough time (a few seconds) to let the pressure controller stabilize at the new pressure, 1000 samples were collected with a frequency of one sample every 500 ms. Then, the average value of the 1000 measurements was calculated and plotted; the standard deviation of the 1000 measurements (σ) was also calculated, using the following formula:

$$\sigma = \sqrt{\frac{1}{N} \sum_{i=1}^N (x_i - \bar{x})^2} \quad \text{Eq. 3. 7}$$

,where N is the number of the samples measured, (x_1, \dots, x_N) are the observed values and \bar{x} is the total range of the values (the difference between the value at 200 kPa and the value at 100 kPa).

If this output signal reacts at the pressure change with a consequent linear variation, it means that the pressure difference is detected by the membrane, therefore the sealing is hermetic. If the output signal does not follow the pressure change (for example, it is a constant value during all the pressure profile), it means that the membrane does not detect the pressure difference because both sides of the membrane are at the same pressure, therefore the sealing is not hermetic.

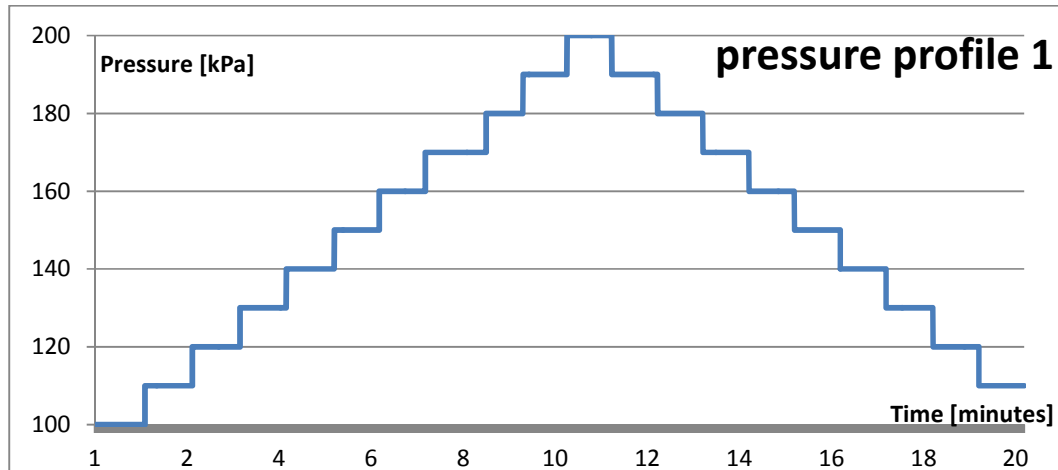


Figure 3. 23: Pressure profile number 1 - gradual and multiple pressure changes.

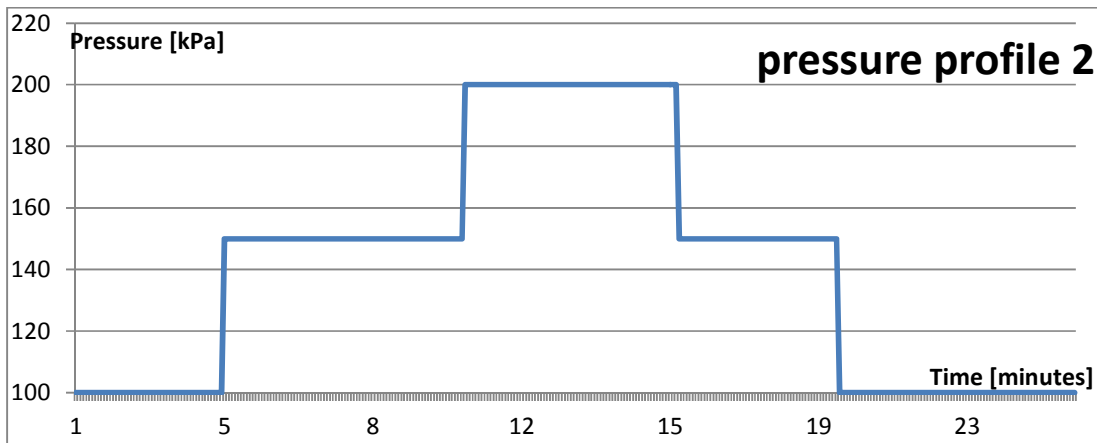


Figure 3. 24: Pressure profile number 2: sudden and significant pressure change.

From the graphics shown in Figure 3. 25, we can see that the output of the all the sealed samples has a linear relationship with the pressure change, therefore the sealing ring is able to keep the hermeticity for a small pressure change and for a short time. On the other hand, the output of the open sample remains essentially unchanged with pressure, as expected from the fact that the membrane is submitted on both side to the same pressure.

For the second test, the samples were submitted to pressure profile nb.2, in which there is a sudden and sharp pressure change, instead of many gradual changes. The output of the Wheatstone bridge was again monitored using the same procedure of above, as well as the standard deviation of the measurements. Also in this case, the response of the samples sealed follows linearly the pressure change, while the open sample shows no apparent relationship with the external pressure change.

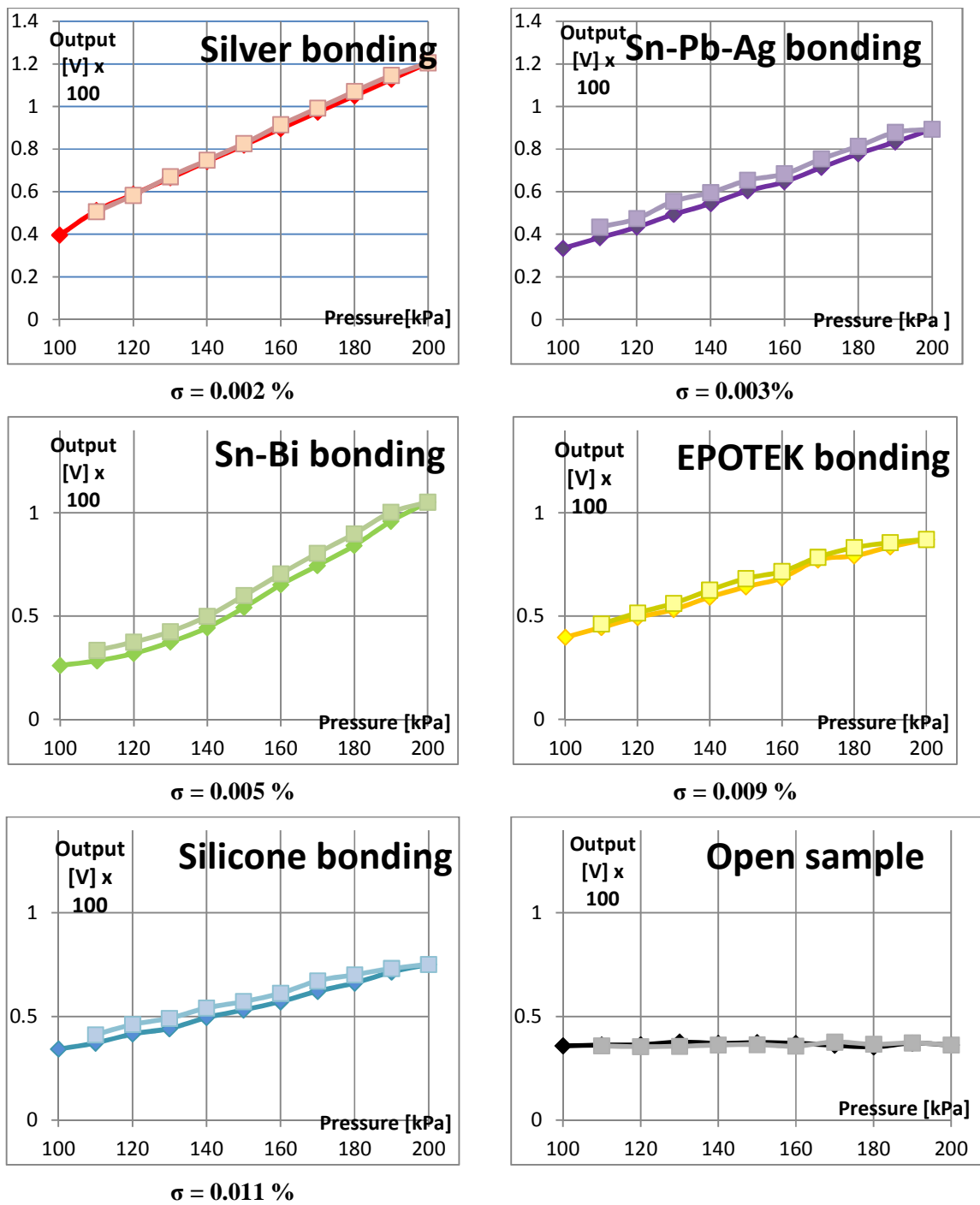


Figure 3. 25: Output voltage of the sensors sealed with different sealing techniques. Pressure profile 1..

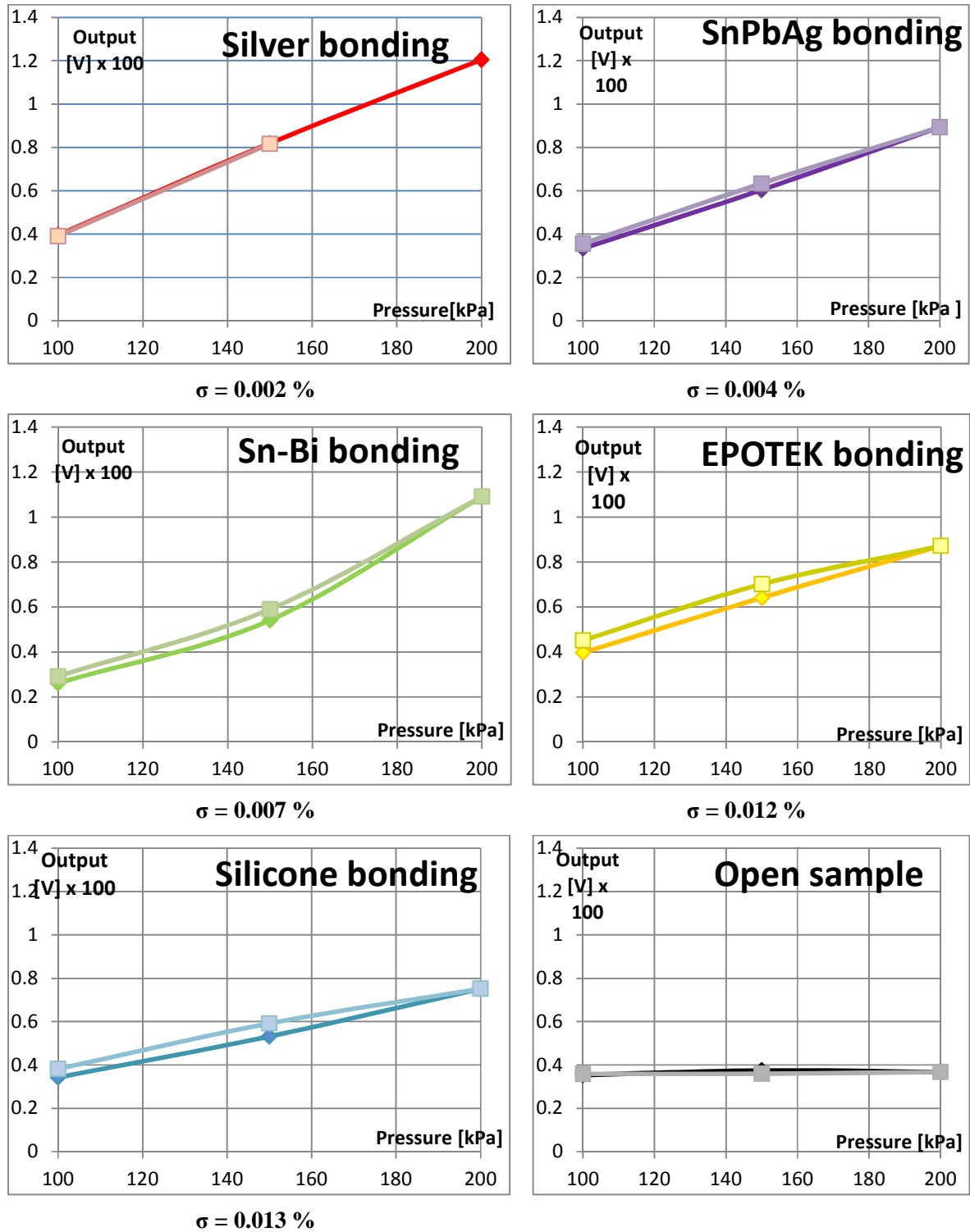
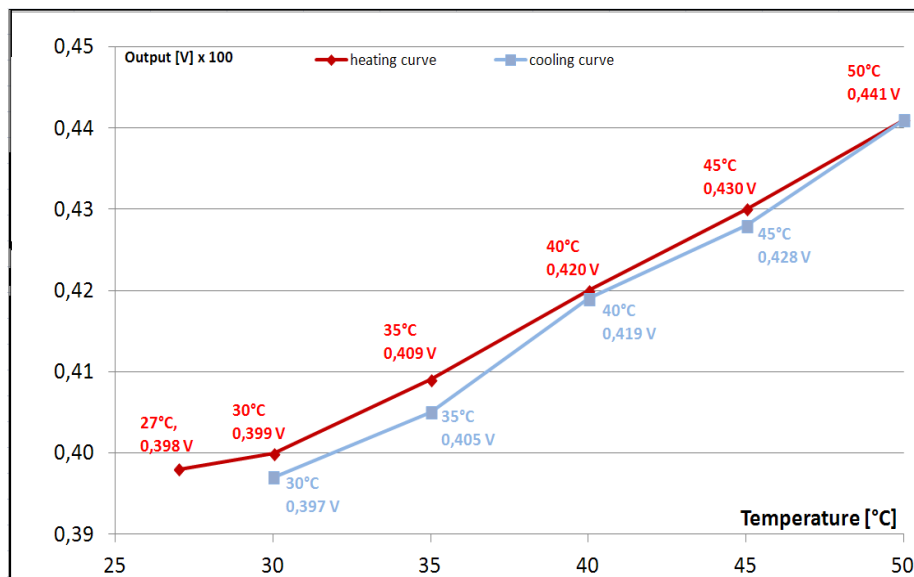


Figure 3. 26: Output voltage of the sensors sealed with different sealing techniques. Pressure profile 2.

3.8.2 Reaction to temperature changes

A temperature drift affects the output of the Wheatstone bridge, because the resistance of the piezoresistive resistors changes with changing temperatures. In order to evaluate how the response is affected by the temperature, and if an increasing and decreasing temperature cycle causes a mismatch of the TCR (Temperature Coefficient of Resistance), the output of the Wheatstone bridge of a hermetic sensor sealed with Sn-Pb-Ag was measured keeping the pressure constant to 1100 mbar, at well defined temperatures following an increasing curve (27°C, 35°C, 40°C and 45°C), and then at the same temperatures following a decreasing curve (45°C, 40°C, 35°C, 30°C, 27°C). Before taking the measurement, enough amount of time was waited in order to make the system stabilize to the new temperature (the amount of time waited was variable, depending on the time the system took to achieve the desired temperature). Once the system stabilized, 1000 samples were collected with a frequency of one sample every 500 ms. Then, the average value of the samples at different temperatures was plotted, and the standard deviation of the measurements was also calculated in order to evaluate if the temperature introduces noise into the measurement. Figure 3. 27 is the plot of the average values. As we can see, the output of the Wheatstone bridge is directly correlated, following an approximately linear relationship, with the temperature. Table 3. 1 shows the standard deviations of the measurements for the different temperatures.



**Sn-Pb-Ag
bonding**
 $p = 1100 \text{ mbar}$

Figure 3. 27: Going from 27 to 50°C (red curve) the output of the sensor follows an almost linear ascendant trend. Going from 50 to 27°C (blue curve) the output follows the same trend.

T [°C]	Standard deviation of the measured values	T [°C]	Standard deviation of the measured values
27	0.002%	45	0.005%
30	0.003%	40	0.005%
35	0.004%	35	0.004%
40	0.004%	30	0.003%
45	0.005%	27	0.002%
50	0.005%		

Table 3. 15: Standard deviation measured on the output of the sensor at different temperatures.

The standard deviation seems to increase with increasing temperatures. This is due to the fact that the high temperature introduces an additional effect on the resistors, and this effect is not perfectly repeatable. In any case, the standard deviation is always less than 0.006 %, which means that the repeatability of the sensor in the short term (ca. 10 minutes) is very good. Another test performed in order to evaluate how the response changes in consequence of a temperature drift was to submit the sensor at the same pressure profile, at different temperatures: one time at 27°C and another time at 50°C. Figure 3. 28 shows this result.

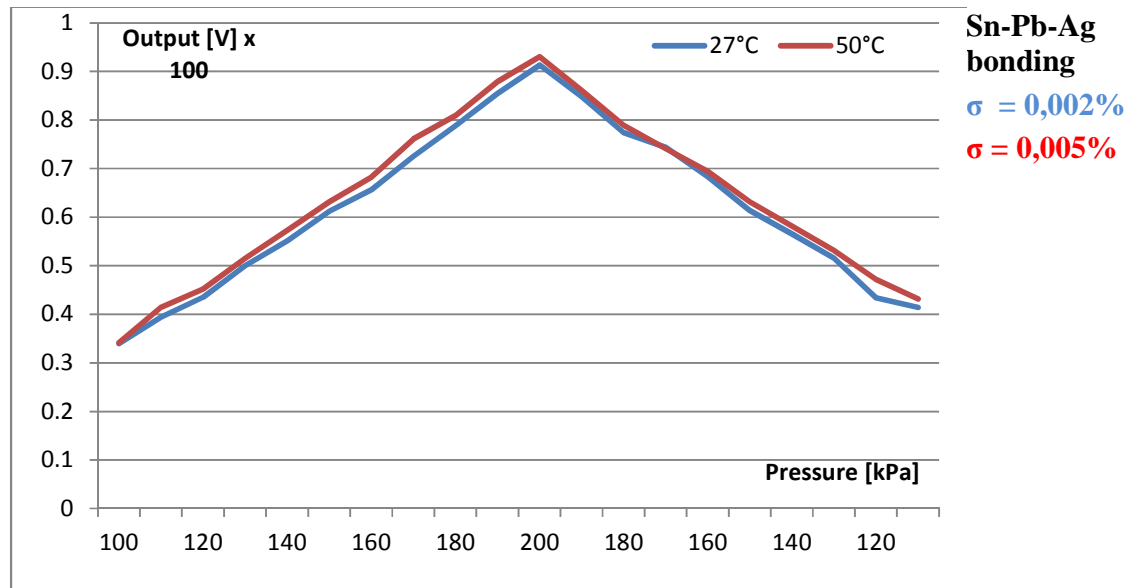


Figure 3. 28 : Same pressure profile at different temperatures.

The plot shows that the measurement at high temperature is slightly noisier (higher value of standard deviation), but the sealing stays hermetic also at 50°C, because the output signal seems to precisely follow the pressure profile.

3.8.3 Long-term measurements

The final step was to make a long-term measurement, to test whether the sealing is able to stay hermetic for long time, in condition of high temperature and high pressure. The sensors were kept at 50°C and at 1500 mbar of pressure, for 25 continuative days. The output of the Wheatstone bridges was registered: one sample per second was taken, so 86.400 samples per day per sensor, and a total of 2.160.000 samples per sensor over the 25 days. Again, silver, Sn-Bi and Sn-Pb-Ag bonding were tested. Every day, the average value of the 86.400 samples per sensor was registered. Also, the standard deviation of all the measurements was registered and the range (max value – min value of ALL the 2.160.000 samples), in order to estimate the dispersion of the measurement. Figure 3. 29 shows the trend of the average values of the measurements over the 25 days of measurements, for the three sensors fabricated with the three different sealing techniques under examination.

As we can see, even in this case the best performance is given by the sensor sealed with silver, because the graphic of the average values is really flat, the standard deviation and the range of variation is the lowest. After 25-day exposure to somewhat elevated temperature and high pressure, the output of the three sensors did not significantly change and the standard deviation was max. 0.061% (for the sample sealed with Sn-Bi), indicating that all the three sensors remained hermetic after 25 days. The small variation observed in the output of the sensors sealed with the two solder pastes is probably due to the creep and stress relaxation of the solder joint[211], [212]. On the other hand, we can observe that the samples sealed with epoxy and silicone are expectedly not hermetic. We measured the output of the sensor before sealing, and then monitored the output during seven days after sealing; during the observation period the samples were kept at 1500 mbar and 50°C. The output voltage of the sample sealed with silicone went back to its original value after the second day of observation; the output voltage of the sample sealed with Epoxy EPOTEK 354 went back to its original value after four days of observation. This means that the sealing are not hermetic, but only air-tight. Figure 3. 30 shows this result.

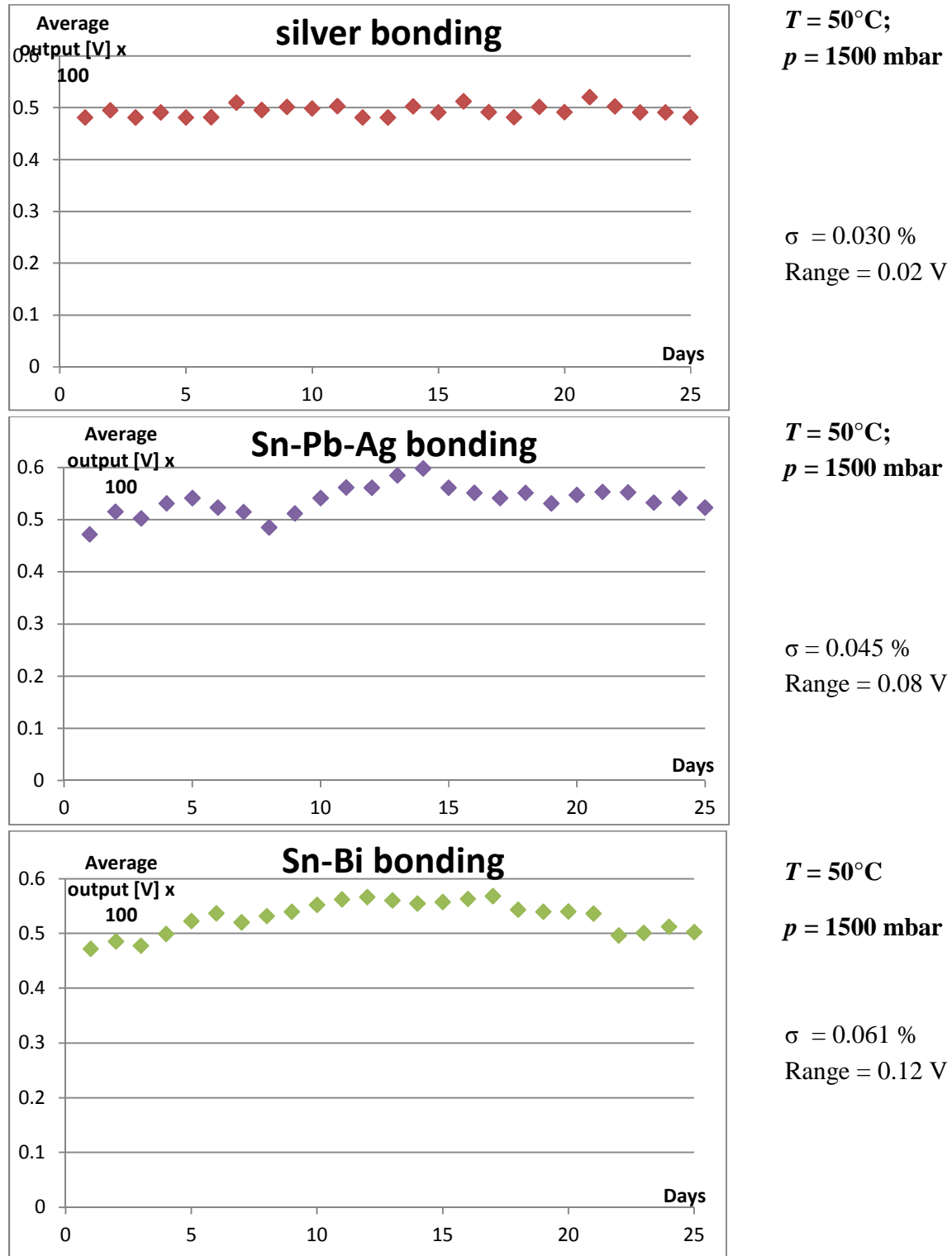


Figure 3. 29: The trend of the average values of the output of the sensors sealed with the three sealing technique under examination remains stable over the 25 days of observation.

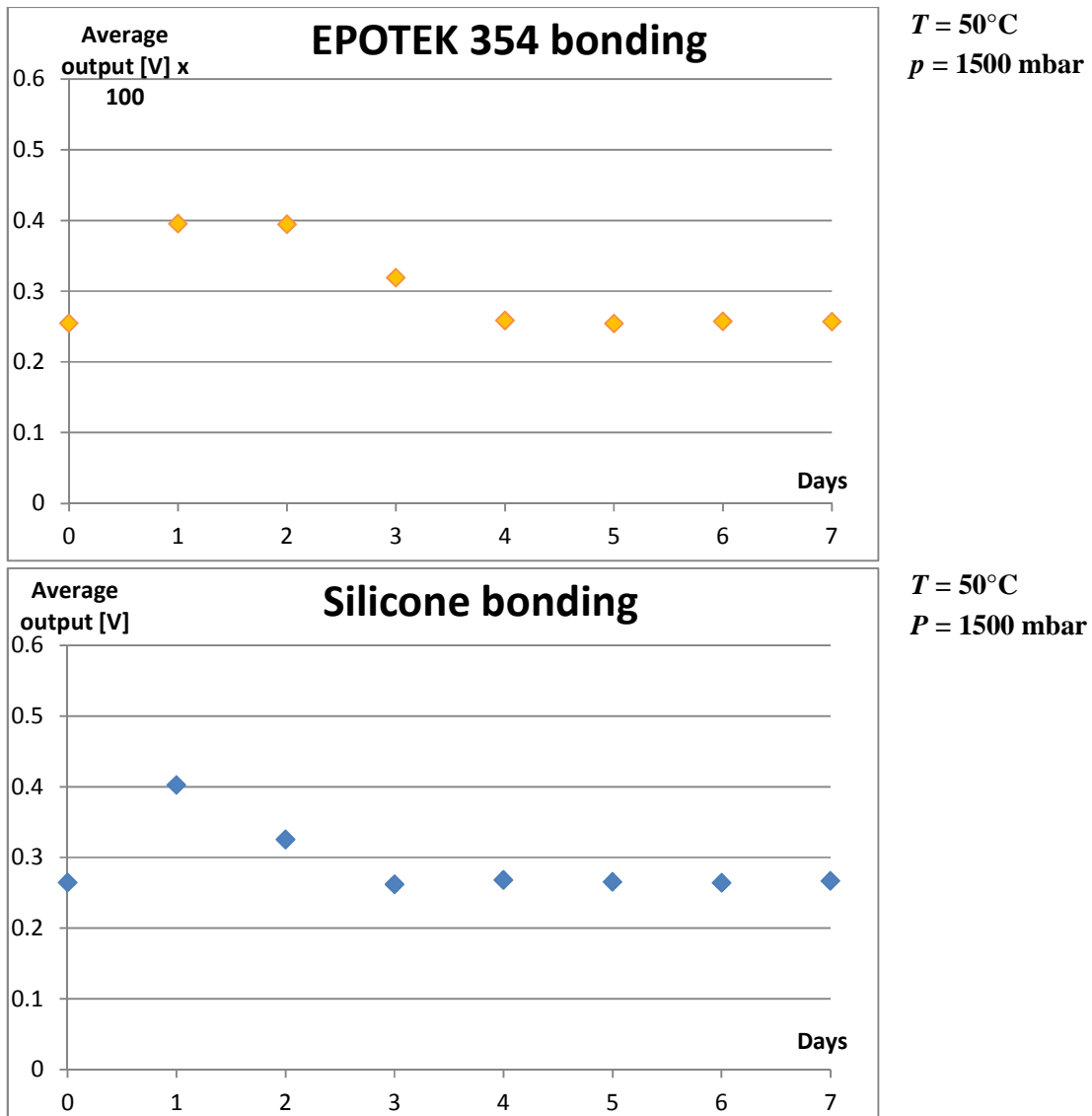


Figure 3. 30: The output of the sensor sealed with silicone went back to its original value (step 0, before sealing) after two days. The same happened to the sample sealed with EPOTEK 354, after 4 days

3.8.4 Discussion of the results of the hermeticity tests

Looking at the graphics of the response of the various sensors at different pressure profiles, it is evident that the best and most stable sealing technique is when silver paste is used. The output of the sensors produced with this technique is very clean and perfectly follows the pressure profile. However, this technique is slow and is performed at high temperatures, which is not desirable when we are sealing Rb, although it can be used when sealing the spacer with the bottom window, when Rb is not yet dispensed into the cell. Also the outputs of the sensors sealed with the two solder pastes retained follows the pressure profile. In particular, looking at the graphic, both Sn-Pb-Ag and Sn-Bi solder pastes followed pressure profiles nb.1 and nb.2, even if the standard deviation measured was slightly higher for the sample sealed with Sn-Bi. For these short tests (duration 20 minutes), also the output of the samples sealed with silicone DOW CORNING 4851 and Epoxy EPOTEK 354 is stable, because the air ingress into the cell is too slow to show a pressure relaxation inside the chamber over 20 minutes only. The studies on the temperature show that measurements at room temperatures are less noisy than measurements taken at high temperatures, therefore high temperature introduces further instability on the sensor response. Even if noisier, the response of the sensor at high temperatures follows the pressure profile; this means that the sensor stays hermetic even at high temperature. The long-term measurements confirmed that the most stable seal is the silver, but also Sn-Bi and Sn-Pb-Ag seals were able to stay hermetic, because during the whole duration of the study (25 days at 50°C and 1500 mbar) they show a minimal change of the output due to the stress relaxation phenomena typical of solder joints. The same test was repeated on the samples sealed with silicone and epoxy, and the result confirmed that these two adhesives are not truly hermetic, as expected. Finally, this study confirms that a system composed by an LTCC module sealed with a glass window using solder paste dispensed on top of a metallization ring composed of two layers of Ag ESL 9562G and one layer of Ag-Pd ESL 9635G is able to stay hermetic for long time and may be used as a base for fabricating reference cells for atomic clocks.

3.9 Test Performed on Cells with Rb

Some cells, with the chosen metallization / solder combination resumed in Table 3. 14 were produced following the procedure described in paragraph 3.5 and tested. In this case, as already explained in paragraph 3.3, the presence of the dodecane in the Rb reservoir is necessary for transferring the cell in the vacuum chamber preventing the oxidation of Rubidium. However, the dodecane stored in the glove box showed violent boiling in vacuum, due to the outgassing of the nitrogen gas dissolved in the solvent (as discussed in section 3.3), causing undesired movements of the glass cap and thus preventing its reliable hermetic bonding to the spacer. However, if the solvent is submitted to a pre-boiling treatment in vacuum, essentially all the nitrogen is driven off, allowing the thus pre-treated dodecane to

be then used safely, without the previously-observed violent boiling and resulting in its desired gentle evaporation. In this way, using this “pre-boiled”, stable dodecane, we were able to fabricate and test cells with Rb. The first qualitative test was visual observation; after sealing, the Rb inside the cell remained in its original position inside the reservoir, and in its original state, silver in color for ca. 20 days (Figure 3. 31a), suggesting that the cell stays hermetic for this time scale. The 20 days elapsed, the Rb transformation to white powder, probably RbO_2 and/or RbOH is very fast and clearly visible (Figure 3. 31b), suggesting that after this time, the cell is not hermetic anymore, therefore ingress of oxygen and water vapor inside the packaging oxidizes the alkali metal.

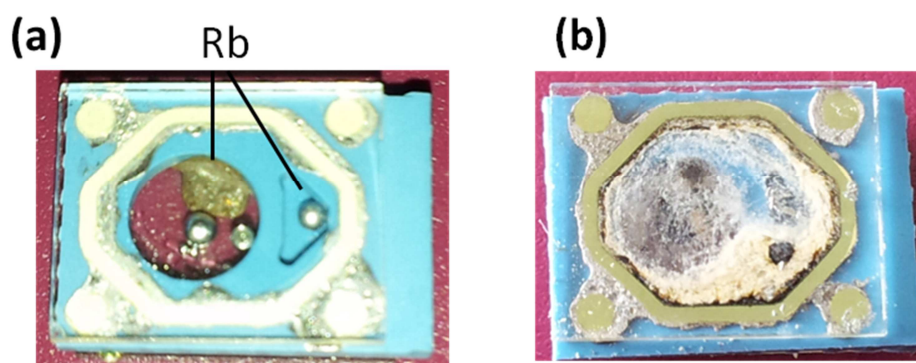


Figure 3. 31: (a), right after sealing, the Rb remains in its original position and its original state for about 20 days. After, (b), it converts into a white powder, probably Rubidium superoxide, due to ingress of oxygen inside the packaging.

The cell shown in Figure 3. 31 was submitted, by our project partners of LTF (Laboratoire Temps–Fréquence) of University of Neuchâtel, at spectroscopic measurements to confirm the presence of Rb. The absorption plot of the heated LTCC cell (Figure 3. 32, red curve) shows the characteristic Rb absorption lines at the wavelength of the Rb D2 line, so the test confirmed the presence of Rb in the cell. When compared with the reference cell spectrum (blue line in Figure 3. 32), the absorption line of our cell is broadened and is slightly shifted towards the right (i.e. towards longer wavelength), which can be attributed to the presence of a buffer gas (nitrogen) [213].

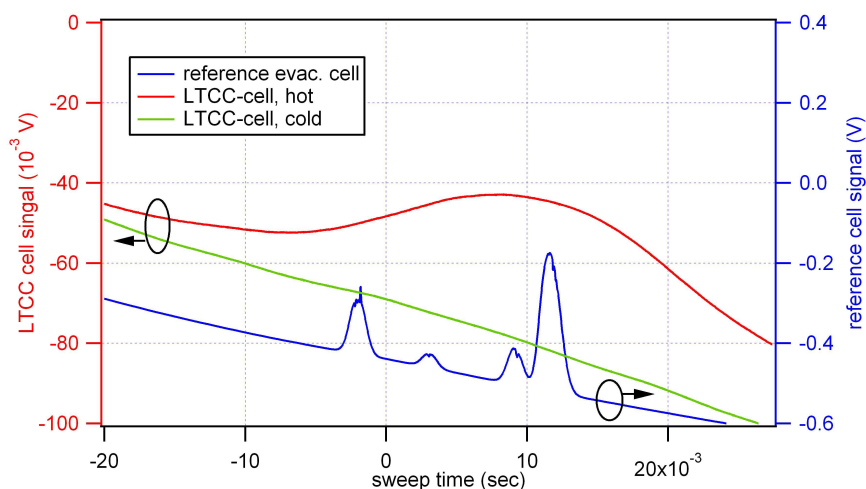


Figure 3.32: Laser absorption spectra from our microfabricated cell, showing characteristic Rb absorption lines. Arrows indicate the corresponding axis for each trace. The spectroscopic measurements were realized by Dr. Affolderbach at LTF (Laboratoire Temps-Fréquence) – Université de Neuchâtel.

After this first successful test proving the presence of Rb, the cell was submitted at the same test one hour later, but it did not show any absorption: most probably, the high temperature (ca. 100°C) at which the cell was submitted during the spectroscopic measurement accelerated the attack of the sealing ring by the rubidium, causing the degradation of the sealing and therefore the rapid oxidation of the alkali metal. This suggests that further studies regarding the interactions between rubidium and solder and metallization metals should be carried out in order to fully characterize the system. Other cells, in which the LTCC spacer was the test variant equipped with the pressure sensor, were also sealed with Rb. In this case, the output voltage of Wheatstone bridge was measured before sealing and monitored periodically after sealing (with a constant, nominally 5.0 V, excitation voltage), in order to monitor the cell inside pressure. The output changed considerably right after the sealing operation, reflecting transition from a zero differential pressure (both membrane sides at atmospheric pressure) to ca. 1 bar immediately after sealing, indicating that the sealing operation was initially successful and the hermeticity inside the cell was achieved. The output voltage of the Wheatstone bridge remained stable for ca. 20 days. When the transformation of Rubidium in white powder highlighted in Figure 3.31b starts, a relaxation of the differential pressure is observed. Therefore, most probably, at room temperature the hermeticity of the sealing is kept for ca. of 20 days; after this time, air ingress inside is observed and it causes the transformation of Rubidium into RbOH, the white powder observed in Figure 3.31b. The measured output voltage of the pressure sensor, sealed with Rb dispensed into the reservoir, is showed in Figure 3.33

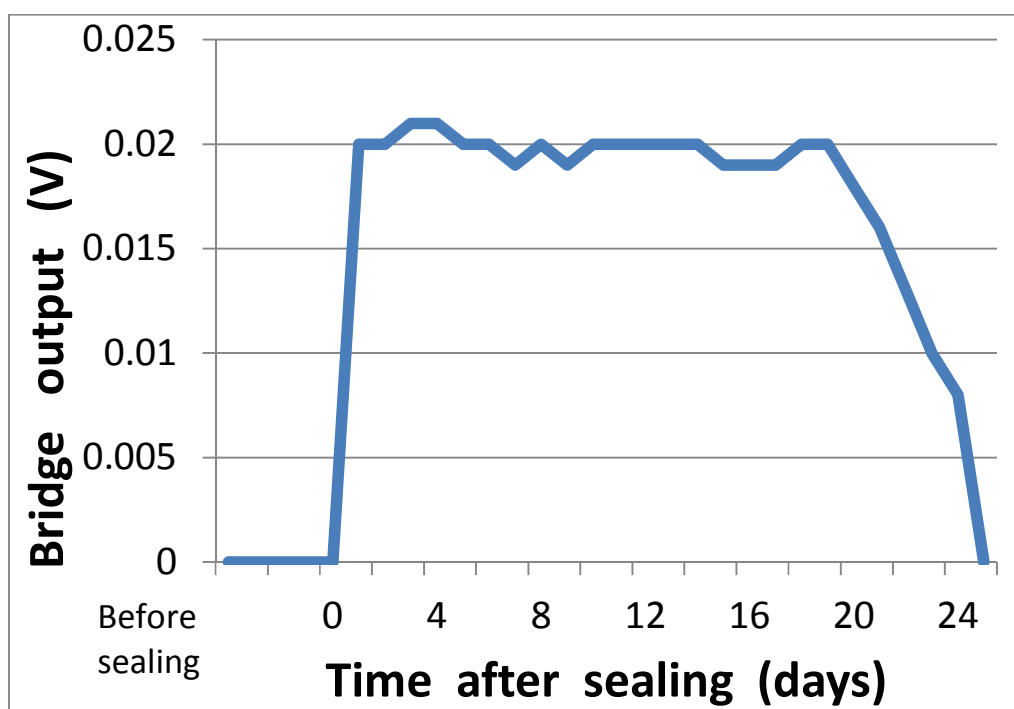


Figure 3. 33: Voltage output of the pressure sensor, when Rb is dispensed into the reservoir. We can see that the hermeticity is maintained for ca. 20 days.

3.10 Conclusions

In this work, a simple low-temperature process for the fabrication of hermetic Rb vapor cells for miniature atomic clocks has been presented, involving handling of the alkali metals under a protective solvent pool, and rapid low-temperature sealing by soldering. The introduction of an LTCC spacer provides an elegant manner to achieve a large cell volume, i.e. increased depth, while also allowing the sealing of the bottom window to be carried out before filling by a stable high-temperature process such as anodic bonding. The LTCC spacer also provides a convenient test platform, as it allows easy integration of a pressure sensor to monitor the cell after sealing. When producing the test modules, with integrated pressure sensors, an important deformation of the membrane was observed, probably due to the high pressure applied during lamination of LTCC, and this brought us to study more in details the lamination and to propose an alternative technique (see chapter 4 for details). Regarding the cell fabrication, the literature and the preliminary tests performed suggested that the bonding should last long time; cells sealed without Rb were submitted to accelerating aging tests (high temperatures and high pressure), and the bonding stayed hermetic. Cells produced with metallic, not oxidized Rb were also successfully produced. However, such cells, when kept at

room temperature, showed lack of hermeticity after 20 days, probably because of diffusion of Rb into the solder or into the metallization metals.

3.11 Possible Improvements to this Technique

The work presented here still suffers from some issues, especially related to the lifetime of the cell. In particular, the microfabricated Rb cells stayed hermetic for ca.20 days when kept at room temperature, while the cell submitted at 100°C for spectroscopic measurement showed Rb absorption lines at the first test, but not at the second test, performed only one hour later. so probably the cell does not tolerate the high temperature. However, cells sealed without Rubidium showed very good stability, so the limited lifetime of the produced Rb cells may be due to interactions between Rb and the solder or metallization metals, suggesting that further studies in this sense should be carried out. Another possibility is that the lack of stability of the sealing is related with the use of dodecane to protect the Rubidium from oxidation during the operation of transferring the cell in vacuum. The dodecane, also after the purification treatment, often causes undesired small movements of the lids, which may compromise the success of the sealing process. Therefore, another solvent may be considered, or, in alternative, a complete purification of dodecane from all impurities should be done before using it for the fabrication. Finally, the design of the cell may also be improved by replacing the Pyrex glass, sensitive to the aggressive presence of Rb vapor, with another glass, for example Schott 8346 [214] , which has been developed to be particularly resistant to alkali vapors.

4 New lamination technique for LTCC

This chapter introduces the current state of the art of low-pressure LTCC lamination techniques, and then will illustrate an innovative and practical technique that we introduced. The proposed technique allows easy fabrication of LTCC pressure sensors with reduced membrane deformation, thanks to the reduced pressure applied during lamination.

4.1 Introduction

When producing the test modules with LTCC pressure sensor showed in Figure 3. 9, we faced an important fabrication issue: the membrane of the pressure sensor was deformed by the high pressure applied during lamination. The consequence was that the produced pressure sensor did not detect any pressure change (not working sample). During the production stage, the LTCC green tape, which eventually forms the sensor, is punched, laser cut, and metalized using screen printing. Then, the tapes are stacked and laminated. After binder burnout and cofiring, the final LTCC pressure sensor shown in Figure 3. 9 is obtained, which must result in a monolithic ceramic block, i.e. the junctions between green tapes must not be visible anymore. For this reason, as already explained, the lamination stage is a crucial aspect to optimize. In chapter 2, we introduced the commonly used lamination technique, the thermocompression: the tapes are joined together at high pressure (usually, 20 MPa) and temperature (usually 70 – 80°C), for ca. 10 minutes [124]. These parameters usually allow good encapsulation, yielding to the production of a monolithic LTCC block after the sintering process. However, sometimes the use of hard binders, the low porosity of the tapes or not optimized lamination conditions can cause small cavities at the interface tape/metallization or tape/tape. These defects can be the origin of delamination and cracks during binder burnout and sintering (see for example [215], [216]. Thermocompression is an efficient process for a traditional circuit, such as electrodes, electronics signal conditioning platform, or heating plate. Such circuits are usually without cavities, holes, or thin membranes. However, as explained, LTCC technology has been widely investigated since ca. 20 years now also to manufacture membrane pressure sensors and microfluidic devices [107]–[109]. These kinds of structures are very delicate to laminate, because the thin membrane of a pressure sensor or the channels/chambers present in a microfluidic circuit can be strongly deformed by high pressure or temperature. The deformation of the membrane is illustrated, step by step, in Figure 4. 1.

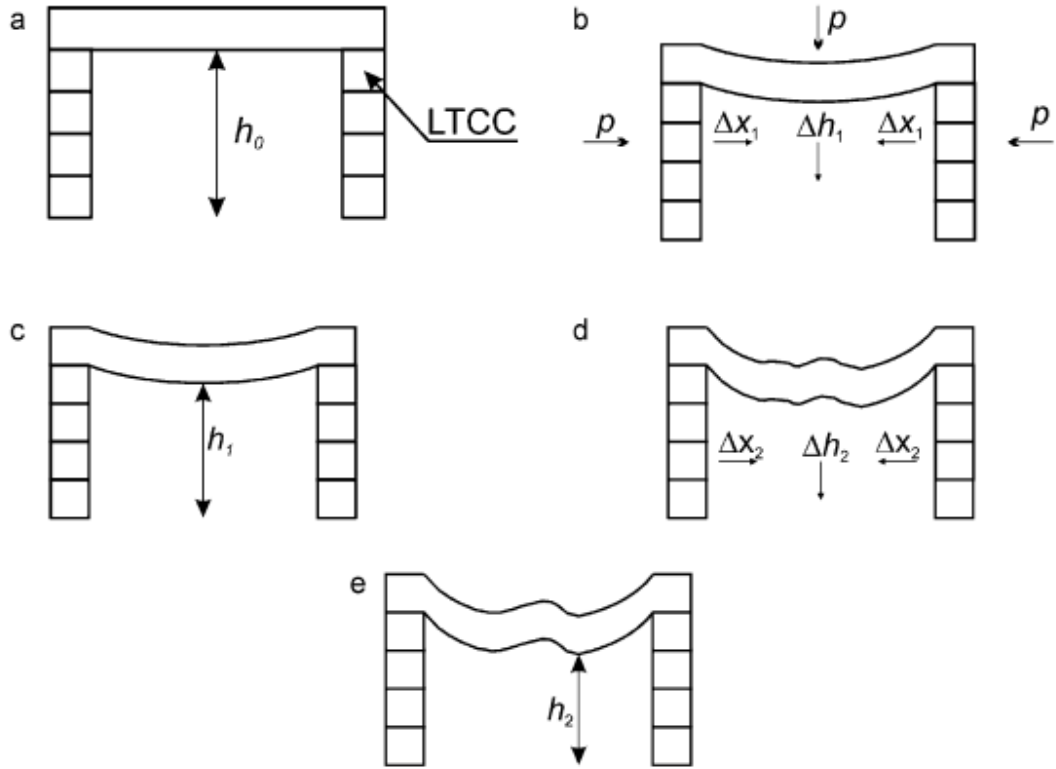


Figure 4. 1: Schematic diagram of deflection: (a), before lamination. (b), during lamination, (c), after lamination, (d), during firing, (e), after firing. Image taken from [125].

The deformation that happens during the lamination process is visible in Fig. Figure 4. 1b. In this case, h_1 is the change in dimension between the bottom of the structure and the membrane upon lamination, x_1 is the change in chamber dimensions in the x and y directions, and p is the lamination pressure) is mainly caused by the applied pressure in the membrane surface area. This deformation due to lamination may be probably reduced by applying lower pressure, even if the densification of the layers after firing must be ensured. The next distortion of the membrane is visible in Figure 4. 1d and it occurs during firing. In this case, the direction and type of the membrane deformation are not so easy to predict as in lamination, because the membrane can bend or become wavy after firing. The case shown in Figure 4. 1d is only one possibility, where h_2 is the dimensional change between the bottom of the structure and the membrane that occurred during firing, x_2 is the change in the chamber dimension in the x and y directions during firing. This deformation due to firing may be probably reduced by using a slower heating rate, gradually heating the membrane. Using the standard lamination technique, thermocompression, and the standard firing profile advised by the manufacturer for producing LTCC pressure sensors, the membrane may often suffer an important deflection, as highlighted by Dr. Fournier in his thesis [33, pp. 57–59] . A

non-flat membrane loses much of its sensitivity, due to the stiffening effect resulting from deformation, resulting in low and inconsistent response of such an LTCC pressure sensor. Therefore, we had to find out a new lamination method, and a better firing profile, which would lead to the production of a monolithic ceramic block after sintering, but that would also assure the flatness of the membrane. The most logical method to avoid deformation of the membrane is to apply less pressure during the lamination process, so the objective was to find a low-pressure lamination technique which would allow the efficient fabrication of LTCC 3D circuits. Previous attempts of various low-pressure lamination techniques are reported in the literature and have been investigated in order to analyze whether one of these techniques might be used for the production of the LTCC test module with membrane pressure sensor.

4.2 State of the Art of Lamination Techniques for LTCC

In the scientific literature, methods for lamination of LTCC tapes while preserving structures are based on three main principles:

- 1) Application of an adhesive tape;
- 2) Application of solvents or glues;
- 3) Application of a sacrificial layer or insert material

4.2.1 Application of adhesive tape

A potentially interesting method was proposed by Piwonski and Roosen [216], [217]. It consists of applying a double-sided adhesive tape (Beiersdorf AG, Hamburg, Germany) on top of the LTCC green tapes. The adhesive layer was based on polyacrylate, with an intermediate carrier layer that was a polyester film of 25 μm thickness. This double-sided adhesive tape was applied on the green tapes, then the pieces were stacked at room temperature and pressed at 5 MPa, and finally the part was fired at 870°C with a low heating rate (max 10 K/min) in order to avoid any damages to the LTCC structure due to excessive gas development. The joining mechanism is due to the formation of a viscous liquid phase from the melting of the polyester carrier film of the adhesive tape. The formation of this liquid phase happens at temperatures around 350°C, during the binder burnout process. The viscous liquid, at interface of the porous microstructure of the green tapes causes capillary forces, which result in an approach of the ceramic layers towards each other, and finally in a re-arrangement of the particles in the interface of the tapes. Samples fabricated with this method showed, after sintering at 870°C, no visible joint. The shape and geometry of channels and chambers were not affected by the pressure applied during lamination. This means that they were able to get a monolithic structure applying a lamination pressure of only 5 MPa at room temperature, and the moderate pressure did not deform the 3D intricate structure of the LTCC. The drawback of this method is that a metallization layer was not

applied on the LTCC tapes, so the interactions between thick film pastes and the tape were not investigated; the tape may alter the properties of the metallization layer.

4.2.2 Application of solvents or glues

This technique was firstly illustrated by Supparkarn et al. in 1998 [218]. They deposited a thin film of a solvent, mixture of ethanol, toluene and propylene glycol (PPG) on top of the LTCC green tapes, and then laminated at low pressure (0.5 kPa) for 5 minutes. The function of the ethanol and of the toluene, volatile solvents, is to soften the tape interface, promoting the joining of the tapes; they evaporate during the firing process. The non-volatile PPG penetrates into the porosity of green tape by capillary action, diffuses into the polymeric binder and causes the bonding of the tapes. Another possible solution was presented by Rocha et al. in 2004 [219]. They covered the LTCC green tapes with an organic liquid (natural honey), using either a paint brush or by screen-printing. They stacked the tapes together, and the liquid glues the layers. A first temporary gluing process between the tapes is realized at room temperature at very low pressure, thanks to the organic agent. Finally, the tapes are permanently joined during the cofiring. A similar method was presented by Jurków and Golonka [220], [221]. In this method, called Cold Chemical Lamination (CCL), a film of the solvent DuPont thinner 4533 [222] is applied on the green tapes surfaces using a paint brush just before lamination, so after screen-printing of the passives. The solvent softens the surface and the next tapes are added on the top by the same method. Then, the tapes are compressed by pressures below 100 kPa and at room temperature. The lamination is based on the diffusion process. In their research, Jurków and Golonka developed a simple LTCC flow sensor equipped with a thermistor. The layout presented two channels and one thin LTCC bridge. They used DuPont LTCC green tape 951AT (thickness 114 μm); the thermistor is used as a heater and temperature sensor at the same time, and it consisted of DuPont NTC thermistor paste NT40. They laminated the sample, covered with the solvent, with a pressure of 100 kPa at room temperature. They also produced some samples using traditional thermocompression lamination (150 MPa, 70°C). The comparison between the two samples showed a similar lamination quality, because both the samples were monolithic. On the other side, the samples produced with thermocompression lamination exhibited deformed channel walls and a high degree of sagging of the bridge, due to the high applied pressure and temperature. This problem was not present in the samples fabricated with CCL lamination. They also analyzed the thermistor properties after fabrication and compared both samples (fabricated with CCL lamination and thermocompression) to see whether the chemical lamination affects the thermistor properties. They reported that the sheet resistance is about 30% and constant B is about 4% higher for thermistors fabricated with CCL lamination. The variability coefficients of sheet resistance and constant B are 14% and 11% lower, respectively, for the CCL method. This means the solvent causes a change of the basic parameters of the thermistor, but this change is constant, and the values of sheet resistance

and constant B of the thermistor have good repeatability. Therefore the CCL method may be successfully applied in the fabrication process of the LTCC modules.

4.2.3 Application of a sacrificial layer or of an insert material

This method was well described, among others, by Jurków and Golonka in 2011 [125]. In this procedure, the tapes are bonded using the thermocompression lamination, so they are submitted at high pressure and high temperatures, but the chambers and channels, whose geometry may be deformed by the application of high pressure, are filled with a sacrificial material which protects the 3D structures from damage. The sacrificial material consists of a rubber-like die and it is intended to disappear during the sintering process. However, in this technique the firing process must be extended to ensure proper burning out of the sacrificial material. The alternative, also proposed by Jurków and Golonka in the same research, is to replace the sacrificial material by an insert material, in case the LTCC 3D structure is open. During the lamination process, performed again at high pressure and high temperature, the insert material protects the structure from deformation. After the lamination, before the firing, the insert material may be removed, and therefore a standard firing profile can be adopted. The lamination with an insert material is illustrated in Figure 4. 2. The LTCC structure is covered by a PCB FR-4 (Young's modulus 24 GPa, Poisson's ration of 0.3 and density of 1850 Kg/m³) from the top and the bottom. The cavity is filled with the insert material PDMS [223] (Young modulus 360-870 kPa, Poisson's ratio of 0.5 and density of 0.97 Kg/m³), which is removed before firing the sample with a standard firing profile. In this case, the insert material protects the 3D structure from deformation during thermocompression lamination. The lamination was performed applying the minimum pressure which allows getting a good bonding between the tapes: 0.5 MPa, 70°C, 10 minutes.

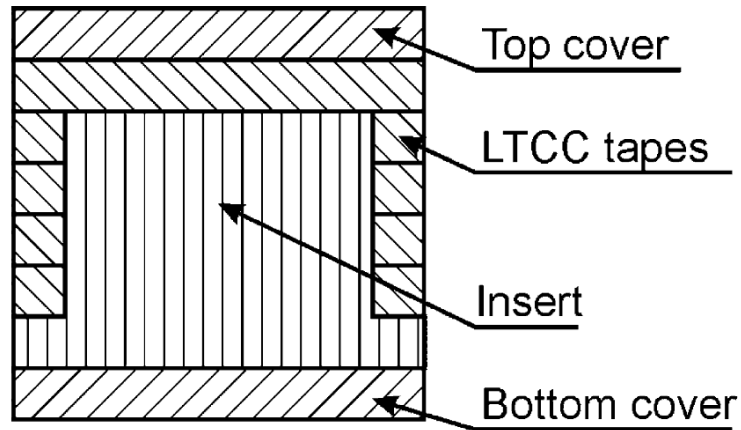


Figure 4. 2: Schematic of the lamination with an insert material. Image taken from [125].

Using this method, they were able to get a good bonding of the tapes after sintering. However, even if an important reduction of the membrane deflection was observed for the

tapes Heraclon HL2000 and Ceram Tape GC, the deflection of the DuPont (DP) 951-based membranes was approximately the same for structures laminated with and without rubber-like inserts; therefore this technique is not advised for this kind of green tape.

4.2.4 Conclusion: need to introduce a new technique

After a detailed analysis of the different techniques reported in the literature, we decided to introduce a new technique: the first two described methods, based respectively on adhesive tape and solvent print gave good performance, but for our applications they also present some drawbacks: the techniques involving the application of a glue material require an extra operation in the processing chain (the gluing material is applied after the tape processing steps), which is not very practical. Moreover, in case the glue layer is applied using a paint brush, the amount of material dispensed is not well controlled; on the other side, if the glue layer is applied by screen-printing, it is required a specific mask for each layer, which is really time-consuming. The advantage of the technique involving the application of the adhesive tapes is that they are widely available and very reproducible, but the tape must be carefully applied on top of the green tapes, especially if they are very thin; if the structure to be laminated is complex, the tape application becomes a very delicate and difficult operation. Moreover, the LTCC tape must be carefully handled for stacking and lamination, and positioning corrections after stacking may be impossible. The third described method, based on insert of a protection material, looks very practical, but apparently it does not offer particular advantages for DP 951 tape, which is the tape that we were planning to use. Therefore, we decided to develop our own technique, that we wished to be practical, easy to apply and efficient, leading to the fabrication of LTCC modules with complex 3D structures without affecting the shape of channels, chambers or membranes, without effort.

4.3 Basic Idea of the Developed Technique

The technique was developed in close collaboration with Mr. Jiang, from LPM-EPFL. The basic idea of the low-pressure lamination technique developed in this research is to create a kind of LTCC glue, a low-melting “hot melt” adhesive layer, which can be applied by screen printing on each LTCC tape before starting the fabrication steps [224]. The consistence of the glue should ideally be viscous, but also liquid enough to allow deposition by screen-printing. The adhesive layer, once dried, must have a low degree of tack at room temperature in order to avoid collecting dust (especially from laser cutting) and allow easy handling. On the other hand, it should melt or soften at moderate temperatures (40-60°C), allowing easy lamination at low pressures. The adhesive layer is dispensed on the entire surface of the green tape, so there is no need to create a separate mask for each layer – the mask can be generic for all designs and layers to be bonded in this manner.

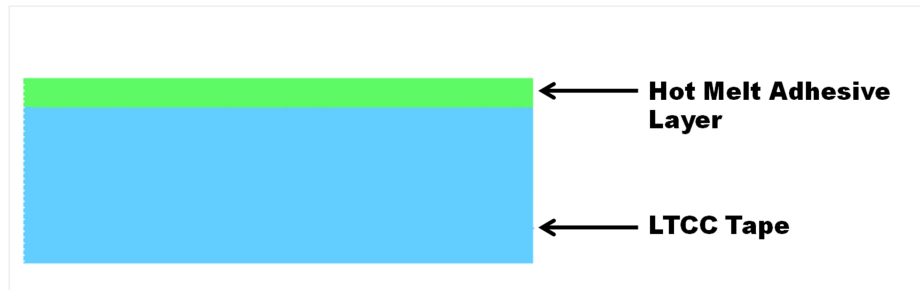


Figure 4. 3: The adhesive layer is dispensed by screen-printing on the entire surface of the LTCC green tape. Image taken from [107].

After applying this special “glue” onto the substrates, the production procedure follows the traditional steps, i.e. laser-cut, screen-printing, lamination, and firing. The lamination may be performed at moderate pressure (less than 5 MPa) and at 60°C, because at this temperature, the adhesive layer deposited onto the green tapes will ideally melt causing the bonding of the tapes. The moderate pressure should avoid or at least significantly reduce the deformation due to lamination pressure, illustrated in Figure 4. 1b. Moreover, the firing profile adopted in this technique is much slower with respect to the standard one, advised by the manufacturer. The slow heating rate will probably avoid the rapid softening of the membrane layer, therefore diminishing the risk of deformation due to firing (illustrated in Figure 4. 1d). Figure 4. 4 shows the procedure to follow for fabrication of LTCC with this method.

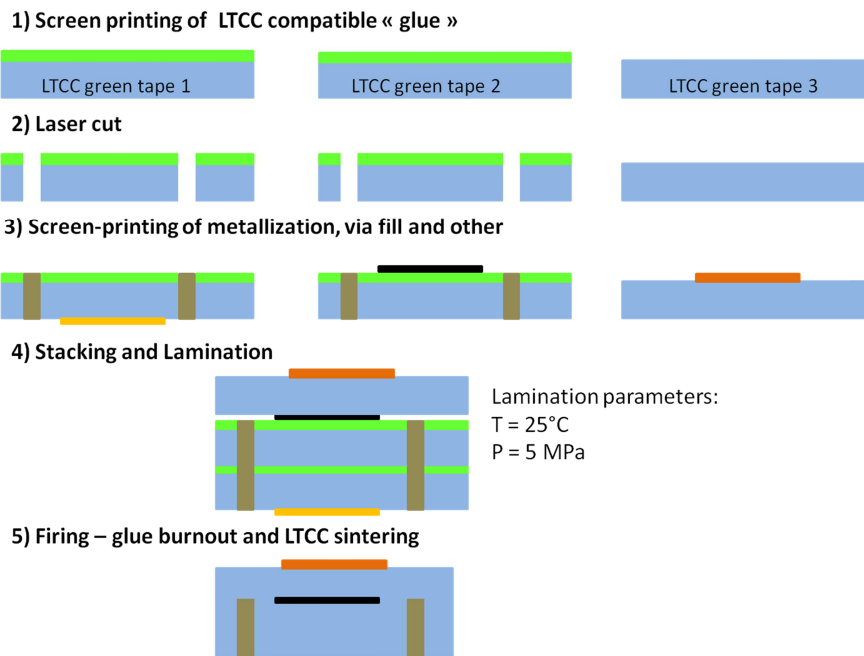


Figure 4. 4: The adhesive layer is dispensed on top of the LTCC tape and then the standard fabrication process can start.

4.4 Composition of the Adhesive Layer

In order to find out the ideal composition for the special glue, different hot-melt adhesives were formulated by mixing at a temperature of 60°C and stirring the ingredients. Many attempts were done to find out a suitable composition: as explained, the “glue” at room temperature must not be sticking and have a low degree of tack, while at moderate temperature (60°C), it must melt to allow the bonding of the various tapes. In addition, the adhesive layer must be easy to screen-print, and not strongly dissolve the LTCC binder. The systems tested were based on a main solvent, which was chosen to be cyclohexanol (CAS number 108-93-0), for the following reasons:

- It has rather high viscosity;
- It does not attack the LTCC green tape too severely;
- It does not pass through the LTCC tape, or at least it does not pass completely through;
- It evaporates at low temperatures (boiling point is 161°C);
- At room temperature, moderate evaporation is observed;
- It dissolves the binders used in the adhesive formulations.

The main solvent was mixed with a soft polymer binder. The tested binders were:

- Ethylcellulose (EC), CAS number 9004-57-3;
- Polyvinylbutyral (PVB), CAS number 63148-65-2;

Then, a plasticizer was also introduced into the formulation of the paste. The function of the plasticizer is to decrease the transition temperature (T_g), which is the temperature at which the glass transition happens (the reversible transition of a hard and relatively brittle amorphous material into a molten, gluing rubber-like material). The plasticizers tested were:

- Polyethylene glycol (PEG-400), CAS number 25322-68-3;
- Triethylene glycol bis (2-ethylhexanoate, TEG-EH), CAS number 94-28-0;
- Acetyl tributyl citrate (ATBC), CAS number 77-90-7.

In some formulations, a wax (cetanol, i.e. hexadecanol, CAS number 8032-89-1) was also introduced. The purpose of the wax is to lower the viscosity of the hot-melt adhesive and thus promoting flow in the molten state (same behavior as the plasticizers), yet crystallize out of the binder at room temperature and thereby reduce tack in this state. In contrast to the molten state, the low-temperature behavior of the wax is different from that of the plasticizer, due to crystal-melt transition of the wax being much sharper than the rather progressive glass transition seen in mixes of amorphous binder and plasticizer. By adjusting the respective levels of wax and plasticizer, one can independently control both high-temperature flow and low-temperature tack characteristics. This creates a final formulation that can be readily applied and fully wet the LTCC surface. The choice of the binder, the plasticizer and the wax was done based on the Hansen parameters[225]: similar values of such parameters indicate

that the components are compatible with each other and that they will be correctly dissolved into the main solvent. Table 4. 1 summarizes the tested formulations, with a short note on the result obtained for each attempt.

Paste No.	Main solvent (weight %)	Binder (weight %)	Plasticizer (weight %)	Wax (weight %)	Note
1	Cyclohexanol (55%)	PVB (9%)	PEG-400 (9%)	Cetanol (27%)	Hard to print – too viscous – sticks on LTCC
2	Cyclohexanol (70%)	EC (5.6%)	TEG-EH (5.6%)	Cetanol (18.8%)	Difficult to print
3	Cyclohexanol (50%)	EC (30%)	ATBC (20%)	-	Print OK, slight tack
4	Cyclohexanol (45.3%)	EC (27.2%)	ATBC (13.6%)	Cetanol (13.9%)	Print OK, no tack

Table 4. 1: Bonding material tested: PVB = Polyvinylbutyral; EC = ethylcellulose; PEG-400 = Polyethylene glycol; TEG-EH = Triethylene glycol bis (2-ethylhexanoate); TBAC = Trybutyl acetyl citrate.

From the table above it is evident that the paste No. 4 was the best, combining a good printability with no visible tack. This paste was used to produce samples of our LTCC pressure sensor, in order to find out the best parameters (lamination pressure and temperature, firing profile), which allow to get the best result. The factors to evaluate in order to determine the quality of the sample were the flatness of the membrane and the satisfactory bonding of the tapes.

4.5 Fabrication Parameters

The resulting paste nb.4 was tested onto DP 951 [36] and Heraeus Heraclon (HL) 2000 [131] green tapes. Different values of moderate pressure p were tried for lamination (1.94, 3.88 and 7.75 MPa). The lamination was performed at 60°C, in order to make the adhesive layer melt and realize the bonding. Table 4. 2 summarizes the densification of the samples after firing, at different moderate values of lamination pressure.

The pressure of 3.88 MPa seems good for both DP and HL tapes, so this was the value of pressure applied for production. The test samples were finally fired with a low rate firing profile in order to slowly burnout the binder at the beginning, and then the firing profile culminated at ca. 875°C. The firing profile adopted is showed in Figure 4. 5.

Green Tape	$p = 1.94 \text{ MPa}$	$p = 3.88 \text{ MPa}$	$p = 7.75 \text{ MPa}$
DP 951	Good densification	Good densification	Little crack
HL 2000	Little crack	Good densification	Good densification

Table 4. 2: Results showing that the best is to apply a pressure of 3.88 MPa, as no tack and good densification were observed.

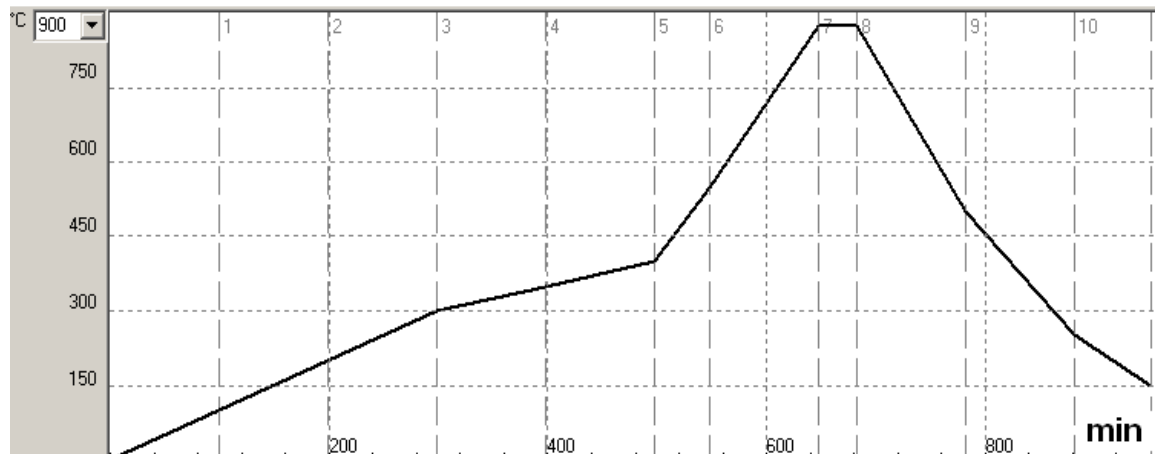


Figure 4. 5: Firing profile used for the tests: the binding burnout was slow (increasing of 1 to 2°C per minute until 430°C) to decrease the deformation of the membrane during firing.

The firing profile adopted is ca. 30% longer than the standard one, advised by the manufacturer (an example of a standard firing profile is illustrated in Figure 2. 16). The principal reason for this is that we need to evacuate extra organic material; moreover, the gradual heating is less traumatic for the membrane, and may therefore decrease the risk of deformation due to firing temperatures, illustrated in Figure 4. 1d.

4.6 Results

The LTCC pressure sensors illustrated in Figure 3. 13 were produced using the standard technique with thermocompression lamination and the proposed lamination technique. The DP 951 and HL 2000 LTCC tapes were used to produce the samples. The produced samples were submitted to the following tests:

- Some samples were broken to examine bonding quality.
- The deflection of the membrane was evaluated by profilometry, to examine the effect of the process on membrane flatness.
- The effects of the adhesive layer on the printed piezoresistive paste were evaluated, in order to determine whether the glue affects the properties of the thick film paste.

4.6.1 Densification

Samples fabricated using paste No.4 showed good densification, with both green tapes. Figure 4.6 shows photos of the samples, with good densification, and the comparison with a sample whose densification was poor.

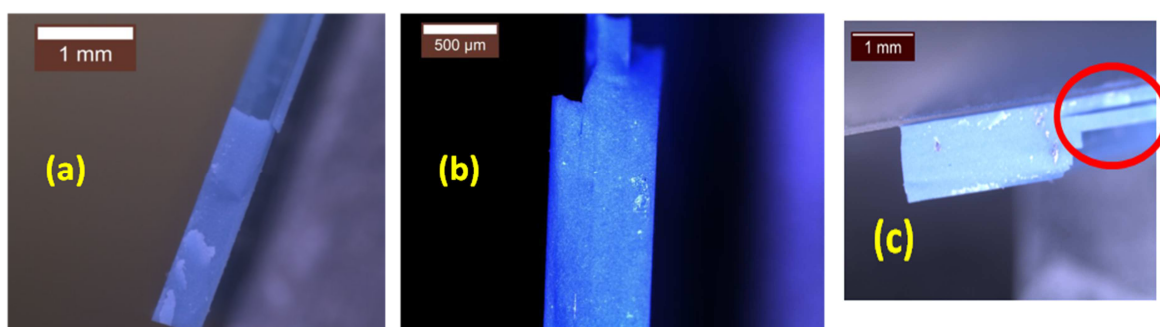


Figure 4. 6: (a), fracture surface of DP951 membrane structure showing good bonding. (b), fracture surface of HL2000 membrane structure, showing good bonding. (c), fracture surface of HL2000 membrane structure, showing poor bonding.

The Figure 4. 6a and the Figure 4. 6b show photos of the samples fabricated with this method, using both green tapes. As it is possible to see, the densification is very good, the bonding of the various layers is excellent and the module is a monolithic structure. In comparison, we can observe the Figure 4. 6c, which was a sample fabricated with a non successful composition, showing a bad densification of the membrane.

4.6.2 Membrane flatness

The other important factor to evaluate the method was the flatness of the membrane. The membrane layer had a thickness before firing of 114 μm . The membrane of samples fabricated with standard technique was analyzed, and compared with the membrane of samples fabricated with our low-pressure lamination technique. We used the non-contact laser profilometer UBM [226] to analyze the flatness of the membranes. A photo of the used profilometer is shown in Figure 4.7, and its probe sweeps the surface of the membranes as illustrated in Figure 4.8, yielding analyses such as the one shown in Figure 4. 9, for a sample fabricated with the standard technique.

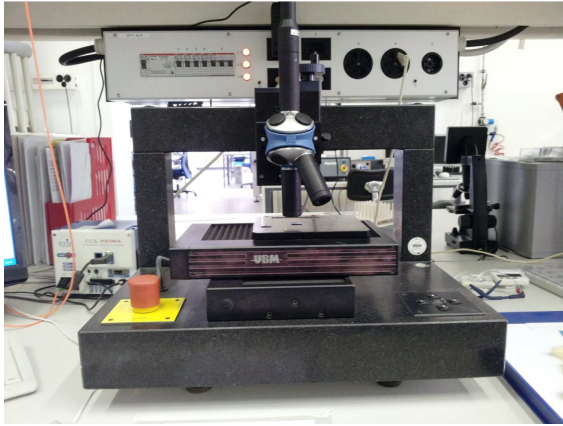


Figure 4. 7: A photo of the non-contact laser profilometer used to analyze the flatness of the membrane of the pressure sensors

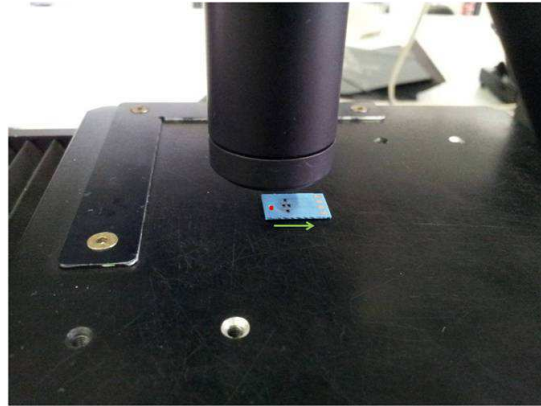


Figure 4. 8: Measurement of the flatness of the membrane. The red dot is the point where the probe is focused. Once the profilometer is focused, the table moves like shown by the green arrow, so that the probe can sweep the entire surface of the membrane

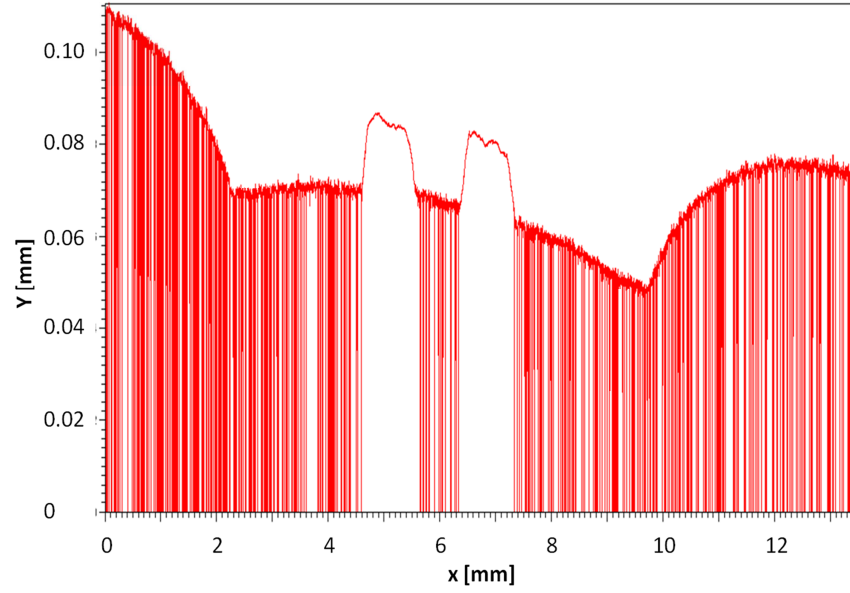


Figure 4. 9: Profile of the membrane fabricated with standard fabrication. The green tape used was DP951: the thickness of the membrane was 114 μm before firing, 97 μm after firing (nominal shrinkage is 15%)

Two factors need to be evaluated: the gap between the “non membrane zone” and the “membrane zone”, and also the flatness of the membrane zone. Both the factors in this sample are not satisfactory: as we can see in Figure 4. 9, the gap between the “non membrane zone” and the membrane zone (the membrane zone starts at $x = 2$ mm) is ca. 40 μm (ca. 40% of the total thickness of the membrane layer). Moreover, the membrane zone is not flat. Not considering the two little “mountains” that are visible, that are the resistors of the membrane, the profile is neither regular nor flat. We can compare this result with a membrane fabricated using our lamination technique (Figure 4. 10). The composition of the layer, of course, is the same for both the samples: we used DP951 green tape, and the thickness of the membrane layer was 114 μm before firing (97 μm after firing). The improvement due to this technique is evident: There is not a visible gap between the “non membrane zone” and the membrane zone (again, the membrane starts at $x = 2$ mm), and also, the membrane zone results almost completely flat; this means that also the slower firing profile efficiently reduced the deformation due to the firing.

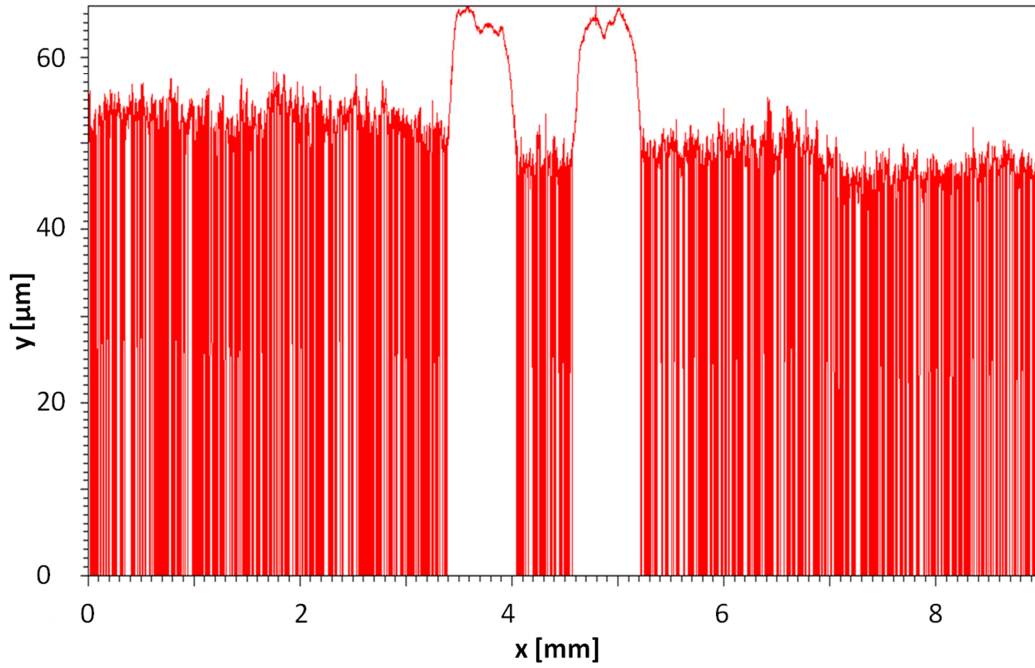


Figure 4. 10: Profile of the membrane fabricated with low-pressure lamination technique

4.6.3 Effect of the adhesive layer on the piezoresistive paste

The piezoresistive resistor paste used to fabricate the LTCC pressure sensor was DP 2041. The nominal HTCR (Hot Temperature Coefficient of Resistance, 25-125°C) of the paste is ≤ 50 ppm/K, and nominal sheet resistivity is 10 kΩ/square [227]. The HTCR was measured by measuring the resistance, with a 4-points measurement, at 25, 50, 75, 100, 125 and 150°C of 8 different samples fabricated with thermocompression lamination and 8 samples fabricated with low-pressure lamination, and then the value retained was the average value of the 8 measurements. We also calculated the standard deviation of the samples, using the formula of Eq. 3. 7. The formula used to calculate the HTCR is:

$$HTCR = \frac{1}{R} \cdot \frac{\Delta R}{\Delta T} \quad \text{Eq. 4. 1}$$

On the same 16 samples (8 samples fabricated with our lamination technique and 8 samples with the standard thermocompression lamination), we also measured the sheet resistivity of the piezoresistive paste, and again we calculated the average value of the 8 measurements, shown together with the standard deviation in Table 4. 3.

	HTCR (ppm/K)	Sheet resistivity (k Ω /square)
Thermocompression lamination	30.1 \pm 0.8	9.8 \pm 1.9
Low-pressure lamination	34.3 \pm 0.8	10.2 \pm 1.6

Table 4. 3: Properties of the DP 2041 resistive paste (average value \pm standard deviation) after firing, for both standard thermocompression and the new adhesive-assisted low-pressure lamination methods.

Given the usual lot-to-lot sheet resistance and TCR variations, the observed differences are negligible. Moreover, one should note that the sheet resistivity is affected by screen-printing effects, such as thickness increase near the termination or ink spreading, and this effect is expected to influence TCR as well, due to significant reactivity of resistors with LTCC. Regarding the standard deviation, we can see that the measurements of the TCR show good reproducibility, with low standard deviation for both types of samples. The higher standard deviation of the measurements of the sheet resistivity is due to the abovementioned and unavoidable screen printing effects.

4.7 Conclusions and outlook

A new, innovative technique is proposed for the fabrication of LTCC microfluidic circuits or membrane pressure sensors. These kinds of systems are equipped with long channels, chambers, or a thin membrane; the geometry of these structures is usually affected by the application of high pressure or high temperature during the standard thermocompression lamination technique, or the high temperature during the firing. For this reason, we decided to develop a new lamination technique which allows the application of a moderate pressure, lower than the one applied in the standard technique, but at the end leading to an excellent bonding of the various tapes. The various methods presented in the literature are either not practical, or do not guarantee the performance needed. The basic idea of this technique is to screen-print, on top on any green tape, a kind of LTCC glue, which is not sticking at room temperature, and that melts at ca. 60°C, becoming stick and fluid, and therefore allowing the bonding of the tapes at moderate pressure. The fabrication steps after the application of the adhesive layer follows the standard procedure described in paragraph 2.5, i.e. laser cut, screen-print, stacking, lamination, firing. The adhesive must be compatible with standard thick film pastes, without affecting their physical properties, and must be viscous, but also enough liquid to be printable. Various formulations were tested, containing a main solvent mixed with a soft polymer as binder, a plasticizer and/or a wax. Finally, a good composition was found: we got an excellent bonding of the LTCC tapes (both HL 2000 and DP 951 green tapes tested), using a moderate lamination pressure (3.88 MPa). A slow firing profile was adopted, in order to gradually reach the peak, preventing the membrane from deforming because of a sudden temperature change and softening of the layer. The membrane of a pressure sensor developed with this technique was analyzed using a profilometer, and

resulted much more flat with respect to the same membrane, fabricated with the standard thermocompression lamination. The physical properties of the resistor screen-printed on the membrane stayed the same, or slightly changed, after application of our “glue”. Therefore, this technique can be successfully used in fabrication of LTCC microfluidic circuits, as it does not affect the shapes of channels, cavities or chamber, and it is also very attractive for the fabrication of LTCC membrane pressure sensors, as it reduces the membrane deformation and also does not affect the physical properties of the piezoresistive paste. The proposed technique is very promising, but further work should be performed in order to fully characterize the adhesive. In particular, an aspect which has not been investigated is whether the connection tracks remain correctly embedded with the LTCC module after firing it in presence of our hot-melt adhesive. An elegant solution which would avoid any problem with the printed elements and that would also further speed up the production chain would be to add the hot-melt adhesive directly into the composition of the LTCC green-tape surface, which would finally consist of ceramic powder plus the soft binder, promoting efficient interlayer bonding, yet avoiding strong deformation due to stabilization by the harder core. Also, this would make the process compatible with the presence of conducting tracks, which would embed easily in the soft surface layer.

5 Thermal studies on LTCC

In this chapter, an LTCC multifunctional module is introduced. The designed module is flexible enough to be used in any microsystem to heat and temperature control any small device in the mm scale. A detailed thermal analysis was performed, together with finite-element simulations, to estimate the amount of heating power consumed by this heating plate, and the loss introduced by convection and conduction. The analysis and the simulations were validated by comparing the data with experimental results. In free air, losses by convection are dominant, and thermal insulation is therefore needed to achieve low-power operation.

5.1 Introduction

One of the objectives of this research was to use LTCC technology to package, interconnect and control the temperature of the components of the atomic clock. Moreover, during our research, we faced many times the issue to precisely control the temperature of various small devices, which were active part of larger microsystems. For this reason, we developed a standard LTCC heating platform, equipped with a positive-temperature-coefficient (PTC) thermistor to measure the temperature, and an Ag-Pd heating meander. The designed device is flexible enough to be used to control the temperature of any small device in the mm scale, as it is equipped with a simple plug & play standard Dual-In-Line (DIL) connector, allowing it to be plugged easily in any PCB and used. One important feature of the LTCC heating plate is its power consumption, which is required to be low, as in most cases, it has to be used in portable low-power microsystems. Therefore, before the final fabrication of the device, a detailed thermal analysis and then finite-element simulations were performed, in order to estimate the power consumption of this device, the losses introduced by free convection and conduction. This analysis aimed to determine whether the LTCC heating plate has sufficient thermal efficiency to be used in portable microsystems. Finally, after the fabrication of the device, we reproduce the experiments in the laboratory to validate the simulations. Various materials were tested in order to efficiently thermally insulate the heating plate, leading to improvements of the heating performance. Finally, the best experimental configuration was established, and in this case, when the module is efficiently thermally insulated, the heating power required is enough low to be used in portable, low-power microsystems in the mm scale.

5.2 Design and Fabrication of the LTCC Heater

5.2.1 Concept and design of the device

Ideally, the heating plate that we aimed to design was supposed to have the following features:

- a) It should be equipped with a heating resistor and a separate temperature-sensing resistor so that it is able to heat and at the same time measure the temperature;
- b) It should be flexible, so that it can easily used in different microsystems;
- c) It should be small enough and feature low thermal losses to minimize power consumption and thus allow its application to portable microsystems
- d) Noise and instabilities on the temperature measurement signal should be avoided or shielded in order to get a precise control (some applications need a stability better than 0.01 K);
- e) Ideally, it should be robust and able to work also in harsh environments, even if this feature is not necessary for our application (atomic clock packaging), but we aimed to develop a flexible and ideally universal heating plate.

For its excellent thermal and chemical stability, the possibility to integrate passive heaters and PTC resistors in one module and also to add by simply soldering, standard connectors to interface the module with the external world, LTCC technology was chosen to produce the device.

5.2.2 Fabrication and description of the device

The designed device (Figure 5. 1 and Figure 5. 2) has an adjustable thickness of 500 μm and it is composed by four different layers (intermediate layers can be added depending on thickness requirements). The fabrication process of this multi-functional module involves the traditional steps of LTCC technology: laser cutting of green tapes, screen-printing, stacking and lamination, and firing. The final device is equipped at the centre with an aperture; this aperture is useful in case of miniature atomic clock packaging, for letting the light coming from the light source passing through. It presents a heating conductive serpentine for local temperature control and a PTC (Positive Temperature Coefficient) thermistor for temperature measurement.

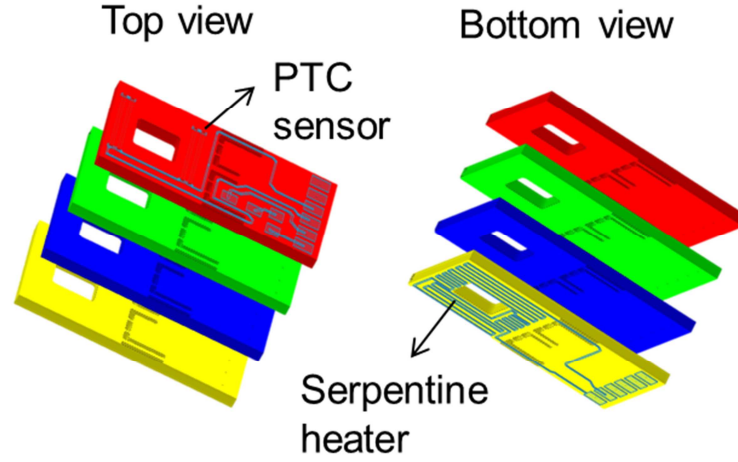


Figure 5. 1: 3D views of the different layers that constitute the LTCC heater and drive circuit platform

Two different types of LTCC green tapes are used to fabricate the device: the top and the bottom layers consist of the zero XY shrinkage Heraeus HL2000 green tape (thickness of ca. $132\text{ }\mu\text{m}$ before firing, and ca. $92\text{ }\mu\text{m}$ after firing). The two intermediate layers, added for increasing the thickness and hence the robustness of the platform, consist of DP951 green tape of thickness (before firing) of $254\text{ }\mu\text{m}$ (nominal XY shrinkage of the tape is 12.7%, while nominal z-shrinkage is 15%, [36]). Using this “sandwich” of HL2000 and DP951 green tapes, the total x shrinkage was 1.08% and total y shrinkage was 0.84%, because the HL tape constrains the shrinkage of DP tape. So, almost zero shrinkage was obtained without having to stack many thin HL layers to get the desired thickness, making the fabrication process easy and low-cost. Conductive paste Ag-Pd DP 6146 [228] was used to pattern and screen-print a serpentine heater on the bottom layer. Solder pads are present on top and bottom layer and they are electrically connected by vias, filled with conductive Ag-Pd paste. The solder pads will be used to place a connector which will be plugged in into the PCB support. For the PTC temperature sensor, DP 5092D composition (sheet resistivity $100\text{ }\Omega/\text{sq}$, HTCR 3000 ppm/K), [229] paste was patterned and screen-printed on the top layer. The heated area of the module (where the heating serpentine is present) is insulated from the external “cold” area, where the electrical connections are placed: both zones only communicate through two small bridges (Figure 5. 2a, yellow arrows), in the low-loss configuration (Figure 5. 2 a). Initially, the module also has 4 additional small bridges (Figure 5. 2b, purple arrows), which reinforce the module during production and are then cut away (as seen in Figure 5. 2a), and another central optional bridge (Figure 5. 2b, red arrow), which is shorter and wider than the outer ones. The central bridge, if not cut away, induces important conduction loss but has the advantage of making the module less fragile. In case

the LTCC hotplate will carry a cumbersome and heavy (for heavy we intend ca. 10 grams) device, it is advisable not to cut off the central bridge: more conduction loss is introduced in this case, but the hotplate will be more robust. The central bridge also carries an electrical track which allows introduction of a controlled temperature gradient. This gradient is regulated by soldering an SMD resistor on the dedicated pads (Figure 5. 2a, red rectangle), which shunts some of the current flow and thereby further reduces heating in the bottom part of the heated area (this can be maximized by shorting the SMD pads altogether). The resulting colder zone is useful when the module is used to temperature-stabilize the alkali-metal reference cell of an atomic clock, as it allows reliably keeping the alkali metal away from the window. On the bottom layer there are also wire-bonding pads (Figure 5. 2b, yellow rectangle), in case additional devices (e.g. external sensors) must be added and connected. Photos of the designed device are shown in Figure 5. 2, and the overall dimensions, and some other important dimensions of the device, are summarized in Table 5. 1.

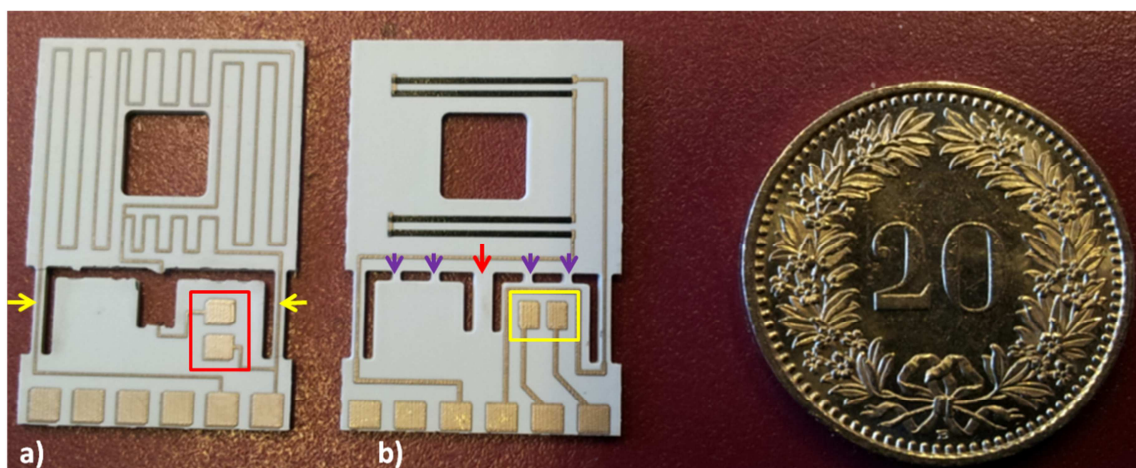


Figure 5. 2: A photo of the fabricated LTCC module; (a) bottom view, module in the low-loss configuration, without central bridge. The heating silver serpentine covers the entire hot zone on the top. The yellow arrows highlight the two small bridges that connect the cold zone (bottom) and the hot zone (top). In the red rectangle there are SMD pads where it is possible to solder a resistor that will alter the current flow through the bottom part of the heated area (if the intermediate bridge is not cut away). (b), top view of the module, with optional central bridge (red arrow) and intermediate fabrication bridges (purple arrows). The PTC resistor consists of the four black lines on the top part. In the yellow rectangle there are the wire-bonding pads.

	Width [mm]	Height [mm]
Overall dimensions	15	22
Heated area	15	12
Aperture for the light	5	5
Dimension of the external bridges	0.6	5
Optional centre bridge	1	3.2

Table 5. 1: Detailed dimensions of the LTCC module designed for atomic clock packaging

5.3 Thermal Analysis of the Designed Device

Since we aimed to reduce the power consumption of the device, before the final fabrication of the module, we performed a physical and thermal analysis to estimate the minimum power required to achieve the desired temperature, in the various possible configurations of the module; we also investigated the possibility to replace the Ag-Pd heating serpentine with simple Ag, which is cheaper, but has a higher thermal conductivity and therefore introduces further loss. This analysis was then validated by thermal simulations.

5.3.1 Physical and thermal analysis

In the ideal situation, depicted in Figure 5.3, the only loss present in the system is the one by conduction from the central hot zone (hypothesized at constant temperature) and the cold zone (where the solder pads are), through the bridges (connection between the two zones). The cold zone is hypothesized to be at 25°C. For each thermal bridge (connection between the hot zone and the cold zone) we can apply Fourier's law:

$$Q = \sum_{i=1}^n \frac{k_i S_i}{L_i} * \Delta T \quad \text{Eq. 5. 1}$$

. where:

- Q = Power given to heater
- n = Number of bridges
- k_i = thermal conductivity of the material of the bridge i
- S_i = cross section area of the bridge i
- L_i = length of the bridge i

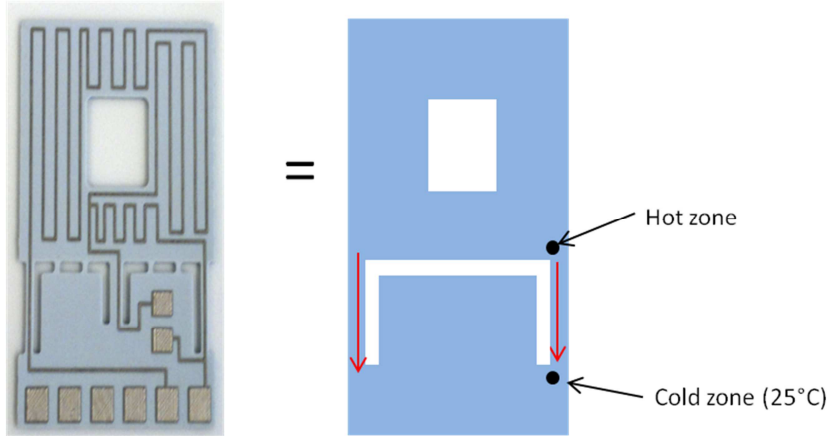


Figure 5.3: The thermal flux by conduction is the one highlighted by the red arrow and it is the only thermal flux present in the ideal situation.

We can now introduce the thermal coefficient C_i introduced by the bridge i , which is a value that only depends on the material and on the geometry of the bridge considered. So:

$$C_i = \frac{k_i S_i}{L_i} \quad \text{Eq. 5. 2}$$

Finally, we can re-write Eq. 5. 2 highlighting the thermal coefficients:

$$Q = \sum_{i=1}^n C_i * \Delta T \quad \text{Eq. 5. 3}$$

Knowing the thermal conductivity of the material which constitutes the bridge and its geometry, it is possible to calculate the thermal coefficient introduced by the bridge. The following are the bridges (i.e. the connections between the hot zone and the cold zone to consider) that introduce conduction loss:

- External outer LTCC bridges
- Optional central LTCC bridge
- Ag-Pd (or Ag) connections (screen-printed on top of the LTCC bridges)

During this analysis, different hypothesis and approximation were done. In the different configurations of the LTCC module, we estimated the power that we needed to get a temperature of 70 °C (typical working temperature of the reference cell) in the hot zone. Therefore the value of ΔT is always the same in all the calculations performed:

$$\Delta T = 70 - 25 = 45 \text{ [K]} \quad \text{Eq. 5. 4}$$

Case 1. Thermal dissipation by conduction loss through the LTCC bridges only

In this first approximation, the contribution of Ag-Pd connection bridge is considered negligible. Table 5. 2 summarizes the thermal coefficient introduced by the LTCC bridges,

calculated using Eq. 5. 2, assuming that k of LTCC is $3 \text{ W} \cdot \text{m}^{-1} \cdot \text{K}^{-1}$ [36] and with the dimensions summarized in Table 5. 1.

Bridge	k_i [W · m ⁻¹ · K ⁻¹]	S_i [mm ²]	L_i [mm]	C_i [mW/K]
LTCC outer bridges	3	0.30	5.0	0.174
LTCC central optional bridge	3	0.55	3.2	0.498

Table 5. 2: Calculation of the thermal coefficients introduced by the LTCC bridges.

LTCC in the low-loss configuration

This is exactly the case summarized in in Figure 5. 3. The only thermal flux present is through the two outer bridges.

$$P = 2 * C_{LTCC,out} * \Delta T$$

$$P = 2 * (1.74 * 10^{-4}) * 45 = \mathbf{15.6 \text{ mW}} \quad \text{Eq. 5. 5}$$

This means that, in the low-loss configuration, taking into account only conduction in LTCC, ca. 16 mW are needed to get a temperature of 70°C in the hot zone.

LTCC equipped with intermediate bridge

In this case we have an additional coefficient to the sum, i.e. that of the central bridge.

$$P = 2 * C_{LTCC,out} + C_{LTCC,central} * \Delta T$$

$$P = 2 * [(1.74 * 10^{-4}) + (4.98 * 10^{-4})] * 45 = \mathbf{38.1 \text{ mW}} \quad \text{Eq. 5. 6}$$

Comparing the result in equation 5.5 with this result, we note that the introduction of the intermediate shorter and wider bridge considerably increases the loss by conduction

Case 2. Study of contribution of the Ag-Pd connections

Let's now consider the Ag-Pd connection on the bridges: they may be considered as additional bridges whose contribution should be added in the sum in order to precisely estimate the losses they introduce. Before applying Fourier's law, though, it is necessary to estimate the thermal conductivity k of the Ag-Pd. The paste used for the heating serpentine is DP 6146 [228]. The nominal sheet resistance (R_s) is $< 60 \text{ m}\Omega/\text{sq}$. We measured the sheet resistance and it was ca.25 mΩ/sq. The estimated resistivity (ρ) of the Ag-Pd is then:

$$\rho = R_s * t = 0.25 * 10^{-6} \Omega \cdot m \quad \text{Eq. 5. 7}$$

, where t is the thickness of the Ag-Pd connection, which we can assume being equal to 10 μm . The obtained value for the electrical resistivity of the Ag-Pd alloy is in line with the value calculated by Butler and Stocks in 1984 [230]: for an alloy of similar composition of Ag-Pd, they estimated a value of electrical resistivity of $\rho \approx 0.2 \cdot 10^{-6} \Omega \cdot m$. Now we can calculate the electrical conductivity of the Ag-Pd, which is equal to:

$$\sigma = \frac{1}{\rho} = 4 * 10^6 \frac{S}{m} \quad \text{Eq. 5. 8}$$

Now, knowing the electrical conductivity of Ag-Pd alloy, calculated in Eq. 5. 8, we can simply apply the Wiedemann-Franz law [231], [232] to calculate the thermal conductivity of the paste:

$$\frac{k}{\sigma} = LT \quad \text{Eq. 5. 9}$$

, where:

- k is the thermal conductivity of the material
- σ is the electrical conductivity of the material
- L is the Lorenz number, equal to $2.44 \cdot 10^{-8} \cdot \text{W} \cdot \Omega \cdot \text{K}^{-2}$
- T is the temperature in K

Applying this law, in the hypothesis of room temperature ($T \approx 300 \text{ K}$), we obtain:

$$k = \sigma LT = (4 * 10^6) * (2.44 * 10^{-8}) * 300 = 29 \text{ W} \cdot \text{m}^{-1} \cdot \text{K}^{-1} \quad \text{Eq. 5. 10}$$

The value of thermal conductivity of the Ag-Pd alloy calculated respectively in Eq. 5. 10 is similar to that obtained by Yarbrough et al. [233].who estimated, for an alloy of similar composition of Ag-Pd, a thermal conductivity of $k \approx 22 \text{ W} \cdot \text{m}^{-1} \cdot \text{K}^{-1}$. We can now use this value of thermal conductivity in our calculation of the ideal power and see if the amount of conduction losses introduced by the Ag-Pd is negligible with respect to the loss introduced by the LTCC bridge. The first thing to do is to calculate the thermal coefficient C introduced by the Ag-Pd bridge, assuming a width of the track of 0.2 mm, while the thickness, as previously assumed, is 10 μm . The length of the Ag-Pd connection is the same of the LTCC bridge crossed.

Bridge	k_i [W · m ⁻¹ · K ⁻¹]	S_i [mm ²]	L_i [mm]	C_i [mW/K]
Ag-Pd outer connection	29	0.002	5.0	0.012
Ag-Pd central optional connection	29	0.002	3.2	0.018

Table 5. 3: Calculation of the thermal coefficients introduced by the Ag-Pd bridges

LTCC in the low-loss configuration

In this case we have the two outer LTCC bridges which introduce a conductive loss, plus the two Ag-Pd bridges screen-printed on top of the LTCC, which also introduce conductive loss.

$$P = [2 * C_{LTCC,out} + 2 * C_{AgPd}] * \Delta T$$

$$P = [2 * 1.74 * 10^{-4} + 2 * 1.17 * 10^{-5}] * 45 = \mathbf{16.7 \text{ mW}} \quad \text{Eq. 5. 11}$$

Compared the result obtained in Eq. 5. 11 with that of Eq. 5. 5, calculated considering only the contribution of the two LTCC bridges, the difference is almost negligible.

LTCC with intermediate bridge

In this case we can apply again Fourier's Law, including the thermal coefficients introduced by the two LTCC outer bridges, the LTCC central bridge, the two Ag-Pd outer bridges and the Ag-Pd central bridge, in order to calculate the power required to get 70°C at the hot zone:

$$P = (2 * C_{LTCC,out} + C_{LTCC,central} + 2 * C_{AgPd,out} + C_{AgPd,central}) * \Delta T$$

$$P = (2 * 1.74 * 10^{-4} + 4.98 * 10^{-4} + 2 * 1.17 * 10^{-5} + 1.83 * 10^{-5}) * 45 = \mathbf{39.9 \text{ mW}} \quad \text{Eq. 5. 12}$$

Again, the value calculated in Eq. 5. 12 is very similar to that calculated in Eq. 5. 6, in which the contribution of the Ag-Pd bridges was not taken into account. We have therefore proved that the contribution of the Ag-Pd to the conduction losses is actually negligible, because the most important contribution to the conduction loss is introduced by the LTCC bridges.

Case 3. Possibility to replace Ag-Pd with Ag

In case the connections are made of Ag instead of Ag-Pd, the contribution changes, because the thermal conduction of Ag is much larger than Ag-Pd alloy. Typically, the sheet resistance of silver conductor pastes is between 4 and 5 mΩ/sq [234], [235]. If we assume a value of

5 mΩ/sq, it means that the sheet resistance of Ag paste is exactly 5 times less than that of its alloy Ag-Pd. Therefore, repeating the steps summarized in paragraph 3.2, we get a thermal conductivity of the Ag paste equal to $145 \text{ W} \cdot \text{m}^{-1} \cdot \text{K}^{-1}$ (five times more than its alloy Ag-Pd). This is a very generous estimation, because the thermal conductivity of bulk silver is $406 \text{ W} \cdot \text{m}^{-1} \cdot \text{K}^{-1}$ [236], and knowing that thick film pastes usually have lower thermal conductivity with respect to their bulk material. We can calculate the thermal coefficient that would introduce the Ag connection on the outer bridges, knowing that its thermal conductivity is $145 \text{ W} \cdot \text{m}^{-1} \cdot \text{K}^{-1}$, its cross section and its length are the same than the Ag-Pd connection.

Bridge	k_i [W · m ⁻¹ · K ⁻¹]	S_i [mm ²]	L_i [mm]	C_i [mW/K]
Ag outer connection	145	0.002	5.0	0.092

Table 5. 4: Calculation of the thermal coefficient eventually introduced by an Ag bridge.

We can now apply Fourier's law, in the hypothesis of module in its low-loss configuration, without central bridge, and with Ag connections:

$$P = (2 * C_{LTCC,out} + 2 * C_{Ag}) * \Delta T$$

$$P = (2 * 1.74 * 10^{-4} + 2 * 9.15 * 10^{-5}) * 45 = \mathbf{23.9 \text{ mW}} \quad \text{Eq. 5. 13}$$

So, the replacement of the Ag-Pd with Ag would increase the dissipated power of about 50 % in the analog configuration (23.9 mW instead of 15.9 mW with Ag-Pd). Therefore, the contribution of the Ag-Pd connection to the thermal loss is almost negligible, but this is not the case of a pure Ag connection. Due to this high loss, the use of Ag for the heating serpentine is not advised, in addition to the resistance being too low to be practical.

5.4 Thermal Simulations Performed

In order to validate the thermal analysis and fully characterize the thermal performance of the designed device, we performed finite-element simulations, using the software ANSYS [237]. The value of heating power required for achieving 70°C was calculated by the simulations, hypothesizing different configurations of the LTCC module:

- 1) The module equipped with all the bridges (as-produced);
- 2) The configuration with both the central bridge and the outer bridges (“high-loss”);
- 3) The configuration with only the outer bridges (“low-loss”).

The temperature distribution along the heated area was observed in the different cases and then compared with the configuration in which the bottom part of the heating serpentine is short-circuited (mounting a $0\ \Omega$ SMD resistor on the dedicated pads of Fig.1a). All these simulations were performed hypothesizing no losses other than conduction in the LTCC bridges (complete vacuum, no radiation). Finally, the effect of convection on the heating and the additional losses that it introduces was also estimated, simulated and experimentally validated. A fine mesh was used for all the simulations, in order to carefully observe what happens at the bridge edge. Figure 5. 4 shows a screenshot of the meshed device during the simulation: it is possible to clearly see that the bridges are finely meshed in order to estimate in the most accurate way the temperature distribution along these areas:

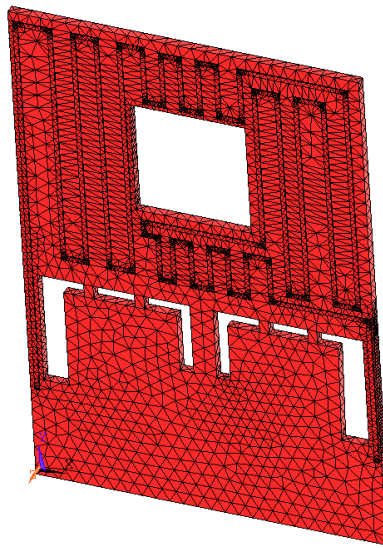


Figure 5. 4: Results of the smart meshing of the LTCC device in its original configuration.

Thermal conductivity of LTCC	$3\ \text{W} \cdot \text{m}^{-1} \cdot \text{K}^{-1}$
Electrical resistivity of Ag-Pd serpentine	$0.5 \cdot \mu\Omega \cdot \text{m}$
Hypothesis	In vacuum (no convection), no radiation
Boundary condition	Cold zone (external) at 25°C

Table 5. 5: Data, hypothesis and boundary condition adopted for the thermal simulations performed

Table 5. 5 summarizes the parameters and the boundary conditions adopted for all the thermal simulations. Using this data the finite element simulations estimated the heating power required to achieve a temperature in the hot zone (where the heating serpentine is placed) of 70°C (typical working temperature of the mini-cell, here maximal temperature in the module). The first simulated case was that of the LTCC module is in its original layout,

with all the 7 bridges intact, which induced a considerable conductivity loss. The finite-element simulation of the first configuration shows a non-homogeneous distribution of the temperature, as expected. In this case, almost all the bottom part of the heated area is 10 to 15°C colder than the top part, due to the considerable conduction loss between both zones brought about especially by the short bridges. In this case, for achieving a temperature of 70°C, 5 V and 13.6 mA of current were necessary, which corresponds to a total power of 69 mW. The results of this simulation are shown in Figure 5. 5:

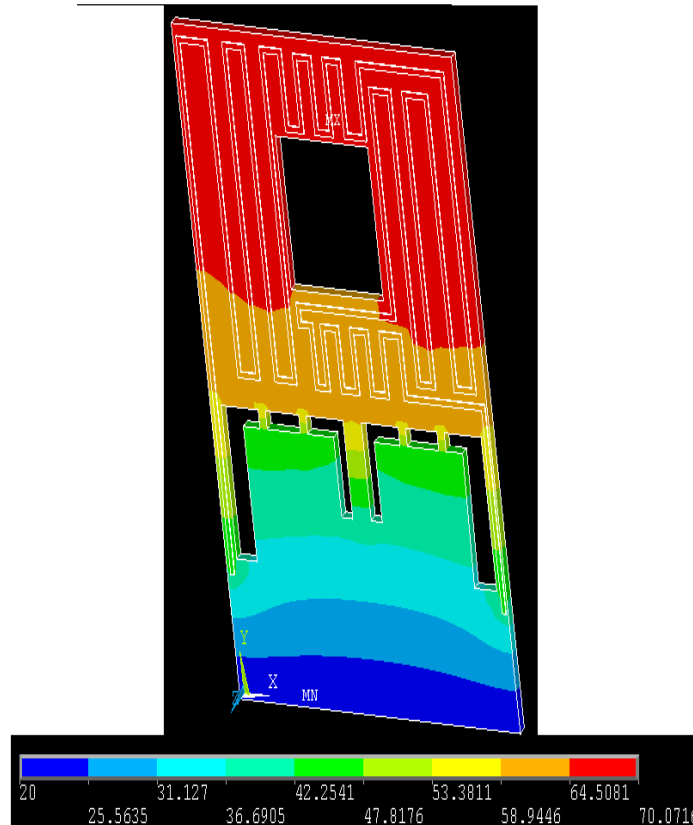


Figure 5. 5: Results of the finite-element simulation of the LTCC module in its original configuration.

The next step was to simulate the LTCC module without the 4 intermediate small bridges, i.e. with the two outer bridges and the central one. It is possible to see in this case (Figure 5. 6) that the temperature distribution is more homogeneous respect to the first case, and only the zones close to the bridges are significantly colder than the top part of the heated area, the temperature of the hot zone otherwise being within a 5°C range. In this case, 3.2 V and 10.9 mA of current, corresponding to a power of 35 mW, were necessary to achieve a maximal temperature of 70°C, i.e. a decrease of ca. 35% with respect to the first case. This is expected from the decreased conduction loss due to the elimination of the 4 short intermediate bridges that created a thermal short-circuit between the heated area and the cold zone. If we do not consider the hottest point, but the average hot zone temperature, the decrease in required power is even larger than 35%.

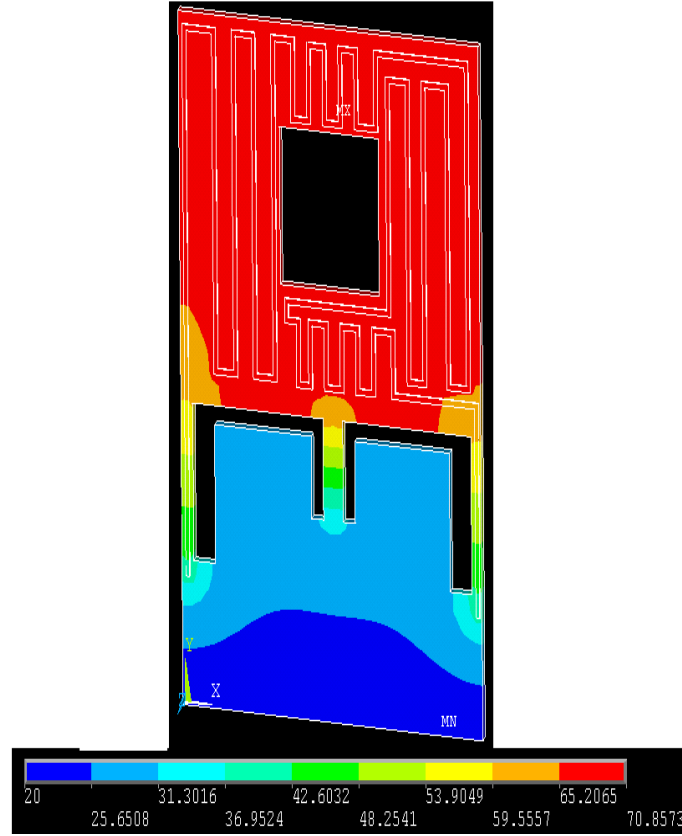


Figure 5. 6: Results of the thermal simulation of the LTCC device equipped with the external and the outer bridges.

Finally, we simulated the LTCC device in its low-loss configuration: the central bridge is cut away as well, leaving the module with the two outer bridges only (which carry the heating and temperature-measurement conductor tracks). The module in this configuration is more fragile, but still it can carry without any problem most of the small devices that it is going to temperature-stabilize. On the other hand, it offers better performance in terms of conduction loss, resulting in an even more homogeneous temperature distribution within the hot area: colder zones are observed only in the bottom corners, i.e. close to the outer bridges. In this configuration, 2.5 V and 7.5 mA, a heating power of 19 mW, was necessary to achieve a maximal temperature of 70°C, an almost further 50% improvement over the configuration with the central bridge. The result of this simulation is shown in Figure 5. 7. This result is consistent with that obtained with the physical analysis: in this case, making many approximations, we got, for the low-loss configuration, that 70°C were achieved using a heating power of 16 mW (equation 3.15), while the finite-element simulations show that 19 mW were necessary. The two values are fairly close to each other; therefore the simulations performed validated the physical analysis.

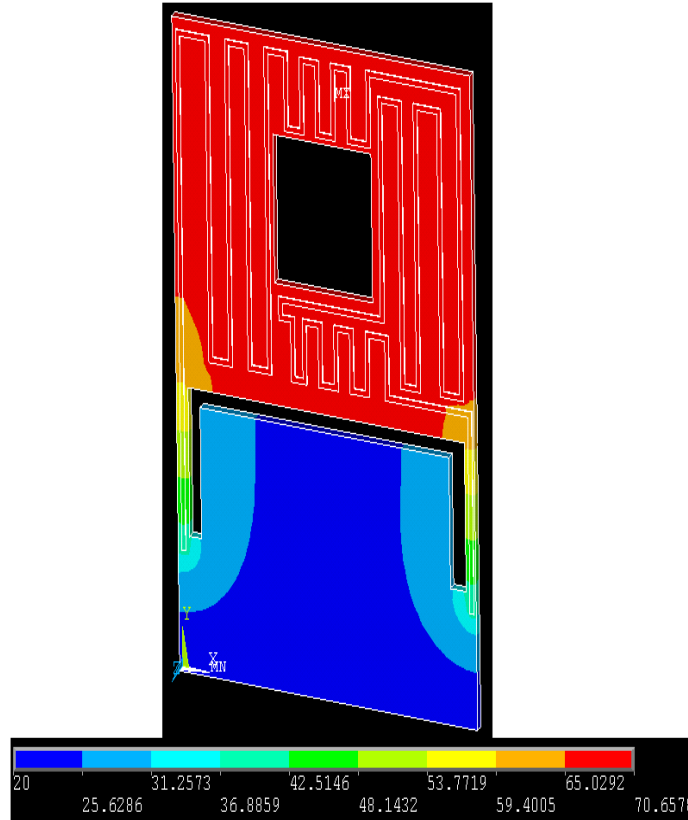


Figure 5. 7: Result of the thermal simulation of the LTCC module in its low-loss configuration.

As previously explained, this module, when the central bridge is active, allows further alteration of the temperature distribution along the heated area by an SMD resistor that regulates the current flow on the bottom of the heated area. It is desirable to have a colder zone in case the LTCC acts as carrier/temperature controller for the reference mini-cell of an atomic clock, for keeping the alkali metal which it contains away from the window. Another finite element simulation was performed hypothesizing that the value of the SMD resistor that regulate the flow of current into the bottom part of the serpentine is equal to $0\ \Omega$: this means that there is no current flowing on the bottom part of the serpentine, so the temperature gradient along the heated area is further increased, beyond that due by the losses stemming from the bridges. The result of this simulation is shown in Figure 5. 8. As it may be seen, the temperature difference achieved between the bottom and the top of the heated area is ca. 10°C , i.e. more or less doubled compared to the same configuration without shorting the resistor and thereby disabling the bottom part of the heater. Expectedly, the power required for achieving a maximal temperature of 70°C is essentially unchanged: 43 mW (3.7 V, 11.7 mA). This configuration of the heater, therefore, allows fine-tuning the temperature distribution without introducing large additional losses. Conversely, achieving an even more homogeneous distribution than the low-loss configuration would be possible by

applying a higher heating density near the bridges to compensate the additional current losses, or even by using an independent “guard” heater to cancel out the temperature gradient along the bridges. Table 5. 6 summarizes the results of the simulations of the LTCC in its various configurations.

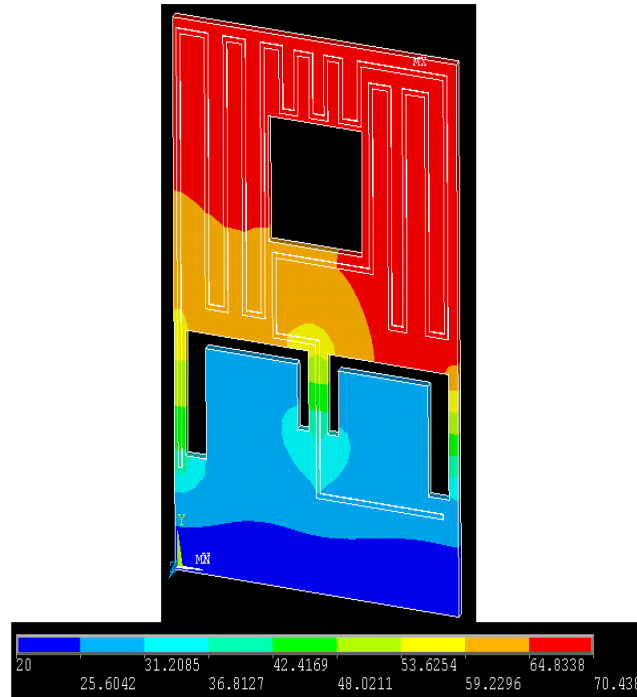


Figure 5. 8: Result of the thermal simulation of the LTCC module with the bottom part of the heating serpentine shorted out.

Configuration of the LTCC	Heating power required to achieve 70°C in the hot zone [mW]	Temperature gradient in the hot zone
Original layout (7 bridges)	69	Not homogeneous, due to the presence of the small bridges
Outer Bridges + Intermediate bridge	35	Within a 5°C range
Low-loss configuration (outer bridges only)	19	Homogeneous
With intermediate LTCC bridge; bottom part of the heating shorted	43	Bottom part is ca.10°C colder than top part, as wished

Table 5. 6: Summary of the results of the thermal simulations performed

5.4.1 Simulation of the effects of free convection

All the simulations presented until now were done hypothesizing that the module was placed in a perfect vacuum (no convection and conduction through the ambient atmosphere) and without any radiative losses. It is interesting to simulate also the effect of convection, and estimate the losses that it introduces into the system. In order to simulate this effect, the convection film coefficient h must be calculated, i.e. the proportionality factor between the heat loss flux and the temperature difference between the hot surface and the ambient fluid. The first required step is to calculate the Rayleigh number, which, in case of free convection near a vertical wall is equal to [238]:

$$Ra_x = \frac{g\beta\Delta T x^3}{\nu\alpha} \quad \text{Eq. 5. 14}$$

In Eq. 5. 14, Ra_x is the Rayleigh number at the position x , g is the acceleration due to gravity, β is the thermal expansion coefficient, ΔT is the temperature difference between the air and the wall (LTCC), x is the characteristic length (in case of free convection near a vertical wall, it may assumed as the distance from the leading edge), ν is the kinematic viscosity and α is the thermal diffusivity of the fluid. The calculation of the Rayleigh number gives $Ra_x = 2'006'311$. Since $Ra < 10^9$, we may assume the case of laminar flow. Knowing that the Prandtl (Pr) number of the fluid (the air) is fixed because it only depends on the properties of the fluid and is equal to ca. 0.7, the next step is to calculate the Nusselt (Nu) number, that in case of laminar flow, free convection on a vertical wall can be calculated using the empirical correlations of Churchill and Chru [239]:

$$Nu = 0.68 + \frac{0.67Ra^{1/4}}{[1 + (\frac{0.492}{Pr})^{9/16}]^{4/9}} \quad \text{Eq. 5. 15}$$

The calculation of the Nusselt number gives $Nu = 20$. Finally, we are now able to calculate the h coefficient, using the same Churchill and Chru empirical correlations:

$$h = \frac{k}{L} Nu \quad \text{Eq. 5. 16}$$

The calculation of the h coefficient gives $h = 22.7 \text{ W/(m}^2\cdot\text{K)}$, which is a value in line with that calculated by other researchers in a similar case (free convection with air) [240]. Knowing this coefficient and hypothesizing the air bulk temperature to be 22°C, it was possible to make another finite-element simulation for estimating the loss introduced by convection into the system. The result of this simulation is shown in Figure 5. 9. The external “cold” part in this case is at homogeneous temperature, precisely the temperature of the outside air, since the convection effect is dominant to the conduction with the hot zone. For achieving the temperature of 70°C, in this case, a total power of 850 mW was necessary (16 V, 49 mA), so an increase of the power dissipated of about 2000% with respect to the

corresponding case in vacuum. From this important result is evident that, in order to reduce the required heating power, an efficient thermal insulation of the package is required.

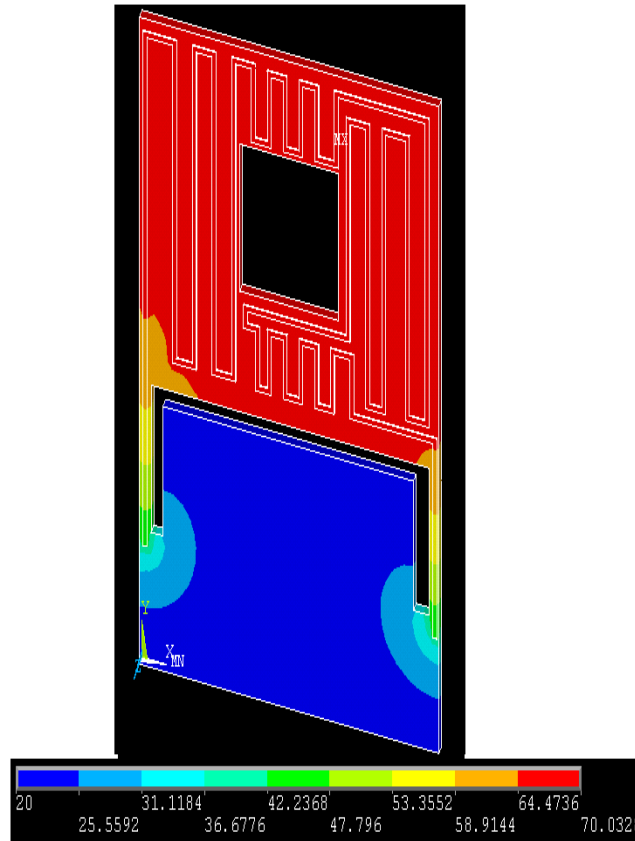


Figure 5. 9: Result of the thermal simulation when the module is in contact with air (convection loss).

5.5 Experimental Results

Finally, after the mathematical analysis and the finite-element simulations, we tested the module in the laboratory, to compare the experimental and the analytical results [241]. Different heating configurations were tested. First, in order to evaluate the importance of an efficient thermal insulation, conduction and/or convection loss were maximized:

1. The LTCC heating plate was held vertically and heated in open still air – CONF. A - free convection is maximized;
2. The LTCC module was heated when in contact with an Al block (thickness 20 mm) on the bottom layer and the top is in contact with open still air– CONF B, both conduction and convection loss are present;

3. The LTCC module was heated when in contact with an Al block (thickness 20 mm) on the top and the bottom layer – CONF C - conduction loss is maximized .

Figure 5. 10 illustrates the configurations tested.

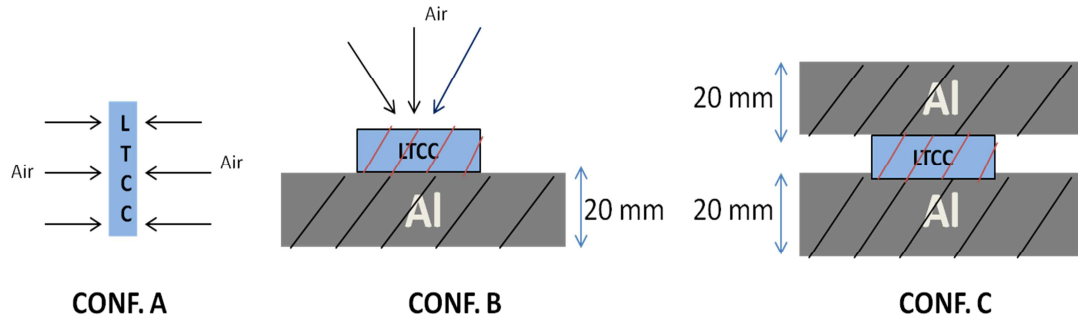


Figure 5. 10: CONF A: the convection loss is maximized. CONF. B: both convection and conduction losses are present. CONF. C, conduction loss is maximized.

The power required achieve 70°C at the hot zone was, as expected, very high in the three configurations. In particular, if we consider the result of the heating experiment of CONF. A, we can affirm that it is consistent with the simulation performed, because the required power to achieve 70°C at the hot zone was ca. 900 mW, a value very close to what we got through analytical calculations (850 mW). When the conduction is maximized, the losses are still higher, ca.20% more than the case of convection (CONF. A vs. CONF. C). Figure 5. 11 shows the results of the heating experiment:

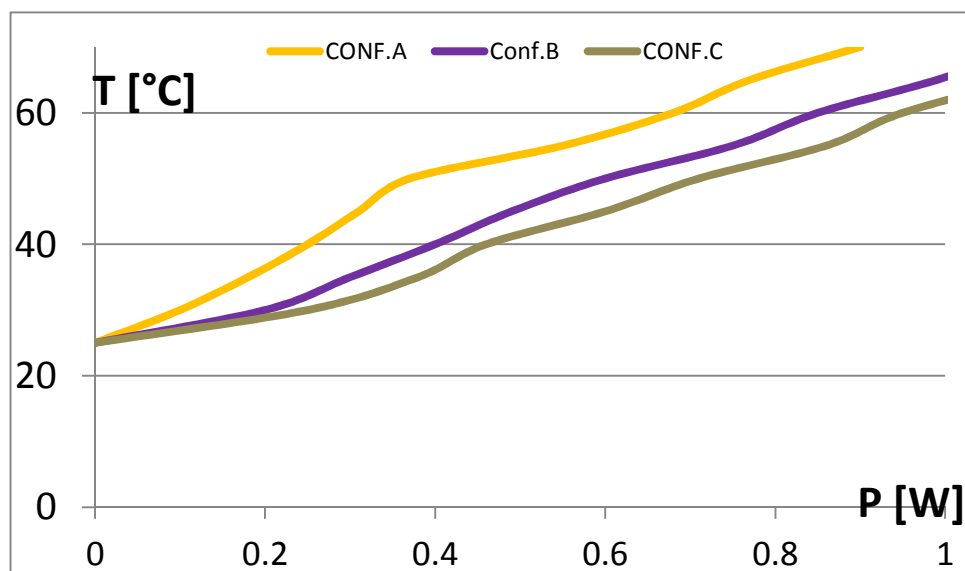


Figure 5. 11: The thermal performance of the LTCC module when it is not insulated and convection and / or convection loss are present.

From this result it is again evident that the module must be efficiently thermally insulated, in order to reduce or eliminate the thermal losses and get a heating performance satisfactory. The idea to reduce the losses is to surround the LTCC module of an insulating material, which would reduce the effects of convection because of its low thermal conductivity, and eliminate or significantly reduce the convection (depending on the porosity of the insulation). Figure 5. 12 shows the heating configuration tried.

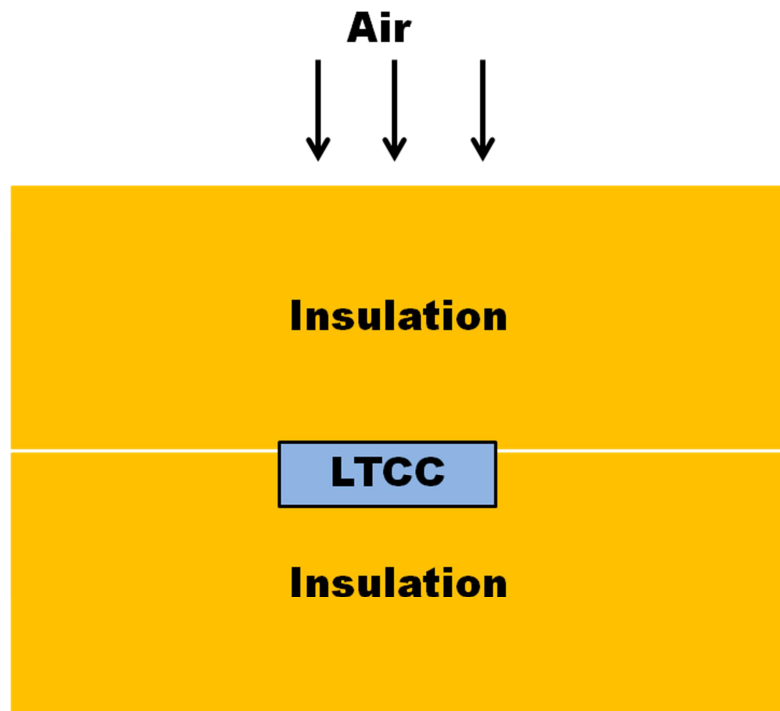


Figure 5. 12: The heating configuration tested to minimize the losses and to get a good heating performance.

5.5.1 Thermal conductivity measurement system

In order to find out the best insulating material to use, we developed a system able to measure the thermal conductivity of samples consisting of large-cell foam.

The platform developed for thermal conductivity measurement is depicted in Figure 5. 13.

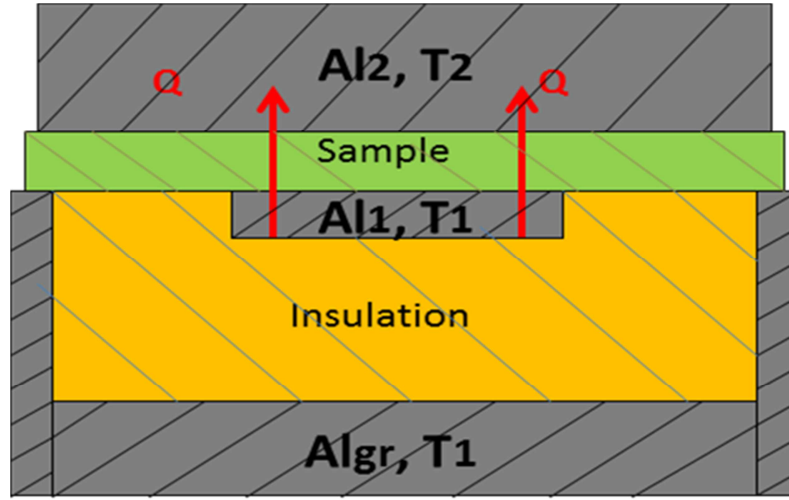


Figure 5.13: Platform for measuring the thermal conductivity of materials.

The developed platform consists of two heated aluminum blocks (Al_1 and Al_2), with the sample placed in between. Both aluminum blocks are thermally regulated to a well-defined temperature (T_1 and T_2). The system is designed so that the only thermal flux Q (Figure 5.13, red arrows) possible is the one going from the inner block to the top block. For this purpose, there is a "guard envelope" (Al_{gr}) all around Al_1 , kept at the same temperature T_1 as Al_1 , yet physically separated from it by insulating foam. Since Al_{gr} and Al_1 are kept at the same temperature and thermally insulated from each other, no parasitic heat flow occurs between them, ensuring the heating power on Al_1 truly corresponds to the thermal flux Q . Therefore, knowing Q and temperatures T_1 and T_2 , the thermal conductivity k of the sample is calculated using Fourier's law:

$$Q = - \frac{k \cdot (T_1 - T_2) \cdot S}{h} \quad \text{Eq. 5.17}$$

In equation (1), Q is the heating power given to Al_1 , k the thermal conductivity of the sample, S the cross sectional area of the sample and h the thickness of the sample.

With respect to other methods for measuring the conductivity [242], [243] this system offers the following advantages:

- 1) It allows the use of insulating material basically "as is", with no need to adjust size.
- 2) It is not sensitive to coarse-structure materials such as large-cell foams.

5.5.2 Best heating performance – experimental configuration

The experimental configuration that gave the best heating performance was the one illustrated in Figure 5.12. The LTCC is surrounded by a 20 mm layer of low-density, rigid, insulating foam, the Rohacell 51HF [244]. We measured the thermal conductivity of the

foam using the system illustrated in Figure 5. 13, and we got $k = 0.038 \text{ W} \cdot \text{m}^{-1} \cdot \text{K}^{-1}$. An alternative solution is to use plywood instead of Rohacell. Plywood is easier to find with respect to Rohacell, but its thermal conductivity is higher: we measured it using the platform illustrated in Figure 5. 13, and we got $k = 0.14 \text{ W} \cdot \text{m}^{-1} \cdot \text{K}^{-1}$. This higher thermal conductivity will introduce additional conductive loss (conduction with of the LTCC heating plate with the plywood insulation is higher). We compared the heating performance of the module, when surrounded by 20 mm of Rohacell 51HF and when surrounded by plywood. The comparison is showed in Figure 5. 14

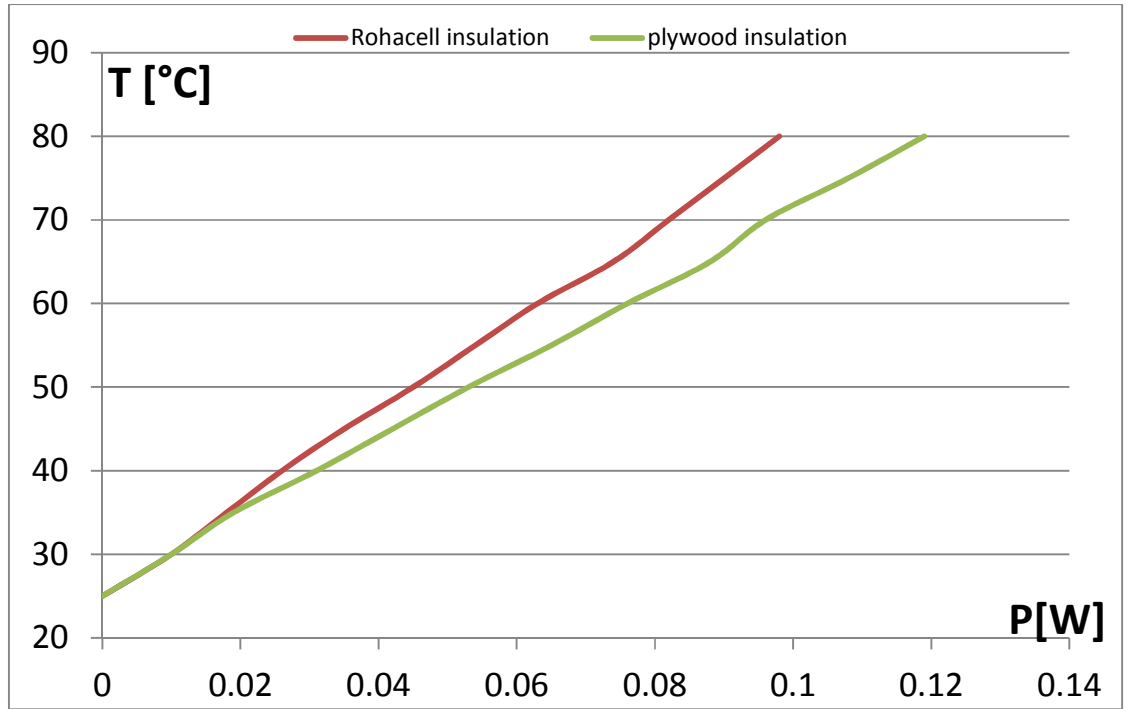


Figure 5. 14: The thermal performance of the LTCC module when it is efficiently insulated with Rohacell foam (red curve) or with plywood (green curve).

As expected, the Rohacell insulation allows obtaining a better result: 70°C were achieved with a power of ca. 80 mW, while the same module, insulated with plywood, achieved the 70°C using a heating power of 100 mW, yielding an increase of heating power of 20%. The heating performance obtained is acceptable, because it is low enough to be used in microsystems with total power consumption of ca. 500 mW. Moreover, if a further improvement of the performance is needed, it is possible to put the sample, surrounded by the Rohacell foam, in low-pressure atmosphere, instead of open still air. In this case, the conduction loss is further minimized; the lower is the pressure inside the chamber, the longer will be the mean free path of air molecules. So by reducing the pressure it is possible to reduce the conduction loss, provided the mean free path exceeds the foam pore size. In the laboratory, with our instrumentation, we were able to reduce the pressure down to 16 Pa (mean free path $\approx 0.4 \text{ mm}$), and repeating the experience in this low-pressure atmosphere, we

got an improvement of the performance at high temperatures of ca. 15% (Fig. 5.15). In low-pressure atmosphere, with the module surrounded by 20 mm of Rohacell foam, we were able to get 70°C using ca. 70 mW of heating power. This corresponded to the best heating performance we were able to achieve in the lab.

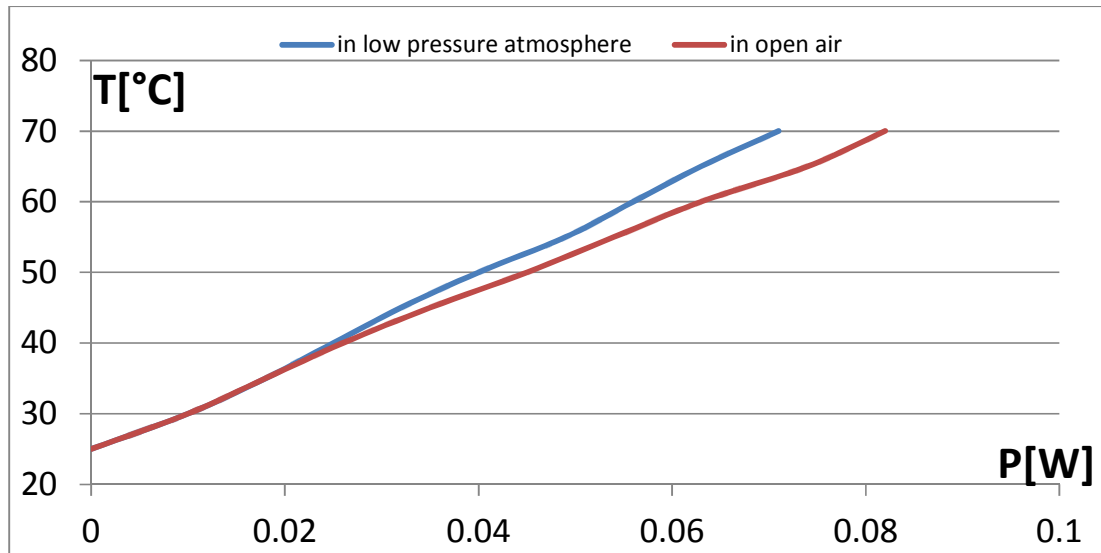


Figure 5. 15: Comparison of the heating performance: the same experimental configuration, repeated in low-pressure atmosphere, shows an increasing of the performance due to a decrease of the convection loss.

5.5.3 Comparison between the best heating performance and the ideal one

Finally, it is interesting to compare the best performance obtained in the laboratory (module surrounded by Rohacell foam, in low-pressure atmosphere), with the ideal one, obtained using the finite-element simulations. The ideal case is when the module is in perfect vacuum and there are no losses other than the conduction through the small external bridges. Figure 5. 16 shows this comparison.

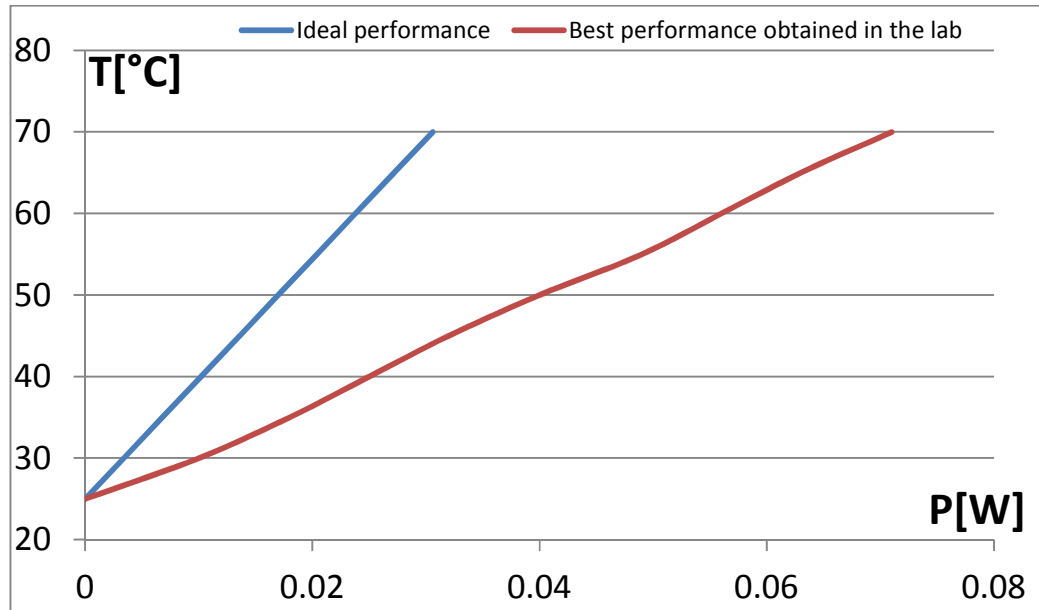


Figure 5. 16: Comparison between the ideal performance calculated using finite-element simulations and the best performance obtained in the lab.

The difference of the performance obtained in the lab with the ideal one is evident, as highlighted in Figure 5. 16. The losses present in our laboratory configurations are:

- Conduction loss from the LTCC through the foam material. The conduction of the foam structure, even if low, exists.
- Conduction loss by gas: the residual gas molecules still causes an additional conduction loss, which may be further reduced by further decreasing the pressure inside the chamber.
- Radiation loss: we did not consider the radiation loss, which is of course present and plays a role in the heat transfer

5.6 Discussion of the Results

The last comparison in Figure 5. 16 shows that theoretically there is still room for further improvement of the heating performance, by further reducing the pressure. However, this experimental configuration is associated with extra manufacturing difficulties and costs, due to the necessary hermetic packaging. The best practical heating configuration tested that can be used without resorting to this technique is the one in Figure 5. 12, when the module is surrounded by a 20 mm layer of Rohacell foam. This configuration offers a heating performance which is good enough (70°C were achieved with 80 mW of power) for most applications included in the present work. Finally, LTCC technology is a very elegant solution for the packaging of microsystems, as it offers the possibility to integrate various functions in one unique module; LTCC is also a low-cost solution, because cost production

of LTCC is moderate, and it is possible to make a batch series production, drastically decreasing the manufacturing cost. Finally, LTCC is also an acceptable platform in terms of power required for the heating, if the packaging is efficiently insulated.

5.7 Conclusions

In this chapter, an LTCC heating platform is presented. This heating platform will be used to temperature stabilize and interconnect the key components of the atomic clock and may be eventually integrated in any other microsystem to provide local temperature control. The module was designed to be flexible enough to be used in different applications, as it can be easily plugged into a PCB support, simply using a standard DIL connector. Since one of the key parameters of microfabricated systems and portable devices is that their power consumption must be kept at the minimum, we investigated the heating power required to achieve a temperature of 70°C in various configurations of the module and estimated the impact of the convection and conduction losses to the power consumption. First, a physical/mathematical analysis was performed, in order to estimate the minimum amount of power required in the ideal situation, when all conduction, convection and radiation loss from LTCC to the external world are zero. Then, in order to validate our analysis, finite-elements simulations were performed hypothesizing the same situation, and the results were consistent with the analysis. The thermal simulations highlighted the importance of thermally insulate the LTCC module to get a satisfactory heating performance, because when free convection was introduced into the model, the increase of the power was drastic. Finally, we made experiments in the laboratory, which proved again that if convection and conduction are not reduced, the power required for heating is very high. We found a good experimental configuration, by efficiently thermally insulating the module, yielding to a satisfactory heating performance. The best heating performance that we got is still far from the ideal performance calculated by the finite-element simulations; this means that there is still room for further improvement. This difference is mainly due to the fact that in the finite-element simulations we hypothesized the ideal case, i.e. in complete vacuum, so no convection loss. In the experience made in the lab, convection was present, even if it was limited by the insulating foam which surrounded the module. As we can see from the last experience (Figure 5. 16), we got a significant improvement of the performance by repeating the same experience in low-pressure atmosphere. By further reducing the pressure, it is possible to further approach the curve of the obtained performance with that of the ideal one; the two curves will overlap in case we are able to repeat the experience in complete vacuum.

6 Packaging Solutions Provided for Microsystems

This chapter illustrates the different microsystems that we contributed to improve by providing new packaging solutions. We contributed to reduce the size and/or the power consumption of the microsystems, or, in alternative, we contributed to make the microsystem working properly ensuring proper interconnection and precise temperature control of the different components.

6.1 Introduction

During this thesis, we faced many challenges related with the development of specific microsystem packaging solutions. We designed and fabricated different modules for the packaging of the miniature atomic clock and for other side products (see the following for more details about the side products). For each case, according to the particular needs of the user, we used LTCC, thick-film or PCB as the base, or, sometimes, a combination of the various technologies. In particular, we provided intelligent packaging solutions for the following microsystems:

- A frequency-stabilized laser source/module (which can be used as light source for the miniature atomic clock);
- A Rb mini-lamp system integrating the lamp and the conditioning LC circuit (that can also be used as light source for the miniature atomic clock);
- A Rb miniature atomic clock DR reference cell / resonator cavity module.

6.2 The Frequency-stabilized Laser

Laser sources with accurate frequency stability are widely used and necessary in many applications, such as interferometric detection, spectroscopy [245], optical communications, atomic magnetometers [246] and atomic clocks [67], [70]. Moreover, they are also used in commercial applications, such as precision machining tools, laser vibrometers [247] and gravimeters [248]. In such applications, on one hand, there is the need of reducing the power consumption and the dimensions of the laser source, in order to facilitate the fabrication of portable devices; on the other hand, the demand for highly-stable laser sources is rapidly increasing, with the ever more widespread diffusion of applications based on, e. g. high-resolution spectroscopy or precise navigation systems using atomic clocks [249]. The main components of this system are a Vertical-Cavity Surface-Emitting Laser (VCSEL) [250], [251], a reference cell which contains metallic Rb or Cs vapor, and a photodetector. The beam is directed towards the reference cell by a beam splitter, and precisely locked at the frequency of absorption line of the atoms of the alkali metal; the output of the system is the

beam with a fixed frequency. An existing system, but with a different layout and packaging solution, was already developed by our project partners of LTF (*Laboratoire Temps-Fréquence*) – University of Neuchâtel, and was also presented [252]: the total volume of the existing system was ca. 1.5 dm^3 , and its frequency stability in terms of Allan deviation was 5×10^{-10} for an observation period of 1 s; our goal was to introduce new packaging ideas to improve the original design in terms of dimensions, power consumption and/or performance. In order to accomplish this objective, we decided to control the temperature of the VCSEL laser diode and of the reference cell using our LTCC multifunctional heater device described in Chapter 5. The LTCC heating module designed and presented in Chapter 4 perfectly fits for this application, as, how explained, it has been designed to control the temperature of any device in the cm scale; the dimensions of the VCSEL and of the reference cell are within this range. The total weight of the two elements (VCSEL and reference cell) is less than 10 g, so the LTCC heating plate is able to withstand without rupture risk due to the weight. Both elements can be glued using a thin layer of silicone adhesive (Dow Corning Q5-8401) onto one LTCC heating module. The photo-detector, which does not need any temperature regulation or interconnection, can be attached/plugged on a simple PCB support using standard connectors. The three modules are mounted vertically, together with the beam splitter, on a horizontal support PCB, which acts as a carrier for the whole system and also carries the required electronics for temperature measurement (Wheatstone bridge using the PTC on the LTCC module as sensitive element coupled with a first pre-amplification of the temperature signal) and transimpedance amplifier for the photo-detector. Standard DIN connectors are used to vertically connect the various modules to the main PCB. Figure 6. 1 shows a 3D block diagram of the original packaging idea of this system. The total dimensions of the designed PCB are $70 \times 40 \text{ mm}^2$. The total volume of the assembled device is ca. 0.14 L [253], a photo of which is shown in Figure 6. 2 and can be compared with the block diagram in Figure 6. 1.

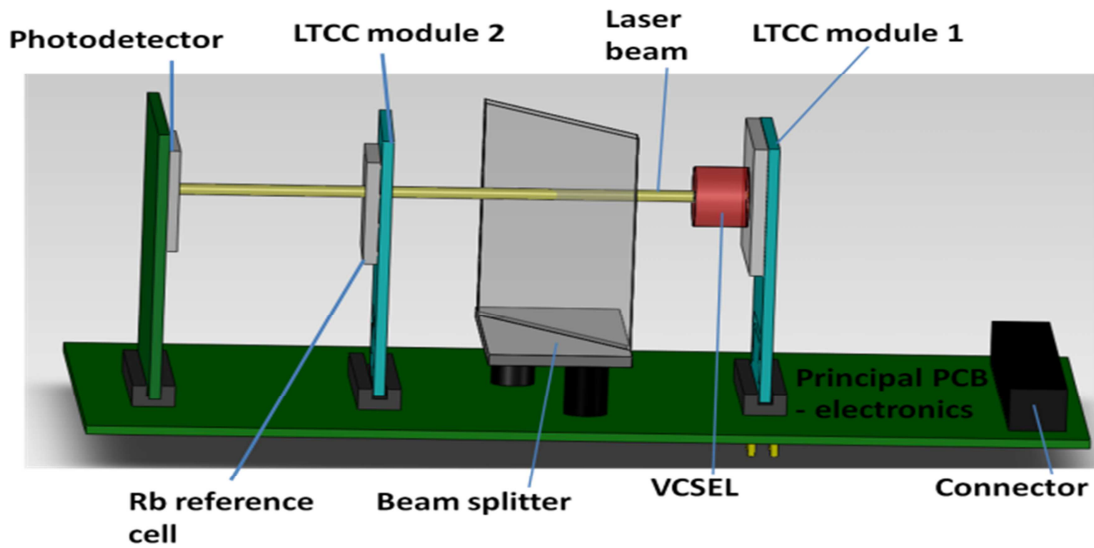


Figure 6. 1: 3D block diagram of the stabilized laser.



Figure 6. 2: Picture of the assembled stabilized laser with: (1) laser, (2), beam splitter, (3), Rb cell, (4), photodetector.

After manufacturing and assembly of the modules and the main circuit, the device was tested at the *Laboratoire Temps-Fréquence* (LTF) of the University of Neuchâtel. The tests were performed by Mr. Gruet and Dr. Affolderbach, our project partners. Using the LTCC modules to heat the VCSEL and the reference cell at different temperatures, and also changing the optical light power emitted by the VCSEL, we were able to find out the best

experimental configuration which allowed getting high stability of the output signal, i.e. allowed minimizing the sensitivity of the stabilized laser frequency to external variations. A VCSEL temperature of 48°C, a cell temperature of 104°C and a light power through the cell of 40 μ W are identified as best operation parameters for optimized frequency stability. With this configuration, a stability of 1.3×10^{-10} at 1 second and $\leq 8 \times 10^{-10}$ up to one day for ^{85}Rb is obtained by our stabilized laser [253]. This result is up to a factor of four better, depending on the timescale, than previously reported results obtained with a significantly larger setup [252]. The dissipated power for the heating of the laser at the optimum temperature of 48°C and the cell to its optimum temperature of 104°C has been measured to be 75 mW and 920 mW, respectively. Thus, the assembled laser system shows low heating power consumption with less than 1 W for the laser and the cell. This dissipation, which can be further reduced by improving on the system's thermal insulation, is anyway heavily reduced with respect to the layout previously presented, which had a power consumption of several watts. Therefore, thanks to the introduction of the LTCC modules to precisely control the VCSEL and the reference cell temperatures, a considerable improvement of the performance of the system is observed with respect to the previous layout: in fact, the stability of the output signal is improved of a factor of four, and the dimensions and the power consumption of the device have been considerably reduced. The temperature variation of the reference cell has been estimated to be ca. 0.05 K over one day; this value still remains quite high for our requirements. This might be possible considering the fact that the cell in this layout is heated on one side only (see Figure 6. 2, photo of the assembled system), and it is not perfectly thermally insulated, so temperature gradients across the cell may be present. Future work in this sense can be improving the precision of the temperature control of the cell, achieving a maximum drift of 0.01 K. This is possible by adding an efficient thermal insulation around the cell. With such a precise temperature control, the long-term stability limit for the laser frequency may be reduced to around 5×10^{-11} .

6.3 Integrated Mini-lamp Module

Rb vapor discharge lamps (typically spherical, inductively-coupled and glass-blown) are widely used in compact ($100\text{-}1000\text{ cm}^3$) double-resonance atomic clocks and atomic magnetometers for their intrinsically stable and long-term reliable optical pumping for high precision time-keeping and measurement accuracy [254]. With the increasing interest in chip-scale ($< \text{few cm}^3$) DR clocks [255], that would significantly improve the performance of various portable device applications including GPS receivers, there is an active effort in developing a compact, low power, easily integrable and long-term stably emitting Rb discharge lamp and use it as light source for the system. The use of Rb mini-lamp as light source for atomic clocks would bring the following advantages with respect to VCSELs or inductively-coupled glass blown discharge lamps [256]:

- VCSELs systems are extremely sensitive to temperature and ageing effects [257].
- Rb mini-lamp needs a simpler drive circuitry than that of the inductively-coupled lamps and make way for a highly space and power efficient module.
- The Rb mini-lamp needs an LC circuit for impedance matching; moreover, both the Rb cavity and the LC circuit must be temperature-stabilized. Table 6. 1 shows the components of this microsystem, their rough dimensions, and the working temperature.

Component	Dimensions	Working temperature
Rb Dielectric Barrier Discharge lamp (DBD lamp)	$10 \times 10 \text{ mm}^2$	110°C
LC electronics circuitry	$6 \times 5 \text{ mm}^2$	$\approx \text{room temperature}$

Table 6. 1: The components of the microsystem under investigation, their dimensions and working temperatures.

This work was carried out in strict collaboration with our project partners of LMTS (Laboratory of Microsystems for Space Technology) - EPFL. Before our intervention, they already developed, tested and optimized a Rb DBD light source, to produce power-efficient and short-term stable Rb D line power [258]. However, their layout had a volume of several dm^3 : our principal objective in this project was to develop an efficient and integrated solution to control the temperature of the DBD light source at a high enough temperature (typically 100-130 degree Celsius; Rb vapor density increases with increase in temperature) to emit long-term (several years) stable and high intensity of Rb D lines and reduce drifts in optical power. In order to integrate the mini-lamp and the LC drive circuit, which, as explained, must be kept at room temperature, we developed, together with V. Venkatraman and H. Shea of LMTS, a new version of our LTCC module [259], slightly different from the first version, including the SMD solder pads for the LC circuit. A photo of the developed LTCC module is shown in Figure 6. 3.

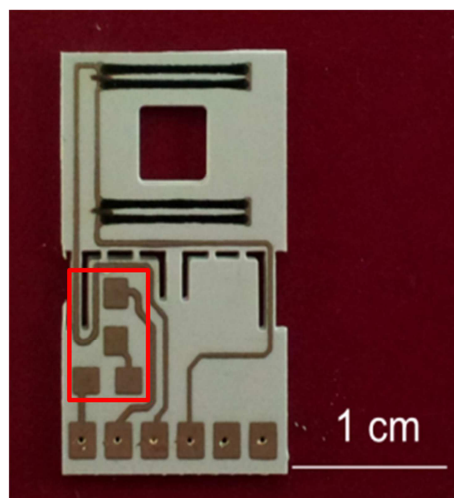


Figure 6. 3: The version of our LTCC module developed for the Rb mini-lamp packaging is equipped with solder SMD pads for the LC circuit (red rectangle).

As we can see in Figure 6. 3, the zone for the LC circuitry (red rectangle in Figure 6. 3) is thermally insulated from the hot zone, as there is an air gap of ca. 2 mm between the two zones. In this way, the bottom zone is kept cool, and insulated from the hot zone on the top (where the black resistors are placed). The module is operated through two connectors:

- SMA for the rf input power
- D-pin connector for heating and temperature sensing (Figure 6. 4).

The light source is powered at 11.5 MHz (hence requiring a high-frequency connector), which was found to be optimal for the test cell used in this system (Rb and 15 mbar Ar). The designed system, together with the control and the supply, is illustrated in Figure 6. 4.

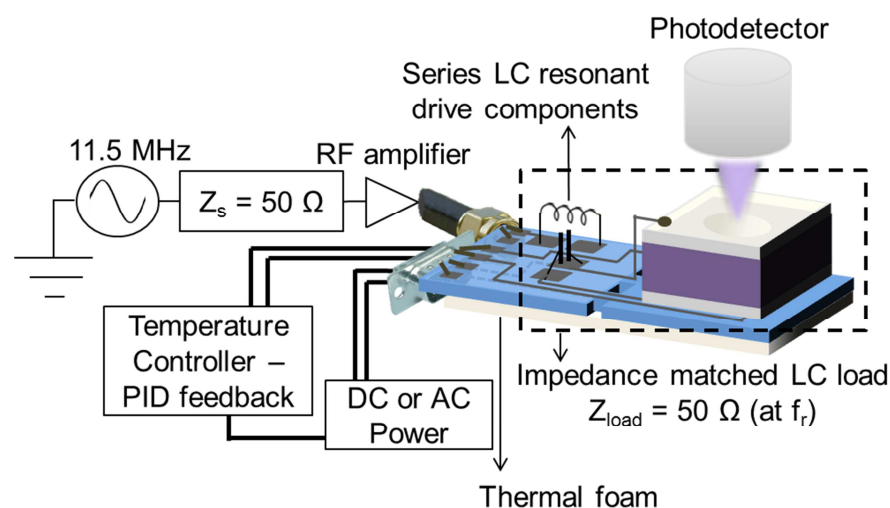


Figure 6. 4: Schematic of the module operation and test measurement setup, image taken from [258].

The system, as illustrated in Figure 6. 4, emitted Rb D2 (780 nm) lines and the temperature stability of the Rb lamp-cell recorded over time results constant and stable. The LTCC heater was powered by a DC source (total dissipated power was 1.42 W, 7.1 V, 0.2 A for 110°C); the temperature of the lamp was set and controlled using a PID feedback loop and fluctuations of less than 0.1°C were observed with time. The optical power was detected using a standard broadband silicon photodiode and a photodiode amplifier. The results show the capacity of the LTCC module to enable highly stable and long-term reliable optical pumping in miniature atomic clocks and other applications. The Rb DBD light source has also been observed to be very robust being ignited thousands of times and run continuously for several months without showing any degradation in the output power level. Moreover, the components of this system can be batch fabricated and the module can be independently used for optical pumping in other applications including magnetometers and gyroscopes. Finally, for this system, we significantly reduced the dimensions, integrating everything in a packaging of dimensions $15 \times 26 \times 4 \text{ mm}^3$, providing an elegant and efficient solution to integrate the RBD lamp, the temperature control and the LC drive circuit. The system is very stable and efficient.

6.3.1 Alternative Solution for the Packaging of the Rb mini-lamp

An alternative and more accurate packaging solution for this system was also provided. In this new configuration proposed, it is possible to individually temperature control the L and C components, because we integrated dedicated heaters and temperature controllers for each passive, in addition to the one for the lamp. In this way, it is possible to achieve a high LC series resonant quality factor and minimize the rf reflected power. The system is based on a PCB, which carries generic ceramic (thick-film on alumina) mini-heaters of dimension of $7 \times 4 \text{ mm}^2$. The mini-heaters, equipped also with a PTC thermistor for temperature measurement, are used as dedicated heaters for the L and C components; they are soldered by flip-chip on the carrier PCB. Photos of the system are shown in Figure 6. 5.

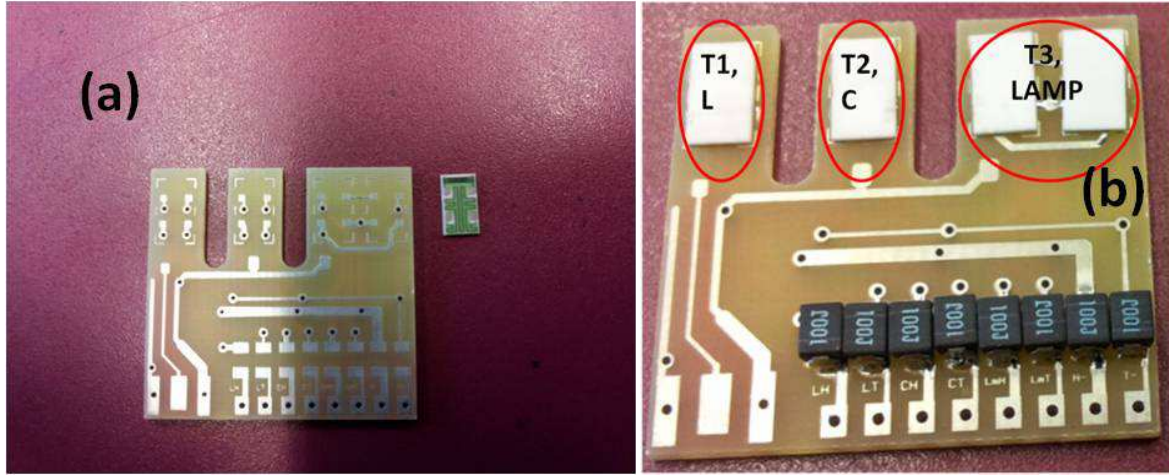


Figure 6. 5: (a), The PCB and the hybrid mini-heaters. (b), the mini-heater is soldered by flip-chip on the PCB, finally leading to the creation of three thermal zones (T1 for the inductor, T2 for the capacitor, T3 for the mini-lamp).

The PCB, because of its low thermal conductivity ($k \approx 0.25 \text{ W} \cdot \text{m}^{-1} \cdot \text{K}^{-1}$, [48]) is not only a support for the system, but it also has the function to thermally insulate the components from each other, by creating three different and well defined temperature zones (one for the inductor, one for the capacitor, one for the mini-lamp). The creation of the three different zones is further promoted by the geometry of the PCB: we created holes to further improve the thermal insulation and therefore creating the three different thermal zones. The inductors which are visible at the bottom of the PCB shown in Figure 6. 5 have the function to decouple the high-frequency noise from the DC part.

In order to test the system, we powered the first heater (T1, on the left hand side of the PCB) and monitored the temperatures of the three different thermal zones. The module was placed, horizontally and surrounded by a 20 mm layer of Rohacell foam, similarly to the heating configuration used for the LTCC module and shown in Figure 5. 12. The results are shown in Figure 6. 6.

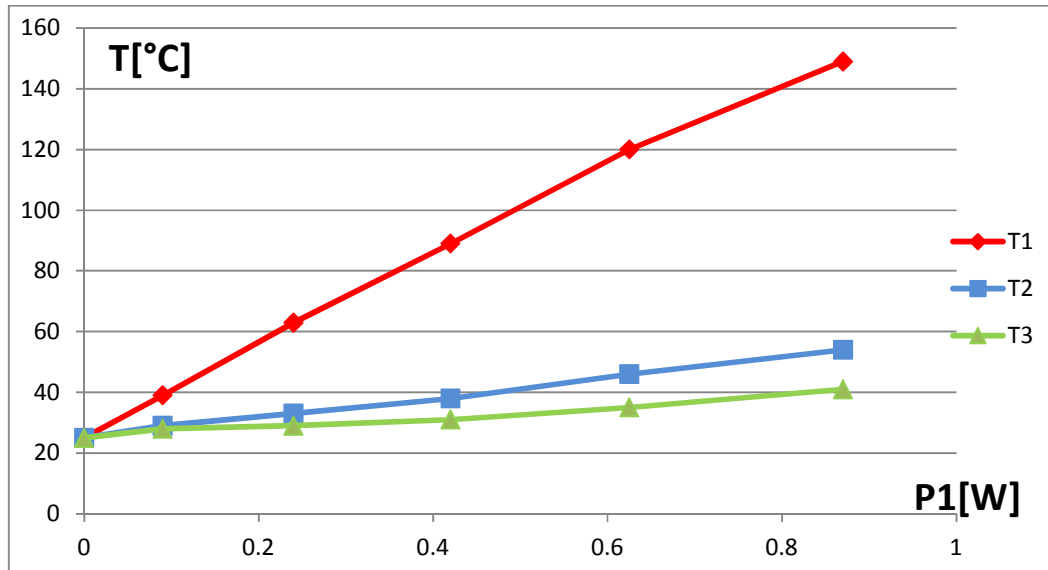


Figure 6. 6: Temperature of the three thermal zones, for different values of heating power (only T1 is supplied). The heating module is surrounded by a 20-mm layer of insulating foam to minimize the losses.

As we can see in the graph above, zone T1 achieved a temperature of 120°C, with a total heating power of 0.63 W, which means that we obtained ca. 50% reduction of the dissipated power with respect to the previous packaging configuration for this system (in which 110°C were achieved with a dissipated heating power of 1.42 W). Moreover, when the temperature of T1 was 120°C, T2 was at 46°C and T3 at 35°C; this means that the three thermal zones are efficiently thermally insulated from each other.

The second test was to power the central heater, T2, and to monitor the temperatures of the three thermal zones. Figure 6. 7 illustrates this result.

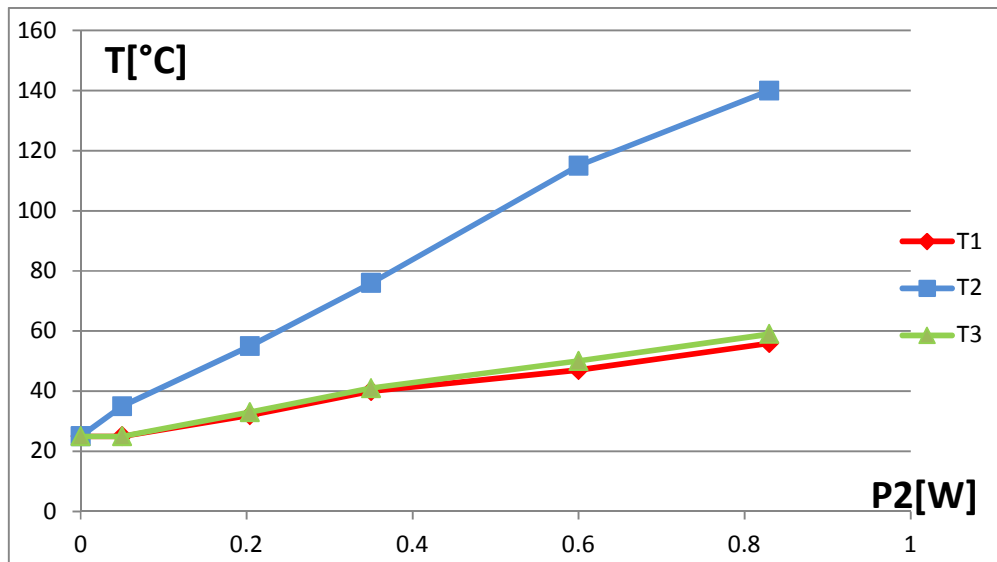


Figure 6. 7: Temperatures of the three thermal zones for different values of heating power (only T2 is supplied). The heating module is surrounded by a 20-mm layer of insulating foam to minimize the losses.

Chapter VI: Packaging Solutions Provided for Microsystems

In this case, the power required to achieve a temperature at T2 of 120°C was again around 0.62 W, while T1 and T3 remained at a temperature of around 50°C; this means that the thermal insulation provided between the thermal zones is efficient. Finally, we powered T3, and monitored the temperatures of the three zones for different values of power.

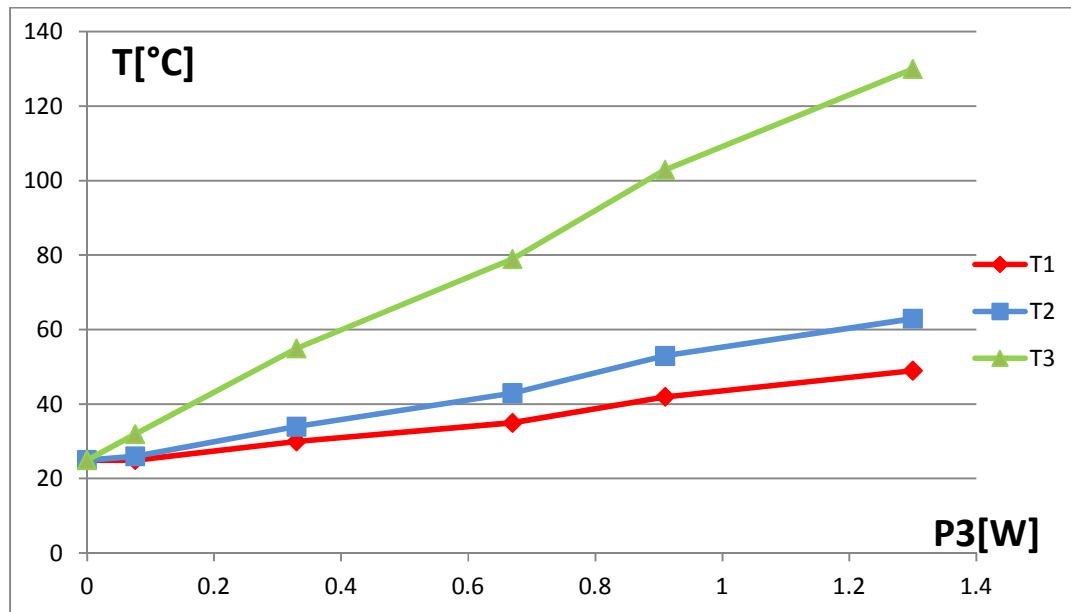


Figure 6. 8: Temperature of the three thermal zones, for different values of heating power (only T3 is supplied). The heating module is surrounded by a 20-mm layer of insulating foam to minimize the losses.

Also in this case we again note an efficient thermal insulation provided by the air gaps between the three thermal zones, because when T3 is heated up at 130°C (1.25 W), T2 is at 60°C and T1 at 50°C.

This new solution gives the possibility to control three temperatures separately, to find out the best temperature of the LC circuit yielding to a high quality factor. Moreover, because of the presence of mini-heaters that locally heat each component, the heating power is sensibly reduced (ca. 50% with respect to the first solution).

For zone T3 (lamp), two small heaters are used, instead of a larger one, a solution which was selected for two reasons:

- 1) The heaters remain generic; local hotplates may thus be created with a wide degree of freedom, without having to resort to many different design-specific components.
- 2) Due to the large thermal mismatch between PCB and alumina (CTE of FR-4 PCB material is ca. 15 ppm/K, while that of Al_2O_3 is 6 ppm/K), soldering large alumina heaters on PCBs is not advisable, especially if thermal cycling is to be expected. Note that solutions for better CTE matching exist, e.g. by using insulated steel substrates instead of alumina, but are somewhat more costly.

6.4 Miniature Double-Resonance Atomic Clock

The DR atomic clock, its principle of operation and its principal components, is already described in chapter 2. We developed a full working demonstrator of DR atomic clock. This work was performed in strict collaboration with our project partners; each laboratory had its own role and objective in the project, and in particular:

- LTF (Laboratoire Temps-Fréquence), from University of Neuchâtel, was the group that coordinate the project, providing their expertise on all aspects of the atomic clock microfabrication;
- LMTS (Laboratory of Microsystems for Space Technology), from EPFL, had the objective of developing a microfabricated Rb discharge light source (Rb mini-lamp);
- SAMLAB (Sensors, Actuators and Microsystems Laboratory), from EPFL, worked on the development of Rb reference cells, both anodically bonded (high-temperature) and Indium bonded (low-temperature)
- LEMA (Laboratory of Electromagnetic and Acoustics), from EPFL, focused on designing and developing an innovative microwave cavity
- LPM (Laboratoire de Production Microtechnique), from EPFL, which is our laboratory, worked on the fabrication of Rb cells (solder technique, described in chapter 3), and on the packaging of the overall device.

The atomic clock is a complex system, and providing an efficient packaging solution for it is really challenging, because many are the requirements to meet: its key components (light source, Loop-Gap Resonator cavity with reference cell inside, photodetector) must be stacked and precisely aligned on top of a support; some of the components (in particular the light source and the reference cell) need a precise temperature regulation (with a stability of 0.01 K). Moreover, the size and the power consumption of the final device should be kept at the minimum, to allow its portability: the maximum power consumption allowed to temperature-stabilize a component of the atomic clock was 100 mW. The original idea for the packaging of this complex system was to control the temperature of each component separately, by using, for each of them, one of our standard LTCC heating platforms. The components to be stabilized can be easily attached on top of the developed LTCC using a thin layer of silicon glue. The final system is then built up by simply plug all the LTCC modules on a PCB support, which would provide the electronics for the temperature control. A schematic drawing of the original packaging idea is shown in Figure 6. 9.

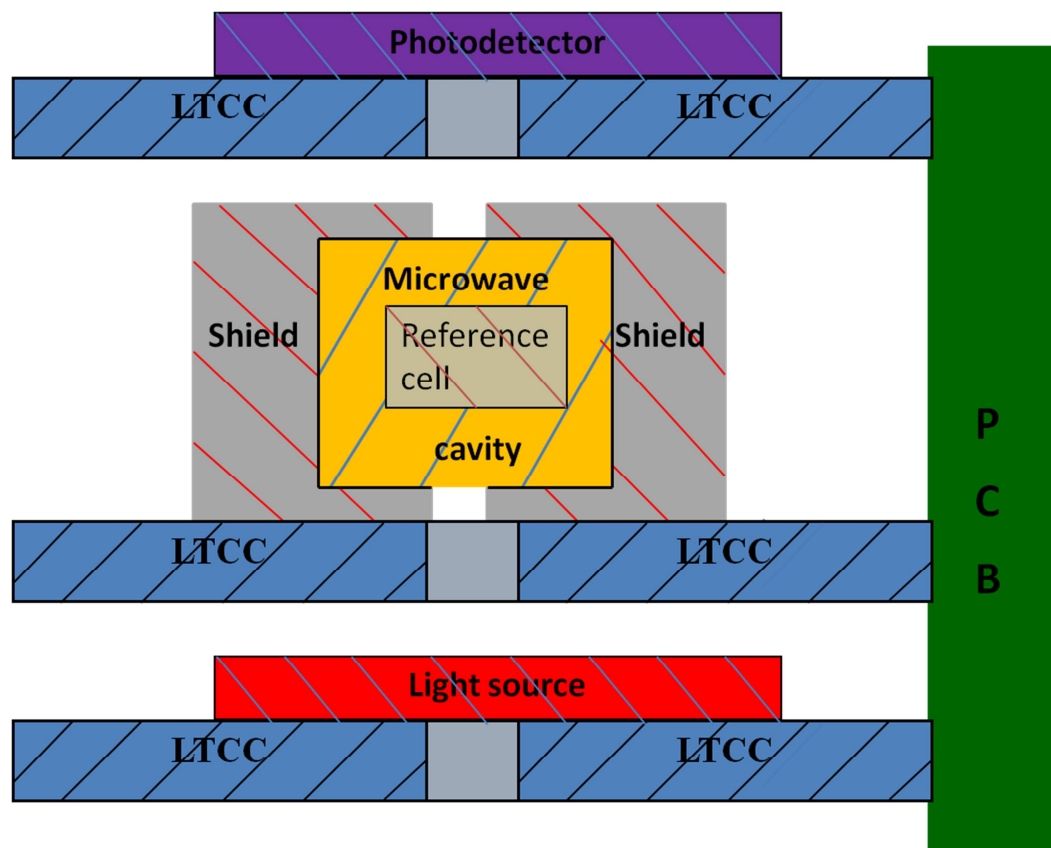


Figure 6. 9: The original concept idea for the packaging of the miniature atomic clock. The components are attached on a standard LTCC platform and then vertically stacked on a PCB support.

6.4.1 Refined packaging system for microwave cavity

The shield around the LGR cavity (which was designed and fabricated by LEMA, [260]) in Figure 6. 9 is needed to magnetically insulate the cavity from the rest of the system. In order to sustain the microwave field to be applied to the Rb atoms, in fact, the cavity has to be resonant with the $\nu_0 = 6.835$ GHz frequency of the ^{87}Rb hyperfine transition used as atomic reference in the DR Rb atomic clock (see Figure 2. 4), so it needs to be shielded from any static or low-frequency magnetic field. The magnetic shield consists of a cylinder of high-magnetic permeability metal (mumetal), which contains and surrounds the microwave cavity, as shown in Figure 6. 10. The mumetal used was an alloy composed (in weight %) of 80% Ni, 10% Fe, 6% Mo, 3% Cu and 1% other materials (Si, Mn); the relative permeability of the mumetal used was 200'000.

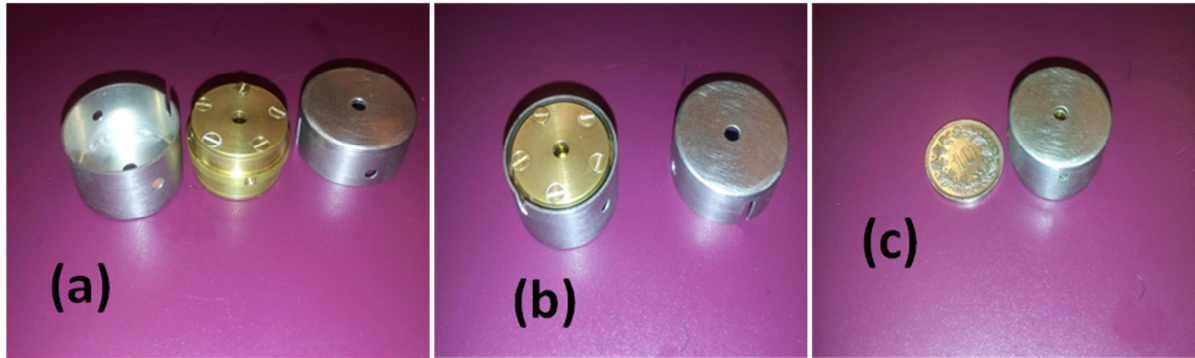


Figure 6. 10: The LGR cavity (the brass cylinder) is inserted into a magnetic shield, a cylinder made of mumetal.

Since the mumetal has a relatively low thermal conductivity ($k = 19 \text{ W} \cdot \text{m}^{-1} \cdot \text{K}^{-1}$), the system, as designed, does not allow a precise temperature control, as it would be impossible to keep the temperature constant on the entire surface of the mumetal cylinder. Therefore it was decided to add another 2 mm thick external aluminum ($k = 205 \text{ W} \cdot \text{m}^{-1} \cdot \text{K}^{-1}$ [236]) cylinder, which acts as a “thermal shield”: in fact, because of its high thermal conductivity and thickness, this cylinder essentially ensures a constant temperature in the whole LGR cavity, protecting it from possible external temperature influences.

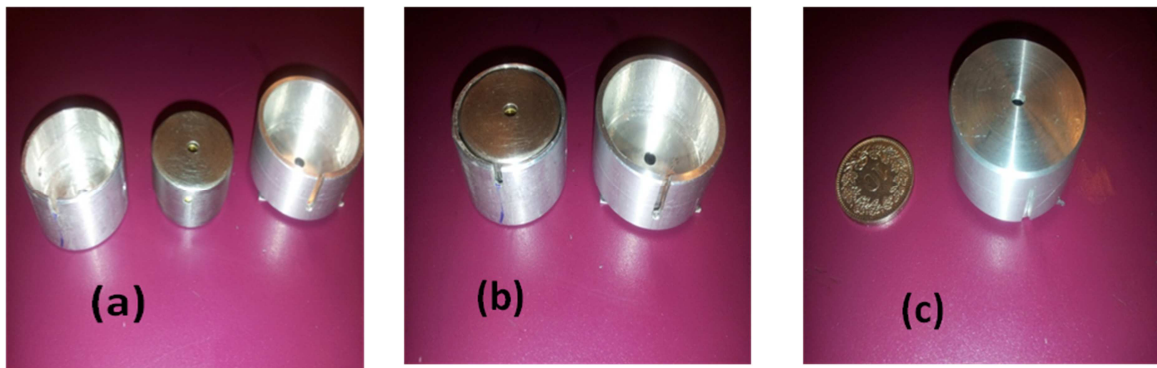


Figure 6. 11: The magnetic shield is inserted into another aluminum cylinder, which acts as thermal shield for the system.

With the additional magnetic shield, and the external aluminum cylinder, the system became relatively large in volume (ca. 15 cm^3), therefore it was decided to heat the cylinder from the top and bottom side, using two separate heaters. In this way, the temperature gradient was reduced, allowing a more homogeneous distribution of the temperature along the cavity. Another issue was the weight of system to mechanically attach and temperature-stabilize: the external aluminum cylinder, with the mumetal and the cavity inside, weigh 90 g altogether. This weight is too much for our standard LTCC heating platform, because, as already explained in paragraph 1.2, LTCC is limited by its low flexural strength ($\sigma_f \approx 300 \text{ MPa}$) and

brittleness (rendering the device too sensitive to mechanical shock). To overcome this problem it was decided to use another module in substitution of our standard LTCC to carry this bulky reference cell / LGR cavity / shield assembly. The heating system, in analogy with the second solution provided for the packaging of the Rb DBD lamp, is based on a PCB of thickness of 1.6 mm, with the heating and temperature measurement functions performed by 5 ceramic mini-heaters of the same type than those used for the heating of the Rb DBD lamp. The heaters are assembled by flip-chip soldering on the carrier PCB. On top of the heaters, the aluminum cylindrical "thermal shield", containing the mumetal cylinder and the microwave cavity, can be adhesively bonded. The heating, as already explained, is performed at both ends of the cylinder, in order to minimize the temperature gradient along the system. Figure 6. 12 shows a schematic drawing of the packaging concept of the microwave cavity, and of the developed PCB and mini-heaters.

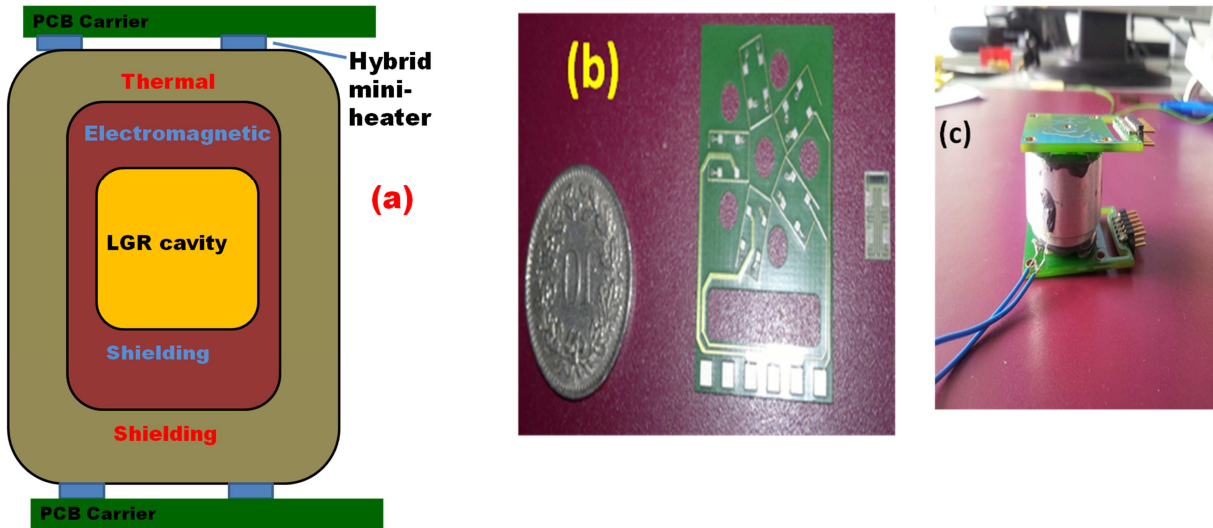


Figure 6. 12: (a), The refined packaging/temperature control concept of the Loop Gap Resonator (LGR) cavity; (b), The PCB and the hybrid mini-heater developed to control the temperature of the Loop Gap Resonator (LGR) cavity.; (c), A photo of the assembled system; the aluminum cylinder contains the electromagnetic shield and the LGR cavity. In this case, several Pt1000 thermistor elements glued on the surface of the aluminum cylinder were used to monitor the temperature and testing the performance of the system.

Again the PCB, with its low thermal conductivity ($k \approx 0.25 \text{ W} \cdot \text{m}^{-1} \cdot \text{K}^{-1}$), has not only the function to carry the system, but also to thermally insulate the heated zone, where the mini-heaters are soldered, from the cold zone, while ensuring electrical interconnection to the main PCB of the atomic clock. In line with the considerations in section 1.2, the use of several small heaters is also recommended in order to limit the stress due to the thermal mismatch between FR4 and Al_2O_3 . In this case the use of several heaters may introduce additional mismatch between the ceramic modules and the Al shield, but this can be easily taken up by using thermally conductive, but flexible, silicone adhesive. Finally, the system

was tested, hypothesizing a typical configuration used in atomic clocks: the system, plugged to the principal PCB, is covered with a cap of insulating material. The used cap was simply cardboard ($k = 0.18 \text{ W} \cdot \text{m}^{-1} \cdot \text{K}^{-1}$), placed on top of the assembled system as shown in Figure 6. 12c in order to limit free convection of air around the device. Then, we powered the heater and the temperature was monitored using several Pt1000 thermistors glued at different zones of the cylinder, in order to make sure that the temperature was homogeneous along the surface of the thermal shield.

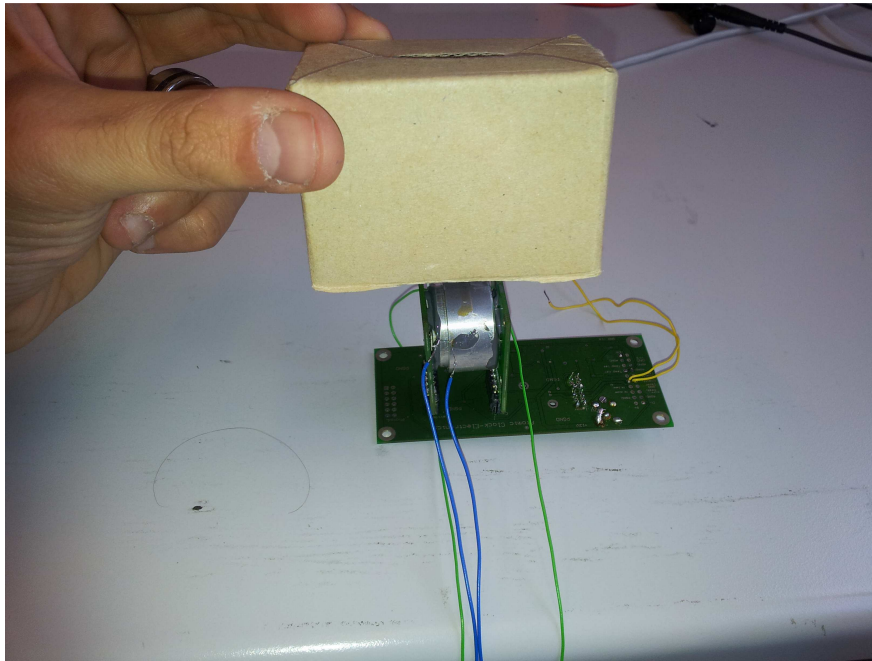


Figure 6. 13: For testing the LGR cavity heating system, we covered it with a cap of insulating carton in order to limit the convection with air. Then, we powered the heater and monitored the temperature at different zone of the cylinder using some Pt1000 resistors.

After having waited enough time to let the system stabilize (ca. 30 minutes), the values of resistance of the Pt1000 was the same, or in some cases there was just a difference of 2 or maximum 3Ω (corresponding to a change of 0.8°C); this means that the thermal shield essentially allowed a homogeneous distribution of the temperature along its surface. Figure 6. 14 shows the temperatures achieved on the surface of the cylinder for different values of heating power.

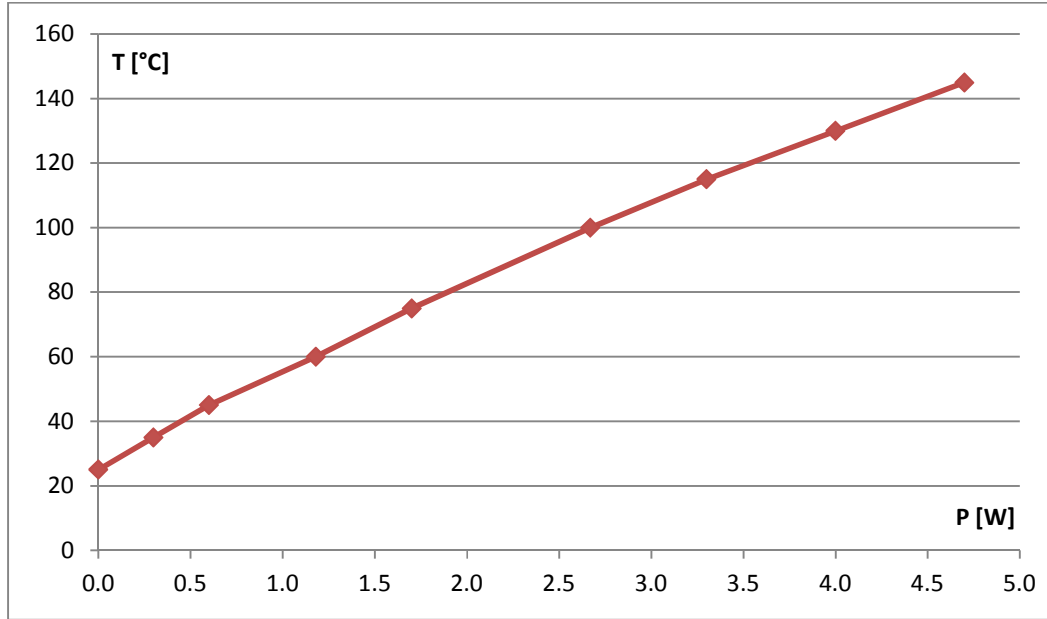


Figure 6. 14: The graphic temperature – heating power for the LGR cavity heating system.

We can see from the above graph that this heating system achieved a 70°C typical working temperature of the LGR cavity using ca. 1.6 W of heating power, when insulated as shown in Figure 6. 13. This is a satisfactory performance considering that the cavity is quite a bulky device. The equivalent thermal conductance C_{ref} of the complete reference cell / LGR cavity assembly module, which is the slope of the curve of Figure 6. 14, is given by:

$$C_{ref} = \frac{dP}{dT} = 40.2 \text{ mW/K} \quad \text{Eq. 6. 1}$$

6.4.2 The assembled miniature atomic clock demonstrator

In analogy with the frequency-stabilized laser, we decided to assemble the elements vertically (edge-wise), on top of a horizontal principal PCB, which carries all the necessary electronics. Also, as previously done for the frequency-stabilized laser, the photodetector can be simply attached on a PCB support, since it does need temperature regulation. The refined 3D schematic concept of the system is illustrated in Figure 6. 15. Finally, the system, as designed and illustrated in Figure 6. 15, was assembled, together with all the project partners. A photo of the atomic clock demonstrator is shown in Figure 6.16.

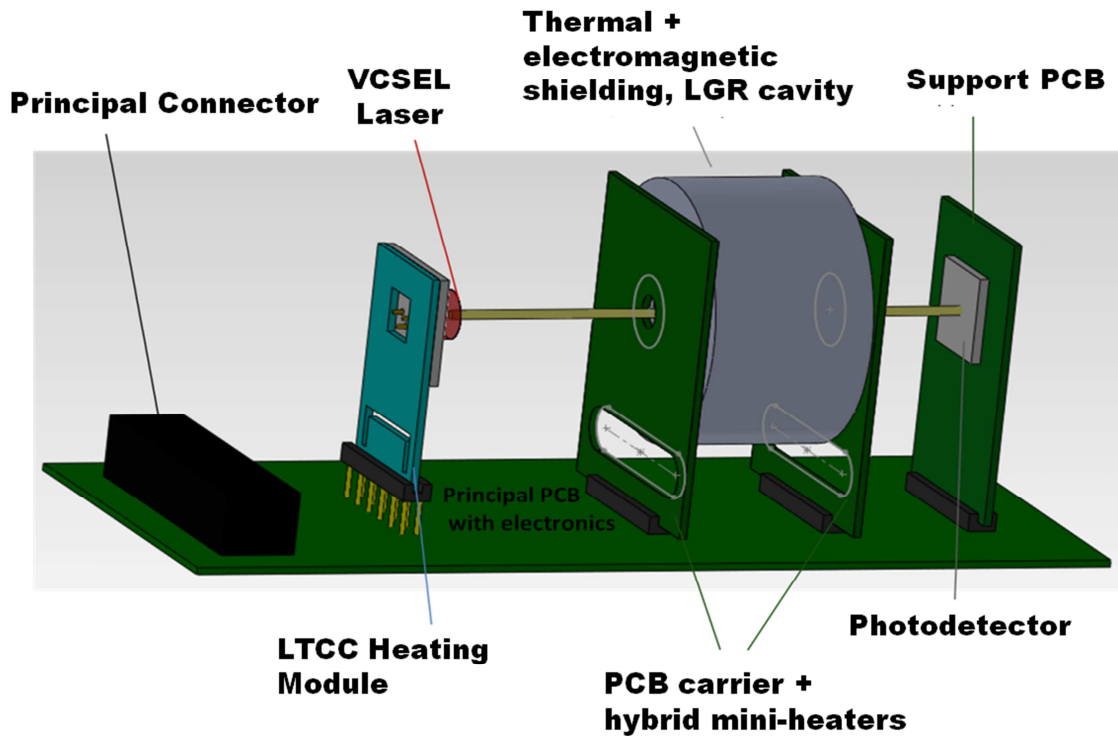


Figure 6. 15: 3D schematic view of the refined packaging concept of the atomic clock.

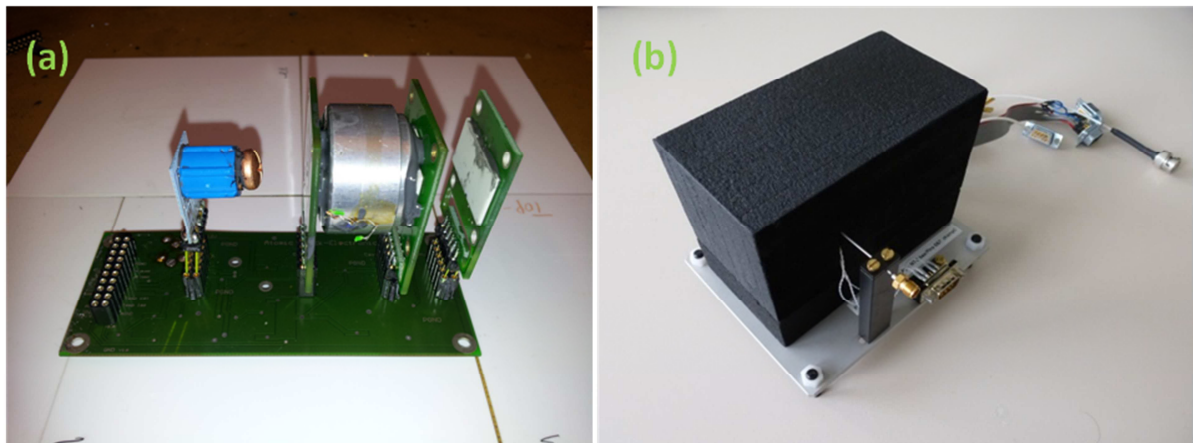


Figure 6. 16: (a), The atomic clock demonstrator assembled; (b), the system is covered by a thermally insulating black foam to limit convection in air.

6.4.3 Performance and comparison with the device currently on the market

As for the frequency-stabilized laser (section 6.2), the device was characterized at the LTF, Université de Neuchâtel. Even if further characterization needs to be done, a DR spectroscopy signal was obtained from the system, as shown in Figure 6. 17. The short-term stability in terms of Allan deviation of this device was very good, as shown in Figure 6. 18.

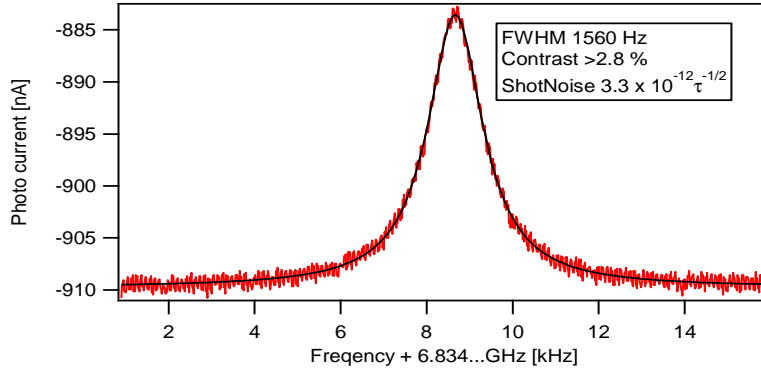


Figure 6.17: DR signal obtained using our demonstrator. Measurements performed by M.Pellaton of LTF – Université de Neuchâtel.

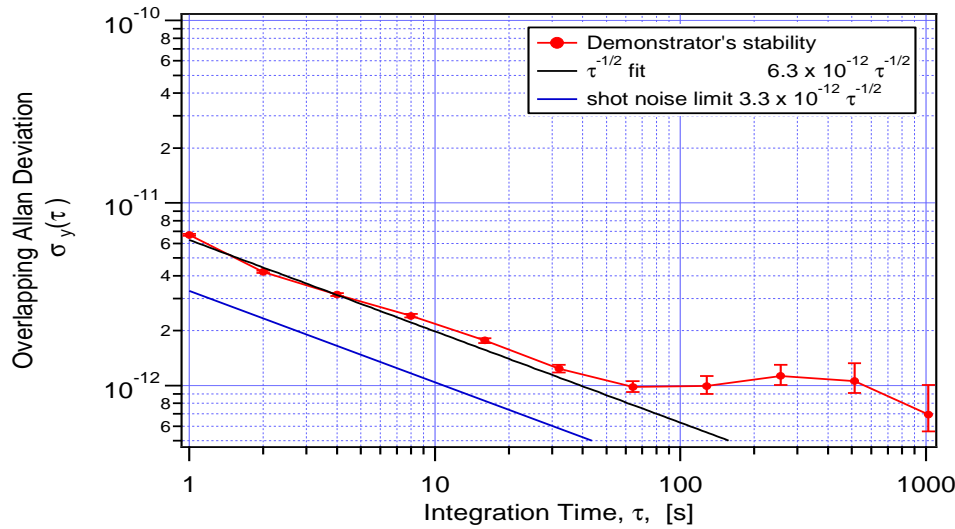


Figure 6.18: Short term stability of the clock demonstrator. Measurements performed by M. Pellaton of LTF – Université de Neuchâtel.

As we can see from the above graph, the short-term stability of this device is below $7 \times 10^{-12} \tau^{1/2}$ at 1000 s, which is a very good value, better compared to all other devices in the market. If we compare this device with the Spectratime StarLPRO [261], which is the Spectratime low-cost Rubidium oscillator currently on the market, we see that the device fabricated by our consortium is more compact and has better short term stability. For a fair comparison, it is important to specify that in the StarLPRO all the electronics is included, while in our demonstrator the step of integrating the electronics is only partially undertaken. Therefore, the final volume of our demonstrator will slightly increase once all the electronics will be included. Figure 6.19 compares our device with the Spectratime StarLPRO.



Spectratime StarLPRO , [261]

- Short-term stability : 2×10^{-11} @ 1 s
- Dimensions : $128 \times 95 \times 38.1$ mm
- Volume : 460 cm^3

Our atomic clock demonstrator

- Short-term stability : 7×10^{-12} @ 1 s
- Dimensions : $102 \times 43 \times 55$ mm
- Volume : 220 cm^3

Figure 6. 19: Comparison between Spectratime StarLPRO, miniature atomic clock currently in the market, and our demonstrator.

From Figure 6.19, we can affirm that our demonstrator is the state-of-the-art for short term stability for rubidium oscillators. Regarding the size, the total volume of our system is significantly less than the volume of the product currently in the market, but this comparison is not exhaustive, because the electronics is only partially integrated in our system, while the Spectratime StarLPRO clock integrates all the electronics in the system.

7 Conclusions

This chapter summarizes the different results achieved and the novelties introduced by this thesis, with an outlook on the possible future improvements of the techniques and devices described.

7.1 Summary

The work presented in this thesis was performed mainly in the frame of the Miniature Atomic Clock and Quantum Sensors (MACQS) project, funded by the Swiss National Science Foundation (SNSF, grant #CRSI20-122693), which involved laboratories with different scientific backgrounds that extensively collaborated to achieve a common ambitious objective: to realize and study a demonstrator of a chip-scale Double Resonance Rubidium Atomic Clock, and optionally other Quantum Sensors and side products. In this context, our laboratory, with a vast expertise in design and microfabrication of microsystems using thick film technology, had the objective of proposing innovative solutions for the packaging and interconnection of the various components of the clock. LTCC was chosen as the main packaging platform for the atomic clock modules, due to its many advantages: excellent 3D structurability and high integration capabilities (particularly attractive is the possibility to add suspended heaters for local temperature control), very good hermeticity and resistance to harsh environments, together with moderate production costs.

However, some limitations and unknowns were identified. First, LTCC has rather low mechanical strength and is brittle. Also, previous work in fabricating intricate structures often resulted in deformed devices. Finally and not directly related to LTCC we sought a low-temperature soldering technique for hermetic closure of Rb vapor cells, that does not require the high process temperatures and long times associated with anodic bonding.

This work was therefore essentially divided along the following lines:

- Fabrication of a hermetic Rb vapor cell based on an LTCC body, glass windows and solder bonding (chapter III)
- Improvement in 3D structuration of LTCC, by development of a lamination technique able to achieve bonding at modest temperatures and pressures, avoiding excessive deformation (chapter IV)
- Development, analysis and characterization of a generic LTCC carrier / hotplate for atomic clock modules (chapter V)
- Applications of the packaging solutions to the realization of several integrated microsystems, in close collaboration with the project partners (chapter VI)

7.2 Hermetic package for Rb vapor cell

An innovative design based on an LTCC body / spacer and Pyrex glass windows was developed for the reference cell or the Rb lamp of the atomic clock. The function of the spacer is to increase the volume of the cell in order to achieve efficient interaction with Rb vapor, and integrated special functions: a separate Rb reservoir for better confining the alkali metal, and a pressure sensor for monitoring the seal quality after bonding, for testing purposes. The Pyrex and the LTCC spacer are bonded using solder paste, which is dispensed on top of a metallization ring. This technique allows realizing the sealing in some minutes, at relatively low temperatures (200°C max), therefore preventing the evaporation of significant amounts of Rb during the sealing process associated with traditional bonding techniques (anodic bonding). A review of the metallurgical interactions between Rb (and alkali metals in general) and the commonly used metals for the solder and metallization ring was carried out, with encouraging results: Rb has low solubility with Ag and especially Ag-Pd (unlike Au, which must be avoided). Moreover, despite the low melting point of both Rb and traditional solder metals (Sn, Bi, Pb), these systems form intermediate essentially stoichiometric compounds with very high melting points, due to the strong difference in electronegativity, with very limited solubility of the solder metals in Rb or Cs, which led us to expect a stable system due to formation of passive intermetallic compounds on the solder surface.

The tests performed proved the hermeticity of the sealing, and its stability during at least 25 days. For fabrication of Rb cells, a convenient Rb handling technique under an inert solvent (dodecane) was developed and applied, allowing the packages to be handled for a limited time in ambient air. Dodecane shows significant solubility for gases, which raises two issues: 1) boiling out of the gases in vacuum, causing undesired movements of the assemblies and potentially partial loss of alignment of the solder rings during the sealing operation, a serious process reliability concern, and 2) oxidation of Rb by dissolved O₂ and H₂O from air. These issues are addressed by thoroughly degassing the dodecane prior to assembly or storage, and by long-storage in an inerted glove box.

In spite of these accomplishments, final process yield of Rb cells was very poor, with only one cell exhibiting significant Rb signal, and for a limited time only. As degradation was also observed in similar work parallel to ours involving In thermocompression, we suppose that significant interactions between materials still do occur; more work is therefore necessary to identify their nature and extent, and develop efficient countermeasures allowing reliable, extended operation of alkali vapor cells bonded using these techniques.

7.3 Low-pressure, low-temperature lamination of LTCC

In the production of the LTCC test modules with an integrated pressure sensor, we faced a new challenge: the membrane of the sensor was, in most cases, too deformed by the high

pressure applied during lamination; this deflection yielded a lowered and inconsistent sensitivity. Therefore, we developed a new innovative technique for LTCC lamination, which involves the application of a special low-melting “hot melt” adhesive layer on top of the LTCC green tape, allowing lamination at low pressure (≈ 4 MPa) and moderate temperature (50-60°C) and thereby resulting in much flatter membranes with respect to samples fabricated using standard thermocompression lamination. This method allowed producing working LTCC pressure sensors that were used to test the hermeticity of the sealing.

Compared with similar previous developments on adhesive tape or solvent-assisted bonding of LTCC, the developed adhesive layer is compatible with standard thick film pastes, so, after having deposited the “glue” on top of the starting green tapes by screen-printing, the fabrication process can follow the standard procedure. This requires the adhesive to have low or no tack at room temperature, yet melt reliably at moderate ones. To achieve this objective, we introduced crystalline waxes such as cetanol in the adhesive formulation, which result in compositions having good flow properties at moderate temperature 50-60°C, yet practically no tack after cooling. This approach is clearly promising, and needs to be expanded in the future by better studying the interactions between the adhesive formulations and the LTCC binder.

7.4 LTCC hotplate

For the second part of this work, in order to provide intelligent packaging solutions for interconnection and low-power temperature regulation for the atomic clock components, we designed and fabricated a standard LTCC multifunctional module. This module, equipped with a heating serpentine for local temperature control and a PTC resistor for temperature measurement, was designed to be a “plug & play” device (using a standard DIL connector), and to be flexible enough to temperature-stabilize and interconnect between them all the component of the atomic clock and any other device in the mm range. Since in this project we aimed to develop a portable, low power consumption device, before fabrication, a detailed thermal analysis and then finite-element thermal simulations were performed in order to estimate the power consumption of the designed LTCC multifunctional module. The thermal investigations, both by FEM and experimental, highlighted the importance of thermally insulating the LTCC module to get a satisfactory heating performance, as losses were dominated by convection, requiring thermal insulation (foam or even vacuum for the most demanding applications) in order to achieve low-power operation.

Nevertheless, we proved that LTCC is not only an elegant solution for generic packaging, but it is also attractive in terms of power consumption, as the intrinsic conduction losses are very low: it is not a utopia to use this technology where low-power consumption is required.

7.5 Applications and PCB-ceramic hybrid hotplate for large payloads

Turning to applications, to illustrate the various developed packaging solutions, we were confronted with the mechanical limitations of LTCC for carrying large payloads, specifically the DR atomic clock reference cell – LGR cavity – thermal/magnetic shield assembly. Therefore, we developed an alternative to LTCC, consisting of a carrier PCB, with miniature thick-film ceramic heaters. The PCB is mechanically more robust than LTCC, and the ceramic heaters are easier to produce with respect to LTCC; the drawback is that this system cannot withstand temperatures higher than 200°C (problems with thermal expansion mismatch and limited thermal stability of PCB materials). Nevertheless, this low-cost, simple kind of hotplate proved an attractive alternative to LTCC for our application, given the modest (<100°C) and constant (no thermal cycling) operating temperature.

On the other hand, the developed LTCC hotplate was found to be an excellent match for the other, lighter microsystems, of which several are illustrated. First, a frequency-stabilized laser, in which the frequency of a VCSEL laser beam is locked at the frequency of absorption line of the atoms of Rb, was developed. The principal components of this system are the VCSEL laser and a reference Rb cell. To ensure reliable interconnection between the parts and a precise temperature control for this microsystem, an LTCC heater module was used to control the temperature of the VCSEL and another to control the temperature of the Rb reference cell. The system, which is mounted on top of a horizontal PCB also carrying the electronics, exhibited a significant size reduction with respect to the previous version of the laser, together with an improvement in terms of stability.

Another microsystem that focused our attention was a Rb mini-lamp system integrating the lamp and the conditioning LC circuit. The mini-lamp can be used as optical source for a Rb atomic clock, and needs an LC circuit, which must be kept ideally at constant, moderate temperature, while the lamp should be temperature-stabilized at temperatures around 100°C. Here also, an LTCC module was used to carry the LC circuit and to locally heat the Rb mini-lamp, the Rb mini-lamp and its LC circuits being far enough from each other to ensure good thermal decoupling. This elegant solution allowed reduction of the size, providing proper interconnection and temperature control in a very small package.

For the Rb lamp application, the developed PCB platform was also envisioned, as it allowed easy creation of three different thermal zones (one for the inductor L, one for the capacitor C, one for the mini-lamp); in this way the three components may be controlled independently using hybrid mini-heaters, allowing the additional function of dynamic rf power matching by exploiting the temperature dependence of the L and C passive components. Moreover, this solution, by using the ceramic mini-heaters to locally heat the components, is less power-consuming with respect to the first solution.

Given the potential of this relatively simple, low-cost hybrid PCB / thick-film technology, further studies should aim at developing and characterizing the process towards achieving precise temperature control and optimizing the assembly. Also, the long-term reliability limitations under severe operation (high temperatures and thermal cycling) should be examined in more detail.

Finally, the Rb Double Resonance Atomic Clock demonstrator is presented. Achieving this demonstrator together with the project partners was the ambitious objective of the whole research project. We combined thick film, PCB and LTCC technology to ensure the most reliable interconnection and packaging system for this system. The fabricated device, in this case, showed very good short-term stability and good potential for size reduction with respect to the currently product present in the market.

References

- [1] W. H. Ko, "Solid-state capacitive pressure transducers," *Sens. Actuators*, vol. 10, no. 3–4, pp. 303–320, Nov. 1986.
- [2] W. P. Eaton and J. H. Smith, "Micromachined pressure sensors: review and recent developments," *Smart Mater. Struct.*, vol. 6, no. 5, p. 530, 1997.
- [3] Y. Fournier, G. B. Rouelle, N. Craquelin, T. Maeder, and P. Ryser, "SMD pressure and flow sensor for compressed air in LTCC technology with integrated electronics," *Procedia Chem.*, vol. 1, no. 1, pp. 1471–1474, 2009.
- [4] O. Akar, T. Akin, and K. Najafi, "A wireless batch sealed absolute capacitive pressure sensor," *Sens. Actuators Phys.*, vol. 95, no. 1, pp. 29–38, 2001.
- [5] L. E. Felton, N. Hablutzel, W. A. Webster, and K. P. Harney, "Chip scale packaging of a MEMS accelerometer," in *Electronic Components and Technology Conference, 2004. Proceedings. 54th*, 2004, vol. 1, pp. 869–873.
- [6] H. Gan, Y. Jin, M. Miao, and X. Sun, "A novel LTCC capacitive accelerometer embedded in LTCC packaging substrate," in *Nano/Micro Engineered and Molecular Systems (NEMS), 2011 IEEE International Conference on*, 2011, pp. 796–799.
- [7] R. Barbieri, E. Farella, L. Benini, B. Ricc , and A. Acquaviva, "A low-power motion capture system with integrated accelerometers [gesture recognition applications]," in *Consumer Communications and Networking Conference, 2004. CCNC 2004. First IEEE*, 2004, pp. 418–423.
- [8] N. Yazdi, F. Ayazi, and K. Najafi, "Micromachined inertial sensors," *Proc. IEEE*, vol. 86, no. 8, pp. 1640–1659, 1998.
- [9] R. H. Dixon and J. Bouchaud, "Markets and applications for MEMS inertial sensors," in *MOEMS-MEMS 2006 Micro and Nanofabrication*, 2006, pp. 611306–611306.
- [10] D. J. Jones, W. A. Edblad, J. S. Pringle, D. M. Oravetz, and J. R. Patelunas, "Universal process control device and method for developing a process control loop program," 4,663,704May-1987.
- [11] R. L. Thibault, G. S. Couper, and B. S. Canna, *Methods and apparatus for remote process control*. 2013.
- [12] X. Ma and G.-S. Kuo, "Optical switching technology comparison: optical MEMS vs. other technologies," *Commun. Mag. IEEE*, vol. 41, no. 11, pp. S16–S23, 2003.
- [13] M. C. Wu, O. Solgaard, and J. E. Ford, "Optical MEMS for lightwave communication," *Light. Technol. J. Of*, vol. 24, no. 12, pp. 4433–4454, 2006.
- [14] A. Neukermans and R. Ramaswami, "MEMS technology for optical networking applications," *Commun. Mag. IEEE*, vol. 39, no. 1, pp. 62–69, 2001.
- [15] P. De Dobbelaere, K. Falta, S. Gloeckner, and S. Patra, "Digital MEMS for optical switching," *Commun. Mag. IEEE*, vol. 40, no. 3, pp. 88–95, 2002.
- [16] H. A. Tilmans, W. De Raedt, and E. Beyne, "MEMS for wireless communications: from RF-MEMS components to RF-MEMS-SiP," *J. Micromechanics Microengineering*, vol. 13, no. 4, p. S139, 2003.
- [17] J. Zou, C. Liu, J. Schutt-Aine, J. Chen, and S.-M. Kang, "Development of a wide tuning range MEMS tunable capacitor for wireless communication systems," in *Electron Devices Meeting, 2000. IEDM'00. Technical Digest. International*, 2000, pp. 403–406.

References

- [18] T. Stieglitz, M. Schuetter, and K. P. Koch, "Implantable biomedical microsystems for neural prostheses," *Eng. Med. Biol. Mag. IEEE*, vol. 24, no. 5, pp. 58–65, 2005.
- [19] A. M. Sodagar, K. Najafi, K. D. Wise, and M. Ghovanloo, "Fully-integrated CMOS power regulator for telemetry-powered implantable biomedical microsystems," in *Custom Integrated Circuits Conference, 2006. CICC'06. IEEE*, 2006, pp. 659–662.
- [20] Y. Haga and M. Esashi, "Biomedical microsystems for minimally invasive diagnosis and treatment," *Proc. IEEE*, vol. 92, no. 1, pp. 98–114, 2004.
- [21] C. D. Fung, *Micromachining and Micropackaging of Transducers*. Elsevier, 1985.
- [22] K. Najafi, "Micropackaging technologies for integrated microsystems: Applications to MEMS and MOEMS," in *Micromachining and Microfabrication*, 2003, pp. 1–19.
- [23] A. B. Ucok, J. M. Giachino, and K. Najafi, "The WIMS Cube: A Microsystem Package with Actuated Flexible Connections and Re-Workable Assembly," *Ann Arbor*, vol. 1001, pp. 48109–2101, 2004.
- [24] J. Yeom, C. R. Field, B. Bae, R. I. Masel, and M. A. Shannon, "The design, fabrication and characterization of a silicon microheater for an integrated MEMS gas preconcentrator," *J. Micromechanics Microengineering*, vol. 18, no. 12, p. 125001, 2008.
- [25] J. L. Gonzalez-Vidal, A. Reyes-Barranca, and W. C. Arriaga, "Technological processes for microheater and micro-hot-plate in the implementation of a MEM gas sensor," in *Electrical and Electronics Engineering, 2005 2nd International Conference on*, 2005, pp. 440–443.
- [26] T. Bechtold, E. B. Rudnyi, and D. Hohlfield, "System-level model of electrothermal microsystem with temperature control circuit," in *Thermal, Mechanical and Multi-Physics Simulation and Experiments in Microelectronics and Microsystems (EuroSimE), 2011 12th International Conference on*, 2011, pp. 1–5.
- [27] M. Graf, D. Barrettino, S. Taschini, C. Hagleitner, A. Hierlemann, and H. Baltes, "Metal oxide-based monolithic complementary metal oxide semiconductor gas sensor microsystem," *Anal. Chem.*, vol. 76, no. 15, pp. 4437–4445, 2004.
- [28] D. Barrettino, M. Graf, W. H. Song, K.-U. Kirstein, A. Hierlemann, and H. Baltes, "Hotplate-based monolithic CMOS microsystems for gas detection and material characterization for operating temperatures up to 500 C," *Solid-State Circuits IEEE J. Of*, vol. 39, no. 7, pp. 1202–1207, 2004.
- [29] G.-S. Chung, "Fabrication and characterization of micro-heaters with low-power consumption using SOI membrane and trench structures," *Sens. Actuators Phys.*, vol. 112, no. 1, pp. 55–60, 2004.
- [30] D. Barrettino, M. Graf, M. Zimmermann, A. Hierlemann, H. Baltes, S. Hahn, N. Bârsan, and U. Weimar, "A System Architecture of Micro-Hotplate-Based Chemical Sensors in CMOS Technology."
- [31] D. Barrettino, M. Graf, M. Zimmermann, A. Hierlemann, H. Baltes, S. Hahn, N. Barsan, and U. Weimar, "A smart single-chip micro-hotplate-based chemical sensor system in CMOS-technology," in *Circuits and Systems, 2002. ISCAS 2002. IEEE International Symposium on*, 2002, vol. 2, pp. II–157.
- [32] D. Barrettino, M. Graf, S. Hafizovic, S. Taschini, C. Hagleitner, A. Hierlemann, and H. Baltes, "A single-chip CMOS micro-hotplate array for hazardous-gas detection and material characterization," in *Solid-State Circuits Conference, 2004. Digest of Technical Papers. ISSCC. 2004 IEEE International*, 2004, pp. 312–313.

- [33] Y. Fournier, “3D Structuration Techniques of LTCC for Microsystems Applications,” EPFL, Lausanne, 2010.
- [34] Y. K. Jain and V. K. Khanna, “Thick film, LTCC or silicon microhotplate for gas sensor and other applications,” in *Physics of Semiconductor Devices, 2007. IWPSD 2007. International Workshop on*, 2007, pp. 714–717.
- [35] D. Kharbanda, P. K. Khanna, C. Shekhar, and A. Mohan, “Design, simulation and modelling of LTCC based micro hotplate for gas sensor applications,” in *Physics and Technology of Sensors (ISPTS), 2012 1st International Symposium on*, 2012, pp. 257–260.
- [36] “Green Tape Dupont 951 Datasheet.” [Online]. Available: http://www2.dupont.com/MCM/en_US/assets/downloads/prodinfo/951LTCCGreenTape.pdf.
- [37] H. Dannheim, U. Schmid, and A. Roosen, “Lifetime prediction for mechanically stressed low temperature co-fired ceramics,” *J. Eur. Ceram. Soc.*, vol. 24, no. 8, pp. 2187–2192, 2004.
- [38] R. Bermejo, P. Supancic, F. Aldrian, and R. Danzer, “Experimental approach to assess the effect of metallization on the strength of functional ceramic components,” *Scr. Mater.*, vol. 66, no. 8, pp. 546–549, 2012.
- [39] T. Maeder, C. Jacq, and P. Ryser, “Long-term mechanical reliability of ceramic thick-film circuits and mechanical sensors under static load,” *Sens. Actuators Phys.*, vol. 186, pp. 210–218, 2012.
- [40] H. Birol, “Fabrication of Low Temperature Co-fired Ceramic (LTCC)-based Sensors and Micro-fluidic Structures,” EPFL, 2007.
- [41] H. Birol, T. Maeder, and P. Ryser, “Processing of graphite-based sacrificial layer for microfabrication of low temperature co-fired ceramics (LTCC),” *Sens. Actuators Phys.*, vol. 130, pp. 560–567, 2006.
- [42] H. Birol, T. Maeder, C. Jacq, and P. Ryser, “Investigation of interactions between co-fired LTCC components,” *J. Eur. Ceram. Soc.*, vol. 25, no. 12, pp. 2065–2069, 2005.
- [43] American Society for Testing and Materials, “Standard Test Methods for Flexural Properties of Unreinforced and Reinforced Plastics and Electrical Insulating Materials,” ASTM Subcommittee D20. 10 on Mechanical Properties, 1997.
- [44] C. Mauney, “Thermal Considerations for Surface Mount Layouts,” Texas Instruments, 2005.
- [45] J. Coonrod, *Thermal Design Begins At The Circuit Board*. PENTON MEDIA, INC 249 W 17TH ST, NEW YORK, NY 10011 USA, 2011.
- [46] M. Davis-Marsh, “Thermal Design By Insight, Not Hindsight,” 2010.
- [47] W. H. Gitzen, *Alumina as a Ceramic Material*. American Ceramic Society, 1970.
- [48] T. Siewert, S. Liu, D. R. Smith, and J. C. Madeni, “Database for solder properties with emphasis on new lead-free solders,” *NIST Colo. Sch. Mines Release*, vol. 4, 2002.
- [49] F. Bechtold, “A comprehensive overview on today’s ceramic substrate technologies,” in *Microelectronics and Packaging Conference, 2009. EMPC 2009. European*, 2009, pp. 1–12.
- [50] Q. Qi, “Reliability studies of two flip-chip BGA packages using power cycling test,” *Microelectron. Reliab.*, vol. 41, no. 4, pp. 553–562, 2001.

References

- [51] A. D. Trigg and A. R. Corless, "Thermal performance and reliability aspects of silicon hybrid multi-chip modules," in *Electronic Components and Technology Conference, 1990., 40th*, 1990, pp. 592–599.
- [52] R. Lutwak, D. Emmons, W. Riley, and R. M. Garvey, "The chip-scale atomic clock-coherent population trapping vs. conventional interrogation," DTIC Document, 2003.
- [53] J. Levy, *Really Useful: the Origins of Everyday Things*. Firefly Books, 2003.
- [54] E. Bruton, *The history of clocks and watches*. Rizzoli, 1979.
- [55] D. S. Landes, *Revolution in time: Clocks and the making of the modern world*. Harvard University Press, 2000.
- [56] D. R. Hill, "Arabic Mechanical Engineering: Survey of the Historical Sources," *Arab. Sci. Philos.*, vol. 1, no. 2, pp. 167–186, 1991.
- [57] D. R. Hill, "Mechanical engineering in the medieval near east," *Sci. Am.*, vol. 264, no. 5, pp. 100–105, 1991.
- [58] T. Proctor, "Innovations in Time: What can we learn from history?," *Creat. Innov. Manag.*, vol. 7, no. 4, pp. 204–211, 1998.
- [59] R. Pearsall, *Connoisseur's Guide to Antique Clocks and Watches*. New Line Books, 1998.
- [60] L. L. Lewis, "An introduction to frequency standards," *Proc. IEEE*, vol. 79, no. 7, pp. 927–935, 1991.
- [61] J. R. Vig, "Introduction to Quartz Frequency Standards. Revision," DTIC Document, 1992.
- [62] W. G. Cady, "Piezoelectricity: an introduction to the theory and applications of electromechanical phenomena," 1964.
- [63] L. Essen and J. V. L. Parry, "The caesium resonator as a standard of frequency and time," *Philos. Trans. R. Soc. Lond. Ser. Math. Phys. Sci.*, vol. 250, no. 973, pp. 45–69, 1957.
- [64] N. F. Ramsey, "History of atomic clocks," *J. Res. Natl. Bur. Stand.*, vol. 88, pp. 301–320, 1983.
- [65] D. W. Allan, "Statistics of atomic frequency standards," *Proc. IEEE*, vol. 54, no. 2, pp. 221–230, 1966.
- [66] S. A. Diddams, J. C. Bergquist, S. R. Jefferts, and C. W. Oates, "Standards of time and frequency at the outset of the 21st century," *Science*, vol. 306, no. 5700, pp. 1318–1324, 2004.
- [67] S. Knappe, "MEMS atomic clocks," *Compr. Microsyst.*, vol. 3, pp. 571–612, 2007.
- [68] F. Droz, P. Rochat, G. Barmaverain, M. Brunet, J. Delporte, J.-F. Dutrey, F. Emma, T. Pike, and U. Schmidt, "On-board Galileo RAFS, current status and performances," in *Frequency Control Symposium and PDA Exhibition Jointly with the 17th European Frequency and Time Forum, 2003. Proceedings of the 2003 IEEE International*, 2003, pp. 105–108.
- [69] R. Lutwak, P. Vlitaz, M. Varghese, M. Mescher, D. K. Serkland, and G. M. Peake, "The mac-a miniature atomic clock," in *Frequency Control Symposium and Exposition, 2005. Proceedings of the 2005 IEEE International*, 2005, p. 6–pp.
- [70] S. Knappe, P. D. D. Schwindt, V. Gerginov, V. Shah, L. Liew, J. Moreland, H. G. Robinson, L. Hollberg, and J. Kitching, "Microfabricated atomic clocks and magnetometers," *J. Opt. Pure Appl. Opt.*, vol. 8, no. 7, p. S318, 2006.

- [71] S. Knappe, P. D. D. Schwindt, V. Shah, L. Hollberg, J. Kitching, L. Liew, and J. Moreland, "A chip-scale atomic clock based on 87Rb with improved frequency stability," *Opt Express*, vol. 13, no. 4, pp. 1249–1253, 2005.
- [72] "NIST web page on frequency standards." [Online]. Available: <http://www.nist.gov/pml/div688/grp50/primary-frequency-standards.cfm>.
- [73] "Symmetricom - the CSAC: Chip Scale Atomic Clock." [Online]. Available: <http://www1.symmetricom.com/csac/>.
- [74] M. Arditi and T. R. Carver, "The principles of the double resonance method applied to gas cell frequency standards," *Proc. IEEE*, vol. 51, no. 1, pp. 190–202, 1963.
- [75] S. Knappe, V. Shah, P. D. Schwindt, L. Hollberg, J. Kitching, L.-A. Liew, and J. Moreland, "A microfabricated atomic clock," *Appl. Phys. Lett.*, vol. 85, no. 9, pp. 1460–1462, 2004.
- [76] D. I. Pomerantz, "Anodic bonding," 3,397,278Aug-1968.
- [77] R. Lutwak, A. Rashed, M. Varghese, G. Tepolt, J. LeBlanc, M. Mescher, D. K. Serkland, K. M. Geib, G. M. Peake, and S. Römisch, "The Chip-Scale Atomic Clock-Prototype Evaluation," DTIC Document, 2007.
- [78] R. Lutwak, J. Deng, W. Riley, M. Varghese, J. Leblanc, G. Tepolt, M. Mescher, D. K. Serkland, K. M. Geib, and G. M. Peake, "The chip-scale atomic clock-low-power physics package," DTIC Document, 2004.
- [79] J. F. DeNatale, R. L. Borwick, C. Tsai, P. A. Stupar, Y. Lin, R. A. Newgard, R. W. Berquist, and M. Zhu, "Compact, low-power chip-scale atomic clock," in *Position, Location and Navigation Symposium, 2008 IEEE/ION*, 2008, pp. 67–70.
- [80] R. Kulke, M. Rittweger, P. Uhlig, and C. Gunner, "LTCC-multilayer ceramic for wireless and sensor applications," *IMST GmbH Httpwww Ltcc De*, 2001.
- [81] C. Q. Scrantom and J. C. Lawson, "LTCC technology: where we are and where we're going. II," in *Technologies for Wireless Applications, 1999. Digest. 1999 IEEE MTT-S Symposium on*, 1999, pp. 193–200.
- [82] H. Jantunen, "Low Temperature co-fired ceramic (LTCC) materials for telecommunication devices," University of Oulu, Finland, 2001.
- [83] T. Thelemann, H. Thust, and M. Hintz, "Using LTCC for microsystems," *Microelectron. Int.*, vol. 19, no. 3, pp. 19–23, 2002.
- [84] C. Gorecki, M. Hasegawa, N. Passily, R. . Chutani, and V. Giordano, "Towards the realization of the first European MEMS atomic clock," presented at the Optical Mems and Nanophotonics, 2009 IEEE/LEOS International Conference on, 2009.
- [85] "The MAC-TFC project." [Online]. Available: <http://www.mac-tfc.eu/>.
- [86] Y. Imanaka, *Multilayered low temperature cofired ceramics (LTCC) technology*. Springer Science+ Business Media, 2005.
- [87] M. R. Gongora-Rubio, P. Espinoza-Vallejos, L. Sola-Laguna, and J. J. Santiago-Aviles, "Overview of low temperature co-fired ceramics tape technology for meso-system technology (MsST)," *Sens. Actuators Phys.*, vol. 89, no. 3, pp. 222–241, 2001.
- [88] J. J. Avilès Santiago and M. Gongora Rubio, "Sensors, Actuators and Other non-packaging Applications of LTCC tapes," presented at the Conference on Ceramic Interconnect Technology, 2004, pp. 7–12.
- [89] P. Barnwell, W. Zhang, J. Lebowitz, K. Jones, N. MacDonald, C. Free, and T. ZHENGRONG, "An investigation of the properties of LTCC materials and compatible

References

- conductors for their use in wireless applications,” in *SPIE proceedings series*, 2000, pp. 659–664.
- [90] R. L. Brown and W. R. Smith, “Embedded passive functions for RF and mixed-signal circuits,” in *Multichip Modules, 1997., 6th International Conference on*, 1997, pp. 351–356.
- [91] S. X. Dai, R.-F. Huang, and D. L. Wilcox, “Use of Titanates to Achieve a Temperature-Stable Low-Temperature Cofired Ceramic Dielectric for Wireless Applications,” *J. Am. Ceram. Soc.*, vol. 85, no. 4, pp. 828–832, 2002.
- [92] S. Annas, “Advances in low temperature co-fired ceramic (LTCC) for ever increasing microelectronic applications,” in *Electronic Components and Technology Conference, 2003. Proceedings. 53rd*, 2003, pp. 1691–1693.
- [93] E. P. Holmes, *Handbook of thick film technology*. 1976.
- [94] S. Al-Taei, D. Haigh, and G. Passiopoulos, “Multilayer ceramic integrated circuits (MCICs) technology and passive circuit design,” in *Proc. 6th London Communication Symposium, Imperial College, London*, 2001.
- [95] S. Scrantom, G. Gravier, T. Valentine, G. Gravier, D. Pehlke, and B. Schiffer, “Manufacture of embedded integrated passive components into low temperature co-fired ceramic systems,” in *PROCEEDINGS-SPIE THE INTERNATIONAL SOCIETY FOR OPTICAL ENGINEERING*, 1998, pp. 459–466.
- [96] R. L. Brown, A. A. Shapiro, and P. W. Polinski, “Integration of passive components into MCMs using advanced low-temperature cofired ceramics,” *Int. J. Microcircuits Electron. Packag.*, vol. 16, no. 4, pp. 328–338, 1993.
- [97] H. Watanabe, N. Yamada, and M. Okaji, “Linear Thermal Expansion Coefficient of Silicon from 293 to 1000 K,” *Int. J. Thermophys.*, vol. 25, no. 1, pp. 221–236.
- [98] K. A. Peterson, K. D. Patel, C. K. Ho, S. B. Rohde, C. D. Nordquist, C. A. Walker, B. D. Wroblewski, and M. Okandan, “Novel Microsystem Applications with New Techniques in Low-Temperature Co-Fired Ceramics,” *Int. J. Appl. Ceram. Technol.*, vol. 2, no. 5, pp. 345–363, 2005.
- [99] L. J. Golonka, B. W. Licznarski, K. Nitsch, H. Teterycz, R. Bauer, and K. J. Wolter, “Examples of gas sensors by application of thick film technology,” in *Proceedings of the 43rd International Scientific Colloquium, TU Ilmenau*, 1998, pp. 465–470.
- [100] N. Craquelin, T. Maeder, Y. Fournier, and P. Ryser, “Low-cost LTCC-based sensors for low force ranges,” *Procedia Chem.*, vol. 1, no. 1, pp. 899–902, 2009.
- [101] M. Gongora-Rubio, L. Sola-Laguna, M. Smith, and J. J. Santiago-Aviles, “LTCC technology multilayer eddy current proximity sensor for harsh environments,” in *SPIE proceedings series*, 1999, pp. 676–681.
- [102] H. Teterycz, J. Kita, R. Bauer, L. J. Golonka, B. W. Licznarski, K. Nitsch, and K. Wiśniewski, “New design of an SnO₂ gas sensor on low temperature cofiring ceramics,” *Sens. Actuators B Chem.*, vol. 47, no. 1, pp. 100–103, 1998.
- [103] R. A. Blechschmidt-Trapp, O. Hohlfeld, R. Müller, and R. Werthschützky, “Piezoresistive sensors for medical applications exemplified by a probe for measure pressure in the rectum],,” *Biomed. Tech. (Berl)*, vol. 47, no. 3, p. 43, 2002.
- [104] Y. Fournier, G. B. Rouelle, N. Craquelin, T. Maeder, and P. Ryser, “SMD pressure and flow sensor for compressed air in LTCC technology with integrated electronics,” *Procedia Chem.*, vol. 1, no. 1, pp. 1471–1474, 2009.

- [105] T.-Y. Tsai, N.-H. Tai, and I.-N. Lin, "Characteristics of carbon nanotube electron field emission devices prepared by LTCC process," *Diam. Relat. Mater.*, vol. 13, no. 4, pp. 982–986, 2004.
- [106] K. L. Zhang, S. K. Chou, and S. S. Ang, "Development of a low-temperature co-fired ceramic solid propellant microthruster," *J. Micromechanics Microengineering*, vol. 15, no. 5, p. 944, 2005.
- [107] T. Maeder, Y. Fournier, S. Wiedmer, H. Birol, C. Jacq, and P. Ryser, "3D structuration of LTCC/thick-film sensors and fluidic devices," in *Proceedings of the 3rd Int'l Conference on Ceramic Interconnect and Ceramic Microsystems Technologies (CICMT)*, 2007.
- [108] Y. Fournier, R. Willigens, T. Maeder, and P. Ryser, "Integrated LTCC micro-fluidic modules—an SMT flow sensor," in *Proceedings of the 15th IMAPS European Microelectronics and Packaging Conference (EMPC)*, 2005, pp. 577–581.
- [109] L. J. Golonka, H. Roguszcak, T. Zawada, J. Radojewski, I. Grabowska, M. Chudy, A. Dybko, Z. Brzozka, and D. Stadnik, "LTCC based microfluidic system with optical detection," *Sens. Actuators B Chem.*, vol. 111, pp. 396–402, 2005.
- [110] R. M. German, "Sintering theory and practice," *Sinter. Theory Pract. Randall M Ger. Pp 568 ISBN 0-471-05786-X Wiley-VCH January 1996*, vol. 1, 1996.
- [111] C. Herring, "Effect of change of scale on sintering phenomena," *J. Appl. Phys.*, vol. 21, no. 4, pp. 301–303, 1950.
- [112] Y. Fournier, L.-S. Bieri, T. Maeder, and P. Ryser, "Influence of lamination parameters on LTCC shrinkage under unconstrained sintering," in *Proceedings of the 4th IMAPS European Microelectronics and Packaging Symposium (EMPS)*, 2006, pp. 165–170.
- [113] F. Lautzenhiser, E. Amaya, and C. M. D. Heraeus, "HeraLock™ 2000 Self-constrained LTCC Tape," in *Proceedings of the 2002 International Conference on Advanced Packaging and Systems (ICAPS)*, Reno, Nevada, 2002, pp. 43–49.
- [114] T. Rabe, W. A. Schiller, T. Hochheimer, C. Modes, and A. Kipka, "Zero Shrinkage of LTCC by Self-Constrained Sintering," *Int. J. Appl. Ceram. Technol.*, vol. 2, no. 5, pp. 374–382, 2005.
- [115] R. E. Mistler, "Tape casting: past, present, potential," *Am. Ceram. Soc. Bull.*, vol. 77, no. 10, pp. 82–86, 1998.
- [116] X. Kuang, G. Carotenuto, and L. Nicolais, "A review of ceramic sintering and suggestions on reducing sintering temperatures," *Adv. Perform. Mater.*, vol. 4, no. 3, pp. 257–274, 1997.
- [117] R. R. Tummala, "Ceramics in Microelectronics and Packaging," in *Advanced Materials and Processes—Proceedings of the First European Conference. EUROMAT'89.*, 1989, vol. 2, pp. 817–828.
- [118] B. Schwartz, "Review of multilayer ceramics for microelectronic packaging," *J. Phys. Chem. Solids*, vol. 45, no. 10, pp. 1051–1068, 1984.
- [119] R. R. Tummala, "Ceramic and Glass-Ceramic Packaging in the 1990s," *J. Am. Ceram. Soc.*, vol. 74, no. 5, pp. 895–908, 1991.
- [120] "Dupont Material Systems, Design and Layout Guidelines, DuPont de Nemours & Co," 1994. [Online]. Available: http://www2.dupont.com/MCM/en_US/assets/downloads/prodinfo/GreenTape_Design_Layout_Guidelines.pdf.

References

- [121] Y. Wang, P. J. Ollivier, and C. R. Needes, "Thick film conductor paste compositions for LTCC tape," EP 1534053 May-2005.
- [122] W. Yue, C.-W. Li, T. Xu, and M. Yang, "Screen Printing of Solder Resist as Master Substrates for Fabrication of Multi-level Microfluidic Channels and Flask-shaped Microstructures for Cell-based Applications," *Biosens. Bioelectron.*, 2012.
- [123] N. M. White and J. D. Turner, "Thick-film sensors: past, present and future," *Meas. Sci. Technol.*, vol. 8, no. 1, p. 1, 1997.
- [124] L. J. Golonka, "Technology and applications of low temperature cofired ceramic (LTCC) based sensors and microsystems," *Bull Pol. Acad Sci Tech Sci*, vol. 54, no. 2, 2006.
- [125] D. Jurków and L. Golonka, "Low-pressure, thermo-compressive lamination," *J. Eur. Ceram. Soc.*, vol. 32, no. 10, pp. 2431–2441, 2012.
- [126] S. Kemethmüller, M. Hagymasi, A. Stiegelschmitt, and A. Roosen, "Viscous Flow as the Driving Force for the Densification of Low-Temperature Co-Fired Ceramics," *J. Am. Ceram. Soc.*, vol. 90, no. 1, pp. 64–70, 2007.
- [127] G. C. Kuczynski and I. Zaplatynskyj, "Sintering of glass," *J. Am. Ceram. Soc.*, vol. 39, no. 10, pp. 349–350, 1956.
- [128] I. B. Cutler and R. E. Henrichsen, "Effect of particle shape on the kinetics of sintering of glass," *J. Am. Ceram. Soc.*, vol. 51, no. 10, pp. 604–604, 1968.
- [129] K. Makarovi\vc, A. Meden, M. Hrovat, J. Holc, A. Ben\vc, A. Dakskobler, D. Belavi\vc, and M. Kosec, "The Effect of the Firing Temperature on the Properties of LTCC."
- [130] S. Nishigaki, J. Fukuta, S. Yano, H. Kawabe, K. Noda, M. Fukaya, and M. Denjiyama, "A New Low Temperature Fireable Ag Multilayer Ceramic Substrate having Post-Fired Cu Conductor (LFC-2)," in *ISHM Proceedings*, 1986, pp. 429–437.
- [131] "Green tape Heraclon 2000 Datasheet." [Online]. Available: http://www.heraeus-thickfilm.com/media/webmedia_local/media/datasheets/lccmaterials/HL2000.pdf.
- [132] M. P. Bradley, J. V. Porto, S. Rainville, J. K. Thompson, and D. E. Pritchard, "Penning Trap Measurements of the Masses of ^{133}Cs , ^{87}Rb , and ^{23}Na with Uncertainties ≤ 0.2 ppb," *Phys. Rev. Lett.*, vol. 83, no. 22, p. 4510, 1999.
- [133] F. A. Anderson, "Primer for the Safe Use of Liquid Alkali Metals," Oak Ridge National Lab., Tenn., 1967.
- [134] C. B. Alcock, V. P. Itkin, and M. K. Horrigan, "Vapour pressure equations for the metallic elements: 298–2500K," *Can. Metall. Q.*, vol. 23, no. 3, pp. 309–313, 1984.
- [135] D. A. Steck, *Rubidium 85 D line data*. 2008.
- [136] C. R. C. Press, "CRC handbook of chemistry and physics," *N. Y. N. Y.*, 2003.
- [137] H. Figger, W. Schrepp, and X. Zhu, "Chemiluminescent reaction between alkali dimers and oxygen molecules," *J. Chem. Phys.*, vol. 79, pp. 1320–1325, 1983.
- [138] D. Fischer, Z. Cancarevic, J. C. Schön, and M. Jansen, "Zur Synthese und Struktur von K_3N ," *Z. Für Anorg. Allg. Chem.*, vol. 630, no. 1, pp. 156–160, 2004.
- [139] D. Fischer and M. Jansen, "Synthesis and Structure of Na_3N ," *Angew. Chem. Int. Ed.*, vol. 41, no. 10, pp. 1755–1756, 2002.
- [140] J. L. Magee, "The Mechanism of Reactions Involving Excited Electronic States The Gaseous Reactions of the Alkali Metals and Halogens," *J. Chem. Phys.*, vol. 8, p. 687, 1940.

- [141] M. P. Rosynek and Y.-P. Wang, "Correlations between the physical/chemical properties and catalytic behaviors of alkali metal-graphite intercalation compounds," *J. Mol. Catal.*, vol. 27, no. 1, pp. 277–291, 1984.
- [142] S. Knappe, V. Gerginov, P. D. D. Schwindt, V. Shah, H. G. Robinson, L. Hollberg, and J. Kitching, "Atomic vapor cells for chip-scale atomic clocks with improved long-term frequency stability," *Opt. Lett.*, vol. 30, no. 18, pp. 2351–2353, 2005.
- [143] R. Lutwak, D. Emmons, T. English, and W. Riley, "The chip-scale atomic clock-recent development progress," DTIC Document, 2004.
- [144] K. Deng, T. Guo, D. W. He, X. Y. Liu, L. Liu, D. Z. Guo, X. Z. Chen, and Z. Wang, "Effect of buffer gas ratios on the relationship between cell temperature and frequency shifts of the coherent population trapping resonance," *Appl. Phys. Lett.*, vol. 92, no. 21, pp. 211104–211104, 2008.
- [145] J. H. Stang, E. M. Simons, J. A. DeMastry, and J. M. Genco, "Compatibility of Liquid and Vapor Alkali Metals with Construction Materials," DTIC Document, 1966.
- [146] R. E. Witkowski, F. G. Arcella, and A. R. Keeton, "Vital support systems for liquid metal collector homopolar machines," *Power Appar. Syst. IEEE Trans. On*, vol. 95, no. 4, pp. 1493–1500, 1976.
- [147] P. E. Kueser, M. F. Parkman, and J. W. Toth, "Ceramic-metal bore seal development," 1970.
- [148] R. Lutwak, A. Rashed, D. K. Serkland, G. M. Peake, M. Varghese, G. Tepolt, J. R. Leblanc, and M. Mescher, "The miniature atomic clock-Pre-production results," in *Frequency Control Symposium, 2007 Joint with the 21st European Frequency and Time Forum. IEEE International*, 2007, pp. 1327–1333.
- [149] M. Hasegawa, R. K. Chutani, C. Gorecki, R. Boudot, P. Dziuban, V. Giordano, S. Clatot, and L. Mauri, "Microfabrication of cesium vapor cells with buffer gas for MEMS atomic clocks," *Sens. Actuators Phys.*, vol. 167, no. 2, pp. 594–601, 2011.
- [150] A. D. Yoffe and C. B. Colburn, *Developments in Inorganic Nitrogen Chemistry*. New York Publisher, 1966.
- [151] L.-A. Liew, J. Moreland, and V. Gerginov, "Wafer-level filling of microfabricated atomic vapor cells based on thin-film deposition and photolysis of cesium azide," *Appl. Phys. Lett.*, vol. 90, pp. 114106–1 – 114106–3, 2007.
- [152] F. Blatter and E. Schumacher, "Production of High-Purity Caesium," *J. -Common Met.*, vol. 115, pp. 307–313, 1986.
- [153] P. Knapkiewicz, J. Dziuban, R. Walczak, L. Mauri, P. Dziuban, and C. Gorecki, "MEMS caesium vapour cell for european micro-atomic-clock," *Procedia Eng.*, vol. 5, pp. 721–724, 2010.
- [154] F. Vecchio, V. Venkatraman, H. R. Shea, T. Maeder, and P. Ryser, "Dispensing and hermetic sealing Rb in a miniature reference cell for integrated atomic clocks," *Sens. Actuators Phys.*, vol. 172, no. 1, pp. 330–335, 2011.
- [155] L.-A. Liew, S. Knappe, J. Moreland, H. Robinson, L. Hollberg, and J. Kitching, "Microfabricated alkali atom vapor cells," *Appl. Phys. Lett.*, vol. 84, no. 14, pp. 2694–2696, 2004.
- [156] Z. Mei and J. W. Morris, "Characterization of eutectic Sn-Bi solder joints," *J. Electron. Mater.*, vol. 21, no. 6, pp. 599–607, 1992.
- [157] A. Z. Miric and A. Grusd, "Lead-free alloys," *Solder. Surf. Mt. Technol.*, vol. 10, no. 1, pp. 19–25, 1998.

References

- [158] J. Glazer, “Microstructure and mechanical properties of Pb-free solder alloys for low-cost electronic assembly: a review,” *J. Electron. Mater.*, vol. 23, no. 8, pp. 693–700, 1994.
- [159] W. Yang, R. W. Messler, and L. E. Felton, “Microstructure evolution of eutectic Sn-Ag solder joints,” *J. Electron. Mater.*, vol. 23, no. 8, pp. 765–772, 1994.
- [160] H. Theuss, T. Kilger, and T. Ort, “Solder joint reliability of lead-free solder balls assembled with SnPb solder paste,” in *Electronic Components and Technology Conference, 2003. Proceedings. 53rd*, 2003, pp. 331–337.
- [161] R. Straessle, M. Pellaton, C. Affolderbach, Y. Pétremand, D. Briand, G. Mileti, and N. F. de Rooij, “Low-temperature indium-bonded alkali vapor cell for chip-scale atomic clocks,” *J. Appl. Phys.*, vol. 113, no. 6, pp. 064501–064501, 2013.
- [162] Y. Pétremand, C. Schori, R. Straessle, G. Mileti, N. de Rooij, and P. Thomann, “Low temperature indium-based sealing of microfabricated alkali cells for chip scale atomic clocks,” in *Proc. European Frequency and Time Forum (EFTF)(Noordwijk, NL, 13–15 April 2010)*, 2010, p. 119.
- [163] R. Straessle, Y. Pétremand, D. Briand, N. F. de Rooij, M. Pellaton, C. Affolderbach, and G. Mileti, “Towards wall-coated microfabricated cells: Alkali vapor-cells using indium thin-film low-temperature bonding,” in *European Frequency and Time Forum (EFTF)*, 2012, 2012, pp. 309–311.
- [164] R. Straessle, M. Pellaton, C. Affolderbach, Y. Pétremand, D. Briand, G. Mileti, and N. F. de Rooij, “Low-temperature indium-bonded alkali vapor cell for chip-scale atomic clocks,” *J. Appl. Phys.*, vol. 113, no. 6, pp. 064501–064501, 2013.
- [165] R. Straessle, Y. Pétremand, D. Briand, and N. F. de Rooij, “Evaluation of thin film indium bonding at wafer level,” *Procedia Eng.*, vol. 25, pp. 1493–1496, 2011.
- [166] R. Straessle, “Low Temperature Hermetic Wafer Bonding and Microfabrication of Wall-Coated Alkali Vapor Cell for Chip Scale Atomic Clocks,” EPFL, 2013.
- [167] A. D. Pelton, “The Au- Rb (Gold-Rubidium) system,” *Bull. Alloy Phase Diagr.*, vol. 7, no. 2, pp. 139–142, 1986.
- [168] O. Loebich and C. H. J. Raub, “Reactions between some alkali and platinum group metals,” *Platin. Met Rev*, vol. 25, no. 3, pp. 113–120, 1981.
- [169] G. Kienast, J. Verma, and W. Klemm, “Das Verhalten der Alkalimetalle zu Kupfer, Silber und Gold,” *Z. Für Anorg. Allg. Chem.*, vol. 310, no. 3, pp. 143–169, 1961.
- [170] B. Predel and O. Madelung, “Ag-Rb(Silver-Rubidium),” *Landolt-Börnstein-Group IV Phys. Chem.*, vol. 5a, pp. 1–2, 1991.
- [171] J. Sangster and C. W. Bale, “The Rb-Sn (rubidium-tin) system,” *J. Phase Equilibria Diffus.*, vol. 19, no. 1, pp. 82–85, 1998.
- [172] J. A. Meijer and W. Van der Lugt, “Resistivity of liquid K-Bi and Cs-Bi alloys,” *J. Phys. Condens. Matter*, vol. 1, no. 48, pp. 9779–9784, 1989.
- [173] B. Predel and O. Madelung, “Pb-Rb (Lead-Rubidium),” *Landolt-Börnstein-Group IV Phys. Chem.*, vol. 5i, pp. 1–2, 1998.
- [174] J. D. Corbett, “Polyatomic Zintl anions of the post-transition elements,” *Chem. Rev.*, vol. 85, no. 5, pp. 383–397, 1985.
- [175] D. Ambrose and C. Tsonopoulos, “Vapor-liquid critical properties of elements and compounds. 2. Normal alkanes,” *J. Chem. Eng. Data*, vol. 40, no. 3, pp. 531–546, 1995.
- [176] D. Mackay and W. Y. Shiu, “A critical review of Henry’s law constants for chemicals of environmental interest,” *J. Phys. Chem. Ref. Data*, vol. 10, p. 1175, 1981.

- [177] R. Battino, T. Rettich, and T. Tominaga, "The Solubility of Nitrogen and Air in Liquids," *J. Phys. Chem. Ref. Data*, vol. 13, no. 2, pp. 563–600, 1984.
- [178] W. Gao, R. L. Robinson, and K. A. Gasem, "High-pressure solubilities of hydrogen, nitrogen, and carbon monoxide in dodecane from 344 to 410 K at pressures to 13.2 MPa," *J. Chem. Eng. Data*, vol. 44, no. 1, pp. 130–132, 1999.
- [179] P. J. Hesse, R. Battino, P. Scharlin, and E. Wilhelm, "Solubility of Gases in Liquids. 20. Solubility of He, Ne, Ar, Kr, N₂, O₂, CH₄, CF₄, and SF₆ in n-Alkanes n-C₁H₂l+2 (6 ≤ l ≤ 16) at 298.15 K," *J. Chem. Eng. Data*, vol. 41, no. 2, pp. 195–201, 1996.
- [180] R. Battino, "The Ostwald coefficient of gas solubility," *Fluid Phase Equilibria*, vol. 15, no. 3, pp. 231–240, 1984.
- [181] T. Boublík, V. Fried, and E. Hála, "The vapour pressures of pure substances," 1984.
- [182] C. Tsonopoulos, "Thermodynamic analysis of the mutual solubilities of normal alkanes and water," *Fluid Phase Equilibria*, vol. 156, no. 1, pp. 21–33, 1999.
- [183] R. N. Hazlett, J. M. Hall, and M. Matson, "Reactions of aerated N-dodecane liquid flowing over heated metal tubes," *Ind. Eng. Chem. Prod. Res. Dev.*, vol. 16, no. 2, pp. 171–177, 1977.
- [184] P. Schatzberg, "Solubilities of Water in Several Normal Alkanes from C₇ to C₁₆," *J. Phys. Chem.*, vol. 67, no. 4, pp. 776–779, 1963.
- [185] Y. Fournier, T. Maeder, G. Boutinard-Rouelle, A. Barras, N. Craquelin, and P. Ryser, "Integrated LTCC Pressure/Flow/Temperature Multisensor for Compressed Air Diagnostics†," *Sensors*, vol. 10, no. 12, pp. 11156–11173, 2010.
- [186] J. E. Gragg Jr, "Silicon pressure sensor," 4,317,126Feb-1982.
- [187] H. C. Lim, B. Schulkin, M. J. Pulickal, S. Liu, R. Petrova, G. Thomas, S. Wagner, K. Sidhu, and J. F. Federici, "Flexible membrane pressure sensor," *Sens. Actuators Phys.*, vol. 119, no. 2, pp. 332–335, 2005.
- [188] R. Singh, L. L. Ngo, H. S. Seng, and F. N. C. Mok, "A silicon piezoresistive pressure sensor," in *Electronic Design, Test and Applications, 2002. Proceedings. The First IEEE International Workshop on*, 2002, pp. 181–184.
- [189] Z. Yulong, Z. Libo, and J. Zhuangde, "A novel high temperature pressure sensor on the basis of SOI layers," *Sens. Actuators Phys.*, vol. 108, no. 1, pp. 108–111, 2003.
- [190] J. Martin, W. Bacher, O. F. Hagen, and W. K. Schomburg, "Strain gauge pressure and volume-flow transducers made by thermoplastic molding and membrane transfer," in *Micro Electro Mechanical Systems, 1998. MEMS 98. Proceedings., The Eleventh Annual International Workshop on*, 1998, pp. 361–366.
- [191] F. Hua, Z. Mei, and J. Glazer, "Eutectic Sn-Bi as an alternative to Pb-free solders," in *Electronic Components & Technology Conference, 1998. 48th IEEE*, 1998, pp. 277–283.
- [192] J. M. Parsey Jr, S. Valocchi, W. Cronin, J. Mohr, B. L. Scrivner, and K. Kyler, "A metallurgical assessment of SnPbAg solder for GaAs power devices," *JOM*, vol. 51, no. 3, pp. 28–31, 1999.
- [193] L. Li, Y. Rao, and J.-K. Lin, "Pb-free solder paste reflow window study for flip chip wafer bumping," in *Advanced Packaging Materials: Processes, Properties and Interfaces, 2001. Proceedings. International Symposium on*, 2001, pp. 112–118.
- [194] C. Melton, "Reflow soldering evaluation of lead free solder alloys," in *Electronic Components and Technology Conference, 1993. Proceedings., 43rd*, 1993, pp. 1008–1011.

References

- [195] T. Laine-Ylijoki, H. Steen, and A. Forsten, "Development and validation of a lead-free alloy for solder paste applications," *Compon. Packag. Manuf. Technol. Part C IEEE Trans. On*, vol. 20, no. 3, pp. 194–198, 1997.
- [196] W. Vogel, *Glass chemistry*. Springer-Verlag, 1994.
- [197] Y.-Y. Chen, J.-G. Duh, and B.-S. Chiou, "The effect of substrate surface roughness on the wettability of Sn-Bi solders," *J. Mater. Sci. Mater. Electron.*, vol. 11, no. 4, pp. 279–283, 2000.
- [198] T. A. Powers, T. J. Singler, and J. A. Clum, "Role of tin content in the wetting of Cu and Au by tin-bismuth solders," *J. Electron. Mater.*, vol. 23, no. 8, pp. 773–778, 1994.
- [199] C. A. MacKay and W. D. Von Voss, "Effect of compositional changes and impurities on wetting properties of eutectic Sn-Bi alloy used as solder," *Mater. Sci. Technol.*, vol. 1, no. 3, pp. 240–248, 1985.
- [200] R. L. Turner, "Water-soluble soldering flux," 5,085,365Feb-1992.
- [201] F. M. Zado, "Solder flux," 4,342,607Aug-1982.
- [202] J. F. Shipley, "Influence of Flux, Substrate and Solder Composition on Solder Wetting," *WeZding Res. SuppZement*, 1975.
- [203] P. G. Kim and K. N. Tu, "Morphology of wetting reaction of eutectic SnPb solder on Au foils," *J. Appl. Phys.*, vol. 80, no. 7, pp. 3822–3827, 1996.
- [204] H. Shimokawa, M. Okamoto, and K. Serizawa, "Evaluation of soldering properties with various types of metallization," in *Environmentally Conscious Design and Inverse Manufacturing, 2003. EcoDesign'03. 2003 3rd International Symposium on*, 2003, pp. 821–828.
- [205] A. Nicholson and D. Bloomfield, "The Use of Bismuth Alloy Systems for Reflow and Wave Soldering," *Solder. Surf. Mt. Technol.*, vol. 4, no. 1, pp. 23–26, 1992.
- [206] C. Melton, "The effect of reflow process variables on the wettability of lead-free solders," *JOM*, vol. 45, no. 7, pp. 33–35, 1993.
- [207] "ESL 590G datasheet." [Online]. Available: <http://www.electroscience.com/pdf/590.pdf>.
- [208] "ESL 9912A datasheet." [Online]. Available: <http://www.electroscience.com/pdf/9912-A.pdf>.
- [209] "Information about Dow Corning adhesive." [Online]. Available: www.dowcorning.com.
- [210] "Information about EPOTEK Epoxy." [Online]. Available: www.epotek.com.
- [211] S. G. Jadhav, T. R. Bieler, K. N. Subramanian, and J. P. Lucas, "Stress relaxation behavior of composite and eutectic Sn-Ag solder joints," *J. Electron. Mater.*, vol. 30, no. 9, pp. 1197–1205, 2001.
- [212] P. Hall, "Creep and stress relaxation in solder joints of surface-mounted chip carriers," *Compon. Hybrids Manuf. Technol. IEEE Trans. On*, vol. 10, no. 4, pp. 556–565, 1987.
- [213] M. D. Rotondaro and G. P. Perram, "Collisional Broadening and Shift of the Rb D1 and D2 lines by Rare Gases, H₂, D₂, N₂, CH₄ and CF₄," *J. Quant. Spectrosc. Radiat. Transf.*, vol. 57, no. 4, pp. 497–507, 1997.
- [214] "Information about Schott glass." [Online]. Available: www.schott.com.
- [215] Y. Wang, G. Zhang, and J. Ma, "Research of LTCC/Cu, Ag multilayer substrate in microelectronic packaging," *Mater. Sci. Eng. B*, vol. 94, no. 1, pp. 48–53, 2002.

- [216] A. Roosen, "New lamination technique to join ceramic green tapes for the manufacturing of multilayer devices," *J. Eur. Ceram. Soc.*, vol. 21, no. 10, pp. 1993–1996, 2001.
- [217] M. A. Piwonski and A. Roosen, "Low pressure lamination of ceramic green tapes by gluing at room temperature," *J. Eur. Ceram. Soc.*, vol. 19, no. 2, pp. 263–270, 1999.
- [218] N. Suppakarn, H. Ishida, and J. Cawley, "Roles of Poly(propylene glycol) during Solvent-Based Lamination of Ceramic Green Tapes," *J. Am. Ceram. Soc.*, vol. 84, no. 2, pp. 289–294, 2001.
- [219] Z. M. Da Rocha, N. Ibañez-Garcia, N. A. Oliveira, J. R. Matos, and M. R. Gongora-Rubio, "Low temperature and pressure lamination of LTCC tapes for meso-systems," in *IMAPS Conference and exhibition on ceramic interconnect technology*, Denver, 2004.
- [220] D. Jurkow and L. Golonka, "Cold Chemical Lamination—New Bonding Technique of LTCC Green Tapes," *Int. J. Appl. Ceram. Technol.*, vol. 7, no. 6, pp. 814–820, 2010.
- [221] D. Jurków and L. Golonka, "Novel cold chemical lamination bonding technique—A simple LTCC thermistor-based flow sensor," *J. Eur. Ceram. Soc.*, vol. 29, no. 10, pp. 1971–1976, 2009.
- [222] "DuPont thinners and reducers." [Online]. Available: http://pc.dupont.com/dpc/en/US/html/visitor/common/pdfs/b/product/dic/MSDS/US_en_GNRC_8-0_DIC.pdf.
- [223] "Web material data PDMS." [Online]. Available: <http://www.mit.edu/~6.777/matprops/pdms.htm>.
- [224] T. Maeder, B. Jiang, F. Vecchio, C. Jacq, P. Ryser, and P. Muralt, "Lamination of LTCC at low pressure and moderate temperature using screen-printed adhesives," *Proc. 8th Int. Conf. Ceram. Interconnect Ceram. Microsyst. Technol. CICMT*, pp. 348–352, 2012.
- [225] J. Burke, *Solubility parameters: theory and application*, vol. 3. American Insitute for Conservation of Historic and Artistic Works, 1984.
- [226] "UBM Laser Profilometer - specifications." [Online]. Available: <http://www.iot.rwth-aachen.de/index.php?id=910>.
- [227] "Dupont 2000 Resistor Series datasheet." [Online]. Available: http://www2.dupont.com/MCM/en_US/assets/downloads/prodinfo/2000.pdf.
- [228] "Dupont 6146-Silver/palladium cofireable solderable conductor datasheet." [Online]. Available: http://www2.dupont.com/MCM/en_US/assets/downloads/prodinfo/6146.pdf.
- [229] "DuPont 5092D - PTC Thermistor Composition Datasheet." [Online]. Available: http://www2.dupont.com/MCM/en_US/assets/downloads/prodinfo/5091D_5092D_5093D.pdf.
- [230] W. H. Butler and G. M. Stocks, "Calculated electrical conductivity and thermopower of silver-palladium alloys," *Phys. Rev. B*, vol. 29, no. 8, p. 4217, 1984.
- [231] R. Franz and G. Wiedemann, "Ueber die Wärme-Leitungsfähigkeit der Metalle," *Ann. Phys.*, vol. 165, no. 8, pp. 497–531, 1853.
- [232] G. V. Chester and A. Thellung, "The law of Wiedemann and Franz," *Proc. Phys. Soc.*, vol. 77, no. 5, p. 1005, 1961.
- [233] D. W. Yarbrough, R. K. Williams, and R. S. Graves, "Transport Properties of Concentrated Ag-Pd and Cu-Ni Alloys from 300–1000 K," in *Thermal Conductivity 16*, Springer, 1983, pp. 319–324.

References

- [234] “ESL - Silver paste ESL 9912 datasheet.” [Online]. Available: <http://www.electroscience.com/pdf/9912-A.pdf>.
- [235] “ESL - Silver paste ESL 9910 Datasheet.” [Online]. Available: <http://www.electroscience.com/pdf/9910-C.pdf>.
- [236] F. W. Sears, M. W. Zemansky, and H. D. Young, *University physics, 7th Ed.* Addison-Wesley Reading, UK, 1982.
- [237] F. Vecchio, C. Slater, T. Maeder, and P. Ryser, “Thermal Characterization of an LTCC Module for Miniature Atomic Clock Packaging,” presented at the Ceramic Interconnect and Ceramic Microsystems Technologies (CICMT), Erfurt, Germany, 2012, pp. 484–491.
- [238] J. W. Elder, “Laminar free convection in a vertical slot,” *J Fluid Mech*, vol. 23, no. 1, pp. 77–98, 1965.
- [239] S. W. Churchill and H. H. Chu, “Correlating equations for laminar and turbulent free convection from a vertical plate,” *Int. J. Heat Mass Transf.*, vol. 18, no. 11, pp. 1323–1329, 1975.
- [240] H. B. Awbi, “Calculation of convective heat transfer coefficients of room surfaces for natural convection,” *Energy Build.*, vol. 28, no. 2, pp. 219–227, 1998.
- [241] F. Vecchio, T. Maeder, C. Slater, and P. Ryser, “Effects of thermal losses on the heating of a multifunctional LTCC module for atomic clock packaging,” *Solid State Phenom.*, vol. 188, pp. 244–249, 2012.
- [242] D. G. Cahill, “Thermal conductivity measurement from 30 to 750 K: the 3omega method,” *Rev. Sci. Instrum.*, vol. 61, no. 2, pp. 802–808, 1990.
- [243] T. C. Harman, J. H. Cahn, and M. J. Logan, “Measurement of thermal conductivity by utilization of the Peltier effect,” *J. Appl. Phys.*, vol. 30, no. 9, pp. 1351–1359, 1959.
- [244] Q. M. Li, R. A. W. Mines, and R. S. Birch, “The crush behaviour of Rohacell-51 WF structural foam,” *Int. J. Solids Struct.*, vol. 37, no. 43, pp. 6321–6341, 2000.
- [245] S. Schilt and K. P. Petrov, “Diode laser spectroscopic monitoring of trace gases,” *Encycl. Anal. Chem.*, 2011.
- [246] D. Budker and M. Romalis, “Optical magnetometry,” *Nat. Phys.*, vol. 3, no. 4, pp. 227–234, 2007.
- [247] P. A. Roos, M. Stephens, and C. E. Wieman, “Laser vibrometer based on optical-feedback-induced frequency modulation of a single-mode laser diode,” *Appl. Opt.*, vol. 35, no. 34, pp. 6754–6761, 1996.
- [248] G. P. Amautov, D. Boulanger, and E. N. Kalish, “‘Gabl’, an Absolute Free-Fall Laser Gravimeter,” *Metrologia*, vol. 19, pp. 49–55, 1983.
- [249] T. Bandi, C. Affolderbach, C. E. Calosso, and G. Miletì, “High-performance laser-pumped rubidium frequency standard for satellite navigation,” *Electron. Lett.*, vol. 47, no. 12, pp. 698–699, 2011.
- [250] R. Michalzik, *VCSELs: Fundamentals, Technology and Applications of Vertical-cavity Surface-emitting Lasers*. Springer, 2013.
- [251] C. W. Wilmsen and H. Temkin, *Vertical-cavity surface-emitting lasers: design, fabrication, characterization, and applications*, vol. 24. Cambridge University Press, 2001.
- [252] J. Di Francesco, F. Gruet, C. Schori, C. Affolderbach, R. Matthey, G. Miletì, Y. Salvadé, Y. Pétremand, and N. De Rooij, “Evaluation of the frequency stability of a

- VCSEL locked to a micro-fabricated Rubidium vapour cell,” in *SPIE Photonics Europe*, 2010, p. 77201T–77201T.
- [253] F. Gruet, F. Vecchio, C. Affolderbach, Y. Pétremand, N. F. de Rooij, T. Maeder, and G. Miletì, “A miniature frequency-stabilized VCSEL system emitting at 795nm based on LTCC modules,” *Opt. Lasers Eng.*, 2013.
- [254] Y. Koyama, H. Matsuura, K. Atsumi, K. Nakamuta, M. Sakai, and I. Maruyama, “An ultra-miniature rubidium frequency standard,” in *Frequency Control Symposium and Exhibition, 2000. Proceedings of the 2000 IEEE/EIA International*, 2000, pp. 694–699.
- [255] M. Pellaton, C. Affolderbach, Y. Pétremand, N. de Rooij, and G. Miletì, “Study of laser-pumped double-resonance clock signals using a microfabricated cell,” *Phys. Scr.*, vol. 2012, no. T149, p. 014013, 2012.
- [256] W. E. Bell, A. L. Bloom, and J. Lynch, “Alkali metal vapor spectral lamps,” *Rev. Sci. Instrum.*, vol. 32, no. 6, pp. 688–692, 1961.
- [257] D. K. Serkland, K. M. Geib, G. M. Peake, R. Lutwak, A. Rashed, M. Varghese, G. Tepolt, and M. Prouty, “VCSELs for atomic sensors,” in *Integrated Optoelectronic Devices 2007*, 2007, pp. 648406–648406.
- [258] V. Venkatraman, Y. Petremand, C. Affolderbach, G. Miletì, N. F. de Rooij, and H. Shea, “Microfabricated chip-scale rubidium plasma light source for miniature atomic clocks,” *Ultrason. Ferroelectr. Freq. Control IEEE Trans. On*, vol. 59, no. 3, pp. 448–456, 2012.
- [259] V. Venkatraman, H. Shea, F. Vecchio, T. Maeder, and P. Ryser, “LTCC integrated miniature Rb discharge lamp module for stable optical pumping in miniature atomic clocks and magnetometers,” in *Design and Technology in Electronic Packaging (SIITME), 2012 IEEE 18th International Symposium for*, 2012, pp. 111–114.
- [260] M. Violetti, F. Merli, J.-F. Zurcher, A. K. Skrivervik, M. Pellaton, C. Affolderbach, and G. Miletì, “New miniaturized microwave cavity for Rubidium atomic clocks,” in *Sensors, 2012 IEEE*, 2012, pp. 1–4.
- [261] “Information about Spectratime StarLPRO.” [Online]. Available: <http://www.spectratime.com/products/isource/rubidium/StarLPRO/>.

References

Curriculum Vitae

VECCHIO FABRIZIO

RUE DE LA SOURCE, 5. 1020
RENENS (VD) SUISSE.

Tel: 0041 78 936 09 24

vecchio.fabri@gmail.com

Italian

29 years old

- **Microtechnology engineer**

- Innovative solutions for the electronic packaging of microsystems
 - LTCC and thick film technology
 - Analogue and digital electronics
 - Continuous improving of a production process
 - Polyglot : FR, ENG, ITA, SPA, PRT
-

EDUCATION

July 2009 – expected October 2013
(4 years and 5 months)

Ph.D in microtechnology at EPFL – LPM (Laboratoire Production Microtechnique).

Objective: Conception, design, simulation, fabrication and test of sensors (mm-scale) and of electronic temperature control modules for the electronic packaging of microsystems, using LTCC and thick film technologies.

Results : Conception of a new layout, cheaper and easier to produce, for a force sensor which is produced in series and sold worldwide

January 2007 – April 2009 (2 years and 4 months)

Master in Electrical Engineering at Università degli Studi di Cassino - Italia

Dissertation : “Thermonuclear Controlled Fusion : Cheese and KINX codes for MHD Stability”

January 2007 – October 2008 (1 years and 10 months)

Bachelor in Electronic Engineering at Glyndwr University – Wales, UK

Dissertation : “Design and test of a PID Temperature Control using a PIC Microcontroller”

Septembre 2003 – Décembre 2006
(3 ans et 3 mois)

Bachelor in Electrical Engineering at Università degli Studi di Cassino - Italia

Dissertation : “Study of the Performance of field buses, with Particular Emphasis on the CAN bus”

PROFESSIONAL EXPERIENCE - INTERNSHIPS

January 2009 – April 2009 (4 months) Internship at EPFL – CRPP (Centre de Recherche en Physique des Plasmas)

Objective : Develop methods for automatically run some numerical codes in order to accelerate the data acquisition

Results: Creation of a user-friendly GUI (Graphical User Interface), using Matlab. The GUI allows to easily run the numerical codes and it is still used in the lab

PROJECTS

2009 – 2013 : Improving the production chain of a force sensor (Ph.D project - Supervision of 4 students)

Objective : Accelerate the production or improving the efficiency of the production chain of a force sensor

Results: Different aspects of the fabrication and of the test procedure of the final product were improved thanks to my action. This allowed to significantly speed up the production of the sensor, therefore decreasing the production cost.

2008 : Implementation and test of a PID temperature controller (Bachelor project)

Objective : Development of an electronic PID temperature controller (cm-scale)

Results: Production of a complete and working PCB module, with indication of actual temperature and possibility to set up the wished temperature. A microcontroller, programmed in C++, regulate the current flow into a heating resistor, therefore allowing controlling the temperature.

LANGUAGES

- **Italian :** Mother tongue
- **French :** Advanced
- **English :** Advanced
- **Spanish :** Advanced (D.E.L.E., Diplôma de español como Lengua extranjera, nivel superior)
- **Portugues:** Intermediate

TECHNICAL SKILLS

	Informatic skills :
Office	Excellent
Protel Altium (for PCB layout)	Excellent
Hyde (for LTCC layout)	Excellent
SolidWorks	Intermediate
Matlab	Intermediate
PSpice (Electrical Simulations)	Intermediate
Ansys (Finite-element simulations)	Intermediate
C / C++	Intermediate
Labview	Intermediate

Practical skills :

- Quality control : **FMEA** and **6sigma**
- PCB fabrication, soldering and electronic skills
- Practical skills in working in a laboratory of thick film and LTCC production: laser cut, screen-printing technology.
- Trained for working in a cleanroom

LIST OF PRINCIPAL PUBLICATIONS

Vecchio F., Maeder T., Ryser P. , “Assessment of the Hermeticity of different Low-temperature LTCC-Glass bonding Techniques”, Solid State Phenomena, in press

Vecchio F., Slater C., Maeder T., Ryser P., “Thermal Characterization of an LTCC Module for Miniature Atomic Clock Packaging”, Proceedings of CICMT 2012 Erfurt, Germany, pp. 484-491

Vecchio F., Maeder T., Slater C., Ryser P., “Effects of Thermal Losses on the Heating of a Multifunctional LTCC Module for Atomic Clock Packaging”, 2012, Solid State Phenomena, Vol 188, pp. 244-249

Vecchio F., Venkatraman V., Shea H., Maeder T., Ryser P., “Dispensing and Hermetic Sealing Rb in a Miniature Reference Cell for Integrated Atomic Clocks”, 2011, Sensors and Actuators A: Physical, pp. 330-335